Charles University

Faculty of Science

Study program: Applied Geology

Martin Bachura

The Structure of the West Bohemian Earthquake Swarm Source Zone

Doctoral thesis

Supervisor: Prof. Tomáš Fischer, PhD.

Prague, 2017

Univerzita Karlova

Přírodovědecká fakulta

Studijní program: Aplikovaná Geologie

Martin Bachura

Struktura zdrojové oblasti západočeských rojových zemětřesení

Dizertačná práca

Školiteľ: Prof. Tomáš Fischer, PhD.

Praha, 2017

Declaration of Authorship

I, Mgr. Martin BACHURA, declare that this thesis titled, "The Structure of the West Bohemian Earthquake Swarm Source Zone" and the work presented in it are my own. I confirm that:

- This work was done wholly or mainly while in candidature for a research degree at this University.
- Where any part of this thesis has previously been submitted for a degree or any other qualification at this University or any other institution, this has been clearly stated.
- Where I have consulted the published work of others, this is always clearly attributed.
- Where I have quoted from the work of others, the source is always given. With the exception of such quotations, this thesis is entirely my own work.
- I have acknowledged all main sources of help.
- Where the thesis is based on work done by myself jointly with others, I have made clear exactly what was done by others and what I have contributed myself.

Signed: _____

Date: _____

Prehlásenie o autorstve

Ja, Mgr. Martin BACHURA, prehlasujem, že prácu "Struktura zdrojové oblasti západočeských rojových zemětřesení" som vypracoval samostatne. Ďalej prehlasujem, že:

- Táto práca slúži predovšetkým k získaniu titulu na Univerzite Karlovej.
- Práca, ani jej podstatná časť neboli predložené k získaniu iného alebo rovnakého akademického titulu.
- Všetky časti práce, ktoré som vypracovával a konzultoval s ďalšími osobami, sú jasne označené.
- Tam, kde som citoval práce iných autorov je vložený odkaz na danú prácu. S výnimkou citovaných častí som text a jeho obsah vypracoval samostatne.
- Vymenoval som všetky osoby a zdroje, ktoré mi boli nápomocné v tvorbe práce.
- Miesta, kde je obsah práce výsledkom skúmania vo vedeckom týme alebo v spolupráci s ďalšími autormi sú jasne označené. Je tiež zdôraznené, čo konkrétne som v danej tématike vypracovával sám.

Podpísaný: _____

Dátum: _____

Abstract

The Structure of the West Bohemian Earthquake Swarm Source Zone

Martin Bachura

Institute of Hydrogeology, Engineering Geology and Applied Geophysics

Faculty of Science, Charles University

We analyzed crustal characteristics of Earth's crust under West Bohemia earthquake swarm region from three different optics. Seismic episodes from 2008, 2011 and 2014 were subjects of relocating using double-difference *HypoDD* technique supplemented with cross-correlated input data. used data processing was proved to be efficient and produced highly precise relative locations of swarm earthquakes distributed on a single fault plane. Results were suitable for statistical and detailed spatio-temporal analyses. Moreover, used procedure was applicable even to a data achieved fully automatically (catalogs, picks) with lower initial quality. In that case the relocations are sufficiently good as a tool for mapping underground structures. On the other hand, resulting completeness and locations of stronger events might be biased as a result of sparse data (picks and differential times) and magnitude differences.

Attenuation properties of the crust were derived from coda of 30 earthquakes from 2008, 2011 and 2014 activity. Reliable frequency dependent quality factors were estimated for coda decay - Q_c, intrinsic loss and scattering - Q_i and Q_{sc} using coda window method and multiple lapse time window analysis. Less reliable results were achieved by coda normalization method for P- and S-waves - Q_P, Q_S. According to obtained results it might be conclude that attenuation is rather low (quality factors up to first thousands) and intrinsic loss is dominant attenuation process afflicting the propagation of seismic waves. We tried to explain alway unclear frequency dependent of intrinsic loss quality factor Q_i as a result of diffusive energy leak towards Earth's mantle. If so, then the magnitude of such a leakage enhances the Q_i estimations and causes its frequency dependence. Constant level of real Q_i is then 3300-4000. Coda methods don't allow to study spatial distribution of attenuation for such a small areas like West Bohemia with its seismic network is.

The rheological properties of Earth materials are expressed by their seismic velocities and V_P/V_S ratio, which is easily obtained by the Wadati method. Its double-difference version based on cross-correlated waveforms enables focusing on very local structures and allows tracking, monitoring and analyzing the fluid activity along faults. We applied the method to three 2014 mainshock–aftershock sequences in the West Bohemia and found pronounced V_P/V_S variations in time and space for different clusters of events located on a steeply dipping fault zone at depths ranging from 7 to 11 km. Each cluster reflects the spatial distribution of earthquakes along the fault plane but also the temporal evolution of the activity. Low values of V_P/V_S ratio down to 1.59 ± 0.02 were identified in the deeper part of the fault zone whereas higher values up to 1.73 ± 0.01 were estimated for clusters located on a shallower segment of the fault. Temporally the low V_P/V_S values are associated with the early aftershocks, while the higher V_P/V_S ratios are related only to later aftershocks. We interpret this behavior as a result of saturation of the focal zone by compressible fluids: in the beginning the mainshock and early aftershocks driven by over-pressured fluids increased the porosity due to opening the fluid pathways. This process was associated with a decrease of the velocity ratio. In later stages the pressure and porosity decreased and the velocity ratio recovered to levels of 1.73, typical for a Poissonian medium and Earth's crust. Another possible interpretation is that the activity is on intersection f two geological units with different rheological properties and observed V_P/V_S is controlled by the position of the cluster.

Abstrakt

Struktura zdrojové oblasti západočeských rojových zemětřesení

Martin Bachura

Ústav hydrogeoloie, inženýrské geologie a užité geofyziky

Přírodovědecká fakulta, Univerzita Karlova

V tejto práci sme sa zamerali na charakteristiky zemskej kôry z rôznych hľadísk. Ako prvé sme relokovali zemetrasenia z aktivít rokov 2008, 2011 and 2014 za použitia relatívnej metódy *HypoDD* v kombinácii s kroskorelovanými vstupnými dátami. Zvolená metodika sa ukázala ako efektívna a umožnila analyzovanie geometrie zlomovej plochy za pomoci presne lokalizovaných zemetrasení na nej sa vyskytnuvších. Zvolená metodka sa nnavyše ukázala ako použiteľmá na spracovanie dát horšej kvality - automatickými katalógmi s automatickými čítaniami. *HypoDD* spolu s kroskoreláciami je schopné dosiahnuť veľmi dobré relokácie vhodné k mapovaniu zlomovej plochu. Na strane druhej však tento prístup trpí nedostatkami ako nepresná lokácia silných javov (dôsledok rozdielnych magnitúd javov pri korelovaní) či vyradenie mnohých zemetrasení v dôsledku filtrovania dát počas beho programu *HypoDD*.

V ďalšom kroku sme skúmali útlmové vlastnosti zemskej kôry v oblasti za pomoci analýzy seismickej kódy. K tomuto účelu sme vybrali 30 javov z rokov 2008, 2011 a 2014. Útlm, vyjadrený bezrozmerných faktorom kvality bol určený pre pokles amplitúd vĺn kódy - Q_c (coda window method), pre stratu premenou energie na teplo a rozptyl - Q_i and Q_{sc} (multiple lapse time window analysis) a pre P a S vlny - Q_P, Q_S (coda normalization method). Zatiaľ, čo prvé tri boli učernené s uspokojivými výsledkami, druhé dve treba brať s rezervou. Z pozorovaných frekvenčných závislotí faktorov kvality sa dá usudzovať, že útlm je relatívne nízky - Q sa pohybujú rádovo v prvých tisícoch. Strata energie v dôsledky nedokonalej elasticity prostredia (anelastický útlm) sa javí byť dominantným faktorom znižujúcim amplitúdy pozorovaným seismickým vlnám v oblasti. Pomocou teórie o úniku "difúznej" seismickej energie do zemského plášťa sme sa pokúsili vysvetliť večne diskutovanú frekvenčnú závislosť anelastického útlmu. Ak pripustíme túto teóriu výjde nám, že konštantná hodnota anelastického útlmu Q_i je v rozmedzí 3300 až 4000. Analýza kódy ako taká neumožňuje detailné rozlíšenie útlmu v priestore pre tak malé územie, ako sú Západné Čechy.

Na záver sme študovali reologické vlatsnosti materiálu v oblasti zdrojovej zóny zemetrasení. K tomu sme použili "double-difference" metódu a určovali V_P/V_S. K tomu sme použili vopred spočítané presné lokácie zemetrasení a kroskorelované vstupné dáta - časy rozdielov príchodov seismických vĺn na staniciach. K analýze bola zvolená aktivita z roku 2014. V prvom kroku sme rozdelili analyzované zemetrasenia na 7 klasterov kopírujúcich časový a priestorový vývoj aktivity a následne sme pre každý klaster určili hodnotu V_P/V_S. Nízke hodnoty V_P/V_S až 1.59 ± 0.02 boli pozorované v hlbšej partii zlomu, zatiaľ čo plytkejšia časť aktivovanej zlomovej zóny niesla V_P/V_S až 1.73 ± 0.01. Zhodou okolností tieto nízke hodnoty vo väčšej hĺbke dobre korelujú s prvými mainshock-ami, začiatkami aktivity. Vyššie hodnoty potom pokrývajú oblasť výskytu dotrasov. Toto správanie sa dá intepretovať ako výsledok nasýtenia zlomovej plochy plášťovými fluidami, ktoré pod tlakom spôsobia trhanie (zemetrasenia), dočasné zvýšenie porozity v jeho dôsledku a vyplnenie fluidami. Takýto proces sa vyznačuje znížením V_P/V_S. V následnej etape sa tlak flúid a porozita klesá a V_P/V_S s avracia k svojej tradičnej Poissonovskej hodnote 1.73. Ďalšia možná intepretácia stojí na pozorovaní, že rozdielne hodnoty V_P/V_S iba odzrkadľujú geologické rozhranie dvoch celkov s rozdielnymi vlastnosťami v oblasti pokrytej zemetraseniami.

Acknowledgements

First of all I would like to thank my supervisor Tomáš Fischer for fruitful discussions and positive motivation during the whole PhD. study. Additionally, I would like to thank all the people who have taken part in my educational process, who have helped me to find motivation, who have pushed me forward to a right direction or who have critically reviewed my scientific attempts. Namely Emmanuel Gaucher, Jiří Zahrandík, Oldřich Novotný, Václav Vavryčuk, Josef Horálek and Roland Gritto.

The research was financially supported by the Grant Agency of the Charles University (grant number 1584214: *Attenuation of the seismic waves in real geological environment*) and DAAD agency who supported my research stay in Germany.

Contents

List of Abbreviations

CNM	**C**oda **N**ormalization **M**ethod
CWM	**C**oda **W**indows **M**ethod
NKFZ	**N**ový **K**ostel **F**ocal **Z**one
MLTWA	**M**ultiple **L**apse **T**ime **W**indow **A**nalysis
RTT	**R**adiative **T**ransfer **T**heory
SNR	**S**ignal to **N**oise **R**atio
SXNET	**S**a**X**ony seismic **NET**work
WEBNET	**WE**st **B**ohemian seismic **NET**work

Chapter 1

Introduction

In 2015 NASA space probe Horizon reached the outer rim of the Solar system and sent to Earth the first detailed pictures of Pluto. For the first time in human history we were able to study Pluto's surface, atmosphere, morphology. It was the moment when the picture of a 4 billions km distant object became more detailed than picture of processes and structures occurring in depths bellow 1 km - on our own planet Earth.

Propagation of seismic waves has become one of the key phenomenons helping us to improve our understanding of the Earth's interior. Waves traveling through medium are affected by its physical properties. They might be slowed, attenuated, scattered etc. Seismic waves generated by artificial or natural sources on different scales (frequencies) bear the information of the medium they travel through. Our desire is to retrieve the information.

Chapter 2

Motivation

For studying small surface structures we make use of wave-fields generated by hammer or explosives. For analyzing the Earth's interior we require strong wave-field generators - earthquakes. In this works we analyze weak to moderate earthquakes from West Bohemia region, known for occurrence of so-called earthquake swarms. Our motivation is to describe the physical properties of the Earth's crust as the propagating medium with special focus on the source area of swarm earthquakes. The first objective is reached by studying the attenuation parameters of the crust while the latter by detailed measurements of V_P/V_S velocity ratio and its variations.

Assessing the attenuation properties of West Bohemian crust was carried out by application of methods analyzing seismic coda. We tested the methods applicability on West Bohemian data and then interpreted the results in the light of current knowledge. Quality factors of coda decay Q_c, intrinsic loss and scattering Q_i, Q_{sc}, for P- and S-waves Q_P, Q_S were estimated along with their frequency dependencies. We compare observed levels of different attenuations and discuss the frequency dependence of intrinsic loss - present in almost every coda study and still not explained in a satisfactory manner. Chapter 5 summarizes our efforts.

Analyzing the velocity ratio V_P/V_S might be used as a tool to monitor processes on the fault. The method itself is very sensitive to number of parameters and had to be adapted to a current dataset and carried out carefully. We made use of previously computed precise locations and studied spatial and temporal variations of the V_P/V_S. Discussion whether the observed variations could be interpreted from spatial or temporal optics was held. At the end of the V_P/V_S topic we propose a new method for V_P/V_S estimation, but since its only in its development phase we show only very preliminary results. V_P/V_S estimation is the topic of Chapter 6.

Space in this work was also given to a problem of earthquake relocations as only highly precise locations enabled spatio-temporal analyses of V_P/V_S. A double-difference method *HypoDD* was applied on cross-correlated data. We describe how we took method advantages and how did we attempted to avoid its disadvantages and overcome problems in Chapter 4

Chapter 3

West Bohemia

3.1 Geological and tectonic settings

The West Bohemia/Vogtland region forms the western part of the Bohemian Massif - one of the largest outcrops of pre-Permian rocks in Central and Wester Europe (formed between 500 and 250 Ma). The region is situated in the transition zone among three different Bohemian-Massif Variscan structural units (Figure 3.1): the Saxothuringian (in the north-west), the Teplá-Barrandian (central region), the Moldanubian (in the south-east). The area is intersected by two tectonic structures: ENE-WSW striking Eger Rift and N-S striking Regensburg-Leipzig–Rostock Zone (Figure 3.2). The Eger Rift hits the Regensburg-Leipzig-Rostock Zone in its middle and is delimited by approximately 100 km long Mariáské Lázně Fault striking NNW-SSE. Moreover, the intersection area is covered by up to 300 m of tertiary sediments from Cheb Basin (Fischer et al., 2014).

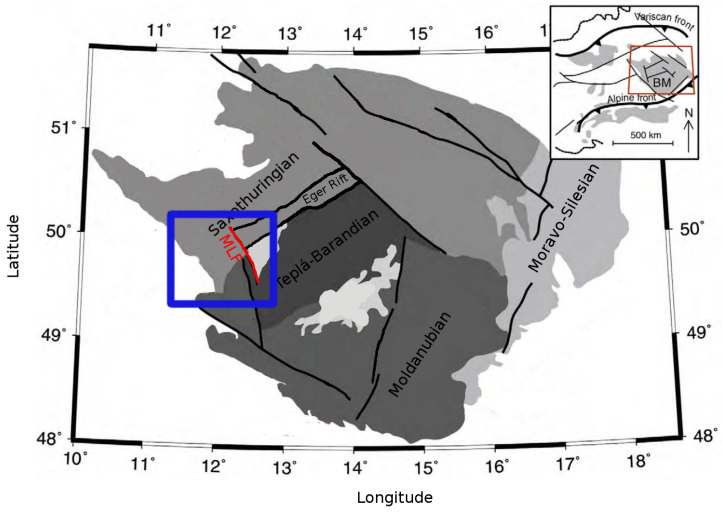

FIGURE 3.1: Basic stetch of Bohemian Massif tectonics with Variscan units: Saxothuringian, Teplá-Barandian and Modlanubian. Red line marks Mariáské Lázně Fault, blue rectangle outlines the zone, where the majority of the earthquakes occur. Figure modified after (Babuška, Plomerová, and Fischer, 2007)

Existence of above mentioned structures and faults is responsible for pronounced geodynamic activity throughout the geological history of the area: Quaternary volcanism (volcanos Komorní Hůrka and Železná Hůrka), numerous CO_2 rich mineral springs, CO_2 degassing sites and the most significant - seismic activity expressed in the form of earthquake swarms.

Deeper structures beneath the West Bohemia have been studied and analyzed by geophysical methods. Passive and active seismic experiments have revealed the high velocity lower

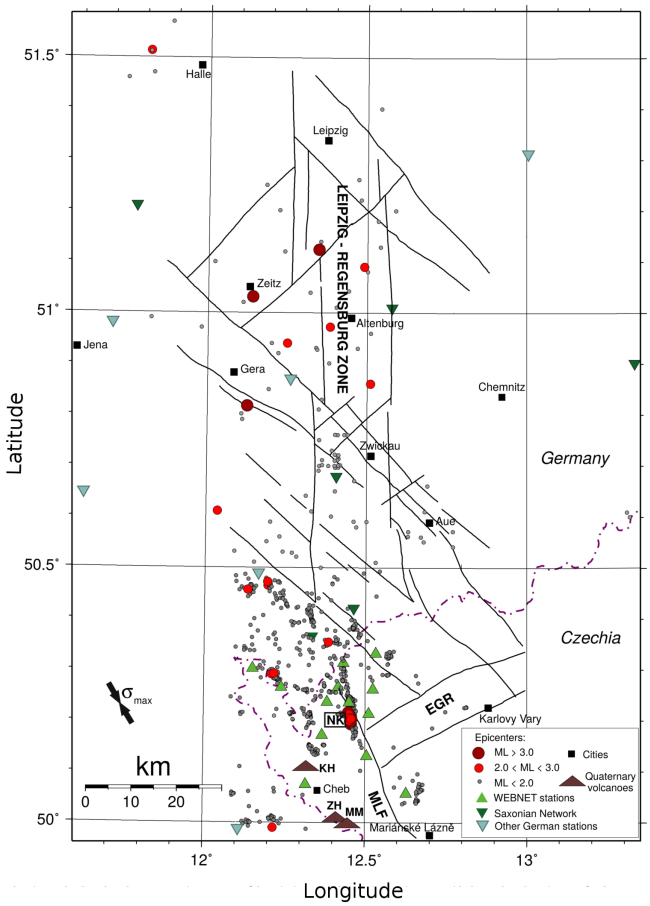

FIGURE 3.2: Overal view of the Leipzig-Regensburg-Rostock Zone with epicneters of earthquakes for the 1991-2011 period (grey and red circles). NK marks Nový Kostel - the most active focal zone with majority of released seismic energy at the intersection of Eger Rift (EGR) and Mariáské Lázně Fault (MLF). Volcanos Komorní Hůrka (KH), Železná Hůrka (ZH) and Mýtina maar (MM) are marked by brown triangles. Maximum compressional stress direction is indicated in the left bottom corner (Fischer et al., 2014).

crust with segmented MOHO discontinuity at depths ranging from 27 to 31 km (Hrubcová et al., 2013). 1-D velocity models have been estimated (Málek, Horálek, and Jánský, 2005; Novotný, Málek, and Bouška, 2016) and been in use for methods like earthquake locations and source parameters estimation. The models are plotted in Figure 3.3. Apart from 1-D velocity models a 3-D models have been estimated (e.g. Ružek and Horálek, 2013; Alexandrakis et al., 2014) adopting tomography approach. All the analyses show structure of the upper crust as the distribution of physical properties - seismic velocities, velocity ratios, wave reflectivities, impedances. Despite limited resolution of the methods some conclusions can be made:

- Crustal area is more or less composed of horiznotal layers with different physical properties, resulting from different geology (Figure 3.3)
- Zones of deformation are present and mapped by earthquake occurrence (Fischer, Matyska, and Heinecke, 2017; Ružek and Horálek, 2013)
- Crust is penetrated by 'channels' allowing mantle fluids to travel through (Fischer, Matyska, and Heinecke, 2017; Mousavi et al., 2015; Hainzl et al., 2016)

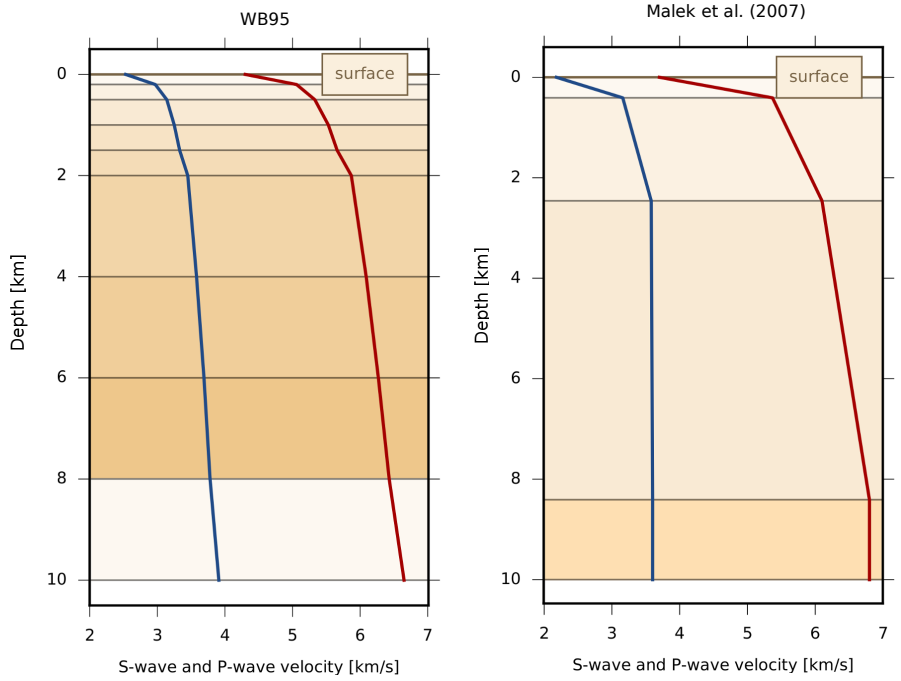

FIGURE 3.3: Velocity models for West Bohemian crust. On the left the model WB95 by (Novotný, 1995), on the right model by (Málek, Horálek, and Jánský, 2005)

3.2 Seismic activity

The West Bohemia region has been the focus of several highly active seismic episodes, expressed in the form of seismic swarms. Previously recorded major episodes have occurred in 1997, 2000, 2008, 2011 and 2014 (Fischer et al., 2014). During the weeks-long or months-long swarm activity, thousands of events have been observed with the strongest magnitudes exceeding $M_L = 3$. The strongest earthquakes occurred in 1986 and 2014, both exceeding $M_L = 4$. A vast majority of earthquakes have been located in a small planar area beneath the village Nový Kostel at depths ranging from 7 to 12 km (3.4). It is known as the Nový Kostel Focal Zone (NKFZ) and during the last 30 years more than 80% of all seismic energy has been released here (Michálek and Fischer, 2013). The NKFC is almost vertical fault with strike azimuth of 169^o, composed of many segments .

Characteristics of a spatio-temporal evolution of local seismicity indicate the presence of overpressured fluids within the focal area which plays significant role as a triggering mechanism of swarms (Fischer et al., 2014; Hainzl, Fischer, and Dahm, 2012; Hainzl et al., 2016). The mantle origin fluids (Brauer et al., 2003) are recurrently saturating the focal zone and decrease the stress necessary for earthquake ignition. However, the dynamics of the fluids, their content, behavior, distribution and transport paths are still unknown. Recent studies along with the surface observations (Brauer et al., 2003; Fischer, Matyska, and Heinecke, 2017) indicate that the fluids in the upper crust are transported via a distinct channels (Mousavi et al., 2015) rather than to be widely spread within pore-space of the crust material. Their character in the deeper crust can be only guessed.

Table 3.1 contains basic information on recent outbursts of activity: year of occurrence, number of recorded (and processed) events, their magnitude range. Locations of the events are shown in Figure 3.4. The locations of earthquakes map the fault and reveal its segmentation. Different source mechanisms are observed for different activated segments (Fischer et al., 2014) with non-double-couple components (Vavryčuk, 2011).

Year	N. of recorded events	M_L range
2000	approx. 7000	from -0.3 to 3.3
2008	approx. 5000	from -1.0 to 3.8
2011	approx. 10000	from -1.0 to 3.5
2014	approx. 4000	from -1.0 to 4.4

TABLE 3.1: Basic information about recent outbursts of seismic activity in West Bohemia region. Duration of the swarms varies from weeks to months with changing intensity. Different total numbers of recorded events don't necessarily reflect the differences in swarm's power , but might be reflecting different data processing.

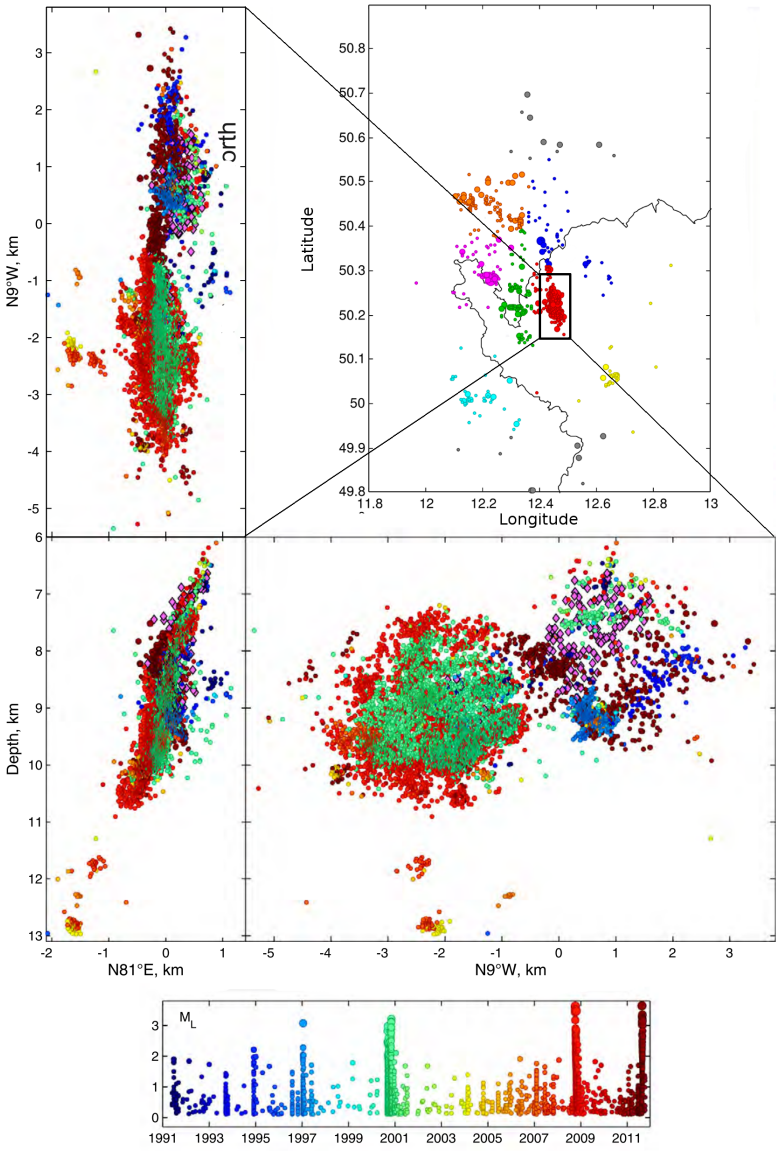

FIGURE 3.4: Hypocenters of earthquakes occurring in West Bohemia. In the figure b) the overal activity over the area during last few decades. Figures a), c) and d) shows cross-sections of the NKFC with swarms in different colors based on temporal evolution, as shown in e) (Fischer et al., 2014).

3.3 Seismic monitoring

A dominant role in the seismic monitoring and data processing of the earthquakes is played by the Institute of Geophysics at the Czech Academy of Sciences and its network WEBNET (WEst Bohemia NETwork) operating since 1994. The network now consists of 13 permanent stations with broadband, three component seismometers and 10 temporary stations (Fischer et al., 2010). Velocity signals are recorded with sampling frequency 250 Hz on one vertical (Z) and two horizontal components (N, E). At the time of this study the stations were equipped with seismometers SM-3 and Guralp 40-T and produced velocigrams in a frequency band at least 0.5-60 Hz with dynamic range exceeding 120 dB.

Aside from the WEBNET there are a number of stations installed on German territory operated by German institutes. The most significant is SXNET (SaXony NETwork) operated by Leipzig University (Korn, Funke, and Wendt, 2008) with 11 broadband, three component seismometers. Eastern part of Germany is monitored by the German Regional Network and with stations operated by Schiller University in Jena. Other stations present in the area belong to Bavarian Network operated from Munich. Velocity records of all three components from German stations are available in online repository provided by EIDA BGR Hamburg. Sampling rate of such data is 100 Hz.

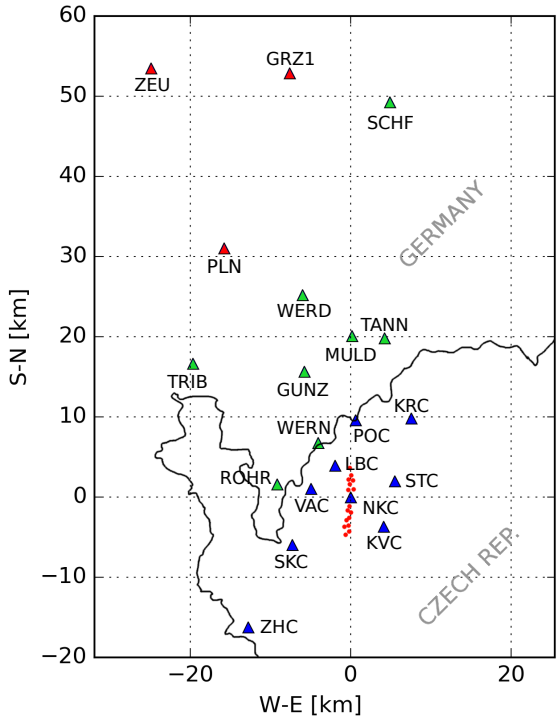

FIGURE 3.5: Locations of seismic stations in West Bohemia region: permanent WEBNET stations (blue), SXNET stations (green), station of TH network (red). Red dots mark epicenters of earthquakes from NKFC, where the majority of events occurred in last 30 years.

Figure 3.5 shows locations of permanent seismic stations over the West Bohemia and Vogtland region, which are used for purposes of this study. It is clear that only the focal zone is densely covered by the WEBNET stations and close SXNET stations. On longer epicentral distances the coverage is sparse and covers only the area towards north. There are no stations located southward from NKFC with epicentral distances longer than 15 km. Current state of seismic monitoring is suitable for wide range of seismological applications and studies: location studies (e.g. Jakoubková, Horálek, and Fischer, 2017; Hainzl et al., 2016), structural studies (e.g.

Hrubcová et al., 2013; Alexandrakis et al., 2014), moment tensor studies (e.g. Vavryčuk et al., 2017; Horálek and Šílený, 2013). However, for more regional studies the set of stations brings a few restrictions which need to be taken into account (Bachura and Fischer, 2016a).

This chapter brou a brief introduction to a wide scientific field of West Bohemian earthquakes in an extent necessary for understanding the next chapters. If the reader is interested in particular details, then we advise to see a review publication of Fischer et al. (2014) and references therein.

Chapter 4

Relocations

4.1 Locating and relocating the earthquakes

Analyzing spatio-temporal distribution of earthquakes is often the best tool for mapping faults and underground structures. A precision of earthquake locations is the limiting factor for deeper interpretations and its improvement is an important topic for modern seismology from smallest scales (acoustic emissions, micro-earthquakes) to the largest ones (mega-thrust earthquakes on subduction zones). The problem of locating the earthquakes from measured arrival time data is one of the oldest challenges in seismology and continues to be an important component of seismic research.

A classic Geiger's method (Geiger, 1910; Geiger, 1912) is iterative least-squares technique for locating single event when at least 5 picks (P- or S- or both) are available (Shearer, 1999). The method is non-linear and have to be linearized. It aims to minimize the differences between observed and predicted travel times at different stations. Quality of resulting location depends on many factors - picking accuracy, suitability of chosen velocity model, distribution of stations etc. Its relatively large error is a limiting factor for detailed study of earthquakes' spatial distribution. A development of single event location techniques is now represented by a global grid search methods like NonLinLoc (Lomax et al., 2000) and so-called back-projection method (Padhy and Subhadra, 2004). Different approach was introduced by Stoddard and Woods (1990) who developed a relative method called master-event technique, searching for a relative position of 'slave' event with respect to 'master' event. Unlike the Geiger method the master-event method is linear and aims to minimize the differences between observed and predicted master-event arrival time differences. Master-event technique is more thoroughly described in Chapter 6, where its modification is used for V_P/V_S estimation.

The relative approach was extended by Waldhauser and Ellsworth (2000) who developed the double-difference *HypoDD* method - joint relocation of numerous clustered earthquakes by minimizing the observed and predicted differential times between pairs of events within the cluster.

Traditional procedure of earthquake location routine consists of two steps: initial raw event location and following relocation. The first step produces raw earthquake location using manual or automatic pickings. Then, if the event is of interest, relocation is provided by improving the picks, velocity models etc. If there are more events of interest and are tightly clustered, the relative location methods can be applied.

4.2 Locating the West Bohemian earthquakes

Seismic activity in West Bohemia is related to Nový Kostel Focal Zone (NKFZ) - almost vertical planar zone approximately 8 km long and 6 km high (Figure 3.4). The presence of tightly clustered earthquakes and good station coverage provided by installed seismic networks (Figure 2.5) makes the activity suitable for application of relative methods like the master event technique (Fischer and Horálek, 2003; Bouchaala, Vavryčuk, and Fischer, 2013) and HypoDD (Čermáková and Horálek, 2015; Jakoubková, Horálek, and Fischer, 2017). The latter one became routinely used.

The monitoring of the earthquake activity is provided by Institute of Geophysics at Czech Academy of Sciences. Continues waveforms recorded by WEBNET network are processed here - each earthquake is manually picked and located/relocated. This procedure requires time for picking, but produces the most complete catalogs with magnitude of completeness down to $M_L = -0.5$ (Fischer and Bachura, 2014). Catalogs are often not final and are updated as the new methods and re-processing are applied.

We relocated 2014 dataset with intentions to have as precise relative locations of clustered earthquakes as possible. With such a dataset applied methods could go deep into details: analyzing the evolution of focal mechanisms (Fischer, Matyska, and Heinecke, 2017), spatio-temporal and statistical analyses of aftershock series (Hainzl et al., 2016) and detailed V_P/V_S monitoring (Bachura and Fischer, 2016b, Chapter 6 in this study).

4.3 Relocating with *HypoDD* and cross-correlations

The *HypoDD* is a package of programs designed for joint relocation of high number of tightly clustered earthquakes. The cluster, from the *HypoDD* point of view is defined as an assemble of connected event pairs. Instead of arrival times of P- and S-waves the method makes use of arrival time differences between events in the pairs.

The process of relocation consists of two steps:

- generating the network of event pairs within the earthquake cluster - *ph2dt* program
- iterative relocation - *hypoDD* program

The *ph2dt*, as the event pairs network generator can work properly only if input locations have at least some level of accuracy. A success of following *hypoDD* run depends on the event pairs network quality and on arrival time differences precision.

A broad spectrum of settings of *HypoDD* can be adjusted, however, they are the initial locations and the differential times what controls the success of relocating. Especially the improvement of differential times precision is the way how to get rapidly better results. The improvement in our case lies in use of the waveform cross-correlation technique as a tool for precise differential time measuring. The technique takes two events and cross-correlate their waveforms. If the waveforms are similar a high cross-correlation coefficient (close to 1) is obtained and a lag (time shift at which the similarity is highest) is measured (Figure 4.1). From the lag a total differential time can be easily computed. The cross-correlation coefficient quantifying the waveform similarity is used as a weighting parameter in *HypoDD* program.

The use of cross-correlations is reasonable only when relocated events within the cluster have waveforms similar enough. A waveform shape is controlled by a source mechanism $S(t)$, traveling path properties $P(t)$ and sensor characteristics $R(t)$ as

$$A(t) = S(t) * P(t) * R(t), \tag{4.3.1}$$

where $*$ marks convolution and the path effects term $P(t)$ includes geometrical spreading and attenuation. Single differential times are always computed for separate stations, so $R(t)$ is of no influence. If two waveforms on one station are to be similar, their sources must be similar and the must be situated close to each other, so their ray-paths are affected by the Earth's crust equally. Such conditions are achievable only for tight earthquake clusters with events lying on one or more parallel faults or fault segments.

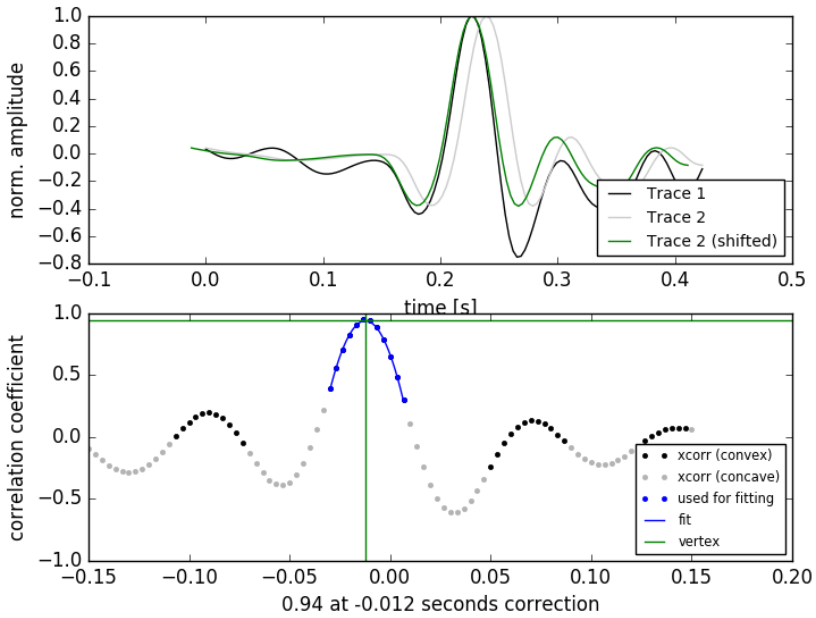

FIGURE 4.1: Top: Cross-correlated waveforms of vertical traces of two events (P-wave onset): trace 1 (black) and trace 2 (grey). Trace 2 is the most similar to trace 1 when shifted 0.012 s backwards (green). Bottom: Cross-correlation coefficient as a function of lag (time shift). Computed and plotted using ObsPy software package.

4.4 Waveform cross-correlation - source of systematic error

The precision of arrival time differences measured by waveform cross-correlations technique may be 10 time higher than that estimated from manual picks (Shearer, 1999; Lay and Wallace, 1995). The assumption is valid when correlated earthquakes are of similar magnitudes, whose first pulse widths are of the same width. With increasing magnitude difference the spectral content of P- or S-wave pulses differs and as a result their widths differ too. Correlated waveforms are usually ≈ 0.5 s long and contain the first arrival pulses followed by early coda pulses. Cross-correlation technique yields the best cross-correlation coefficients when seismograms are shifted to the position of maximum similarity. Unfortunately, the shift is controlled by the whole length of seismogram and differences in the first pulses are ignored.

Estimated differential time is therefore not the time between phase arrivals, but only some time describing the shift to the best similarity. If we want it to be the differential time, we have to be sure that the first pulses of correlated seismograms are of the same width - correlated earthquakes are of similar magnitudes. Bias can reach levels up to 0.1 s (Figure 4.2) and is

pronounced for events with $M_L > 3$. It can lead to a drastic mis-location of such events (Figure 4.3).

To control or prevent the bias it is necessary to adapt data processing by:

- controlling the magnitude differences between selected event pairs chosen for cross-correlation
- more strict filtering of waveforms in attempt to narrow the frequency content of the signal

Both aspects were implemented to a data processing.

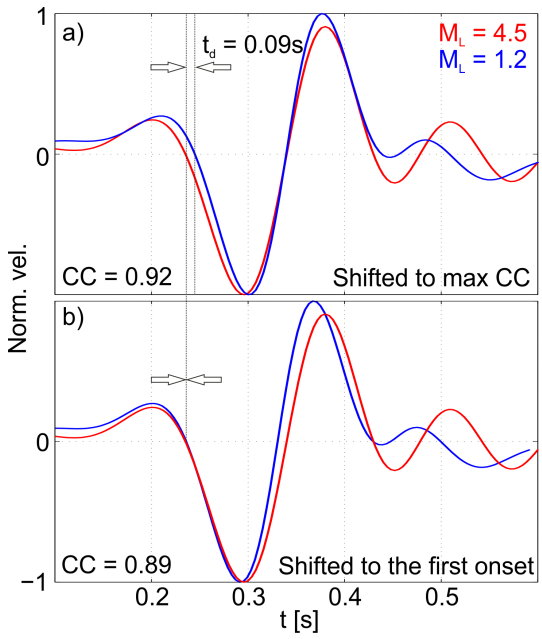

FIGURE 4.2: P-wave arrivals of two events (1-15 Hz) with $M_L = 4.4$ (red) and $M_L = 1.2$ (blue) shifted to position of maximum cross-correlation coefficient (top); to P-wave onsets (bottom). For correct arrival time difference estimation waveforms of similar widths of P pulses (magnitudes) are necessary. Maximum CC does not mark proper arrival (onset) time difference when magnitudes differ significantly. Error can be up to 0.1 s.

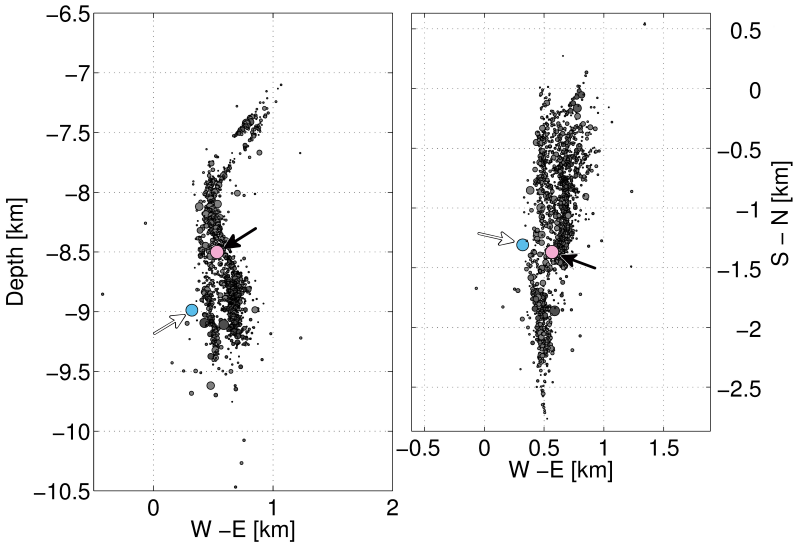

FIGURE 4.3: Relocated earthquakes of 2014 activity using only automatic picks with cross-correlations - Front view (left) and map view (right). Differential times estimated for event pairs with the strongest event $M_L = 4.4$ are systematically biased (Figure 4.2) and resulting relocation is erroneous (blue, white arrow). Correct relocation of the event is about 500 m shallower (pink with black arrow) and in the middle of the cluster.

4.5 Data

We relocated earthquakes of 2014 activity. The activity consists of three separate mainshock-aftershock sequences (Figure 4.5) with events located on the same focal zone where only swarm-type seismicity was present during the last two decades. Activated fault segments form almost a vertical plane of 3x3 km at depths from 7 to 10 km (Figure 4.4). The fault plane is oriented from the south to the north with a strike of 169^o (Fischer et al., 2014). The first sequence started with a $M_L = 3.5$ earthquake (on May 24^{th}) followed by aftershocks activity lasting two days. The second sequence started with a $M_L = 4.5$ earthquake (on May $31st$) and lasted for one week. The third sequence was very similar to the first, with one mainshock of $ML = 3.5$ (on August 3^{rd}), again with the aftershocks lasting for two days (Hainzl et al., 2016).

Raw dataset contained 6491 earthquakes with magnitude range $M_L = \langle -1.0, 4.5 \rangle$. Data were acquired by a combination of automatic (PePIN automatic picker (Fischer, 2003)) and manual picking. Intensity of the activity covers the area with events densely enough to have wide possibilities of 'chaining' the cluster with event pairs necessary for *ph2dt*. Focal mechanisms of earthquakes slightly vary from swarm to swarm, but stay more or less stable during it (Fischer et al., 2014). High level of earthquakes self-similarity is observed (Figure 4.6).

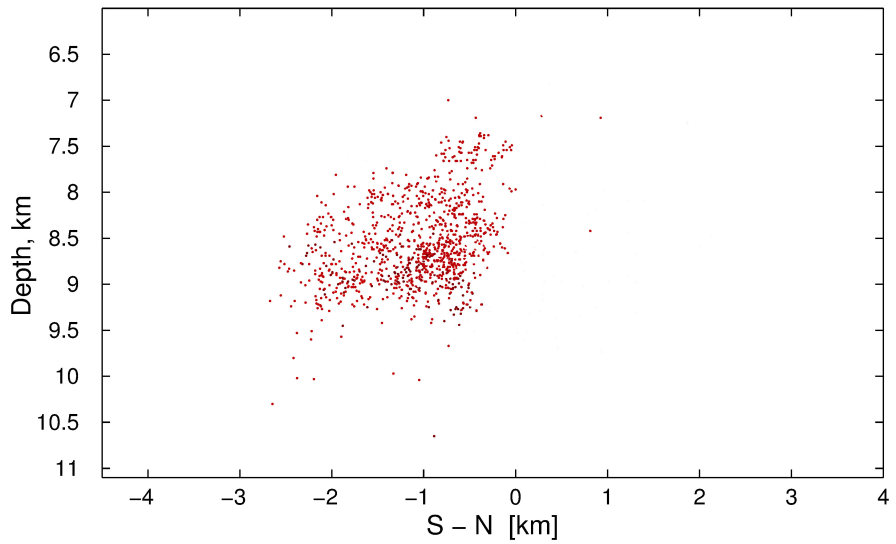

FIGURE 4.4: Raw locations of earthquakes from three mainshock-aftershock sequences of 2014. Only magnitudes $M_L > 1$ are plotted.

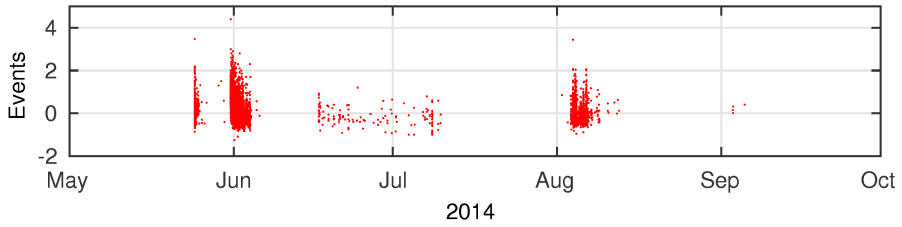

FIGURE 4.5: Temporal evolution of 2014 activity - catalog of relocated earthquakes.

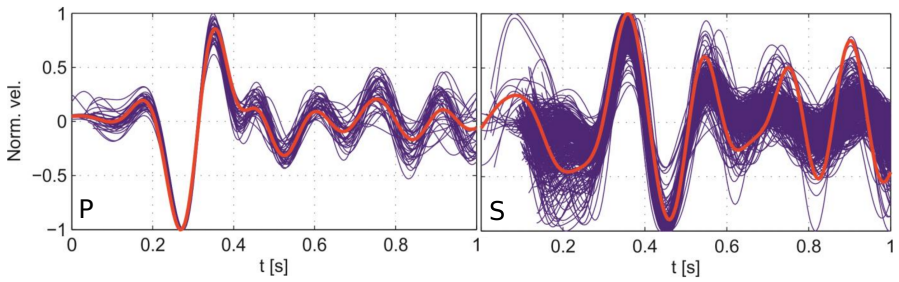

FIGURE 4.6: Waveforms of P- (left) and S-wave arrivals (right). Various earthquakes (blue) are cross-correlated with $M_L = 2$ earthquake (red) and shifted to a position of maximum cross-correlation coefficient. Only waveforms with cross-correlation coefficient exceeding 0.9 are plotted. Records of vertical component on station NKC.

4.6 Data processing - catalog processing, waveform cross-correlations, relocating

For each dataset a catalog containing events with at least 6 readings was available. Magnitudes lower than $M_L = -1$ were filtered out. Every catalog was split into three sub-catalogs with different, but overlapping magnitude ranges: $M_L = \langle -1.0, 0.8 \rangle$, $M_L = \langle 0.5, 2.8 \rangle$, $M_L = \langle 2.5, 5.0 \rangle$. From the sub-catalogs three event pairs networks were generated using *ph2dt* and then concatenated together. Thanks to the magnitude overlap some events were included in two sub-catalogs so the final concatenated event pairs network was sufficiently chained. This rather complicated procedure allows for controlling the magnitude differences between paired events within the network.

The waveforms of every pair of events selected for cross-correlation were filtered to a frequency band 1-10 Hz (to remove the noise effects) or 1-7 Hz when an event with magnitude higher than $M_L = 3$ occurred in the correlated event pair (to help suppressing the effects of different magnitudes on cross-correlations as mentioned above). Three-pole Butterworth band-pass filter was used. Time intervals of 1 s and 1.5 s duration centered at the measured P and S arrival times, respectively, were trimmed and cross-correlated to obtain absolute arrival time difference for P and S waves. Resulting arrival time differences along with the cross-correlation coefficients as weighting factors were used as inputs for *hypoDD* relocation.

Statistics describing the quality of cross-correlated dataset for 2014 activity are shown in Figures 4.7, 4.8 and 4.9. Figures 4.7 and 4.8 compares total number of non-correlated differential times with total number of cross-correlated differential times with cross-correlation coefficient higher than 0.6 and 0.7. The total amounts of P- and S-wave differential times on different stations are plotted. Event pairs with cross-correlation coefficient higher than 0.7 represent about 40-50% of the dataset. Lowering the threshold down to 0.6 slightly improves the content up to 50-60%. S-wave differential times are more numerous and more self-similar (histograms in Figure 4.9).

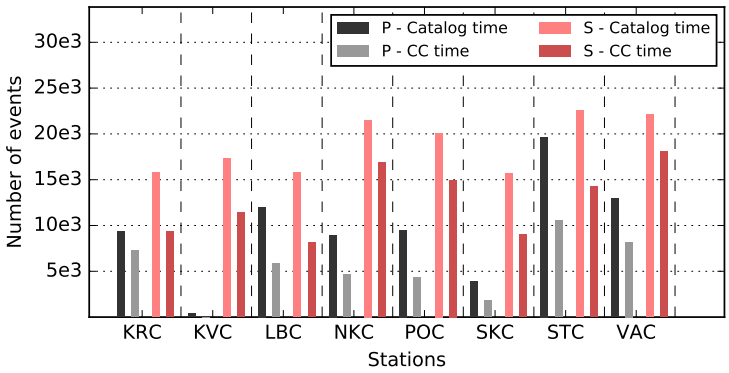

FIGURE 4.7: Comparison of total number of catalog-estimated differential times vs. cross-correlations-estimated ones with cross-correlation coefficient exceeding 0.6. P- and S-wave arrival time differences on different stations for 2014 activity (approximately 4800 events relocated).

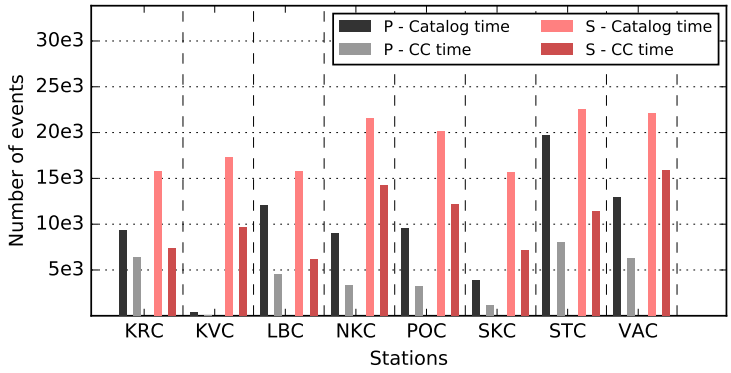

FIGURE 4.8: Comparison of total number of catalog-estimated differential times vs. cross-correlations-estimated ones with cross-correlation coefficient exceeding 0.7. P- and S-wave arrival time differences on different stations for 2014 activity (approximately 4800 events relocated).

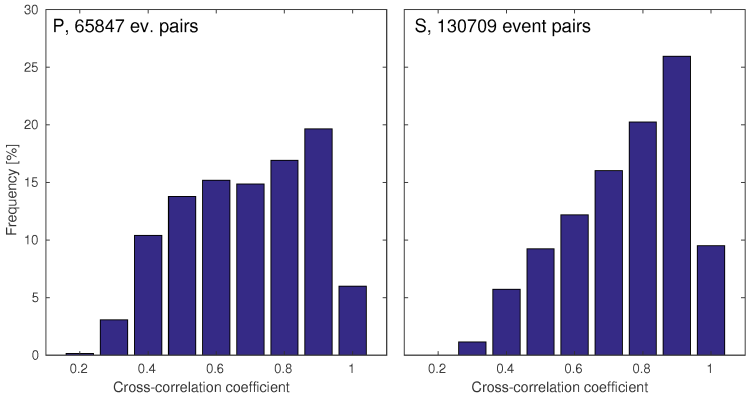

FIGURE 4.9: Distribution of cross-correlation coefficients of event pairs from 2014 activity (approximately 4800 relocated events). Left: P-differential times. Right: S-differential times. Data from 8 stations are plotted.

Final relocations were iteratively computed by *hypoDD* program. Density of the event pairs network and the differential times estimations have the major impact on relocations reliability and amount of successfully relocated earthquakes.

4.7 Results - final relocations of 2014 earthquake

4842 earthquakes out of 6491 were successfully relocated by *HypoDD* (Figure 4.10). Relocation revealed deeper details of the fault zone and were suitable for further analyses.

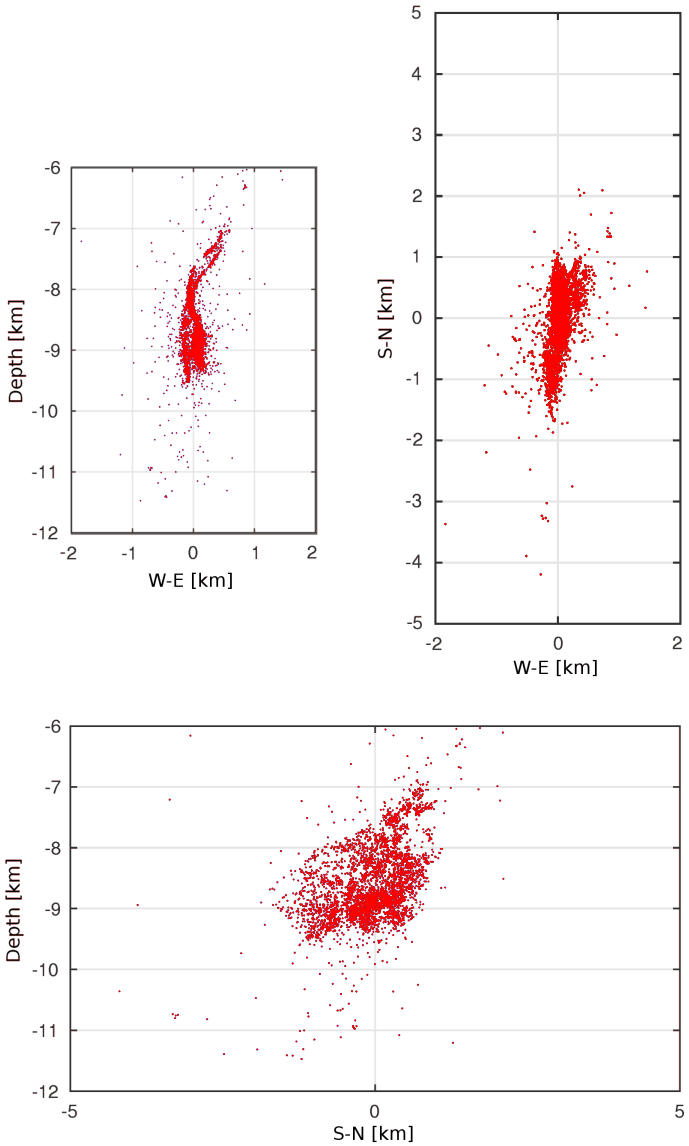

FIGURE 4.10: Relocated earthquakes of 2014 earthquake activity. From 6491 earthquakes 4842 were successfully relocated. Initial locations were computed in a homogeneous velocity model using simplex search algorithm from combination of automatic and manual picks. For relocating a layered 1-D velocity model (Málek, Horálek, and Jánský, 2005) was used, with differential times computed from manual and automatic picks supplemented with cross-correlations.

Activity of 2014 with its mainshock-aftershock character (three mainshock-aftershock sequences) was subject of study provided by Hainzl et al. (2016). Focal mechanisms of stronger events and position of earthquake cluster were the focus of the study. Relocations with enhanced precision (Figure 4.11) were crucial and helped to reveal a co-location of two weaker mainshocks (both with $M = L3.5$) and specific temporal evolution of the early aftershocks following the strongest event ($M = L3.5$).

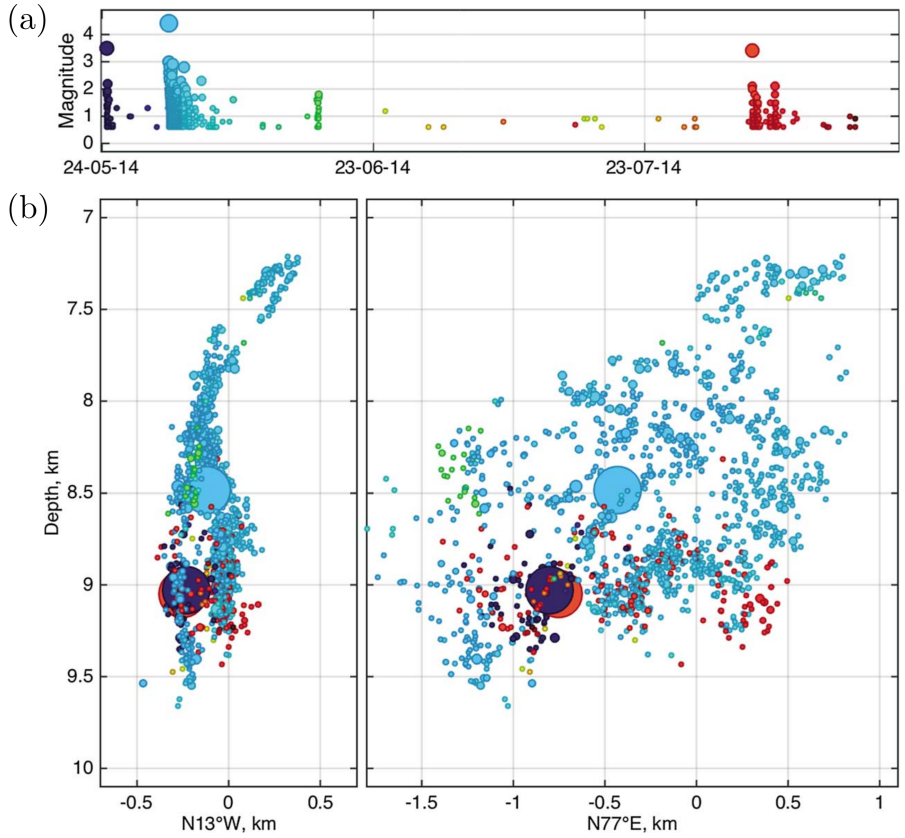

FIGURE 4.11: 2. (a) Magnitude-time plot of the 2014 sequence and (b) two vertical sections oriented across and along the hypocenter trend, where symbol size is proportional to magnitude; the size of main shocks is exaggerated. Events are color coded according to their occurrence times.

Separated processing of events based on magnitudes played an important role in achieving the correct positions of three mainshocks. The comparison of two approaches - one with the separation and one without - is shown in Figure 4.12. Positions of aftershocks are more or less identical. Two weaker mainshocks (purple and red) are slightly mis-located (moved downwards), but the location of the strongest earthquake (blue) is significantly shifted by 500 meters down and outside the fault plane and is concluded to be erroneous.

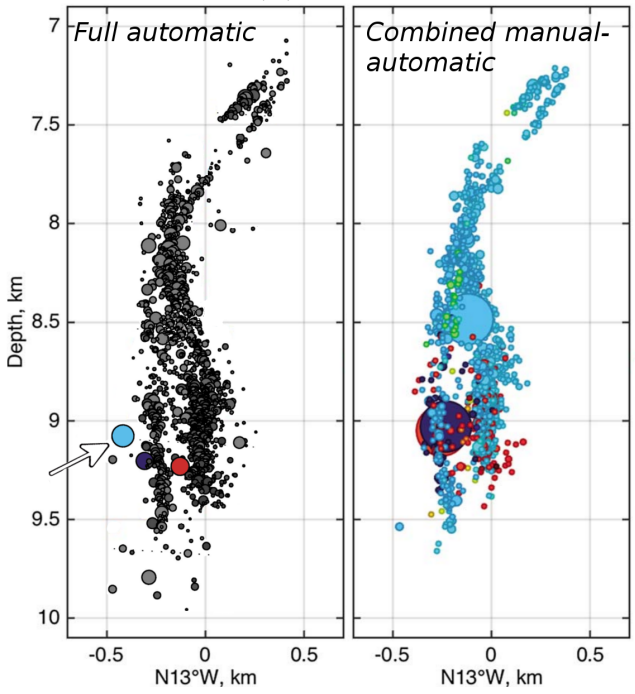

FIGURE 4.12: Comparison of relocations of 2014 activity with ignoring magnitude differences (left) and avoiding cross-correlation of too different events (right). The mainshock of $M_L = 4.4$ (blue, with arrow on the left plot) is drastically shifted down and out of the cluster.

The relocations of 2014 activity was later in this work used for spatial and temporal analysis of V_P/V_S variations (Bachura and Fischer, 2016b). High precision of hypocenter locations was essential for the analysis as the we tried to image the velocity ratio distribution on a fault plane with area of 3x3 km.

4.8 Discussion and conclusions

HypoDD with cross-correlation technique is a powerful tool for relocating tight clusters of earthquakes, when sufficient number of cross-correlated differential times is acquired. It is fully applicable on West Bohemia earthquakes swarms, especially when processed separately on single swarms. Absolute position of such relocated earthquake cluster depends on the initial locations. Separated treatment of earthquakes with different magnitudes is necessary when a wide range of magnitudes is present in catalog and cross-correlations are used. Only that way the mis-location of mainshocks can be prevented. Without using it the overall geometry of relocated clusters is acceptable for further analyses, but one must keep in mind that strong earthquakes might have erroneous locations. *HypoDD* doesn't offer any option how to control the event pairing process with regards to the magnitude differences.

Achieved precision of relative locations is in first tens of meters, however, the absolute position of every event might be shifted by hundreds of meters for earthquake cluster from West Bohemia, as for any other seismic activity relocated by *HypoDD* worldwide.

Chapter 5

Coda Attenuation

5.1 Attenuation of the seismic waves

Seismic waves during their way through the Earth are loosing their energy due to a two phenomenons: geometrical spreading and attenuation. Geometrical spreading reduces the energy of the waves as an effect of increasing wavefront, while attenuation causes the energy loss due to scattering on heterogeneities and internal friction - intrinsic absorption (anelastic loss). While the first one is simply predictable, the attenuation depends on the Earth's material characteristics and magnitude of its influence is often unknown.

Loss of the energy due to attenuation might be described by a simple equation

$$Q = -\frac{2\pi E}{\Delta E} \tag{5.1.1}$$

(Lay and Wallace, 1995) where Q called quality factor (dimensionless) quantifies the loss of energy ΔE per one angular cycle 2π. E is the initial energy. With increasing propagation distance and constant Q higher frequencies are attenuated more than the lower ones. As was mentioned above, the total attenuation consists of two processes: scattering and anelastic loss, described by the quality factors Q_{sc} and Q_i in a way

$$Q_t^{-1} = Q_{sc}^{-1} + Q_i^{-1} \tag{5.1.2}$$

Scattering of the seismic waves takes place when layer boundaries and other velocity heterogeneities are present in the Earth's crust. Their size, velocity contrast and mass density control resulting $Q_{sc}(f)$. Waves with frequency f and wavelength λ are scattered on heterogeneities with dimensions of the same order as λ or larger.

Behavior of $Q_i(f)$ is a complex question with no satisfactory answer. Generally accepted idea is that Q_i is frequency independent on the frequencies ranging from 0.001-1 Hz. This behavior is explained as a result of superposition of many different mechanisms of absorption resulting in final constant Q_i (Michálek and Fischer, 2013; Stein and Wysession, 2003). Earth's crust analyses repeatedly reveal frequency dependent Q_i for high frequency waves. The origin of the dependency is still not fully understood. Recent studies assign the dependency to the leakage of seismic energy into an upper mantle (Margerin, Campillo, and Shapiro, 1999). Seismic waves are absorbed on the MOHO boundary by the mantle instead of being reflected back. Resulting energy deficit decreases with frequency and is a possible explanation for Q_i's frequency dependence.

Muller (1983) introduced a power-law dependence

$$Q(f) = Q^0 f^n \tag{5.1.3}$$

which is applicable on every kind of quality factor and is frequently used now-days among the authors dealing with attenuation of the high frequency waves - especially when analyzing coda waves.

5.2 Seismic Coda

The excitation of S-coda waves is one of he most compelling pieces of evidence supporting the existence of random heterogeneity in the Earth's crust and litosphere. The characteristics of high frequency coda S-waves were summarized by Aki and Chouet (1975):

- The spectral contents of the later portions of S-coda are the same at different stations.
- The total duration of the seismogram, defined as the length of the time between the P-wave onset and the time when the coda amplitude equals the level of noise, is a reliable measure of earthquake magnitude.
- Bandpass filtered S-coda traces of different local earthquakes recorded within given region have a common envelope shape whose time dependence is independent of epicentral distance.
- The temporal decay or S-coda amplitudes are independent of earthquake magnitude at least for $M_L < 6$.
- The S-wave coda amplitudes depends on the local geology of the recording site.
- Coda amplitudes are not regular plane waves from the epicenter, but are composed of plane waves from random directions - are randomly (or pseudo-randomly) scattered plane waves (Aki and Tsujiura, 1959).
- S-coda waves have the same site amplification factor as that of direct S-waves, which confirms that S-coda waves are composed primarily of S-waves (Tsujiura, 1978)
- clear S-waves coda have even been identified on seismograms recorded at the bottom of deep boreholes drilled in hard rock beneath soft deposits (Leary and Abercombie, 1994; Sato, 1978), which means that S-codas are not dominated by near surface scattering.

5.3 Coda and Q

Decay of coda waves energies can be parametrized by a simple algebro-exponential equation as

$$E(t,f) = S(f)t^{-\alpha}e^{-2\pi f t/Q_c(f)} \tag{5.3.1}$$

where $E(t,f)$ is the energy of coda waves at lapse time t from the origin on frequency f. In other words, $E(t,f)$ is a power spectrum. $S(f)$ is a frequency dependent source (or/and site) term, t is the lapse time, f frequency, α is a positive geometrical exponent and Q_c is frequency dependent quality factor (Aki and Chouet, 1975). Decay rate of coda is therefore quantized by the parameter $Q_c(f)$ called coda quality factor. Geometrical term α is 2 for body waves,

1.5 for diffusive wave-field and 1 for surface waves. Physical interpretations of Q_c are still discussed and are related to the models of coda waves excitation, propagation and mechanisms of attenuation.

Aki and Chouet (1975) proposed two physical models describing the propagation of the coda waves: single backscattering model and diffusion model. Single backscattering model assumes that one wave generated in the source travels to the scatterer and is reflected back (backscattered) to the receiver. Scatterers - heterogeneities are distributed randomly and uniformly within the ellipsoidal area with foci in the hypocenter and receiver in homogeneous half-space. Size and volume of the ellipsoid are given by the selected length of the studied lapse time window (with increasing lapse time window length the volume increases). Resulting Q_c then reflects both — intrinsic loss Q_i and scattering Q_{sc} in a way that

$$Q_c^{-1} = Q_i^{-1} + Q_{sc}^{-1} \tag{5.3.2}$$

The use of the single backscattering model itself does not allow us to separate these two attenuation mechanisms. Moreover, there is a trade-off between geometrical term α and Q_c. In other words, the coda decay may be fitted equally well with different α with an impact typically less than 20 % on estimated Q_c value (Calvet and Margerin, 2013).

Second model proposed by Aki and Chouet is a diffusion model. It represents the end-member case of multiple scattering. At large lapse it is reasonable to assume that direct energy is small and that multiple scattering produces a smooth spatial distribution of energy density. In such a diffusive field the energy distribution and behavior can be approximated as a diffusive process and can be described by means of the diffusion theory. The α exponent is then 1.5 and decay rate of coda reflects only intrinsic loss (Aki and Chouet, 1975; Shapiro et al., 2000; Sato, Fehler, and Mayeda, 2012):

$$Q_c^{-1} = Q_i^{-1} \tag{5.3.3}$$

Both single-scattering and diffusion models are valid physical models that predict the observed decay, but imply different physical interpretations of Q_c. Early coda studies primarily adopted the single-backscattering model for homogeneous half-space with Q_c having been estimated in geological regions worldwide. This method was favored by the authors. It was found that Q_c is high in seismically stable areas and that Q_c is not independent of the lapse time in coda—attenuation generally decreases (Q_c rises) with lapse time (e.g. Rautian and Khalturin, 1978; Roecker et al., 1982; Tselentis, 1993; Mukhopadhyay et al., 2008). This dependence was discussed and interpreted by Rautian and Khalturin (1978) in the terms of a single backscattering model—as a spatial decrease of the attenuation properties of the Earth with depth. Scientists expected that with longer lapse time the area covered by coda waves is bigger and reaches into depths where attenuation is weaker. Further research development of this idea was carried out by Gusev (1995) who developed a stratified model of scattering properties in the lithosphere based on single scattering model. On the other hand, Del Pezzo, Allota, and Patané (1990) pointed out that the increase of Q_c with lapse time may be simply caused by the inability of Eq. 5.3.1 to describe the full complexity of the attenuation process in the Earth.

Isotropic single backscattering works properly when fitting the synthetic coda envelopes to the later coda parts, but generally does not work when fitting the early coda at short lapse times (e.g. Gusev and Abubakirov, 1987; Hoshiba, 1995; Calvet and Margerin, 2013). Due to these shortcomings new models and approaches implying multiple scattering and anisotropy have

been developed (Sato, 1989; Saito, Sato, and Ohtake, 2002; Calvet and Margerin, 2013) and are in the center of recent research activities.

In past decades the role of the single scattering has been suppressed and replaced by the idea of multiple scattering (e.g. Wu, 1985; Gusev and Abubakirov, 1987; Frankel and Wennerberg, 1987; Abubakirov and Gusev, 1990). One possible approach to investigate the attenuation parameters is the diffusion approximation (Dainty et al., 1974; Wegler and Luhr, 2001), based on above mentioned assumption that the coda wave-field on late lapse times is fully diffusive and coda decay reflects intrinsic attenuation described by Q_i only. Another approach is to involve the radiation transfer theory (RTT), a modern methodology to describe the propagation of seismic energy in a scattering medium. The radiative transfer theory was first introduced by Chandrasekhar (1960) to describe the transport of light in the turbulent atmosphere and was only later transferred to the field of seismology (Weaver, 1990; Rurner and Weaver, 1994; Rhyznik, Papanicolau, and Keller, 1996; Gaebler, Eulenfeld, and Wegler, 2015). Analytical solutions for isotropic scattering from acoustic RTT equations have been derived (Zeng, Su, and Aki, 1991; Paasschens, 1997) and now they form the base of the methods for separation intrinsic loss Q_i and scattering Q_{sc}, namely MLTWA - Multiple Lapse Time Window Analysis (Fehler et al., 1992).

Further development of the RTT in seismology includes the use of anisotropic scattering for acoustic media (Wegler, Korn, and Przybilla, 2006), application of the elastic approximations (e.g. Zeng, 1993; Margerin, Campillo, and Van Tiggelen, 2000; Przybilla, Korn, and Wegler, 2006) etc.

5.4 Radiative transfer theory

When waves are radiated from a point source in a random medium, single scattering provides a good description of the propagation characteristics at small distances from the source and at short lapses time from the origin time. However, multiple scattering dominates over single scattering as travel distance or lapse time increases (Sato, Fehler, and Mayeda, 2012).

To involve multiple scattering, radiative transfer theory (RTT) was adapted from optics and become an essential tool for attenuation analyses today. Radiation transfer equation is a complex integral-differential equation describing energy density of a scattered wave-field in time and space (for further details see Sato, Fehler, and Mayeda (2012)). Raw form of the equation might be used for Monte-Carlo modeling of the coda energy envelopes (e.g. Fehler et al., 1992; Hoshiba, 1995).

For practical purposes two analytical solutions for case of 3-D isotropic acoustic case have been developed. Hybrid single isotropic scattering diffusion solution by Zeng, Su, and Aki (1991)(Eq. 5.4.1 and 5.4.2) and Paasschens's (1997) (Eq. 5.4.3 and 5.4.4) is valid for 3-D isotropic scattering medium:

$$E(r,t) \approx E_0 e^{\eta v t}\left[\delta\left(\frac{(t-r/v)}{4\pi r v^2}\right)+\eta_s H\frac{(t-r/v)}{4\pi v r t}\ln\frac{1+r/vt}{1-r/vt}\right]+$$

$$cH(t-r/v)\left(\frac{3\eta_{sc}}{4\pi v t}\right)^{1.5} e^{3\eta_{sc}r^2/4vt-\eta_i v t} \tag{5.4.1}$$

where

$$c = E_0 \frac{[1-(1+\eta_{sc} vt)\mathrm{e}^{-\eta_{sc} vt}]}{\frac{r}{\pi}\int_0^{\frac{\sqrt{3\eta_{sc} vt}}{2}} \mathrm{e}^{-\alpha^2}\alpha^2 \mathrm{d}\alpha}, \quad \alpha = \frac{vt}{r} \tag{5.4.2}$$

and

$$E(r,t) \approx E_0 \frac{\mathrm{e}^{-\eta vt}}{4\pi r^2 v}\delta\left(t-\frac{r}{v}\right) + E_0 H\left(t-\frac{r}{v}\right)\frac{(1-r^2/v^2t^2)^{1/8}}{(4\pi vt/3\eta B_0)^{3/2}}$$

$$\mathrm{e}^{-\eta vt} G\left(vt\eta B_0 (1-\frac{r^2}{v^2t^2})^{0.75}\right) \tag{5.4.3}$$

with

$$G(x) \approx \mathrm{e}^x \sqrt{1+2.026/x} \tag{5.4.4}$$

E_0 is the energy at $t = 0$, t is the lapse time from the origin, r is the hypocentral distance, v is the shear wave velocity, H is Heaviside function, δ is delta function, $\eta_i = 2\pi f/vQ_i$ is intrinsic attenuation coefficient, $\eta_{sc} = 2\pi f/vQ_{sc}$ is scattering attenuation coefficient (often marked as g_0), $\eta = \eta_i + \eta_{sc}$ is total attenuation coefficient (or so-called extinction length inverse Le^{-1}), and B_0 is seismic albedo $B_0 = \eta_{sc}/\eta$. An alternative parameter describing the scattering properties is the mean free path $l = \eta_{sc}^{-1}$ - inverse of the scattering coefficient.

Both solutions are in use, but the Paasschens's one is accepted as the better one with generally better fit to numeric solutions in wider range of circumstances. Its error is estimated in the order of 2-3 % except for the direct arrival time (Paasschens, 1997; Ugalde and Carcolé, 2009).

Single backscattering model and diffusion model are valid extreme cases of radiative transfer equation solutions. Based on RTT it might be concluded (simplistically) that early coda is more or less controlled by the single scattering and the energy is controlled by the direct phases and their first scattering events. Later, as more and more scattering events occur the coda wavefield become diffusive, direct phase is almost diminished and energy comes exclusively from scattered waves. Therefore it is reasonable to interpret the early part of the coda by means of single backscattering and later one as in terms of diffusion model. RTT and its approximate solutions are able to cover both previously mentioned approaches and in narrow circumstances (isotropic 3-D scattering) and are able to explain the shape of whole coda envelope.

5.5 Coda and mapped Earth's volume

Single backscattering introduced the idea of coda source ellipsoid with source and receiver in its foci. With increasing lapse time the ellipsoid with isotropically distributed scatterers expands. This idea was often adopted when authors tried to relate the coda characteristics to a particular crust portion. With introducing of RTT the idea of ellipsoids was abandoned and attenuation results were interpreted as mean values for volume (area) covered by earthquakes and stations (Sato, Fehler, and Mayeda, 2012). In 2014 Mayor, Margerin, and Calvet computed so-called sensitivity kernels for scattering and diffusion from the RTT. The kernels show the intensity with which intrinsic absorption and scattering affect energy in coda envelop at different lapse times as a function of space coordinates. Especially the intrinsic loss sensitivity kernel is

of importance since the Q_i is directly estimable from later coda. Mayor, Margerin, and Calvet concluded that:

- For regional hypocentral distances and late lapse times Q_i is dominantly controlled by the attenuation properties of the source-receiver ray path.
- For local earthquakes recorded on local networks with short hypocentral distances and late lapse times Q_i is dominantly controlled by the attenuation properties of the areas surrounding the source and receiver and with minor influence of the area surrounding ray path of a direct wave.
- For local studies it is preferable to mean the single Q_i estimates in order to have one representative attenuation parameter. On the contrary, while doing regional studies it is possible to analyze attenuation parameters spatially (e.g. Mayor et al., 2016).

The nature of the coda methods doesn't allow for focusing on a very local area. As will be seen later, outputs of coda methods are just a few parameters describing the mean attenuation properties of the whole area covered by events and stations. However, Q mapping is possible and its grid resolution strongly depends on a ray coverage. Fine grids with step of 1 km are possible (Prudencio et al., 2017) for specialized field experiments, but usual grid resolution only rarely goes bellow 100 km (Carcolé and Sato, 2010). The majority of coda studies analyze one area and describes it with one Q, or $Q(f)$.

5.6 Normalization by coda amplitudes

At late lapse times the wave-field inside excited the crust becomes diffusive: seismic energy is homogeneously distributed. What is the most important, the energy is weakening with the same rate for all the earthquakes with no regards to magnitudes or site effects. Those two effects affect the amplitude level on each seismogram only, not the decay rate. hence, the amplitude of the late coda can be used as a normalization factor for site effects and source strength removal.

Principles of coda as a normalization factor are widely adapted into a seismological routine and are the cornerstones of methods involving comparison of seismograms like coda normalization method, MLTWA, station amplification estimation etc.

5.7 Data

5.7.1 Data distribution

By coda analyses we analyze the crustal volume mapped by seismic rays: coda waves rays, direct wave rays etc. Quality of the ray coverage of the studied Earth's volume is therefore necessary for assessing the methods suitability and discussing the result and errors.

Figure 5.1 plots stations and common position of hypocenters used in this work. Events are co-located in the center of the network. Hypocentral distances vary from 8 km to 60 km. While the source area is suitably covered (wide range of amplitudes and number of rays), the area outside is poorly mapped with no azimuthal variability and with low number of rays. Influences of anisotropy, attenuation heterogeneity or source radiation effect might be present and must be taken into account in final discussion and results interpretation.

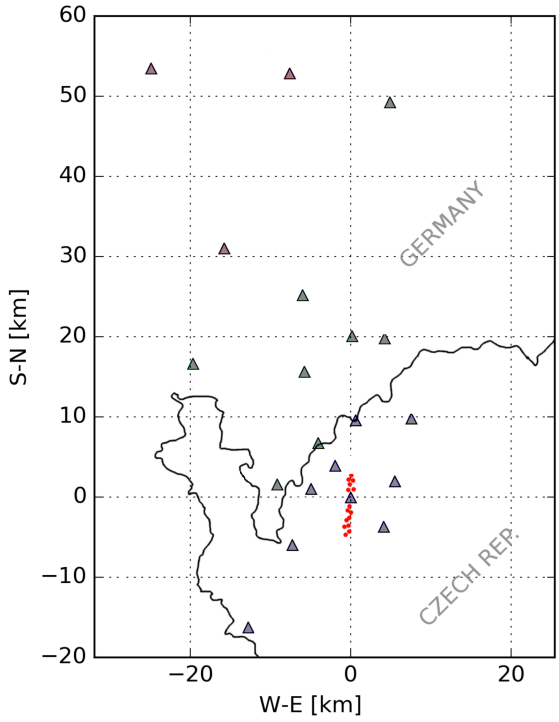

FIGURE 5.1: Stations (grey triangles) distribution with respect to the hypocenters (red dots).

5.7.2 Data selection

Records with strong, uncorrupted, smoothly decreasing coda with good signal to noise ratio (SNR) were demanded for coda analyses. Earthquake swarm activity typical for West Bohemia with lot of events present in a very short time windows introduces a big obstacle in easy event selection. Only a minority of events has codas sufficiently long and uncorrupted by later earthquakes. Proper catalog filtering and visual check of the seismograms is therefore essential. We selected data from three datasets/catalogs: Swarm 2008, Swarm 2011 and 2014 activity (Figure 5.2). It is important to note that the only catalog information we requested was the origin time. Precise direct P- and S-wave arrivals were not necessary and could be estimated automatically when necessary. The precise locations were also not necessary, since the events are very closely co-located. Inter-event distances are too short (up to to 6 km) to have any practical effect on results. In fact, for all the methods applied one single mean location could have been used.

Records were filtered with high-pass filter with corner frequency of 1 Hz to remove microseisms. The selection procedure consisted of 4 steps:

1. **Removing events interrupted by another event**

   Events which started within the coda of previous strong event were filtered out. Events with another event starting within its coda were removed as well. The procedure run automatically with required 'no-event' period of one minute before origin time and two minutes after it. Since not all the events were in the catalogs, visual check was still necessary to ensure that there are no events corrupting the codas.

2. **Magnitude filtering**

   Events with magnitudes lower than $M_L = 2.5$ were removed. Only strong events were expected to have sufficiently long coda even on stations located 50 km from hypocenter.

3. **SNR filtering**

   SNR higher than 3 was required for the whole duration of the coda. Noise levels were computed as a mean of RMS amplitudes of a time window 2 s long preceding P arrival. In some cases the noise sequence was affected by a weak earthquake what resulted in a false SNR decrease followed by undesired event removal. Strong events surviving the first two steps of filtering with suspiciously low SNR were checked visually and different noise window was selected.

   SNR was computed for high-pass filtered seismogram, but also for separate frequency bands later used later in the analyses: 2-4 Hz, 4-8 Hz, 6-12 Hz, 8-16 Hz, 12-24 Hz, 16-32 Hz.

4. **Visual check**

   Due to above mentioned problems a final visual check of the seismograms had to be done in order to ensure that only the valid data were selected for further coda analyses.

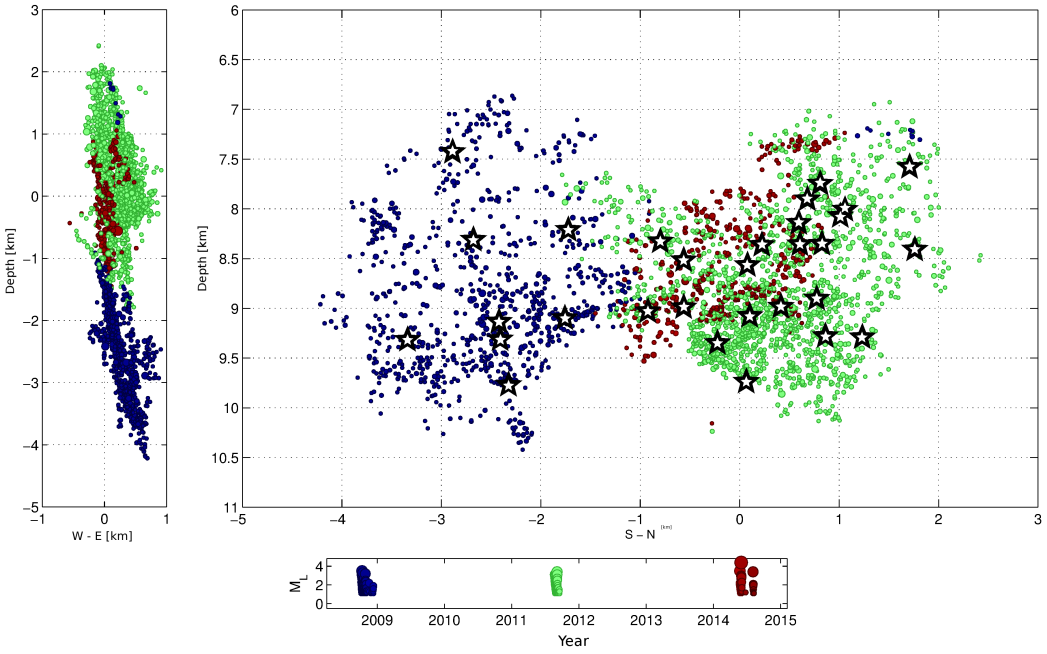

FIGURE 5.2: Distribution of hypocenters for swarms 2008 (blue), 2011(green) and mainshock-aftershock series of 2014 (red). Magnitude larger $M_L = 1$ are plotted. 30 (black stars) events were selected from these three datasets.

After data filtering three different datasets were formed for different purposes. The first one, 'DS60' represents the selection of 30 events recorded during the 2008 swarm (8 events), the 2011 swarm (17 events) and 2014 activity (5 events). Stronger events with pronounced codas were the object of demand for this particular dataset. Magnitudes of the earthquakes included are ranging from 2.6. to 4.4, depths vary from 7 to 10 km and hypocentral distances used are from 7 to 60 km. Records provided uncorrupted codas for at least 60 second after the origin time. The dataset was used for the application of the coda normalization method (CNM). Records come from all possible stations of SXNET, WEBNET and German regional network.

Subset of 10 events with uncorrupted codas as long as 80 s was separated from DS60 and forms 'DS80' dataset. Records were used for analyzing the late coda portions. The coda window method (CWM) and the multiple lapse time windows analysis (MLTWA) were applied to this particular dataset.

The last dataset 'DS2011' is the set of 13 events from the 2011 swarm used for MLTWA and CWM in Bachura and Fischer (2016). Records come from 11 stations of WEBNET and SXNET with local magnitudes from 1.7 to 2.9 and hypocentral distances ranging from 7 to 26 km (50 km for MLTWA). Focal depths ranged from 8 to 9 km. Codas up to 50 s after the S-wave arrival are included within DS2011.

Every accepted earthquake fulfilled the demands on all three components - Z, N, E. Note that the events have not identical station coverage - weaker events had bad SNR on distant stations and therefore those single records were not accepted.

Examples of different codas with different kind of corruption are shown in Figure 5.3.

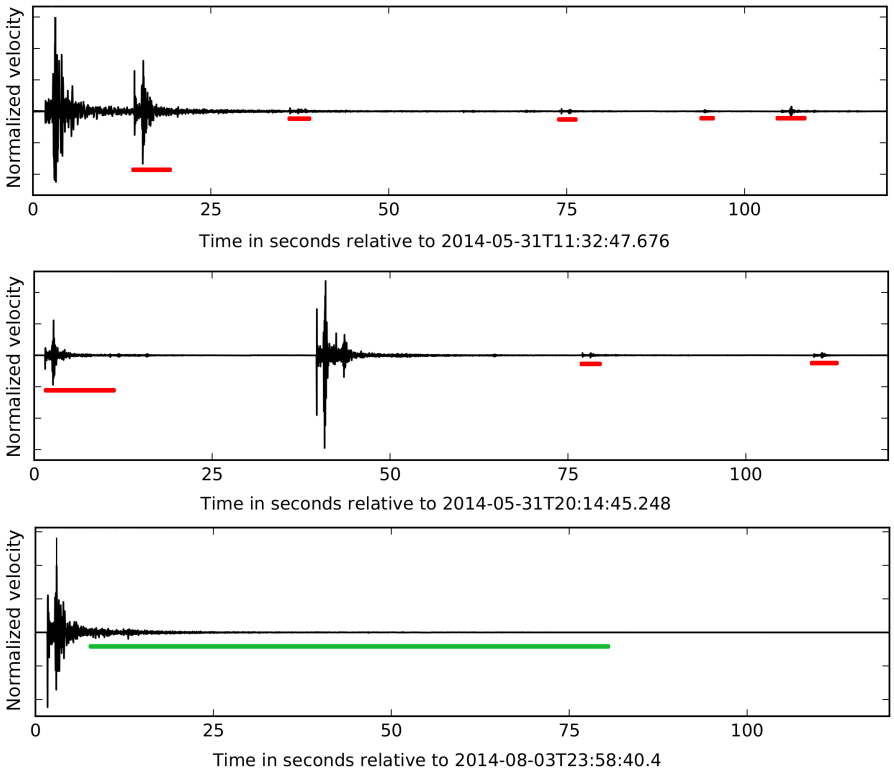

FIGURE 5.3: Examples of codas and their biases. Top: $M_L = 2.6$ with coda biased by at least 5 events (red lines). Middle: $M_L = 2.9$ with coda biased by at least 2 events and also biased by the coda of previous event with $M_L = 2.5$. Bottom: $M_L = 3.44$ with no bias before and during the coda time (green line). All records from station NKC, Z component.

5.7.3 Codas of West Bohemian earthquakes

Earthquakes of our datasets lie within one fault zone with inter-event distances much shorter than station-event ones: maximum inter-event distances are 6 km and hypocentral distances range is from 7 km to 60 km. According to the coda wave-field characteristics codas of different earthquakes should have identical decay rates at longer lapse times on all stations. Moreover, later coda amplitude might be used as a normalizing factor proportional to earthquake size and station amplification.

Figure 5.4 plots the coda envelopes of a single earthquake (Aug. 2^{nd}, 2014, $M_L = 3.44$) recorded on 16 stations. Coda envelope is computed as a RMS of filtered signal (frequency band from 1 to 32 Hz). Raw and smoothed signals are plotted for better clarity. Figure 5.5 shows the same

data, but normalized and stacked into a one axis. Signals are normalized by the mean value of the late coda amplitude within lapse times 60 and 70 s.

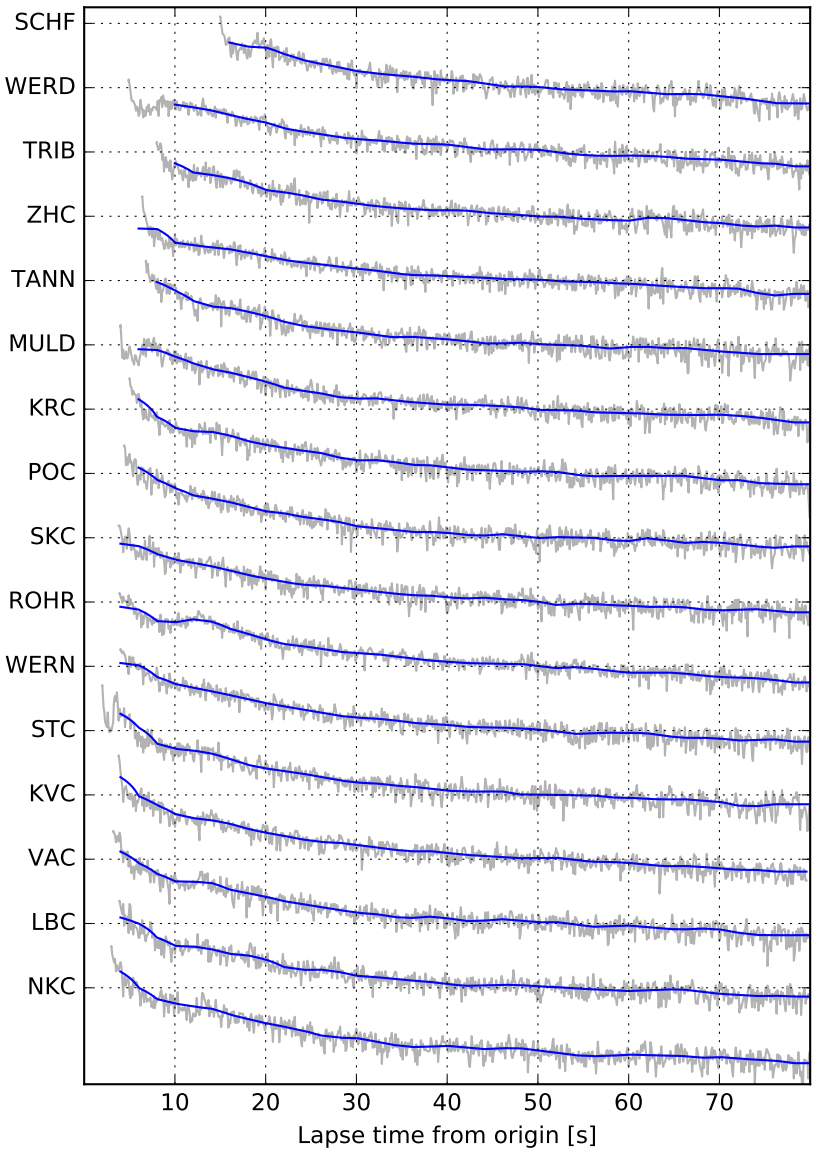

FIGURE 5.4: Coda envelopes on one earthquake on different stations, listed from the closest one (NKC) at the bottom up to the most distant one (SCHF) on top. Coda envelopes are computed as RMS amplitude of filtered signal (1 - 32 Hz). Grey lines represent the signal, blue one its smoothed version (smoothed with 4 s long median window) for better view.

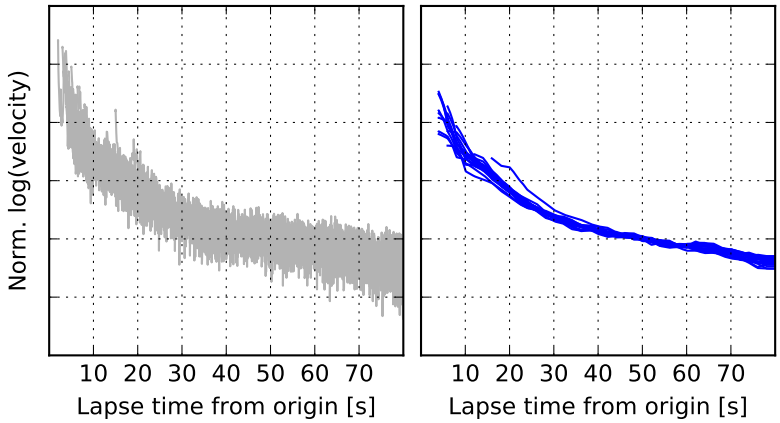

FIGURE 5.5: Stacked coda envelopes on one earthquake on different stations. Coda envelopes are computed as RMS amplitude of filtered signal (1 - 32 Hz). Left column shows raw envelopes, right one smoothed ones (smoothed with 4 s long median window) for better visibility. Signals are normalized by the mean value of envelope amplitude within lapse times 60 and 70 s.

It is clearly recognizable that codas are fairly similar with no obvious dependence on hypocentral distance. Amplitude differences as a results of differences between stations were removed by the normalizing.

In Figures 5.6 and 5.7 we carried out similar analysis, but focusing on possible influence of earthquake magnitude on the observed coda shapes. Figure 5.6 shows several normalized earthquakes on station LBC in raw and smoothed versions (frequency range 1 - 32 Hz). Figure 5.7 plots stacked seismograms of different earthquakes on different stations with hypocentral distances ranging from 7 to 60 km. We can conclude that all the events have fairly similar coda envelopes shapes and their variations in power were removed by normalization as well.

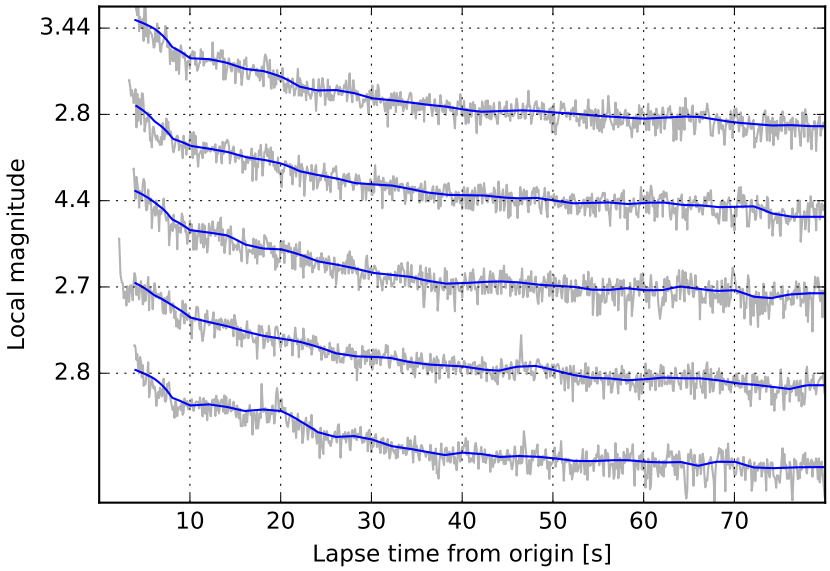

FIGURE 5.6: Coda envelopes of different earthquakes 2008-2014 on stations WERN. *Y* axis is showing the events magnitudes. Coda envelopes are computed as RMS amplitude of filtered signal (1 - 32 Hz). Left column shows raw envelopes, right one smoothed ones (smoothed with 4 s long median window) for better visibility.

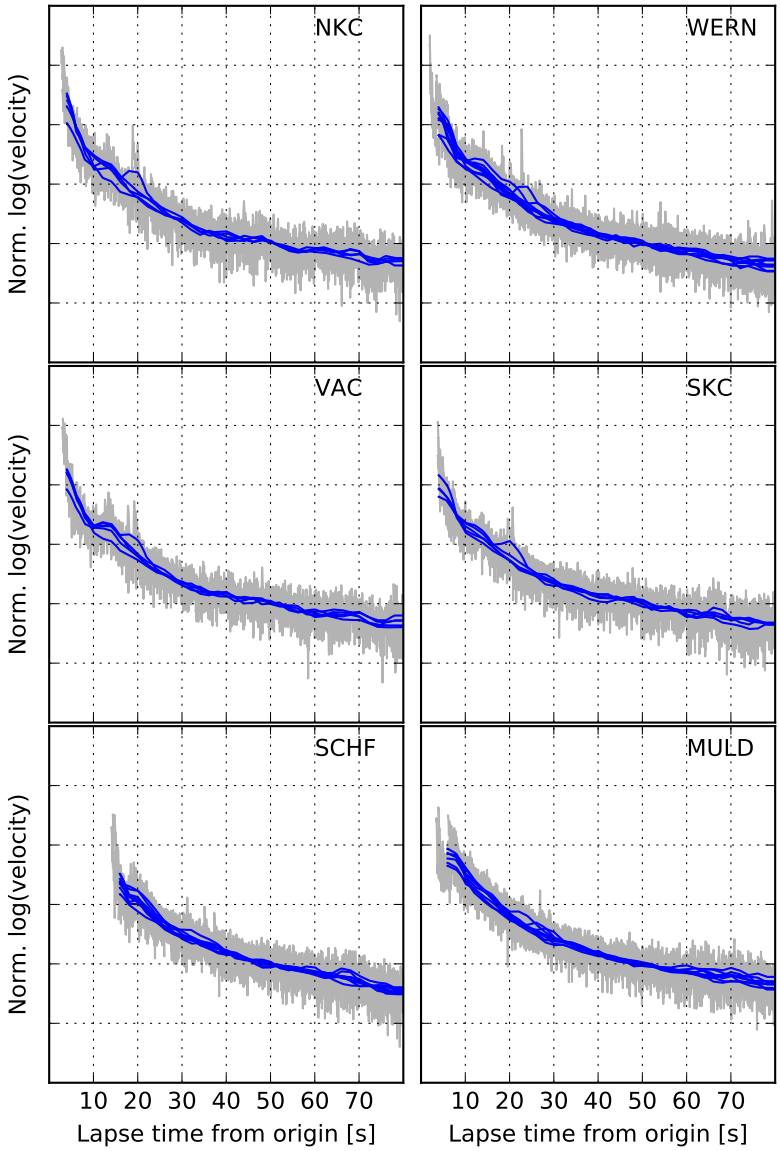

FIGURE 5.7: Stacked coda envelopes of different earthquakes on stations NKC, WERN, VAC, SKC, MULD and SCHF. Coda envelopes are computed as RMS amplitude of filtered signal (1 - 32 Hz). Grey curves show stack of raw envelopes, blue ones smoothed signals (smoothed with 4 s long median window) for better visibility. Signals are normalized by the mean value of envelope amplitude within lapse times 60 and 70 s.

Identical test was carried out to search for possible frequency dependence (Figure 5.8). Again, no obvious dependency of coda shape was found and normalization worked as intended.

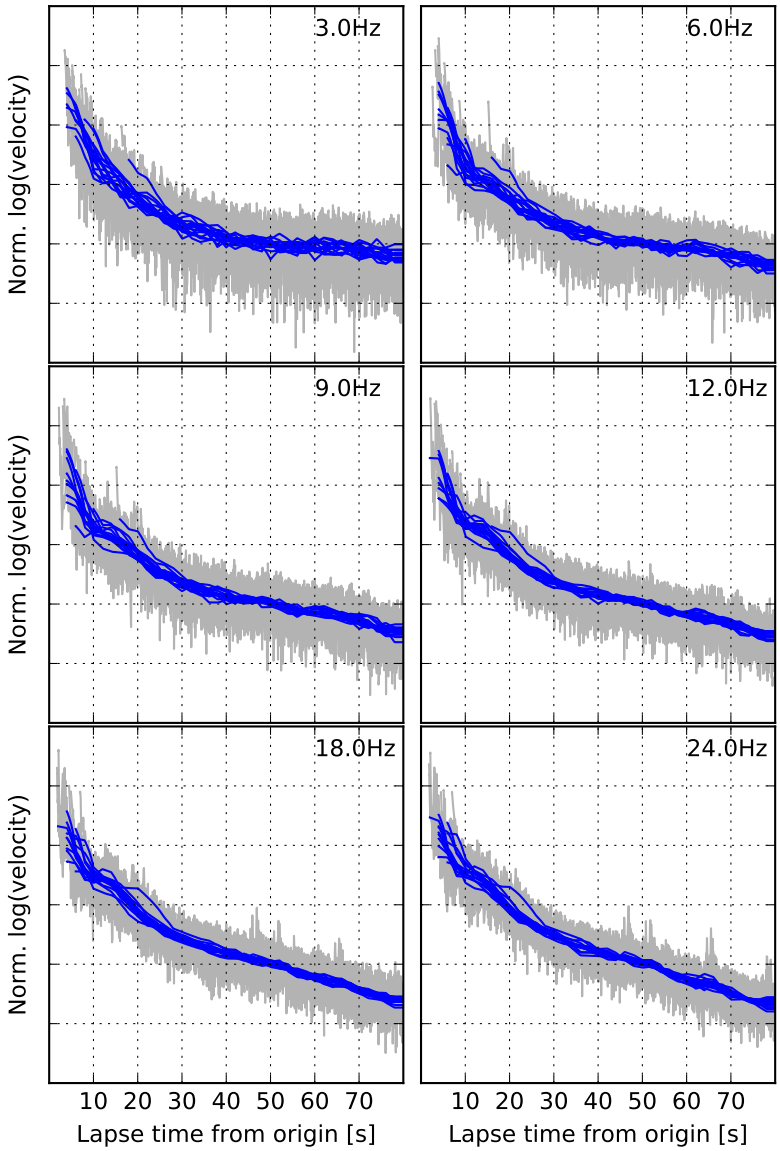

FIGURE 5.8: Coda envelopes on one earthquake on different stations. Frequency bands with central frequencies 3, 6, 9, 12, 18 and 24 Hz are shown (with bandwidths of 2, 4, 6, 8, 12 and 16 Hz). Coda envelopes are computed as RMS of filtered coda signal. Grey curves represent stacked raw envelopes, blue curves are are the same data but smoothed with 4 s long median window for better visibility.

A general coda shape of West Bohemian earthquakes might be clarified as follows: early coda up to a lapse time of 30 s is associated with steep decay, while later coda with flatter decay starts at the lapse time of 40 s and lasts until the end of the observable coda signal. Between lapse times of 30 and 40 s the coda decay is undergoing the steepness change. Terms "early coda" and "late coda" will be used for the purposes of this work, despite different definitions of early and late coda given by other authors. The transition zone between early and late coda is always in the same lapse time - between 30 and 40 seconds, with no obvious dependence on magnitude (Figures 5.6), station (Figure 5.5) or frequency (Figure 5.8).

Seismograms of the West Bohemian earthquakes have similar shapes and differ only in amplitudes as a result of different magnitudes and different site effects. Those two aspects might be removed by seismogram normalizing in terms of the coda normalization theory. After the normalization only the shapes of envelopes remain. The similarity of the West Bohemian codas indicates that they are all controlled by the attenuation properties of the same area. Possible small attenuation variations in space are not separable from single codas. In other words, our stations and earthquakes are too close together to enable us to obtain spatial characteristics of the crust beneath the seismic networks. We can only estimate the attenuation as an integral parameter generally valid for West Bohemian crust.

5.8 Methods and data processing

A number of methods have been developed to study an earthquake coda. Here we describe only the ones used for the purposes of these study.

5.8.1 Q_c - Coda Window Method

Coda window method (CWN) is the first method to quantify the decay of coda amplitudes (Aki and Chouet, 1975). Eq. 5.3.1 might be expressed in the terms of amplitudes instead of energies, where amplitude $A = \sqrt{E}$:

$$A(t,f) = S(f)t^{-m/2}e^{-\pi ft/Q_c} \tag{5.8.1}$$

where $A(f,t)$ is the amplitude of wave with frequency f in lapse time t. Taking natural logarithm of Eq. 5.8.1 leads to

$$ln(A(t,f)t^{m/2}) = ln(S(f)) - (\pi ft/Q_c) \tag{5.8.2}$$

where $Q_c(f)$ can be determined by a linear regression of Eq. 5.8.2 and solved for the slope b:

$$Q_c(f) = -\pi f/b. \tag{5.8.3}$$

Parameter m is set a priori 1.5 for diffusion approximation, since the later coda with expected diffusive behavior is a subject of analysis. By applying Eq. 5.8.2 and 5.8.3 on the selected parts of coda signal (trimmed coda windows) we can directly estimate $Q_c(f)$. To remove codas affected by any kind of signal disturbances (hidden aftershocks, reflections etc.) only measurements with regression cross-correlation coefficient higher than 0.90 was accepted.

The crucial part of using the CWM is selection of the lapse time window length and starting time of the measurement. A traditional approach is to start at the double S-wave travel time and analyze lapse time windows of different lengths. This approach has its limitations, especially in the cases of hypocentral distances shorter than 50 km. Calvet and Margerin (2013) showed that using double S-wave travel time as the starting time of the studied time windows causes strong hypocentral distance dependence of the resulting Q_c. This dependence reflects the fact that at the short distances the coda window starts right after the ballistic S-wave front where the decay of the coda is fastest, while at large distances the analysis starts well after the passage of the ballistic front and presumably samples multiple-scattered waves. So analyzing slopes of later part of coda with fixed start with respect to the origin is preferred now-days. The later lapse times fulfill the assumption that all scattered coda waves recorded by all stations are equally multiply scattered and propagate in the diffusive regime. Therefore, the energy is homogeneously distributed within the studied area.

So the question remains, what time after origin time this diffusion regime takes place in such a way that estimated Q_c fully represents Q_i. Simply applicable method was proposed by Calvet and Margerin (2013). Based on numerical modeling and testing different crust models they concluded that diffusion assumption is fully valid in that part of the coda where the slope (or Q_c) is constant - is not a function of coda window start time.

We took the DS80 dataset and carried out analysis to asses the ideal start time for coda windows. We let the 20 s long time window move over the bandpass-filtered, smoothed and normalized seismograms with step of 1 second. Q_c was computed for every station-event combination and plotted against its window start time (Figure 5.9). Q_c was observed to be constant at lapse times greater than 30 seconds, with no visible station, event, window length or frequency dependence.

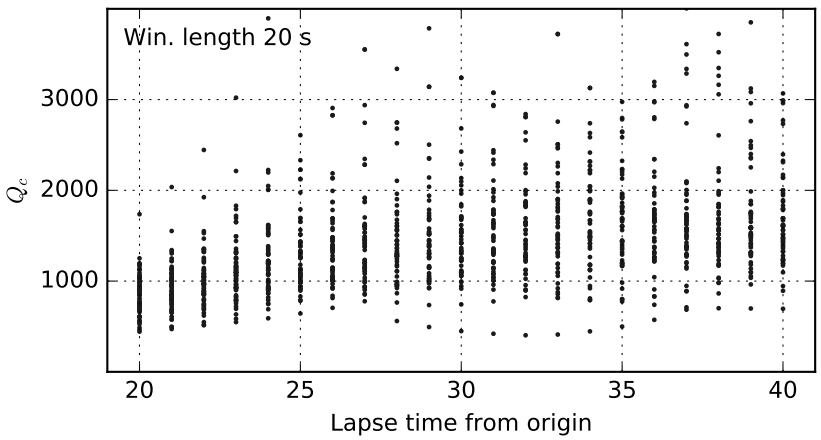

FIGURE 5.9: Lapse time dependence of Q_c for signal with central frequency 9 Hz (bandwidth 6 Hz). 20 s long coda window moved with 1 s step through smoothed coda envelopes (all station-event combinations) and Q_c was computed - every black dot represents one Q_c for one coda on one station with one lapse time start. Attenuation become stable at lapse times larger than 30 s. Diffusion regime of coda wave-field is for lapse times larger than this point.

Starting at this lapse time the coda wave-field behavior is assumed to be diffusive and estimated Q_c is a measure of intrinsic loss Q_i. Diffusive regime start correlates well with the change between early and later coda.

Different lengths of moving coda windows were tested as well. Short windows of 20 s allow analyzing different segments of coda (one can place more of them into studied time interval), longer windows up to 40 s are more resistant against signal fluctuations. For shorter windows the smoothing of coda envelopes is necessary and have to be applied carefully not to affect data

in an undesired manner. Windows of lengths 20, 30 and 40 seconds were applied. Method was fully applied on the DS80 dataset containing stronger events with long uncorrupted codas.

A scheme of the data processing is shown in Figure 5.10. For a single event on a single station the individual processing steps are:

1. **Seismogram filtering**

   Attenuation was studied for different frequency bands. Those were: 2-4 Hz, 4-8 Hz, 6-12 Hz, 8-16 Hz, 12-24 Hz and 16-32 Hz. For simplification central frequencies are used for naming: 3 Hz, 6 Hz, 9 Hz, 12 Hz, 18 Hz, 24 Hz. 3-pole bandpass Butterworth filter was used.

2. **Envelop computation**

   Envelope of a filtered seismogram was computed as the RMS of 1 s window moving over the signal. Visual check validated this way of processing.

3. **Envelope smoothing**

   Moving median window 4 s long was used to smooth seismograms in 2 rounds. Smoothing suppressed local amplitude bursts, but blurred the boundary between the early and late coda, which had to be checked during the analysis. For short lapse time windows of length 20 s the smoothing was crucial for achieving stable results.

4. **Lapse time correction**

   Coefficient $m = 1.5$ in Eq. 5.8.2 was used for geometrical spreading correction. Exponent 1.5 is valid for diffusion approximation of coda wave-field.

5. **Linear regression**

   Standard linear regression was applied on data and Q_c was computed - Eq. 5.8.2 and 5.8.2 were applied. Cross-correlation coefficient of synthetic line and analyzed signal was computed. Measurements with cross-correlation coefficient higher than 0.90 were excluded from the analysis.

6. **Mean Q_c computation**

   Mean Q_c was computed as an inverse of mean $1/Q_c$s:

   $$1/Q_c^{final} = \sum_{i=1}^{N} 1/Qc^i \tag{5.8.4}$$

   where every Q_c^i represents analysis of one event coda on one station. The standard deviation as a measure of error was estimated.

7. **Frequency dependence estimation**

   Results were visually checked and power-law expression (Eq. 5.1.3) was applied for quantifying the $Q_c(f)$ and its frequency dependence.

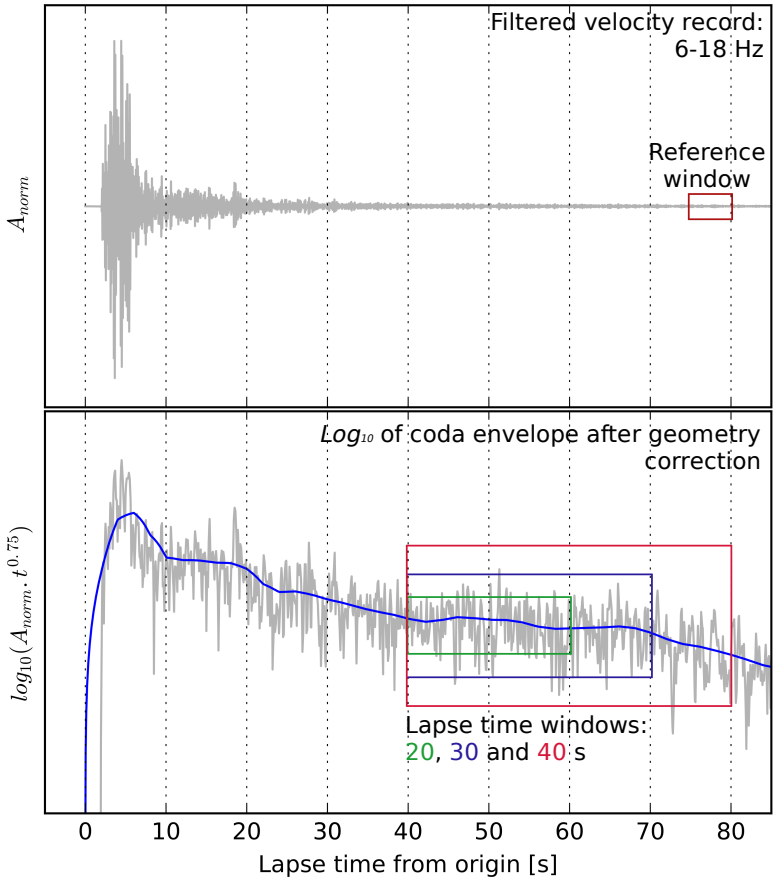

FIGURE 5.10: Processing of the velocity records during Q_c estimation. Top: filtered velocity record, normalized by late coda amplitude (red rectangle). Bottom: Log_{10} of coda envelope (RMS of raw envelope) corrected for diffusion geometry ($*t_{0.75}$). Rectangles show lapse time windows of different lengths for which Q_cs are estimated. They have common starting point at lapse time 40 s.

5.8.2 Q_i and Q_{sc} separation - Multiple Lapse Time Windows Analysis

Multiple Lapse Time Windows Analysis (MLTWA) was introduced by Fehler et al. (1992). It uses approximate solutions of the RTT to model the synthetic seismograms and compares them with observed data. Two approximate solutions have been derived: Zeng's hybrid single scattering diffusion solution (Eq. 5.4.1 and 5.4.2) and Paasschens's solution (Eq. 5.4.3 and 5.4.4).

The MLTWA studies energy distribution within the coda as a function of hypocentral distance. The energy distribution within the coda of a single event is changing with the hypocentral distance and the change - redistribution of energy from early to late coda is controlled by the Q_i and Q_{sc}. The method allows to analyze a large number of events from many stations mutually.

The MLTWA reduces each coda energy envelope into a few points. The energy envelope for a given frequency is divided into a few lapse time windows and each window is integrated - single event-station pair produces a few distinct points (one point for one lapse time window). The same approach is applied to the modeled energy envelopes. Figure 5.11 shows seismogram processing as used in Bachura and Fischer (2016).

For successful application of the MLTWA 3-component seismograms of earthquakes with wide range of hypocentral distances are essential (with uniform distribution). Our datasets undergoing the analysis contain one tight cluster of events in the middle of the network (Nový Kostel

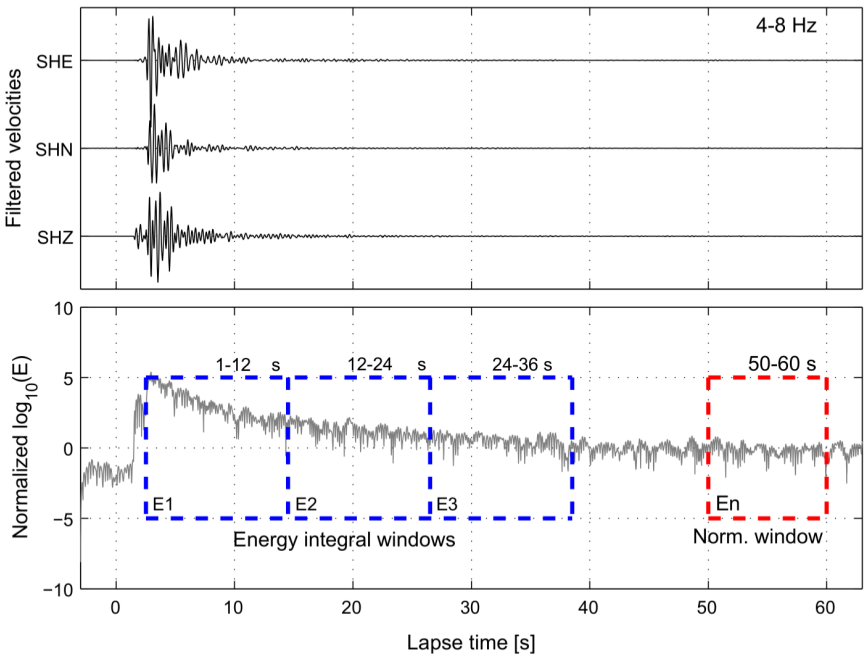

FIGURE 5.11: MLTWA data processing as used in Bachura and Fischer (2016). Top: filtered 3-component record. Bottom: sum of the energies with three consecutive windows starting at the S-arrival (blue) and reference coda window (red) for normalization starting at 50 s after origin time and 10 s long.

focal zone) with stations distributed around. Hypocentral distances are non-uniformly distributed in the extent of 8–60 km. We didn't use the records with hypocentral distances bellow 15 km in order to emphasize the weight of the less numerous farther records.

To compute the energy envelopes we computed the velocity envelopes (RMS) for each component, then squared them to get their energies and then summed them:

$$E^{\text{obs}} = \sum_{i=1}^{K} Ec_i^{\text{obs}}, K = 1, 2, 3 \tag{5.8.5}$$

where E^{obs} is the final energy envelope, Ec_i^{obs} is the energy envelope of ith component.

Resulting energy envelope was normalized by the means of coda normalization theory. Normalizing factor was computed as the mean of coda energy in a reference interval located in the late coda portion long after the origin time. Different reference intervals were used with respect to the analyzed datasets. Normalized energy envelope then is

$$En^{\text{obs}} = Ec^{\text{obs}} / |Ec^{\text{ref}}|_T, \tag{5.8.6}$$

where En^{obs} is the normalized observed energy. Ec^{obs} is the sum of single squared components (energy) and $|Ec^{ref}|_T$ is the normalizing factor in time interval T.

After normalizing, the energy envelope En^{obs} (Eq. 5.8.6) is trimmed into a few (K) consecutive lapse time windows of chosen lengths. The windows might start at the fixed times in coda or their starts can be controlled by the S-wave arrival. Then the windows are integrated.

In the case of $K = 3$ (three windows) energy integrals are

$$E_1^d = \int_{t_1}^{t_2} En^{\text{obs}}, \quad E_2^d = \int_{t_2}^{t_3} En^{\text{obs}}, \quad E_3^d = \int_{t_3}^{t_4} En^{\text{obs}}, \tag{5.8.7}$$

where t marks the beginning and end of every selected time window.

The three energy integrals E_i^d are corrected for geometrical spreading (multiplying by $4\pi r^2$) and plotted against hypocentral distance (dots in Figure 5.12). A similar approach is applied on synthetic coda energy envelopes already modeled using Eqs. 5.4.1 and 5.4.2 or 5.4.3 and 5.4.4) with input parameters Q_i, Q_{sc}. By choosing a regular spacing of hypocentral distances we obtain a line plot of synthetic envelope integrals (lines in Figure 5.12).

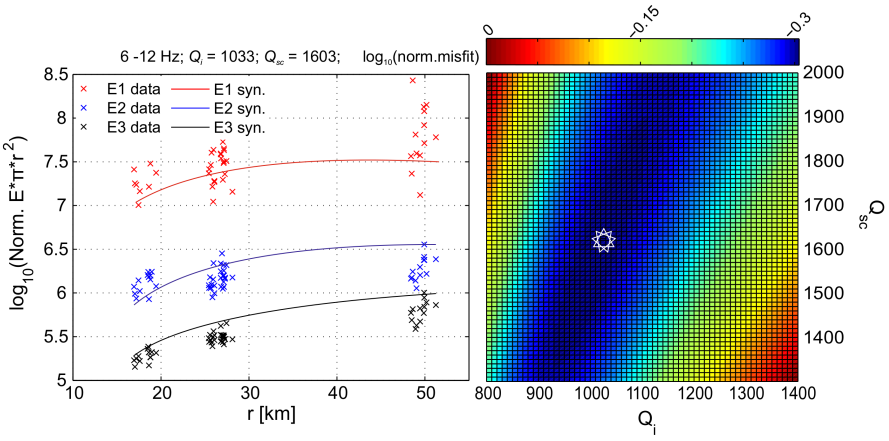

FIGURE 5.12: Comparison of synthetic (lines) and observed (crosses) data: Left plot is in the terms of misfit function (Eq. 5.8.8), right plot is the normalized log_{10} of the normalized misfit function. White star shows the minimal residual (Bachura and Fischer, 2016a).

Finally, the best fit between synthetic curves and scattered data points for selected central frequency f is searched using a misfit function:

$$M(Q_{\text{i}}, Q_{\text{sc}}) = \sum_{k=1}^{N} \sum_{i=1}^{K} w_{\text{i}} (\log_{10} E_i^d(r_k) - \log_{10} E_i^{\text{syn}}(r_k))^2, \; i = 1 \ldots 3, k = 1 \ldots N, \tag{5.8.8}$$

where N is the number of recordings of single event-station combinations on unique hypocentral distance. K is number of lapse time windows used. Weighting term w_i is used to control the weight of integrated windows (later lapse time windows have smaller scatter, since they do not contain the ballistic wave front and, therefore, are not influenced by the source radiation characteristics). A grid search within $Q_i, Q_{sc} \in \langle 100, 6000 \rangle$ intervals is used to find the best solution for Q_i and Q_{sc} (minimum of Eq. 5.8.8). Apart from the best solution we obtain an information on the misfit function useful for error analysis. Figure 5.12 shows the process for three time windows (Bachura and Fischer, 2016a).

From resulting $Q_i(f)$ and $Q_{sc}(f)$ the following parameters are estimated: total quality factor $Q_t(f) = 1/Q_i^{-1}(f) + Q_s c^{-1}(f)$, seismic albedo $B_0(f) = Q_t(f)/Q_{sc}(f)$, total attenuation coefficient called extinction length inverse $Le^{-1}(f) = 2\pi f/vQ_t(f)$, scattering coefficient $g_0(f) = 2\pi f/vQ_{sc}(f)$ and mean free path $l(f) = g_0^{-1}(f)$. Total attenuation Q_t^{-1} or total quality factor Q_t describes total influence of all attenuation processes. Seismic albedo B_0 characterizes which process is stronger. If $B_0 > 0.5$ then scattering dominates, if its lower the intrinsic loss takes the dominance. Extinction length inverse $Le^{-1}(f)$, mean free path $l(f)$ and scattering coefficient $g_0(f)$ are another ways how to describe attenuation properties of medium.

We applied the MLTWA on two datasets in order to study the applicability of the method to a different data type. By the application of the MLTWA on dataset DS2011 (Bachura and Fischer, 2016a) we estimated Q_i and Q_{sc} from early parts of event's codas - the part of the seismograms starting at the S-wave arrival and ending approximately 36 s later. To model synthetic energy envelopes the Zeng's RTT approximation was adopted.

Next, we applied the MLTWA on dataset DS80 in order to test the method applicability on late coda. The coda part starting 40 s and ending 80 s after after origin time was a subject of the analysis. For these purposes the Paaschens's RTT solution was used.

Data processing work-flow for MLTWA was very similar for both our applications, late and early coda:

1. **Single components filtering**

   Both datasets analyzed attenuation parameters for frequency bands 2 - 4 Hz, 4 - 8 Hz, 6 - 12 Hz, 8 - 16 Hz, 12 - 24 Hz and 16 - 32 Hz (the last frequency band was estimated only for late coda dataset). Central frequencies are used for naming: 3 Hz, 6 Hz, 9, Hz, 12 Hz, 18 Hz, 24 Hz. 3-pole bandpass Butterworth filter was used to accomplish the step.

2. **Single components envelope computation**

   Envelop of a single filtered seismogram was computed as the RMS of 1 s window moving over the signal. Visual check validated this way of processing.

3. **Energy envelop computation**

   Energy is computed as a sum of squares of the single components envelopes.

4. **Energy envelop normalization**

   Effects of source and station were removed by normalizing the energy envelope by normalizing factor - the mean energy within the reference window at lapse time 50 - 60 s for DS2011 and 75 - 80 s for DS80.

5. **Trimming lapse time windows and their integration**

   The DS2011 dataset was analysed using three consecutive lapse time windows of length 12 s with the first window starting at S-wave arrival (Figure 5.13). For DS80 analysis we use two lapse time windows with fixed start times at 40 and 60 s after the origin. Lengths of the windows are 20 s (Figure 5.13). Windows were integrated using equation Eq. 5.8.7.

6. **Geometrical spreading correction and plotting against hypocentral distance**

   Each lapse time window integral (event-station pair) was corrected for geometrical spreading by multiplying with $4\pi r^2$ and then plotted against hypocentral distance (Figure 5.12).

After the data processing synthetic coda energy envelopes were computed, processed and compared with the data by means of Eq. 5.8.8. For the DS2011 dataset, where three lapse time windows were used right after the S-wave arrival the weight of the first window was suppressed by using the weighting factor of 0.5. Later lapse time windows were weighted by a factor of 1. The DS80 dataset with lapse time windows in later coda we used equal weights of 1 for each window.

Result were expressed by $Q_i(f)$, $Q_{sc}(f)$, $Q_t(f)$, $B_0(f)$, $l(f)$, $Le^{-1}(f)$ and $g_0(f)$ and by a power-laws (Eq. 5.1.3).

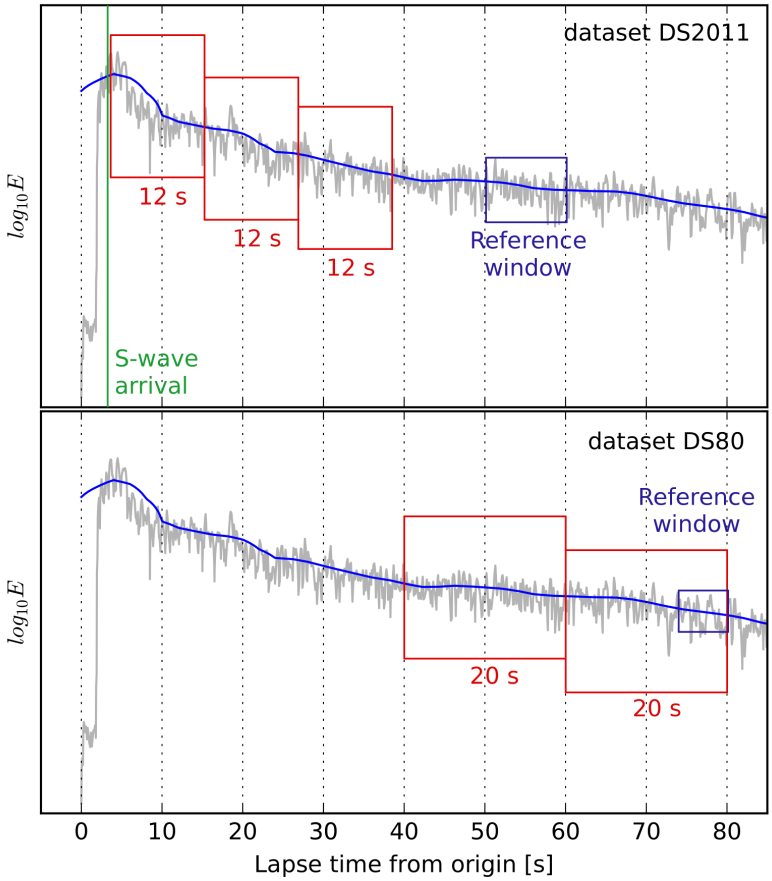

FIGURE 5.13: MLTWA parameters for two datasets. Top: DS2011, raw (grey) and smoothed (blue) $log_{10}E$ of single events. Three consecutive lapse time windows with duration of 12 s (red rectangles) were used. The first one starts at S-wave arrival. Reference interval for coda normalization lies between 50 and 60 s (blue rectangle). Bottom: DS2014, same waveform, different MLTWA parameters: two 20 s long windows (red rectangles) with fixed starting points at 40 and 60 s after the origin time. Reference window between 75 and 80 s.

5.8.3 Q_P Q_S - Coda Normalization Method

The coda normalization method (CNM) proposed by Aki (1980) is based on the idea that at some lapse time the seismic energy is uniformly distributed in volume surrounding the source. The idea of the CNM grew out of the empirical observation that the length of the seismogram recorded by a regional/local seismic network is proportional to the magnitude of the event. Another key observation in support of the CNM is that, for a local earthquake recorded at times greater than roughly twice the travel time of an S-wave from a source to a receiver, band-pass filtered seismograms have a common envelope shape that is independent of the source-receiver distance although the maximum amplitude of the envelope varies with source size and recording site amplification.

Interpreting S-coda as an incoherent superposition of scattered S-waves, we may explicitly write the S-coda power as a convolution of the source, propagation, and site effects as

$$|\dot{u}_{ij}^{S,Coda}(t,f)| \propto W_i^S(f)|N_j^S(f)|^2 t^{-n} e^{-Q_c^{-1}2\pi f t}, \tag{5.8.9}$$

where $\dot{u}_{ij}^{S,Coda}(t,f)$ is the S-coda velocity wave-field at the jth receiver filtered on a frequency band having central frequency f, $W_i^S(f)$ is the energy radiation from the ith source, $N_j^S(f)$

is the S-wave site amplification factor for the jth site and the power n equal to 1, 1.5 or 2 is depending on the assumed dominance of surface, diffusive and body waves. Here we suppose the $Q_c(f)$ is a function of frequency f and is constant in the study area irrespective of source and site locations (Sato, Fehler, and Mayeda, 2012).

On the other hand, the square of the direct S-wave velocity amplitude at station j in a frequency band with central frequency f for local earthquake source i is written as

$$|\dot{u}_{ij}^{S,Direct}(f)| \propto r_{ij}^{-2} W_i^S(f) |N_j^S(f)|^2 t^{-n} e^{-Q_S^{-1} 2\pi f r_{ij}/V_S}, \tag{5.8.10}$$

where r_{ij} is the hypocentral distance of station j from source i and Q_S is the S-wave quality factor. Taking the ratio of the product of hypocentral distance and the direct S-wave amplitude to the average coda amplitude over time interval T, we cancel the site amplification and source terms. Taking the natural logarithm of the ratio, one gets

$$ln \frac{r_{ij} |\dot{u}_{ij}^{S,Direct}(f)|}{\sqrt{\langle |\dot{u}_{ij}^{S,Coda}(f)|^2 \rangle_T}} = -(Q_S^{-1}(f) \pi f / V_S) r_{ij} + constant, \tag{5.8.11}$$

where we suppose that focal mechanisms are random. By using the measurements over a large enough number of earthquakes the radiation patterns differences are smoothed out. At station j, plotting the left-hand side against hypocentral distances r_{ij} for many earthquakes, the gradient (slope) gives the attenuation of direct S-wave amplitude per travel time distance.

Yoshimoto, Sato, and Ohtake (1993) extended the conventional coda normalization method to measure the amplitude attenuation of direct P-waves with travel time distance. They assumed that the ratio of P and S-wave radiated energies $W_i^P(f)/W_i^S(f)$ by individual earthquakes is independent of magnitude for earthquakes (within a small magnitude range even though their spectra are different (Yoshimoto, Sato, and Ohtake, 1993)). Similar to the S-wave case, the square of direct P-wave amplitude at station j is written as

$$|\dot{u}_{ij}^{P,Direct}(f)| \propto r_{ij}^{-2} W_i^P(f) |N_j^P(f)|^2 e^{-Q_P^{-1} 2\pi f r_{ij}/V_P}, \tag{5.8.12}$$

where N_j^P is the site amplification factor of P-wave at station j. Similarly as for S-waves above, we get

$$ln \frac{r_{ij} |\dot{u}_{ij}^{P,Direct}(f)|}{\sqrt{\langle |\dot{u}_{ij}^{S,Coda}(f)|^2 \rangle_T}} = -(Q_P^{-1}(f) \pi f / V_P) r_{ij} + constant, \tag{5.8.13}$$

since the ratio of site amplification factors N_j^P/N_j^S is constant. At the jth station, plotting the left-hand side against hypocentral distance r_{ij}, we estimate Q_P^{-1} from the linear regression gradient (Sato, Fehler, and Mayeda, 2012; Yoshimoto, Sato, and Ohtake, 1993).

Method can be used as "a single station approach", when one station and multiple events on different hypocentral distances are used, as "a single event approach", when one event is measured on multiple stations differently distanced from the event, or as a "combined approach", when multiple events with multiple stations are used.

Coda normalization method is the only coda method directly measuring attenuation along the ray paths of seismic waves. It is also the only method allowing analyzing the P-wave

attenuation. In this study the DS60 dataset underwent the CNM analysis and $Q_P(f)$ and $Q_S(f)$ were estimated.

Data processing work-flow was:

1. **Waveforms filtering**

   We estimated attenuation parameters for frequency bands 2-4 Hz, 4-8 Hz, 6-12 Hz, 8-16 Hz, 12-24 Hz and 16-32 Hz with central frequencies: 3 Hz, 6 Hz, 9, Hz, 12 Hz, 18 Hz, 24 Hz. 3-pole bandpass Butterworth filter was used for the filtration. Vertical component was selected for estimating the P-wave attenuation, north-south (N) component for S-wave attenuation.

2. **P- and S-wave picking**

   The maximum absolute amplitude behind direct wave arrival was used for attenuation estimation - $\dot{u}^{P|S,Direct}$ in Eq. 5.8.11 and 5.8.13 (Figure 5.14). The picks were obtained manually, but automatized routine was tested and almost identically good results were achieved.

3. **Waveforms processing**

   Coda envelope was computed as the RMS of 1 s window moving over the signal.

4. **Selecting coda reference window**

   Used dataset DS60 contains events with uncorrupted codas up to lapse time of 60 s. The mean of coda amplitudes between 50 and 60 s was used as a normalization factor $\dot{u}^{S,Coda}$ in Eq. 5.8.11 and 5.8.13 (Figure 5.14).

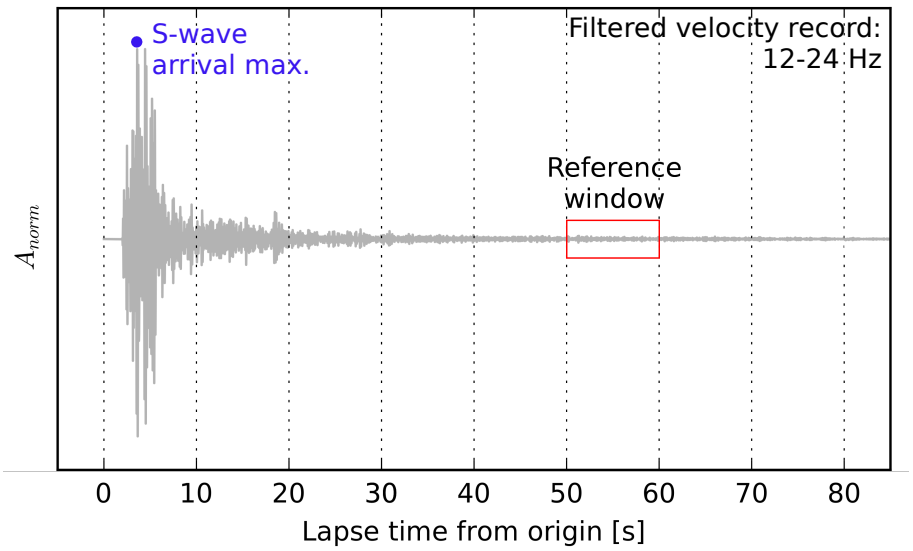

FIGURE 5.14: Coda normalization method data processing. Blue dot: Maximum of S-wave wavefront. Red rectangle: window in coda used to compute the normalization factor - mean of filtered signal (grey) RMS.

5. Q_P **and** Q_S **estimation**

   For each event a set of logarithms of ratios between direct wave amplitudes and reference coda amplitudes multiplied by hypocentral distances was obtained (Eq. 5.8.11 and 5.8.13). When plotted against hypocentral distance the slope of the fitted line gives Q_P, resp. Q_S. The fitting procedure must be done with respect to the data character: data

distribution along x axis - hypocentral distances and y axis - scatter of the coda normalized amplitudes (5.15), which plays significant role in controlling the slope of the fit. We uniformed the distribution of the data by reducing the normalized amplitudes for a more uniform distance step (Figure 5.15) to equal the influence of all hypocentral distances on the line fit.

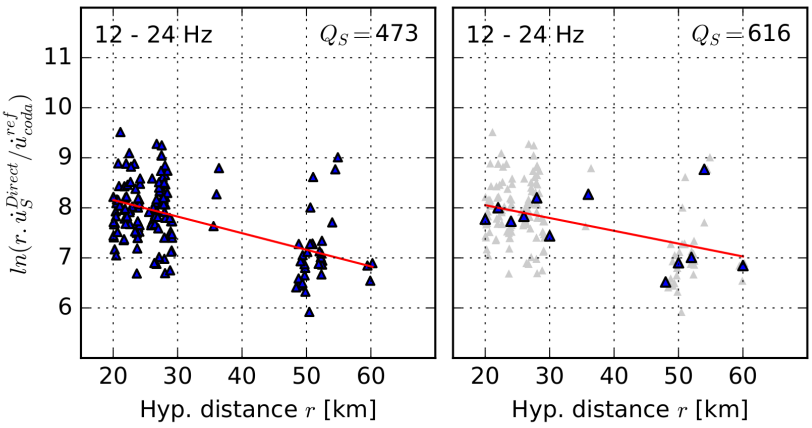

FIGURE 5.15: Differences in Q_S estimation as a result of various fitting approaches. Coda normalized S-wave amplitudes with distance correction (r) vs. hypocentral distance. Each point represent S-wave arrival of one earthquake for one station. Points are non-uniformly distributed along y axis as a consequence of non-uniform station distribution. Left: Q_S estimation from linear regression applied on all possible scattered points. Right: Q_S estimation from reduced data points (mean amplitudes for consecutive distance windows).

5.9 Results

5.9.1 $Q_c(f)$ - Coda Windows Method

We applied the coda windows method (CWM) on 10 earthquakes of DS80 dataset. Q_c's for given frequencies were estimated for lapse time windows of lengths 20, 30 and 40 s. All windows were starting 40 s after origin time. For every event-station pair on each frequency we obtained a single Q_c value. After each measurement the resulting fitted line was cross-correlated with the measured coda envelope and those with cross-correlation coefficient lower than 0.9 were excluded from results list. Final frequency dependencies of mean Q_c's together with error estimates are shown in Figure 5.16.

With increasing lapse time window length the reliability of resolved $Q_c(f)$ increases and the scatter of single estimates (grey dots in 5.16) decreases. For lower frequencies of 3 and 6 Hz a vast majority of measurements is filtered out due to a low cross-correlation coefficient. $Q_c(f)$ varies from 1376 to 2494. It is slightly rising with prolonging the lapse time window, but the increase is still within the error range.

We tested for possible trends in $Q_c(f)$ values: the station dependence, azimuth dependence or source strength (magnitude) dependence. None of them was found to be affecting the results. The strong scatter of single Q_c's is simply a result of differences in individual linear fits. Especially for higher frequencies the small variation in line slope might affect the Q_c level significantly.

The power-law parameters (Eq. 5.1.3) were estimated for every lapse window length with frequency dependence exponents n ranging from 0.36 ± 0.09 up to 0.48 ± 0.06. Those are rather

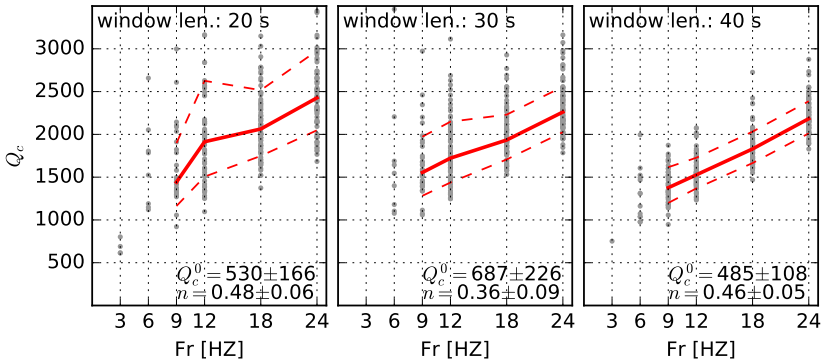

FIGURE 5.16: Frequency dependence of Q_c for lapse time windows of length 20 s(left), 30 s (middle) and 40 s (right). Grey dots represent single coda $Q_c(f)$ estimated for station-events combinations, red line is resulting mean $Q_c(f)$, dashed lines show error intervals represented by a standard deviation. Mean $Q_c(f)$ is estimated only when at least 15 station-event estimates exist. Parameters $Q_c(f)^0$s and n are shown for every lapse time window.

low (in comparison with other studies (e.g. Mukhopadhyay et al., 2008; Tselentis, 1993)). It is necessary to keep in mind that the power-law dependence was computed for frequency range 9 - 24 Hz. Lower frequencies, strengthening the reliability of n estimates are missing.

5.9.2 Q_i and Q_{sc} separation - Multiple Lapse Time Windows Analysis

The MLTWA reduces observed energy envelopes into a few points (energy integrals) and compares them with modeled synthetic ones. The agreement between observations and synthetics is quantified by a misfit function (Eq. 5.8.8) in which the minimum represents the best solution - best combination of Q_i and Q_{sc} for a given frequency f.

We analyzed intrinsic loss and scattering of two datasets: DS2011 and DS80. The first one (Bachura and Fischer, 2016a) was used for early coda analysis while the second estimated attenuation parameters by using late coda portion. An important, but not crucial difference was that the 'early coda' dataset used Zeng's RTT solution while for the 'late coda' we adopted Paasschens's solution of the RTT. Further data processing differences were minor and are described in previous chapters.

For 'early coda' dataset DS2011 there is a rather loose agreement between observed data and synthetics (Figure 5.17), worse than the fits shown by other authors (e.g. Meirova and Pinsky, 2014; Padhy and Subhadra, 2013; Zhang and Papageorgiou, 2010) or than our fit for late coda dataset (see below). The fit is visually improving with increasing frequency. Strong scatter of energy integrals of the first window (the one containing a direct wave arrival, triangles on Figure 5.17) is caused by the S-wave amplitude variations controlled by radiation pattern. Later energy integrals (lapse time windows) positioned in pure coda are more consistent and unaffected by the source effects.

Obtained frequency dependent $Q_i(f)$, $Q_{sc}(f)$ and $Q_t(f)$ are plotted in Figure 5.18. $Q_i(f)$ has lower error than $Q_{sc}(f)$. $Q_t(f)$ is computed as Eq. 5.1.2. All quality factors can be described by the power-law notation. Intrinsic loss has dependency coefficient $n = 0.63$ with negligible error and scattering loss is almost linear with $n = 1.03 \pm 0.15$. Behavior of resulting quality factors, despite visually poor fit mentioned above follows expected (empirically observed) characteristics. Quality factors rise with frequency in a regular manner. Obtained absolute values vary in reasonable range.

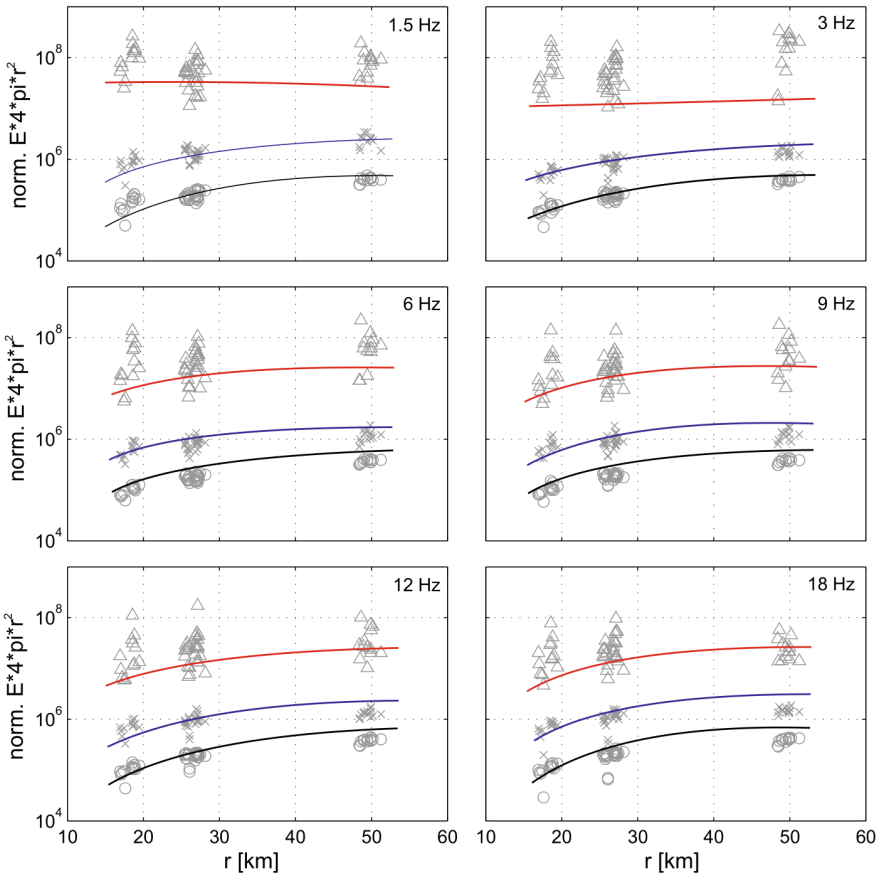

FIGURE 5.17: Normalized energies in three time windows: 1–12 s (triangles), 12–24 s (crosses), and 24–36 s (circles) after S-wave arrival vs. hypocentral distance. The lines represent the best first obtained for the Q_i and Q_{sc} pair giving minimum of the misfit function Eq. 5.8.8.

From the knowledge of $Q_i(f)$ and $Q_{sc}(f)$ derived parameters (scattering coefficient $g_0(f)$, seismic albedo $B_0(f)$, extinction length inverse $L_e^{-1}(f)$ and mean free path $l(f)$) are computed and plotted in Figure 5.19. Intrinsic loss is dominant ($B_0(f) < 0.5$) for all frequencies except 3 Hz. Its influence is increasing as the B_0 decreases with frequency . Mean free path $l(f)$ is constant between 90 and 110 km and its inverse - scattering coefficient $g_0(f)$ fluctuates around 0.01 km^{-1}. Extinction length inverse $Le^{-1}(f)$ varies slightly between 0.02 and 0.03. l, g_0 and Le^{-1} are more or less frequency independent.

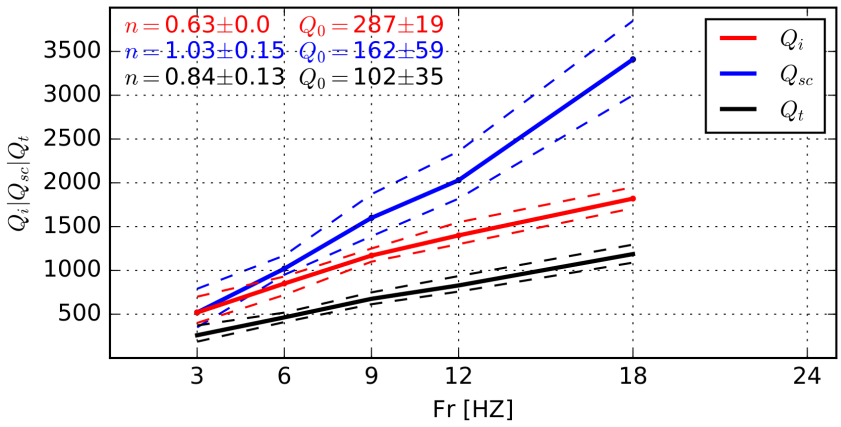

FIGURE 5.18: Resulting frequency dependences of the Q_i, Q_{sc}, Q_t as achieved by the MLTWA applied on DS2011 dataset. Early coda (up to 40 s after S-wave arrival) and Zeng's (1991) approximation of the RTT were used. The frequency power-law parameters Q_0 and n are listed inside the plot.

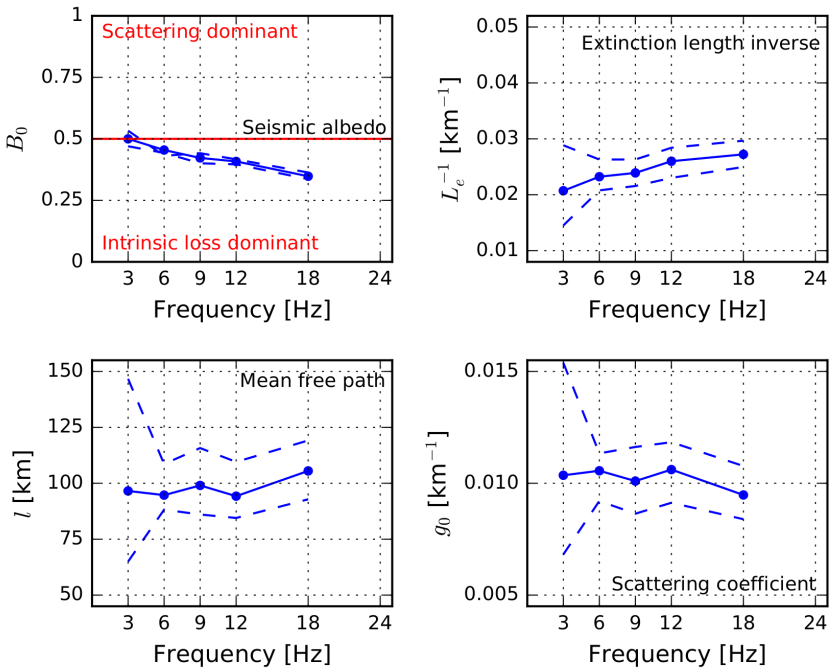

FIGURE 5.19: Resulting frequency dependences of the seismic albedo B_0, total attenuation coefficient (extinction length inverse) Le^{-1}, scattering coefficient g_0 and mean free path l as achieved by the MLTWA applied on DS2011 dataset. Early coda (up to 40 s after S-wave arrival) and Zeng's (1991) approximation of the RTT were used.

From existing misfit functions we evaluated uncertainties of resulting quality factors. Q_i as well as Q_{sc} were searched by grid search in a grid $Q_i, Q_{sc} \in \langle 100, 6000 \rangle$. Inside the 2-D misfit function we chose confidence interval around minimum within which the misfit function did not exceed a chosen threshold. Uncertainties handling is plotted in Figure 5.20. For current dataset we selected 2σ confidence region around minimum: 5% of Q_i, Q_{sc} combinations from $Q_i, Q_{sc} \in \langle 100, 6000 \rangle$ with the lowest misfit lie within the confidence area. The uncertainty range of Q_{sc} is approximately 5 times wider than Q_i for all frequencies.

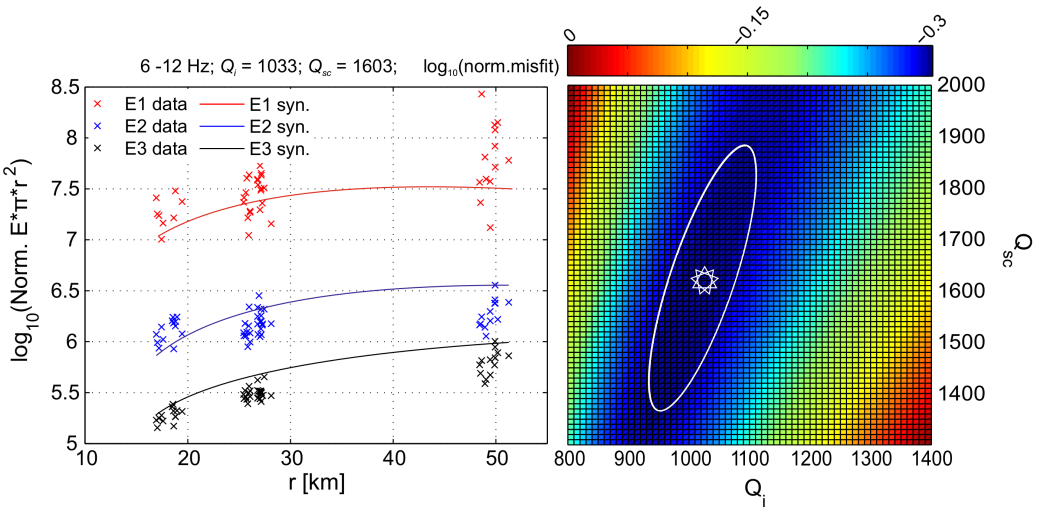

FIGURE 5.20: Misfit function for Q_i Q_{sc} estimation for central frequency 8 Hz. White ellipses engulf the areas with misfit threshold bellow a chosen value. The solid line represents area within which 5% of all misfit estimates of the grid $Q_i, Q_{sc} \in \langle 100, 6000 \rangle$ lie.

For 'later coda' dataset DS80 the fit of synthetics with data is better (from the visual point of view) and for frequencies 12, 18 and 24 Hz its even perfect (Figure 5.21). Surprisingly, resulting frequency dependences are not very clear (Figure 5.22). While Q_i is well estimated on frequencies from 9 Hz higher, the Q_{sc} is biased with such an uncertainty that its relevant interpretation is questionable. As a consequence, B_0, l and g_0 are biased in a way that their computation and interpretation makes no sense. Hence the $Q_i(f)$ estimation is the only valuable result from the MLTWA of late coda dataset. Confidence interval (or error range) was estimated similarly as for previous dataset - the lowest 5 % of all $Q_i, Q_{sc} \in \langle 100, 6000 \rangle$ lie within the confidence region inside the misfit function. Q_i power-law frequency dependence is $545 f^{0.44}$.

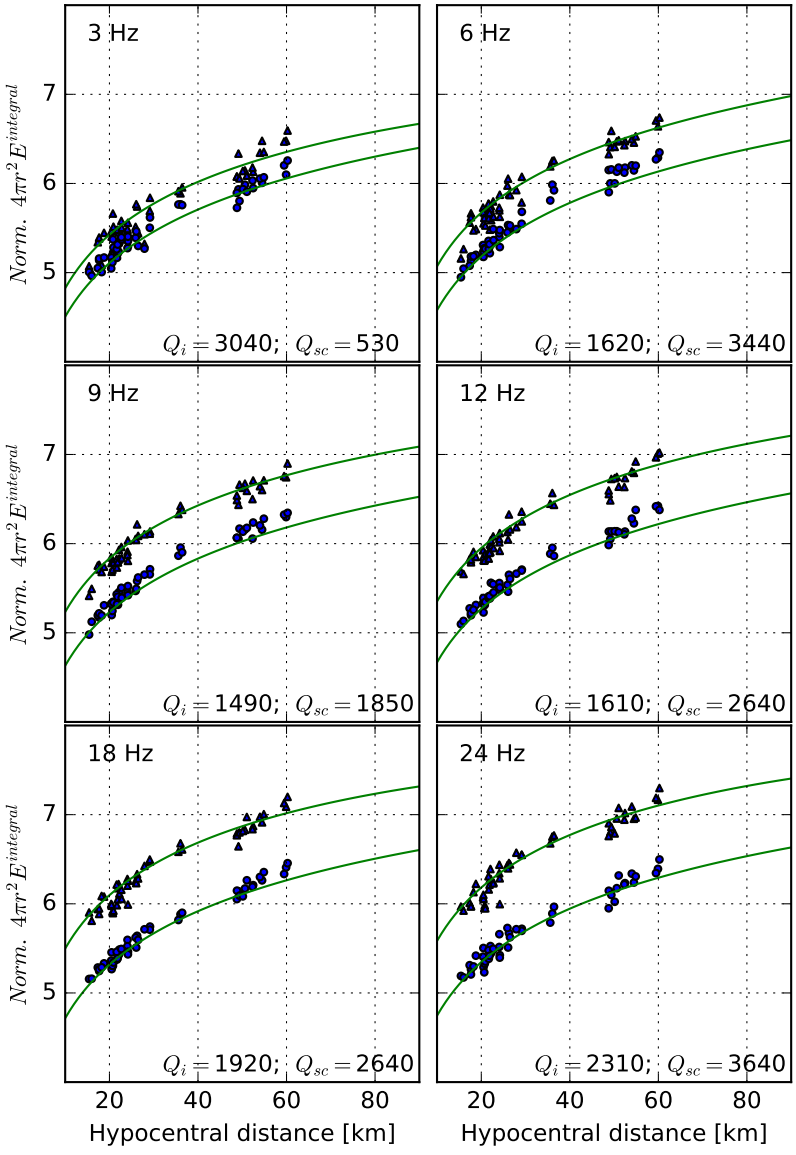

FIGURE 5.21: Normalized energies in two time windows: 40 - 60 s (triangles) and 60 - 80 s after origin (circles) vs. hypocentral distance. The lines represent the best first obtained for the Q_i and Q_{sc} pair giving minimum of the misfit function Eq. 5.8.8.

Figure 5.23 shows comparison of mean $Q_i(f)$ and $Q_{sc}(f)$ estimated from early and late coda by the MLTWA. Only Q_i measurements with acceptable level of uncertainty are plotted. Despite methodological and data differences a high level of similarity is observed. Both datasets - early and late coda - produced similar levels of $Q_i(f)$. $Q_{sc}(f)$, despite its poor resolvability is plotted too and surprisingly the similarity is evident here as well.

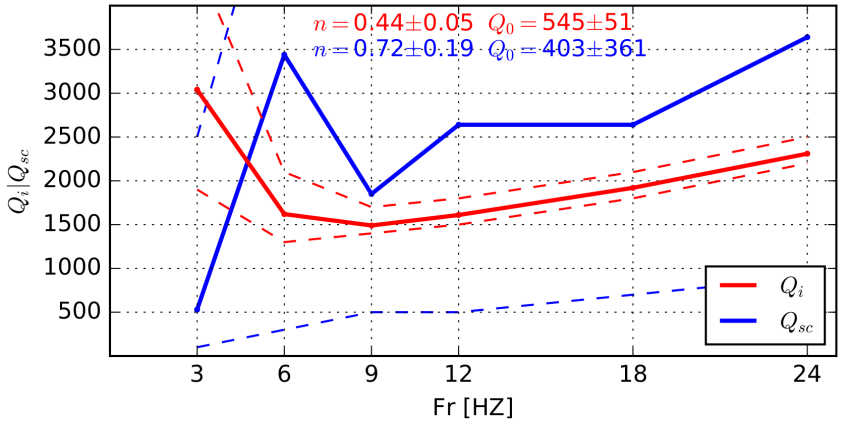

FIGURE 5.22: Resulting frequency dependences of the Q_i and Q_{sc} with their power-law coefficients. Late coda (from 40 to 80 s after origin time) and Paasschens's (1997) approximation of RTT were used. Due to a large Q_{sc} uncertainties (exceeding the limits) other attenuation parameters are impossible to estimate with sufficient reliability.

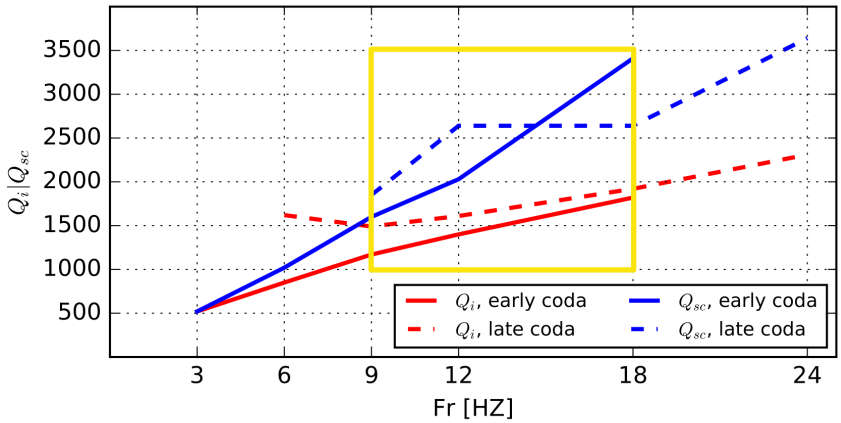

FIGURE 5.23: Late and early coda of mean $Q_i(f)$, $Q_{sc}(f)$ comparison. Too erroneous estimates are not plotted. Common frequencies 9, 12, 18 Hz are highlighted by a yellow rectangle.

5.9.3 Q_P and Q_S - Coda Normalization Method

The coda normalization method (CNM) normalizes P- and S-wave arrivals and quantifies their decrease with hypocentral distance. We analyzed the DS60 dataset and estimated mean $Q_P(f)$ and $Q_S(f)$ describing the whole area covered by stations.

Resulting fits of coda normalized amplitudes for P and S-waves are shown in Figures 5.24 and 5.25. Data points are non-uniformly scattered along y axis (hypocentral distance r) and 're-sampling' (mean of amplitudes in consecutive distance windows) had to be made to equal the influence along the y axis. Data scatter of normalized P-wave amplitudes was not suitable for reliable attenuation measurement what is visible by a naked eye and what resulted in high error. On the contrary, normalized S-wave amplitudes proved to be very good for $Q_S(f)$ estimation and therefore S-wave attenuation values are reliable with reasonable error.

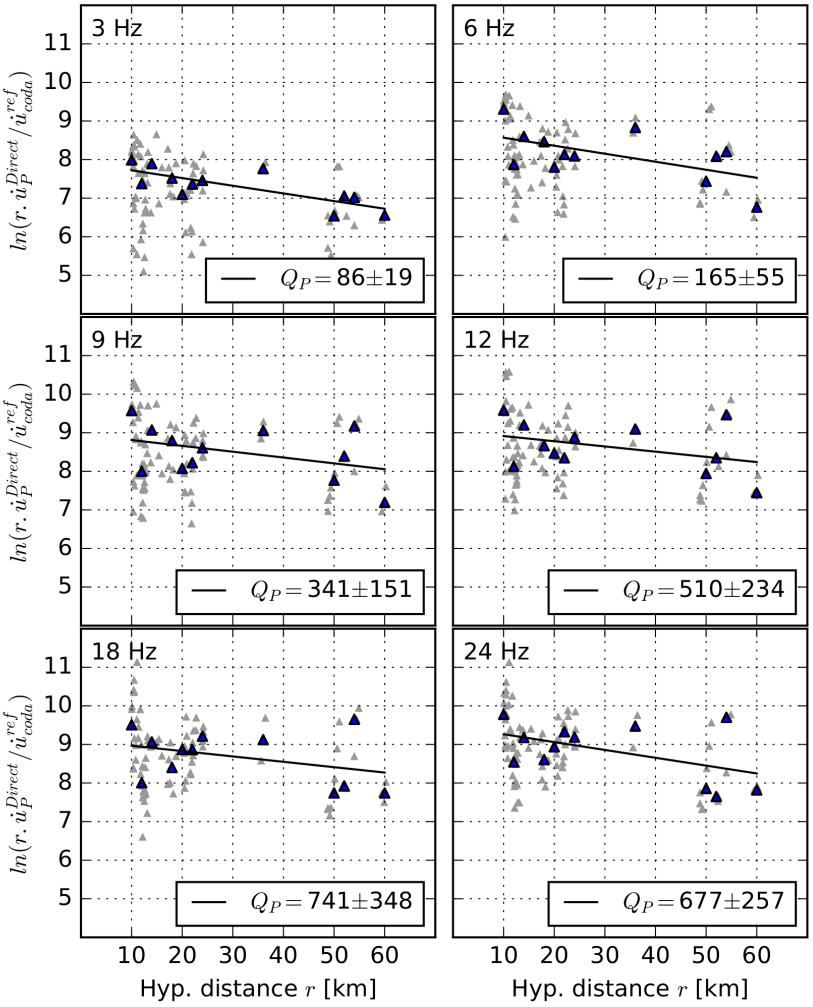

FIGURE 5.24: Normalized P-wave amplitudes vs. hypocentral distance for different central frequencies with the best fit and resulting Q_P - DS60 dataset. Grey triangles represents every single P-wave amplitude on different stations, blue triangles are reduced data - mean values of data for floating distance window. Fit is provided on reduced data.

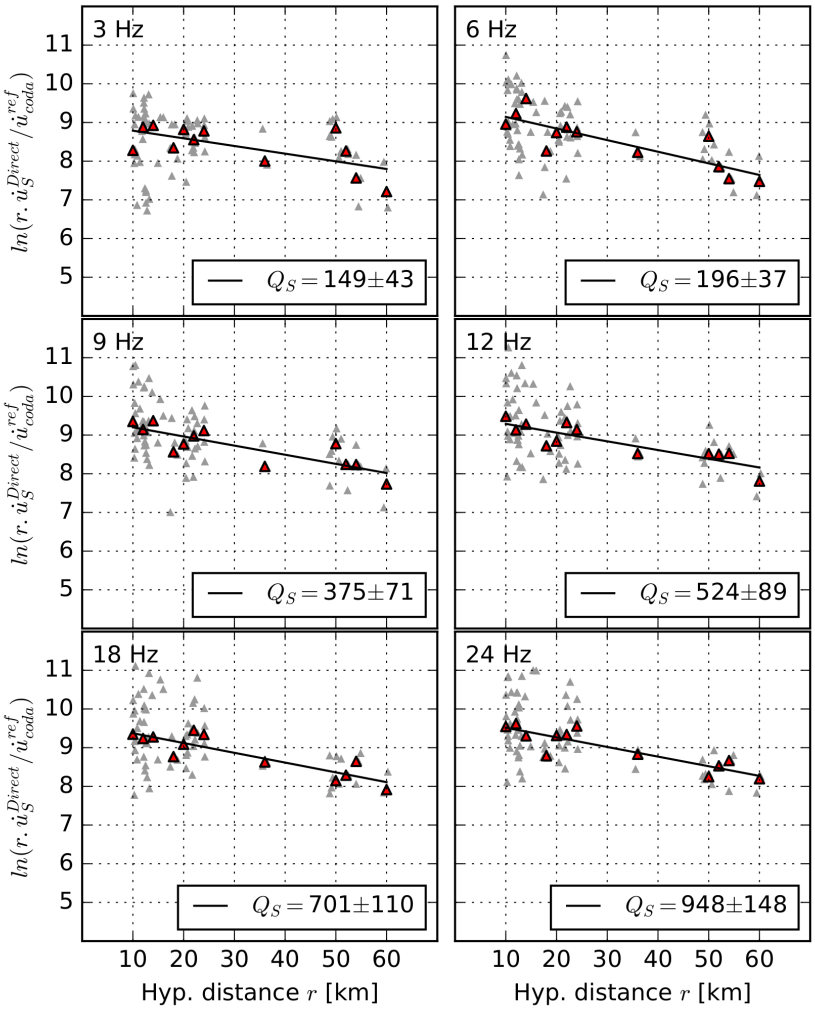

FIGURE 5.25: Normalized S-wave amplitudes vs. hypocentral distance for different central frequencies with the best fit and resulting Q_S - DS60 dataset. Grey triangles represents every single S-wave amplitude on different stations, red triangles are reduced data - mean values of data for floating distance window. Fit is provided on reduced data.

Frequency dependences of Q_P and Q_S are plotted in Figure 5.26. Unlike similar analyses worldwide we got almost identical values of Q for P and S. This might be the first indicator that something is wrong - theoretical Q_S/Q_P ratio is 2.25 (Shearer, 1999). Error estimates for P-waves are very high and disables reasonable interpretation. Both Q_P and Q_S rise with frequency. Power-law coefficients are $Q_P^0 = 26 \pm 10$, $n_P = 1.1 \pm 0.12$ and $Q_S^0 = 46 \pm 15$, $n_S = 0.94 \pm 0.1$

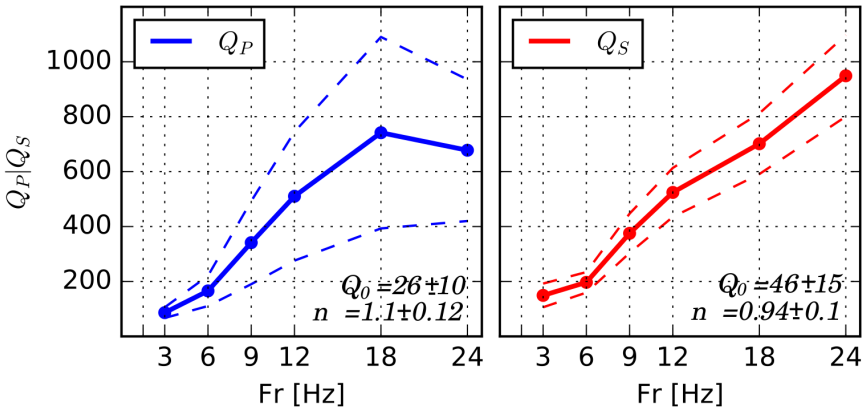

FIGURE 5.26: Frequency dependences of Q_P and Q_S from Coda normalization method along with their frequency power-law constants.

5.10 Discussion

5.10.1 Coda Q_c

Two questions arose after the coda window analysis: of used coda window length and of poor Q_c resolvability for frequencies 3 and 6 Hz.

The first question can be answered easily: the window with the smallest error should be treated as the one with the best solution. From this point of view the lapse time window with length of 40 s is the one. It is long enough to suppress the influence of coda envelope fluctuations (local up and down peaks present even after the smoothing) and it covers the coda part which is more or less monotonously decaying. However, the $Q_c(f)$'s estimated with shorter windows vary only slightly (only 10 to 20%) and differ significantly only in error magnitudes (Figure 5.16). Window of 30 s is almost identical and its values lie within error range of the 40 s window. The lapse time window of 20 s is more influenced by the signal imperfections of shorter durations and as a result the error is three times higher than the one of 40 s window.

To answer the second question we might take a look at the coda envelopes to understand the impact of data quality to the linear fit. Natural logarithm of coda envelopes corrected for geometrical spreading (diffusive wave-field approximation) for analyzed central frequencies is shown in Figure 5.27. After the geometry correction the coda on lower frequencies is not smoothly decaying and forms almost flat area between 40 and 70 s. The effect is pronounced on frequencies 3 and 6 Hz. The decay continues again at lapse times longer than 70 s (not clearly visible on Figure 5.27). Fitting the flat sequence of coda even after strong smoothing on low frequencies produces unstable slopes and therefore highly biased Q_c estimates. Following cross-correlation returns low coefficients and measured quality factors are excluded from analysis.

An existence of the flat portion of for geometry corrected coda envelope is questionable and difficult to explain. One possible way of explanation lies in the assumption that coda wave-field at later lapse times is fully multiply scattered and seismic energy is distributed uniformly in a diffusive regime. Coda decay is a measure of intrinsic loss then (Shapiro et al., 2000). A single wave might be treated as fully multiply scattered after it losts information about its initial orientation due to a scattering. The diffusive wave-field is composed of such waves and is random. According to Calvet and Margerin (2013) the full diffusivity is reached after a few

scattering events (encounters) already. The lapse time when this regime is reached depends on ray wavelengths (frequencies), and on the character (size and impedance) of heterogeneities within geological environment. We might assume that the flatness of coda between the lapse times of 40 and 70 s for 3 and 6 Hz is a result of systematic wave-field behavior what is in direct opposition to the expected randomness of diffusive wave-field.

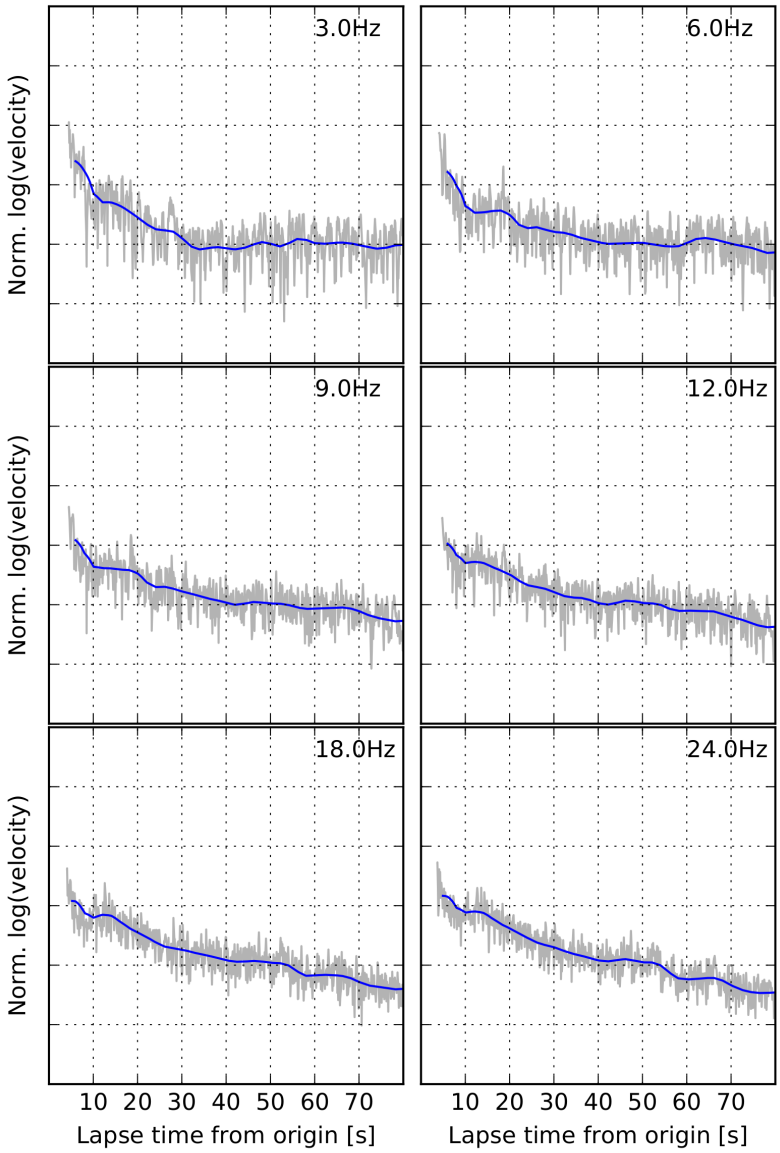

FIGURE 5.27: Normalized coda envelopes of single event on single stations corrected for geometrical spreading of the diffusive waves. Frequency bands with central frequencies 3, 6, 9, 12, 18 and 24 Hz are plotted (with bandwidths of 2, 4, 6, 8, 12 and 16 Hz. Raw data (grey), smoothed ones (blue).

This non-uniformity of the coda wave-field is hard to identify and today a complex monte-carlo simulations are in use for modeling the Earth's interior and coda waves behavior (Calvet and Margerin, 2013; Gaebler, Eulenfeld, and Wegler, 2015; Sato, Fehler, and Mayeda, 2012). Terms like non-uniformity of heterogeneities distribution, scattering and anelastic anisotropy are frequently subjects for discussions.

Taking all possible effects into account the $Q_c(f)$ estimation and its interpretation in terms of multiple scattering is applicable to frequencies from 9 Hz higher and with lapse time windows

longer than 30 s, preferably 40 s. Achieved final results suitable for further applications are those of 40 s long lapse time window (Figure 5.28). Relatively low frequency power-law coefficient was estimated - $n = 0.46$. To fully confirm its validity the low frequency measurements are missing. Authors use to associate low n exponents with strong tectonic activity. This empirical observation is based on comparative studies of a large number of $Q_c(f)$, Q_c^0 and n estimations worldwide.

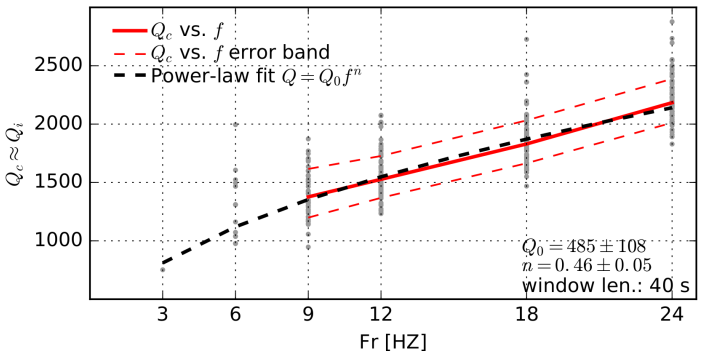

FIGURE 5.28: Frequency dependence of Q_c for lapse time window of length 40 s. Grey dots represent single coda Q_c estimates for station-events combinations, red line is resulting mean Q_c, red dashed lines show error intervals represented by a standard deviation. Black dashed line represents the Q_c in the terms of power law (Eq. 5.1.3) with the best fitting $Q_0 = 485$ and power law exponent $n = 0.46$.

The general problem of any comparison of $Q_c(f)$ and associated parameters is the influence of method variables: mostly the lapse time window length and lapse time window start. It used to be common to estimate $Q_c(f)$ for early coda and interpret the differences in terms of Q depth dependence and single back-scattering. Even today many authors choose this way of interpretation, despite its obsoleteness and questionable validity (Calvet and Margerin, 2013; Havskov et al., 2016). Those estimates are stable, but they degrade the $Q_c(f)$ to be just a dimensionless quantity of coda decay with no clear physical meaning. What is worse, many authors simply compare their findings, ignoring the fact that they could describe totally different phenomenons (Havskov et al., 2016). Normalized and valid methodology how to deal with $Q_c()f$'s is still missing.

We have chosen to apply coda windows method on late coda to estimate $Q_c(f)$ equal to $Q_i(f)$, which, in is physically clear. Later multiple lapse time windows analysis validated our findings. Our results are suitable for comparison with $Q_i(f)$ from any place of the Earth.

5.10.2 Q_i and Q_{sc} separation - Multiple Lapse Time Window Analysis

Application of the MLTWA on both datasets - the early coda and the late coda produced valuable results and exposed phenomenons worth discussing.

The application of the MLTWA on the early coda dataset produced reliable results comparable with every other study in the field. The worse fit of synthetics with observed data might be viewed and explained from several points of view.

The first aspect is the model used - Zeng's approximative solution of RTT. As indicated by name - we are dealing with the approximate solution of a complex problem. The solution (synthetic energy envelope) is valid with a varying level of accuracy for the full waveform from origin time to its end in noise. The level of accuracy is fair for late coda envelope. For direct wave arrival and signal early behind it, the accuracy of approximate solutions (either Zeng's or

Paaschens's) decreases (Sato, Fehler, and Mayeda, 2012) as the amplitudes are controlled not only by the medium, but by the effects of the source as well. This inaccuracy may affect the energy integral estimation for the first lapse time window in our analysis.

Second aspect affecting the model-observation fit is the geology-model constraints relation. The RTT, as used by a vast majority of authors and us as well is derived for homogeneous half-spaced velocity model with uniform distribution of velocity heterogeneities. It is a question if any local geological model can be described by such a simplification. Based on studies of other authors (e.g. Gaebler, Eulenfeld, and Wegler, 2015; Sato, Fehler, and Mayeda, 2012) it can, but one must be aware of its possible influences, despite their apparent insignificance.

The last question is the impact of data characteristics and overall data suitability for the MLTWA application. The MLTWA compares relative energy contents within a few time windows with respect to a source distance. Broad band of hypocentral distances is essential for stable observations. Moreover, a uniform coverage of source-station paths over the studied volume (or area) is required to get proper mean attenuation estimates. In our case the 'star' coverage takes place with sources in the center and stations located all around (Figure 5.29). Possible local effects and anisotropic behavior can express itself in the quality of the fit and be pronounced in final results and their uncertainties.

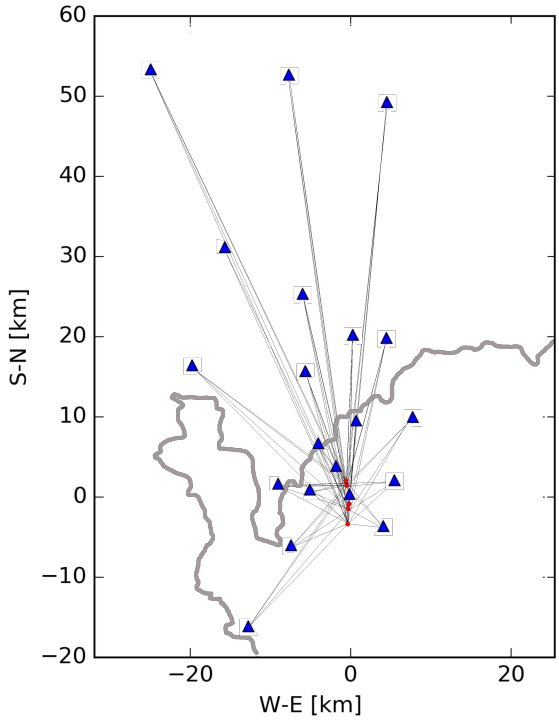

FIGURE 5.29: MLTWA station-event ray paths distribution. 'Star' like shape with hypocenters (red dots) in the middle of the 'star' and stations (blue triangles) all around.

The application of MLTWA on the late coda dataset was a test, if and how the absence of a direct wave arrival and early coda information would affect the general Q_i and Q_{sc} resolvability. As was shown, it did only partially. While the stability of Q_i was very good, comparable to early coda analysis, the resolvability of Q_{sc} was almost impossible due to its error - uncertainty.

To understand the behavior of late coda MLTWA Q_i and Q_{sc} it is best to analyze the shape of misfit functions. The misfit function contains information of a few key phenomenons: model validity, data and data processing suitability. In Figure 5.30 the single misfit functions computed with Eq. 5.8.8 for different central frequencies are plotted. Darker the color gets, the

lower the misfit value is. The minimum is not sharp, but forms a flat area in the shape of a vertical band. The band is narrow in Q_i and wide in Q_{sc} cross-section. The band is very wide for low frequencies 3 and 6 Hz and is getting thinner with frequency increase. The thinner the band is, the better constrained the Q_i estimation gets. However, with increasing skewness of arc area it is not contracting vertically - the Q_{sc} estimation remains unstable. Or in other words - it stays stable for wide range of Q_{sc}. An ambiguity arises.

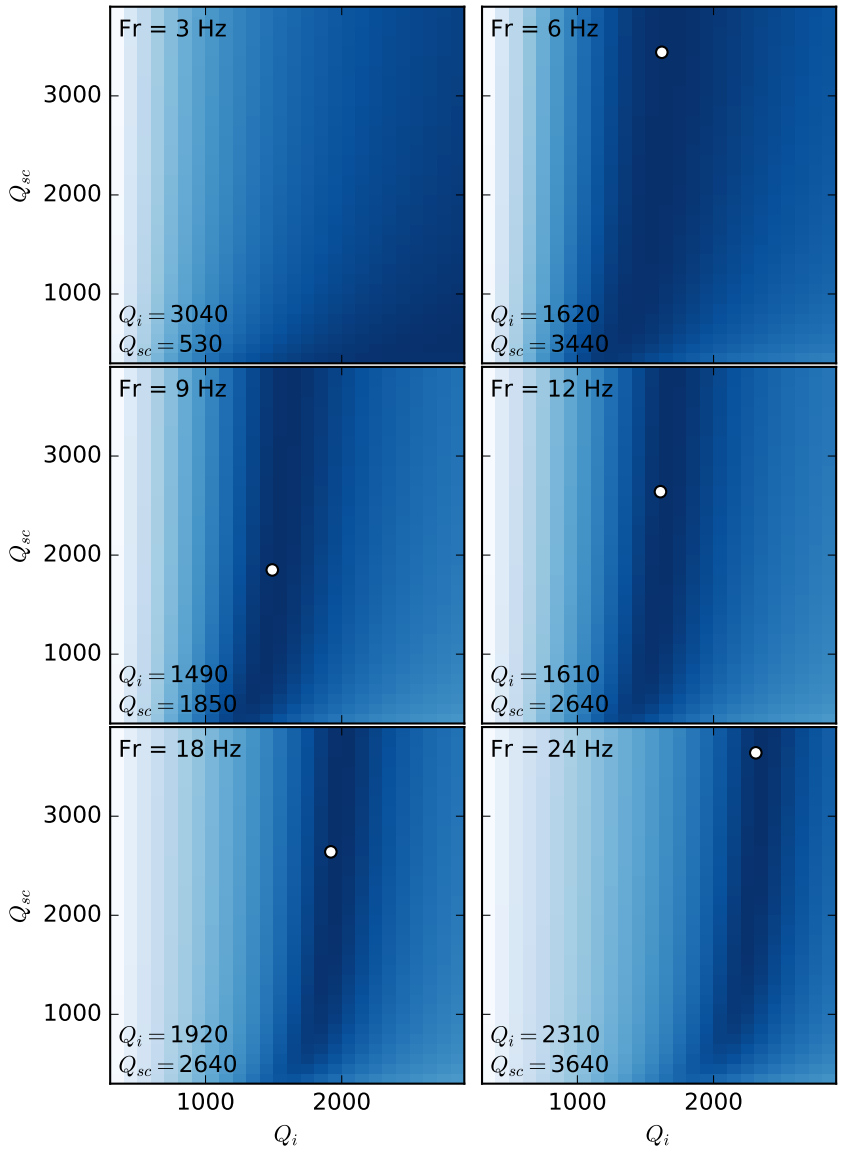

FIGURE 5.30: Normalized misfit functions for Q_i Q_{sc} combinations computed by Eq. 5.8.8 for Paasschens's RTT solution. Late coda dataset used. Position of minimum is marked by white dot. Darker the color gets, lower the minimum is.

Specific shape of the misfit function (the vertical arc) and related poor Q_{sc} resolvability might be better understood in the light of multiple scattering and diffusion assumption. We are working with late coda, ignoring the effects of attenuation and scattering in early coda. By coda normalization we lost the information on real amplitudes and only energy envelope shape remains. As mentioned before, decay rate of the late coda (and its energy) reflects only intrinsic loss, since the coda energy is multiply scattered and seismic energy field is diffusive. Inability to

estimate Q_{sc} is then only a logical consequence. The estimation of Q_i is then stable, while the estimation of Q_{sc} is ambiguous - equally good for wide range of Q_{sc}'s.

Another aspect complementary to the one mentioned above is the choice of lapse time windows (40 - 60 s and 60 - 80 s after the origin). As mentioned above, the MLTWA is called multiple lapse time windows analysis because that it analyses the relative changes of energy in few consecutive time windows. Those changes on different hypocentral distances are the main phenomenon based on which the final Q_i and Q_{sc} estimates are computed. For our hypocentral distances the change of energy might be not significant enough to stabilize the Q_{sc} solution. Maybe with much wider range of hypocentral distances the chosen lapse time windows would be sufficient, bud definitely not for our current method and data settings.

Taking above mentioned phenomenons into account we can conclude that using MLTWA on early part of coda converge to a stable solution for all frequencies. Results and uncertainties are reasonable. Behavior of $Q_i(f)$ and $Q_{sc}(f)$ fulfills generally observed characteristics and can be described by a frequency power-law. The application of MLTWA on late coda produced very stable Q_i estimates for frequencies higher than 6 Hz. On the other hand, $Q_{sc}(f)$ remained poorly determined and its interpretation is questionable, if not impossible.

Figure 5.31 shows comparison of intrinsic loss quality factors derived from the MLTWA (both applications) and from the coda window method. High level of similarity derived from independent methods gives weight to the final $Q_i(f)$ estimates for West Bohemian crust. Interesting is also the common inability of coda windows method and MLTWA to estimate Q_i and Q_c for frequencies 3 and 6 Hz from late coda.

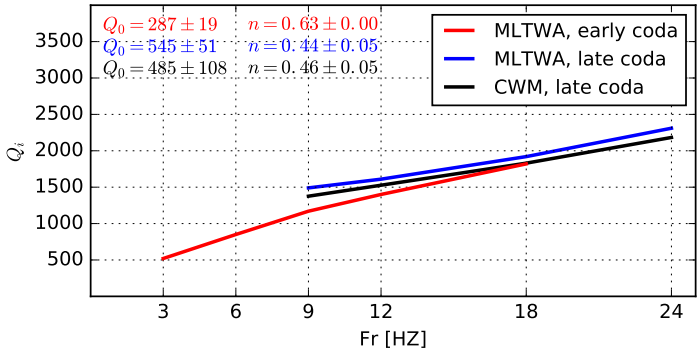

FIGURE 5.31: $Q_i(f)$ revealed by different methods and datasets: the MLTWA on early coda dataset (red), the MLTWA on late coda (blue) and coda window method on late coda (black). Frequency power-law coefficients are listen inside the plot.

MLTWA (the one applied on early coda) shows another significant result — intrinsic loss appears to be a dominant attenuation parameter in West Bohemia. Intrinsic loss is often caused by the presence of fluids in the medium and is associated with higher temperature (Barton, 2007). Post volcanic activity in the studied area is characterized by the presence of hot mineral springs and moffetes with CO_2 of mantle origin. Changes in CO_2 flow correlate with outbursts of seismic activity and earthquakes are believed to be triggered by stress changes controlled by fluid content in the focal area (Hainzl et al., 2016; Fischer et al., 2014; Bachura and Fischer, 2016b; Horálek and Fischer, 2008). The dominance of intrinsic loss is however computed from the data covering the whole area of West Bohemia. It is questionable if such local fluid effects can have any practical impact on the attenuation estimates. Predominance of frequency dependent intrinsic loss is widely observed in Europe (Rachman et al., 2015; Majstorovic et al., 2017; Singh et al., 2017, to mention a few only) for frequencies analyzed in this study.

5.10.3 A leakage of the seismic energy towards the mantle - possible source of Q_i's frequency dependence

High frequency seismic waves are attenuated and their attenuation is described by the quality factor Q, which is frequency dependent. The frequency dependence is widely observed ever since the coda became the subject of scientific interest. The MLTWA reveals frequency dependent $Q_{sc}(f)$, which is interpreted as a result of varying dimensions of scattering heterogeneities influencing waves with different wavelengths. However, laboratory experiments suggest that intrinsic Q_i has a weak to zero frequency dependence. In this classic paper Knopoff (1964) first reviewed the frequency dependence of Q_i^{-1} in homogeneous materials concluding that conversion of energy into heat in solids is nearly independent of frequency (power-law coefficient $n = 0$) while in liquids it is proportional to frequency. Laboratory and field measured levels of constant Q_i were in orders of 1000 (e.g. Faul, Fitzgerald, and Jackson, 2004; Jackson and Faul, 2010; Hasegawa, 1985; Knopoff, 1964; Davis and Clayton, 2013).

In 1999, Margerin, Campillo, and Shapiro proposed a theory that seismic energy in the crust is diffusively leaking into a mantle instead of scattering back into the crust. It results in apparent increase of intrinsic attenuation. The mantle leaking takes place (according to the modeled cases) if the crust's thickness is of the same order as the mean free path l (path necessary for wave to lose its propagation memory). The effect is frequency dependent and authors discuss it in effort to explain the Q_i frequency dependence (Dominguez and Davis, 2013; Margerin, Campillo, and Shapiro, 1999).

Frequency dependence of $Q_i(f)$ in West Bohemian crust is described by a power-law with $Q_0 = 485 \pm 108, 545 \pm 51, 287 \pm 19$ and $n = 0.46 \pm 0.05, 0.44 \pm 0.05, 0.63 \pm 0.0$ for the CWM, MLTWA with late coda and MLTWA applied on early coda. We decomposed all three $Q_i(f)$ estimations to constant and frequency dependent components as

$$Q_i^{-1}(f) = Q_{const}^{-1} + Q_f^{-1}(f) \tag{5.10.1}$$

where Q_{const}^{-1} is the constant part and $Q_f^{-1}(f)$ the frequency dependent part, again describable by a power-law with coefficients n and Q_0. We tested different combinations of Q_{const}, n and Q_0 to match the observed $Q_i(f)$ to achieve the best solution. Results of each decomposition (two MLTWA's and one CWM) are plotted on Figures 5.32, 5.33 and 5.34.

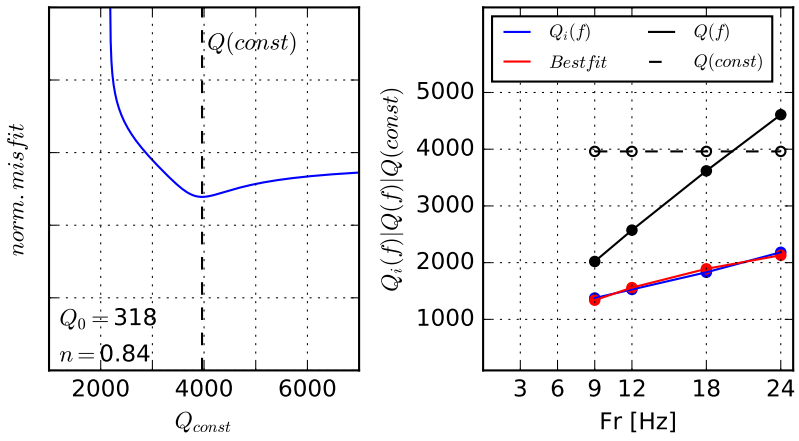

FIGURE 5.32: Decomposition of $Q_i(f)$ (blue line) measured by the CWM to a constant $Q(const)$ (black dashed line) and frequency dependent $Q(f)$ (black solid line). The best fitting combination of $Q(const)$, n and Q_0 is plotted (red line) along with it misfit function (left plot).

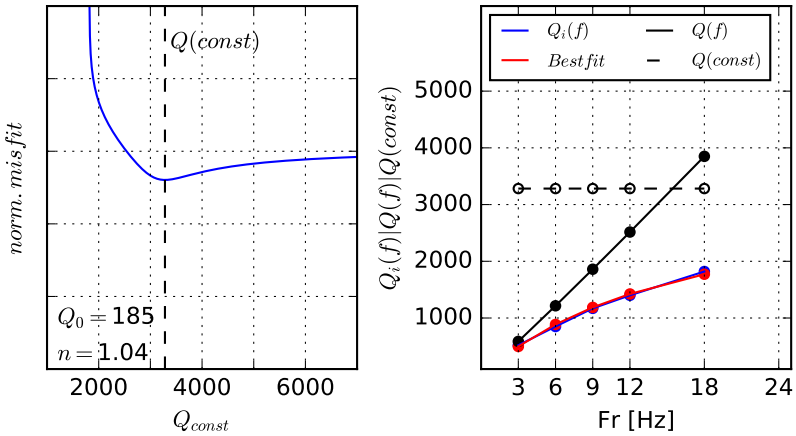

FIGURE 5.33: Decomposition of $Q_i(f)$ (blue line) measured by the MLTWA application on the early coda to a constant $Q(const)$ (black dashed line) and frequency dependent $Q(f)$ (black solid line). The best fitting combination of $Q(const)$, n and Q_0 is plotted (red line) along with it misfit function (left plot).

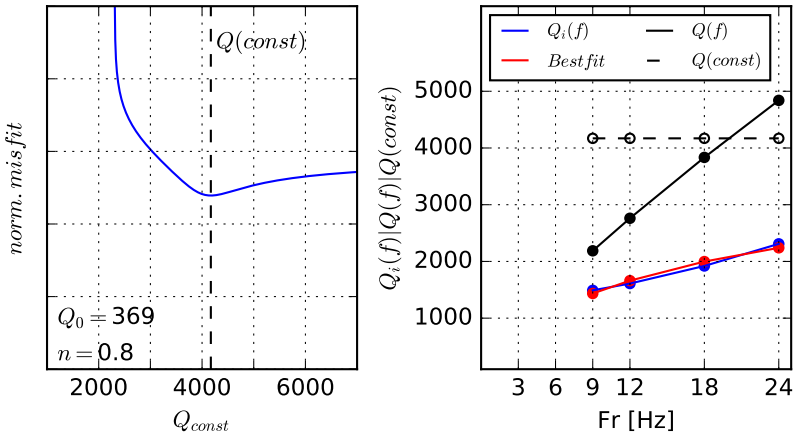

FIGURE 5.34: Decomposition of $Q_i(f)$ (blue line) measured by the MLTWA application on the late coda to a constant $Q(const)$ (black dashed line) and frequency dependent $Q(f)$ (black solid line). The best fitting combination of $Q(const)$, n and Q_0 is plotted (red line) along with it misfit function (left plot).

Results are fairly similar. Constant quality factors are 3300 (MLTWA and early coda), 4100 (MLTWA and late coda) and 3950 (CWM). Frequency dependencies of the dependent components are 1.04, 0.8 and 0.84 for early MLTWA, late MLTWA and CWM. If we would interpret the frequency dependence of $Q_i(f)$ (now apparent intrinsic loss) as the influence of the mantle leakage, then the constant anelastic loss quality factor is $Q \approx 4000$ (true intrinsic loss). This value is rather high but still reasonable. Intrinsic loss Q_{const}^{-1} along with the apparent intrinsic loss $Q_i^{-1}(f)$, scattering $Q_{sc}^{-1}(f)$ and leakage $Q_{leak}^{-1}(f)$ are plotted at Figure 5.35. Influence of leakage is strong on frequencies 3 and 6 Hz and is loosing its influence as the frequency is rising and is overrun by constant intrinsic loss at approximately 20 Hz.

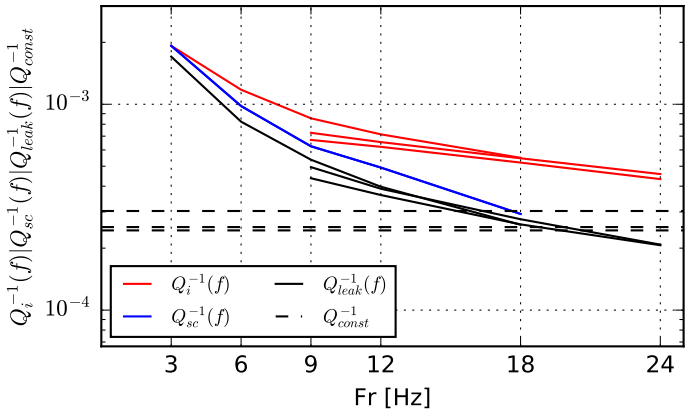

FIGURE 5.35: Resulting frequency dependence of attenuation for different parameters. Measured intrinsic loss (red), measured scattering (blue), derived leakage (black), derived constant component of measured intrinsic loss (dashed black).

In the light of these estimates the above mentioned dominance of the anelastic loss (seismic albedo B_0 bellow 0.5, Figure 5.19, measured from early coda dataset) must be revisited. After correcting the intrinsic loss quality factor $Q_i(f)$ for the leakage the seismic albedo changes drastically - instead of the intrinsic loss dominance the scattering appears to be the dominant attenuation process (Figure 5.36) on frequencies 3 - 18 Hz. The total attenuation coefficient (the extinction length inverse $Le^{-1}(f)$) has the same increase with frequency dependence after the correction, but is decreased (Figure 5.36).

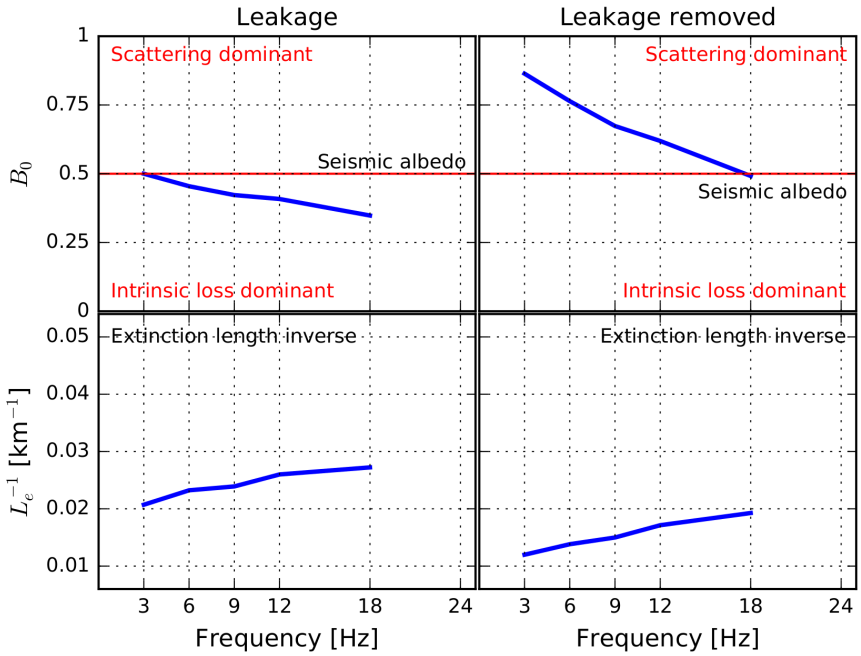

FIGURE 5.36: Comparison of seismic albedo $B_0(f)$ and extinction length inverse $Le^{-1}(f)$ (total attenuation coefficient) for the results achieved by the MLTWA application on the early coda dataset (Bachura and Fischer, 2016a). The left column represent original results, the right one with removed influence of the leakage of the energy into the mantle.

The question now is, if the measured constant Q_{const} and the frequency dependent component $Q_f(f)$ can be interpreted by means of the leakage of seismic energy toward the mantle in West Bohemia. The difference between constant intrinsic loss quality factor $Q_{const} \approx 4000$ and the leakage magnitude is significant and implies the strong influence of the Earth's mantle to the energy distribution in the wave-field at lapse times following the earthquake itself. Dominguez and Davis (2013) did the same analysis and studied the attenuation parameters of the subduction zone on shore of Mexico. They worked with 40 km thick crust and found $Q_{const} \approx 2000$. In West Bohemia we are studying stable intra-continental rift zone with the crust's thickness of 30 km. Mean free path $l(f)$ of the seismic waves is ≈ 90 km, so the Earth's mantle should should be incorporated to the interpretations as diffusive energy absorber apparently increasing intrinsic loss of the crust.

Low intrinsic loss Q_{const} of shear waves is a quality characterizing the behavior of the whole crustal volume bellow West Bohemia and probably even of the area surrounding it. Local effects like weathered surface, local fluid sources or channels should have marginal impact on its estimation, probably much lower that the leakage. Incorporating leakage is a logical step, however, one must be aware of the fact that it radically changes the interpretation of the results.

5.10.4 Q_P and Q_S - Coda Normalization Method

For proper method application a uniform coverage of rays within analyzed Earth's volume is required. Only that way the full range of hypocentral distances is achieved and only that way the radiation patterns and anisotropy effects are neglected. With violating and ignoring these conditions the linear fit of coda normalized amplitudes becomes unstable, results unreliable and overall behavior non-systematic.

For West Bohemian data we used a so-called one-event method modification with scattered stations and 'one event' in the middle of the network. In fact we used many events, but their locations (inside the Nový Kostel focal zone) were so similar (Fischer et al., 2014) that we could approximate them with one representative hypocenter (in fact we didn't). The focal mechanisms from different time episodes vary (Vavryčuk et al., 2017), but it is questionable if the proposed source mechanism variations are strong enough to randomize the influence of radiation patterns.

We observed dubious results for the P-wave attenuation and more reliable values for the S-wave attenuation. P-wave attenuation unreliability is expressed by a large error (Figure 5.26). Another disquieting fact is that the values $Q_P(f)$ and $Q_S(f)$ are very similar. From the theory we assume the Q_S/Q_P ratio to be 2.25 (Shearer, 1999) and field observations (e.g. Farrokhi and Hamzehloo, 2017; Bora and Biswas, 2017) more or less agree with the proposed ratio.

The estimation of $Q_P(f)$ suffers from poor data suitability for a valid linear regression. Normalized amplitudes (Figure 5.24) are too scattered in y direction and decreasing trends are not so clear and evident. Despite the source mechanisms variations among used events we think that their differences are not strong enough to be fully eliminating the radiation pattern effects. Together with non-uniform hypocentral distances distribution along x axis it results in a high Q_P uncertainty for every measured frequency.

The $Q_S(f)$ estimation worked better (Figure 5.25). Normalized amplitudes behave as intended - are systematically decreasing and their vertical scatter is reasonable - effects of the radiation patterns seem to be suppressed. The reason might be in the complexity of the S-wave radiation patterns. They are more complex than the ones of P-waves and appart of them the amplitudes

and polarizations vary more when changing the take-off angle. As a consequence our distribution of stations seems to be providing sufficiently randomized stack of the source effects that afflict the data randomly, not systematically.

Several method modifications (different coda normalization windows, different data downsamplings and different fit procedures) were tested to ensure the results independence on method settings.

Levels of $Q_P(f)$ and $Q_S(f)$ are lower than those of $Q_c(f)$, $Q_i(f)$, $Q_sc(f)$ and $Q_t(f)$ measured by the CWM and MLTWA. This might reflect the fact that CNM analyses the attenuation along the seismic rays, not the quality of the crust as a whole. In fact, CNM can achieve better resolution. In our case we scale the volume of the upper crust, where higher attenuation is expected (Sato, Fehler, and Mayeda, 2012).

Another question to discuss is the problem of a frequency dependence and its source. The frequency dependence of full-scale crustal parameters estimated by the CWM or the MLTWA can be explained (or at least attempted to be explained) by the influence of the energy absorbing mantle (in the case of $Q_i(f)$). Scattering's frequency dependence is often interpreted by the presence of heterogeneities with various dimensions. In our case only the latter one can be discussed, but not clearly proved. Separation of intrinsic loss and scattering cannot be done by means of the CNM.

What we can do is to decompose $Q_S(f)$ into a constant and frequency dependent part under the same assumptions as when we had derived the leakage one chapter earlier. Only in this case we expect the constant part to represent intrinsic loss quality factor and the frequency dependent part the scattering. Both for the upper crust. Result are plotted in Figure 5.37. Constant part is at level $Q_{const} = 1646$. As expected, it is certainly lower than intrinsic loss quality factors $Q_i(const) \approx 4000$ for the crust as a whole (with observed $Q_S(f)$ and $Q_i(f)$ it could hardly be any different). Moreover, if adopting the assumption that Q_S/Q_P ratio is ≈ 2.25, than the theoretical constant intrinsic loss quality factor for the P-waves would be $Q_i(P) \approx 700$. That is a very reasonable value, especially in the lights of previous Q_P estimations (next chapter).

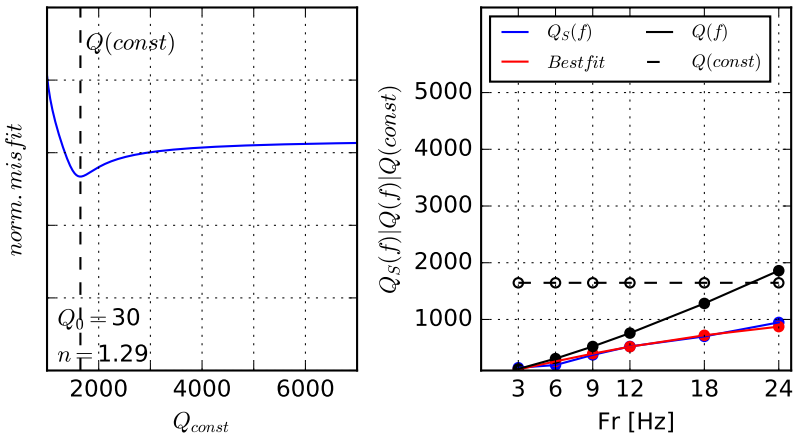

FIGURE 5.37: Decomposition of $Q_S(f)$ (blue line) measured by the CNM to a constant $Q(const)$ (black dashed line) and frequency dependent $Q(f)$ (black solid line). The best fitting combination of $Q(const)$, n and Q_0 is plotted (red line) along with it misfit function (left plot).

Taking all discussed aspects into mind, our conclusion is that the only relatively reliable Q estimates by the CNM are those of S-waves - $Q_S(f)$. And that also only after a careful consideration. Current data settings are not favorable for valid $Q_P(f)$ measurement. The decomposition and its interpretation and conclusions must be carefully considered as well, despite their relative reasonableness.

The last question is if we can see the influence of expected fluids in the results. Unfortunately, after taking all the current CNM aspects (ray paths coverage, method assumptions, data-processing) into an account we can't tell.

5.10.5 Other studies from the area

In recent years the field of seismic attenuation became popular among authors and research teams. Different approaches have been adopted and different aspects discussed. Michalek and Fischer 2013 estimated the quality factors for P-waves as a byproduct during seismic source resolving. They found Q_P to be independent on frequency varying between 80 - 600 with the most common values between 150 and 300 at individual stations (median of all means is 230). Mousavi et al. 2017 used computed P-wave quality factors estimated from source spectra to map the spatial distribution of Q_P by means of tomography. They found low-Q anomaly with $Q_P < 150$ for the source zone beneath Nový Kostel surrounded by the area with Q_P exceeding 500.

These studies were about attenuation, but they estimated the quality factors for the traveled seismic rays. The coda methods generally resolve the attenuation parameters for the crustal area as a whole, with much lower resolution. The only comparable 'ray' results might be achieved via the CNM. However, our CNM results, especially those of $Q_P(f)$ are too questionable. Only conclusion can be made and that is that our values are of the same order as the ones mentioned above.

The most relevant studies for our purposes have been provided by Gaebler, Eulenfeld, and Wegler 2015. They used acoustic and elastic versions of the RTT and compared early codas of 2008 earthquakes with synthetics. They observed similar behavior of $Q_i(f)$ and $Q_{sc}(f)$: the frequency dependence, bad $Q_{sc}(f)$ resolvability for the acoustic case, seismic albedo $B_0(f)$ below 0.5. Their estimates are about 30% lower than ours, what is probably the result of differences in data processing. They however did not try to explain the frequency dependency by the means of the leakage.

5.11 Conclusions

We tested and applied three coda methods - the MLTWA, the coda window method and the coda normalization method. West Bohemian activity with its swarm character is poorly suitable for wide use of mentioned methods in a way authors use to do. Requirement of a long uncorrupted coda limits the use of fully automated coda window method, despite its simplicity. Concentration of the earthquakes in a small area with a sparse station coverage reduces the possibility of proper coda normalization method application. Instead of reliable $Q_P(f)$ and $Q_S(f)$ we can get only $Q_S(f)$ whose low values are suspicious. The MLTWA with careful data processing proved to be only method returning full stack of expected results, some of them more reliable, some of them less. Events and station distribution is not ideal, but the method itself can deal with it.

The most reliable result is the estimation of a frequency dependent $Q_i(f)$. Three methods: coda window methoda and MLTWA on later and early coda returned identical values of $Q_i(f)$. If searching for frequency dependent intrinsic loss, a simple coda window method is sufficient and elegant way how to do it. Of course, one must obey the theoretical assumptions - use the late coda, have sufficiently long lapse time window. Otherwise the results would be referring to a physical phenomenons not intended to cover and would be misinterpreted.

The application of the MLTWA on early coda revealed a leading role of frequency dependent intrinsic loss over scattering for frequencies 3-18 Hz. Mean free path l was found to be relatively constant with $\approx$ 90 km and total attenuation (extinction length inverse Le^{-1}) is increasing with frequency on levels from 0.02 to 0.03 for the mentioned frequencies.

A fully different interpretation of the results has to be adopted if the leakage of the seismic energy towards the mantle is incorporated. The leakage is the one of the ways how to explain the frequency dependence of the Q_i. When we accept the Earth's mantle influence on the energy distribution in the scattered wave-field and so in final coda shapes, the effect of leakage is apparently increasing the intrinsic loss at frequencies up to $\approx$ 20 Hz. Scattering dominates on these frequencies. Constant value of intrinsic quality factor is then $Q_i(const) \approx 4000$. The low internal friction (absorption, heat transform, intrinsic loss, anelastic absorption) $\approx 1/4000$ indicates that the West Bohemian crustal material from MOHO to surface is weakly attenuative and generally homogeneous.

Further development in attenuation field should be directed on the focusing towards the smaller volumes and resolving local Q heterogeneities. For these purposes the suitability of used methods is questionable. Instead the analysis of a single very early coda envelope by the means of the RTT with extensive modeling could be the way that can bring desired results. This approach is now being developed and adopted worldwide.

The work was supported by Grant Agency of the Charles University under the grant number 1584214: Attenuation of the seismic waves in real geological environment.

Chapter 6

V_P / V_S

6.1 V_P / V_S - the velocity ratio

Aside from studying the physical properties of processes causing the seismic activity, analysis of the rheological characteristics of the medium is of utmost importance. The seismic velocity ratio V_P / V_S is one of the most common parameters estimated worldwide (e.g. Gritto and Jarpe, 2014; Konstantinou et al., 2013; Novotný, Málek, and Bouška, 2016, to mention only a few). The classical Wadati diagram approach (Wadati, 1928) is the most widely used method to resolve the mean velocity ratio of the medium beneath a seismic network (e.g. Kisslinger and Engdahl, 1973; Dahm and Fischer, 2014). This method produces the most reliable V_P / V_S estimates for datasets where event-station ray-paths uniformly cover the Earth's volume beneath the seismic network and the earthquakes are widely spread.

However, the non-uniform distribution of events concentrated in source regions has led to the development of new methods enabling us to derive more local information about the seismic velocities and their ratio. Fitch (1975) resolved local seismic velocities for the source region of an earthquake cluster while implementing the master event location method. His approach was further developed by Poupinet and Ellsworth (1984) who monitored velocity variations by analyzing earthquake doublets using cross-correlations to measure precise differential times. Further development in the topic was conducted by e.g. Ito (1985), Scherbaum and Wendler (1986) and Maurer and Deichmann (1995). The last two (Maurer and Deichmann, 1995) pointed out the potential of cross-correlation methods. The most important step in direct V_P / V_S estimation was achieved by Lin and Shearer (2007) and Dahm and Fischer (2014). They both independently developed a double-difference version of the standard Wadati method to estimate the local velocity ratio within the source volume of earthquake clusters. This method allows focusing on very small clusters (up to hundreds of meters in diameter). With suitable datasets and proper data processing the temporal behavior of V_P / V_S can be monitored as well (Dahm and Fischer, 2014).

In addition to the standard Wadati method and its double-difference modification, tomographic approaches are widely used to map the spatial distribution of seismic velocities and their ratio (e.g. TomoDD algorithm by Zhang and Thurber, 2003). The main difference between tomography and the double-difference Wadati method lies in the mapping of an analyzed area. Tomography images the area covered by the seismic rays of various origin (earthquakes, controlled source shots, explosions). Analyzed volumes do not necessarily contain any earthquake hypocentres. As a result, tomography produces a complete picture of the underground sampled by the seismic rays. On the other hand, the double-difference Wadati method focuses on one single area covered by hypocentres and computes V_P / V_S directly for this volume, with no influence of the medium around. Tomography can be applied to any catalog data (locations and arrival times), while double-difference Wadati method requires tightly clustered earthquakes

and provides remarkably better resolution of results in these localized regions. Moreover, tomography is not well suited to deal with temporal changes of seismic velocities.

6.2 Double-difference Wadati method

The double-difference Wadati method was proposed by Lin and Shearer (2007) and in a slightly modified version by Dahm and Fischer (2014). Similar to a double-difference location methods it makes use of arrival time differences between pairs of events, thus canceling the effects of unknown medium variations beyond the studied area with common ray-paths.

For a better understanding we show here the full derivation of the method as proposed by Lin and Shearer (2007). Consider a pair of nearby events, event 1 and event 2, recorded at N stations. Both events lie in an area characterized by (V_P, V_S) and their inter-event distance is small enough compared with the source-receiver distances. The differential P-wave travel time δT_P^i between these two events at station i can be expressed as:

$$\Delta T_P^i = T_{P2}^i - T_{P1}^i = \frac{\Delta l_P^i}{V_P} \tag{6.2.1}$$

where T_{P1}^i and T_{P2}^i are the source–receiver travel times for events 1 and 2, respectively, Δl_P^i is the difference in the ray-path distances between the two events, and V_P is the local P-wave velocity (Figure 6.1).

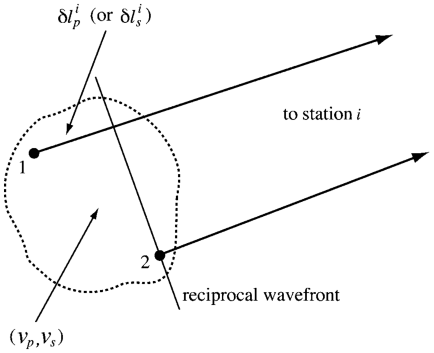

FIGURE 6.1: The ray geometry for a pair of events recorded by a distant station (Lin and Shearer, 2007)

Note that because of source-receiver reciprocity this travel-time difference is identical with that resulting from a source at the station generating a wavefront that is recorded at the two event locations. We assume that the events are sufficiently close together that the seismic velocity is locally constant and that the P-reciprocal wavefront from each station may be approximated as planar. Because the stations are in different directions, the δl_P^i values will vary among the stations.

Under similar assumptions, the differential S-wave travel time may be expressed as:

$$\delta T_S^i = T_{S2}^i - T_{S1}^i = \frac{\delta l_S^i}{V_S} \tag{6.2.2}$$

Provided that the P- and S-ray paths are coincident (we will discuss this assumption in greater detail in a later section), then $\delta l_P^i = \delta l_S^i$ and

$$\frac{V_P}{V_S} = \frac{\delta T_S^i}{\delta T_P^i}. \tag{6.2.3}$$

We could estimate the local V_P/V_S ratio near the events separately from the δT_P^i and δT_S^i times. Given a number of different stations , the $(\delta T_P^i, \delta T_S^i)$ points $(i = 1, 2, 3, ..., N)$ should all lie on the $\delta T_S = (V_P/V_S)\delta T_P$ line.

We do not normally measure the travel times, T, because we do not know the event origin times. Instead, we measure the arrival times, t. Let δt_0 be the difference in origin times between these two events, that is,

$$\delta t_0 = t_{0_2} - t_{0_1} \tag{6.2.4}$$

where t_{0_1} is the origin time of event 1 and t_{0_2} is the origin time of event 2. For station i, $t^i_{P_1} = t_{0_1} + T^i_{P_1}$, $t^i_{P_2} = t_{0_2} + T^i_{P_2}$ and their difference is

$$t^i_{P_2} - t^i_{P_1} = (t_{0_2} + T^i_{P_2}) - (t_{0_1} + T^i_{P_1}) = (t_{0_2} - t_{0_1}) - (T^i_{P_2} - T^i_{P_1}) \tag{6.2.5}$$

and we have $\delta t^i_P = \delta t_0 + \delta T^i_P$ or $\delta T^i_P = \delta t^i_P - \delta t_0$. Similarly for the S-wave we obtain $\delta T^i_S = \delta t^i_S - \delta t_0$, and thus

$$\frac{V_P}{V_S} = \frac{\delta t^i_S - \delta t_0}{\delta t^i_P - \delta t_0}. \tag{6.2.6}$$

The effect of the difference in origin times, δt_0, is to shift the $(\delta t^i_P, \delta t^i_S)$ points in both coordinates by δt_0 or along a 45^o line (Figure 6.2).

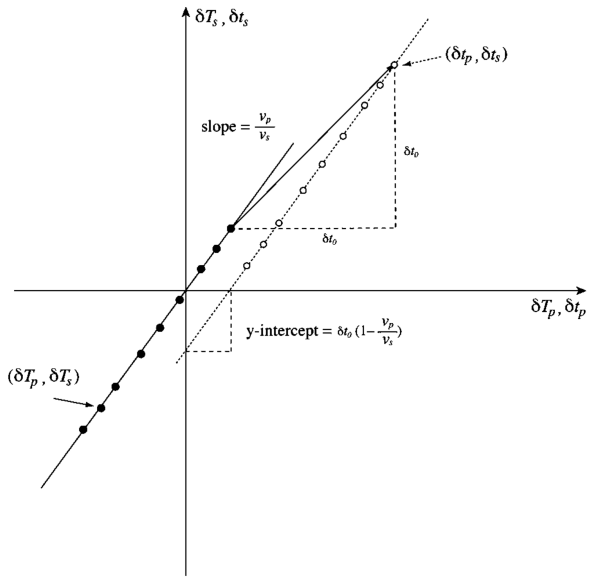

FIGURE 6.2: The filled circles show the differential P and S travel times and the open circles indicate the differential P and S arrival times, which are shifted δt_0 in both coordinates from the P and S travel time line. The slopes of both lines are the local V_P/V_S ratio. The travel time line passes through the origin $(0, 0)$, and the arrival time line has an y intercept of $\delta t_0(1 - V_P/V_S)$ (Lin and Shearer, 2007).

Equation 6.2.6 can be rewritten in a slope-intercept form

$$\delta t_S^i = \frac{V_P}{V_S}\delta t_P^i + \delta t_0(1 - \frac{V_P}{V_S}) \tag{6.2.7}$$

and we see that the $(\delta t_P^i, \delta t_S^i)$ points are on a line with slope V_P/V_S and y intercept $\delta t_0(1 - V_P/V_S)$.

Now assume that we have more stations i. For each station we can write equation

$$\delta t_S^1 = \frac{V_P}{V_S}\delta t_P^1 + \delta t_0(1 - \frac{V_P}{V_S}) \tag{6.2.8}$$

$$\delta t_S^2 = \frac{V_P}{V_S}\delta t_P^2 + \delta t_0(1 - \frac{V_P}{V_S}) \tag{6.2.9}$$

$$\vdots$$

$$\delta t_S^N = \frac{V_P}{V_S}\delta t_P^N + \delta t_0(1 - \frac{V_P}{V_S}). \tag{6.2.10}$$

If we sum these equation and divide them by the number of stations N, we obtain

$$\langle \delta t_S^i \rangle_i = \frac{V_P}{V_S}\langle \delta t_P^i \rangle_i + \delta t_0(1 - \frac{V_P}{V_S}) \tag{6.2.11}$$

where the $\langle \delta t_P^i \rangle_i$ and $\langle \delta t_S^i \rangle_i$ are the mean values of differential P and S times from all the stations. Placing 6.2.11 into 6.2.7 we have

$$(\delta t_S^i - \langle \delta t_S^i \rangle_i) = \frac{V_P}{V_S}(\delta t_P^i - \langle \delta t_P^i \rangle_i) \tag{6.2.12}$$

Angle brackets with index i represents the mean value of a property along ith dimension, in this case the mean value of arrival time differences at N stations indexed by i. Geometrically we move the vector of arrival time differences $(\delta t_P^i, \delta t_P^i)$ to the origin without affecting its slope - we apply the demeaning (Figure 6.3 a).

The possibility of demeaning the $(\delta t_P^i, \delta t_P^i)$ data vector enables us to use numerous event pairs - located closely together in volume with same V_P/V_S. In that case each event pair j produces one vector $(\delta t_P^i, \delta t_P^i)$ moved by δt_{0_j} (Figure 6.3 b). Moving all the event pairs data vectors toward zero (Figure 6.3 c) forms one joint data ensemble $(\delta t_{ij}^P - \langle \delta t_{ij}^P \rangle_i, \delta t_{ij}^S - \langle \delta t_{ij}^S \rangle_i)$ with the slope V_P/V_S:

$$\delta t_{ij}^P - \langle \delta t_{ij}^P \rangle_i = \frac{V_P}{V_S}(\delta t_{ij}^S - \langle \delta t_{ij}^S \rangle_i) \tag{6.2.13}$$

To estimate the slope V_P/V_S an orthogonal fitting procedure has to be done to account for errors in P and S arrival time differences. Method is very sensitive to quality of fit and even the slightest variation in the line slope changes the V_P/V_S significantly (Figure 6.4).

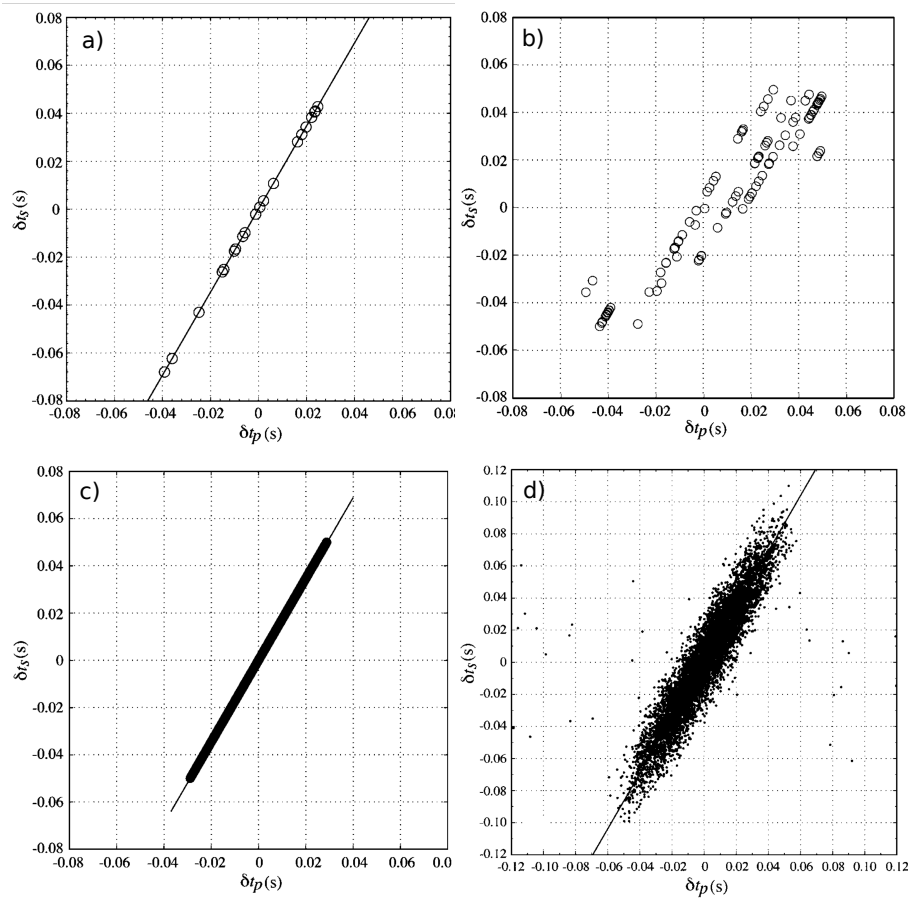

FIGURE 6.3: Doubre-difference version of Wadati method (Lin and Shearer, 2007), from single event pair to noised data from earthquake cluster. a) P differential arrival times vs. S differential arrival times for a single pair of events recorded by 20 random stations on the surface. The straight line passing through the points is the best fitting line with the slope (V_P/V_S) of 1.732; b) P arrival time differences vs. S arrival time differences for different pairs of events in a compact cluster. These points are on different lines parallel to each other, with the same slope as the V_P/V_S ratio for the cluster, but with different y intercepts, which are due to the varying differential origin times; c) Demeaned $\langle \delta t_P^i \rangle_i$ vs. demeaned $\langle \delta t_S^i \rangle_i$. These points align on a straight line at slope V_P/V_S and through the origin $(0,0)$; d) Demeaned $\langle \delta t_P^i \rangle_i$ vs. demeaned $\langle \delta t_S^i \rangle_i$ with added Gaussian noise.

The method is fully valid if:

- All events of analyzed cluster lie close together, so even the longest inter-event distance between two cluster events is small in comparison to cluster-station distances.
- The V_P/V_S inside analyzed volume is constant and stable during analyzed time sequence
- Distance $\delta l_P^i = \delta l_S^i$ and so the take-off angles of P- and S-waves are identical.

The biggest advantage of the method is that it doesn't need the origin times information - it is compensated by the demeaning. However, the demeaning itself brings problems when amplifying the effects of δl_P^i and δl_S^i inequality. The method is fully valid for homogeneous velocity model. In homogeneous model the possible inequality of δl for P- and S-waves is caused by inappropriately large inter-event distance. With complicating the velocity/geological model the equality of δl_P^i and δl_S^i is biased even more and as a consequence V_P/V_S is underestimated (for take-off angles > 90) or overestimated (for take-off angles < 90), as mentioned by Palo, Tilmann, and Schurr (2016). The effect if the most evident for the geologies with low V_P/V_S layers like subductions, with overestimation up to 0.27 (Palo, Tilmann, and Schurr, 2016). Mild

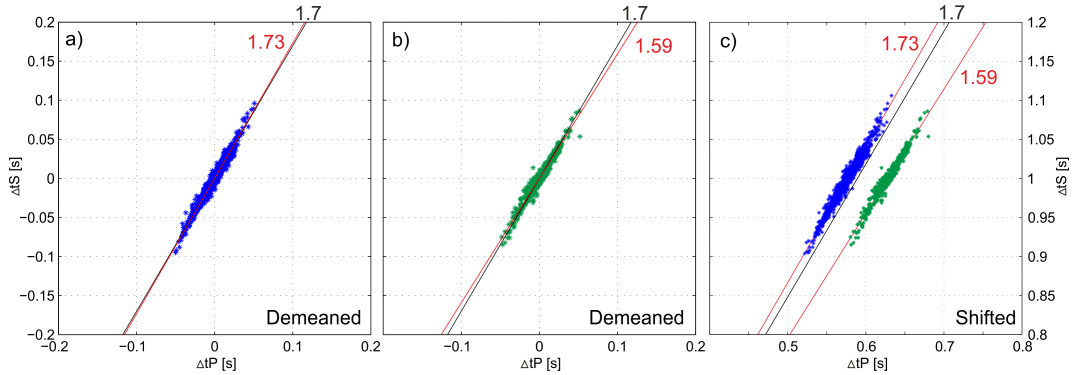

FIGURE 6.4: Two different datasets with different V_P / V_S: a) 1.59; b) 1.73. Black lines represent the velocity ratio of 1.7 for comparison. In plot c the same clusters are shifted from the demeaned zero position to highlight their difference in slopes.

decrease may occur if we have layered models with increasing V_P / V_S up to the surface - up to 0.05, depending on the current model and inter-event distance.

In case of tight earthquake cluster the δl_P^i - δl_S^i difference is controlled by the combination of two factors: velocity model and inter-event distance. Authors must asses if, for a given frequency range, their geology between stations and the cluster can be approximated by a homogeneous or at least layered model with smoothly increasing V_P / V_S. If so, the event pairs with reasonable inter-event distance with respect to the accuracy of δt estimation must be analyzed.

Lin and Shearer (2007, 2009) overcame the problem by using small 3-D clusters widely covered by stations and achieved random distribution of δl azimuths suppressing the errors. Moreover, their problem settings (long hypocentral distances, small clusters, wide distribution of seismic stations) allowed them to more or less approximate the crust by a homogeneous velocity model.

Uncertainties are estimated using a bootstrap method (Lin and Shearer, 2007), where randomly selected events pairs were removed, others were randomly doubled, tripled etc. and the V_P / V_S ratios were computed repeatedly for every "biased" dataset. The error is then estimated as a standard deviation of the resulting velocity ratios of these datasets.Palo, Tilmann, and Schurr (2016) proposed the use of uniform distribution of take-off angles (both up- and down-going ones), or involving on origin time into the computation.

6.3 Data

V_P / V_S estimations were applied to a 2014 activity. Recent seismic episodes in the West Bohemia area were expressed in the form of seismic swarms. Different segments of the Nový Kostel focal zone (NKFC) were activated and as a result thousands of events occurred. The uniqueness of the 2014 activity lies in its non-swarm character. The activity consists of three separate mainshock-aftershock sequences with events located on the same focal zone where only swarm-type seismicity was present during the last two decades. Despite its non-swarm character, statistical analysis of the aftershock sequences (Hainzl et al., 2016) shows an unusually high rate of aftershocks in the first 8-10 h after the strongest earthquake and their migration pattern can be explained by the presence of over-pressured fluids within the focal zone. Activated fault segments form almost a vertical plane of 3x3 km at depths from 7 to 10 km (Figure 6.5). The fault plane is oriented from the south to the north with a strike of 169^o (Fischer et al., 2014).

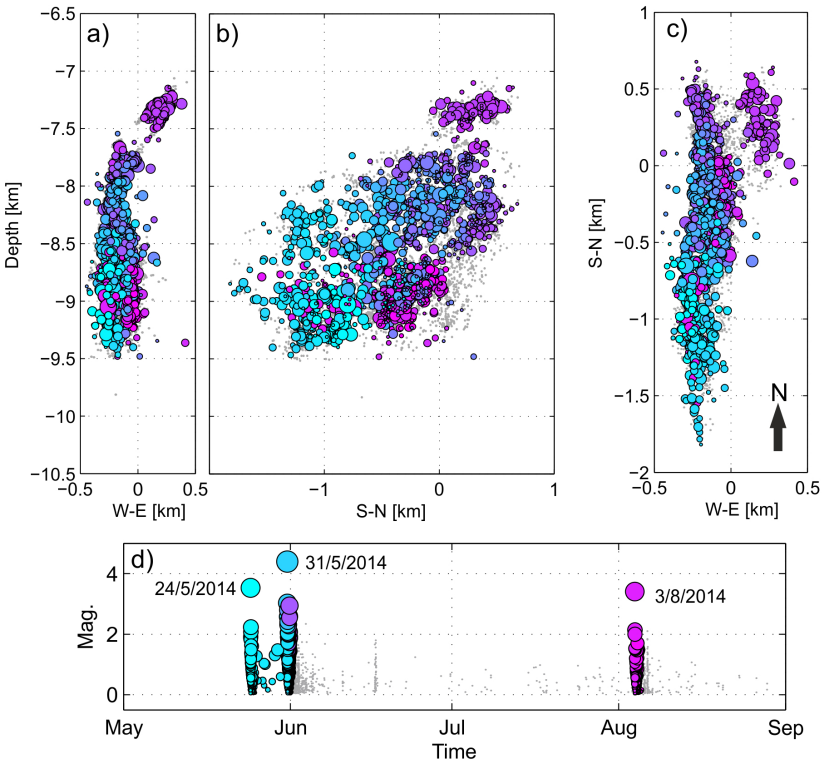

FIGURE 6.5: Locations of the study-selected 1624 events (out of a total number of 3800) that occurred during the 2014 mainshock-aftershock sequences: a) front view; b) side view; c) map view; d) temporal evolution. The size of the circles scales with M_L. Gray dots represent events which were omitted from analysis throughout the data processing.

The first sequence started with a $M_L = 3.5$ earthquake (on May 24^{th}) followed by circularly distributed aftershocks evolving from the south to the north and continuing for two days. The second sequence started with a $M_L = 4.5$ earthquake (on May $31st$), lasted for one week, and aftershocks evolved through the whole fault zone. The third sequence was very similar to the first, with one mainshock of $ML = 3.5$ (on August 3^{rd}) and circular south-north evolution of the aftershocks lasting for two days (Hainzl et al., 2016).

From the total number of more than 8000 events recorded, 3800 with magnitudes ranging $M_L = 0 - 4.5$ were relocated by the HypoDD algorithm (Waldhauser and Ellsworth, 2000). Processing through HypoDD reflected our effort to obtain as precise relative locations as possible. P- and S-wave arrival time differences at 9 stations (Fig. 1) were computed by waveform cross-correlation and checked with care in order to avoid mis-locations due to the wide magnitude range of the events. Different magnitudes with different frequency content of correlated pulses yield the best cross-correlation coefficients when shifted to the maximum, not to the first onset of the wave arrival (Figure 6.6). Therefore it is crucial to correlate only waveforms of earthquakes with similar magnitudes. As a result of our relocation procedure our location errors estimated by the HypoDD SVD inversion method were ± 18 m in the horizontal plane and ± 25 m in the vertical coordinate.

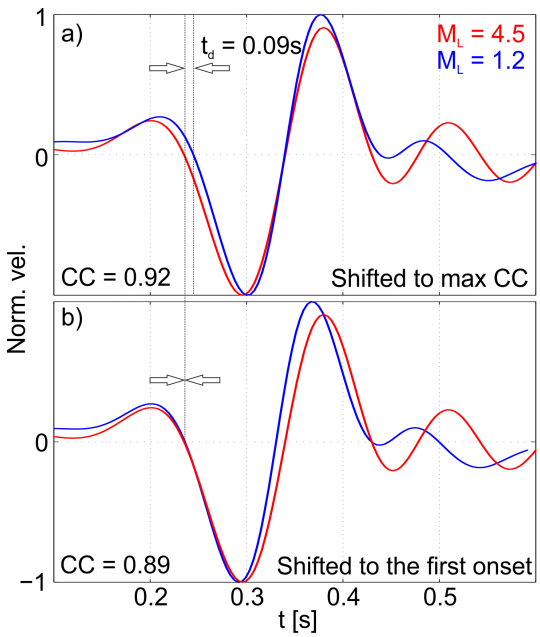

FIGURE 6.6: P-wave arrivals of two events (1-15 Hz) with $M_L = 4.5$ (red) and $M_L = 1.2$ (blue) shifted to: a) position of maximum cross-correlation coefficient (CC); b) P-wave onsets. For correct arrival time difference estimation waveforms of similar widths of P pulses (magnitudes) are necessary. Maximum CC does not mark proper arrival (onset) time difference when magnitudes differ significantly. Error can be up to 0.1 s.

6.4 Method applicability analysis

Before its application we need to asses the method possibilities. The most important questions are, if we can apply it to a crustal geology in West Bohemia with given positions of stations and events. Then we have to asses how distant event pairs can be used to gain acceptable results and how precise the P and S differential times have to be.

We modeled synthetic catalog using velocity model by Málek, Horálek, and Jánský (2005) and tested the V_P/V_S resolvability. Modeled cluster had the same characteristics as real data: the relocated hypocenters were used with same station coverage. We artificially inserted a layer of some V_P/V_S and tried to retrieve the value. Different parts of the cluster were tested for different levels of velocity ratio. Despite such an over-simplification a conclusions could be made:

- Estimated V_P/V_S values tends to be rather underestimated.
- Maximum inter-event distance acceptable for reliable V_P/V_S measurement is 0.5 km (Figure 6.7).
- Maximum arrival time difference error acceptable for rough measurements is 0.01 s (assuming normal distribution of errors with 0.01 as a boundary of 2σ interval). Variations of V_P/V_S bigger than 0.1 are comprehensively observable then.
- With decreasing error the resolution increases and is up to 0.05 (with $2\sigma = 0.005$)
- The use of 5 stations is sufficient for stable V_P/V_S resolving in our 2-D case.
- Stable results are achieved when a large number of event pairs was used.

Figure 6.7 shows one example of modeling. We searched for V_P/V_S ratio 1.7 in data biased up to 0.002 s and retrieved more or less the desired value when using maximum event separation distance of 0.5 km.

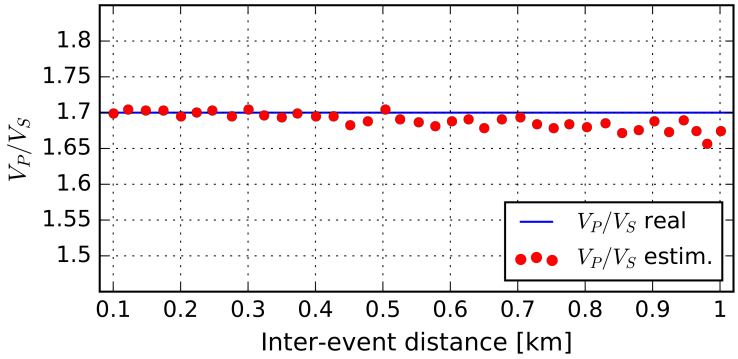

FIGURE 6.7: Estimated V_P/V_S (red dots) in comparison with real V_P/V_S as a function of inter-event distance. Cluster of events similar

No cluster depth or position dependency was observed. Estimations of V_P/V_S are biased by errors in arrival time differences, by errors occurring as a result of inter-event distance and by decreasing number of event pairs in cluster. If the upper crust bellow West Bohemia could be approximated by used velocity model, then, based on the modeling we can be sure find V_P/V_S with accuracy $0.02 - 0.05$. If a systematic bias is present, then the V_P/V_S might be underestimated up to level of 0.02.

6.5 Data processing

The data processing consisted of two steps: first, subdividing the activity into clusters, and then estimating the V_P/V_S ratios using the double-difference method described above.

Appropriate selection of the earthquake clusters was the key factor for success in identifying reliable variations of velocity ratios. We used a nearest-neighbor clustering algorithm for the rough clustering and then manually checked, adjusted, combined and sorted the clusters in order to provide them with desired characteristics: short time window, homogeneous spatial distribution of events, and sufficient number of events within a single cluster.

The first automatic clustering step (the nearest-neighbour clustering algorithm applied to the 2014 data) sorted events into more than 30 initial groups. About 20% of the events were omitted since they did not show an adherence to any cluster or only created small groups of outliers. In the next step, all of the automatically produced clusters were manually checked and processed with respect to their spatial and temporal significance, size and general relation to the whole activity evolution.

The crucial deciding parameter of cluster acceptance/rejection was the rate of events (events per hour) within a single cluster, as we required clusters with a high event rate. These were attainable during the early aftershock sequences (with events rate up to 70 events per hour, Table 1). With the continuation of the aftershock activity, the rate of potential clusters lowers. Therefore, in order to obtain a cluster with a sufficient number of events, a longer time window was necessary.

By testing the method on different test clusters we concluded that only clusters containing at least 100 earthquakes produced reliable V_P/V_S estimates. Generally, we removed the less

numerous clusters from the analysis. In some cases, smaller groups of events were combined into a single acceptable cluster to prevent the loss of the V_P / V_S information for a given time and space window, despite the low value of temporal density (e.g., the first and third mainshock aftershock sequences were treated as single clusters).

As a result of our combined automatic-manual clustering procedure, 7 clusters with a total of 1624 events out of 3800 were selected (Figure 6.8 and Table 6.1). Cluster 1 contains the activity of the first mainshock-aftershock sequence that started on May 24^{th}. Clusters 2-6 monitor the activity of the $M_L = 4.5$ mainshock from May 31^{st} and 1.5 days of its aftershocks. Clusters 2 and 3 cover the first 8 h after the mainshock. They are overlapped in time, but not space. Cluster 2 maps the earthquakes to the south of the main event, while cluster 3 maps the northwardly propagating activity. Clusters 4, 5 and 6 slightly overlap in time, but are also strictly distinguished in space. Cluster 4 is the continuation of cluster 3, cluster 5 covers the separate activity above the fault zone and cluster 6 contains the activity propagated in depth. Further continuation of the aftershock activity was too sparse in time and too scattered in space to generate clusters short enough and small enough to undergo the analysis. The third mainshock-aftershock sequence from August the 3^{rd} was grouped in cluster 7.

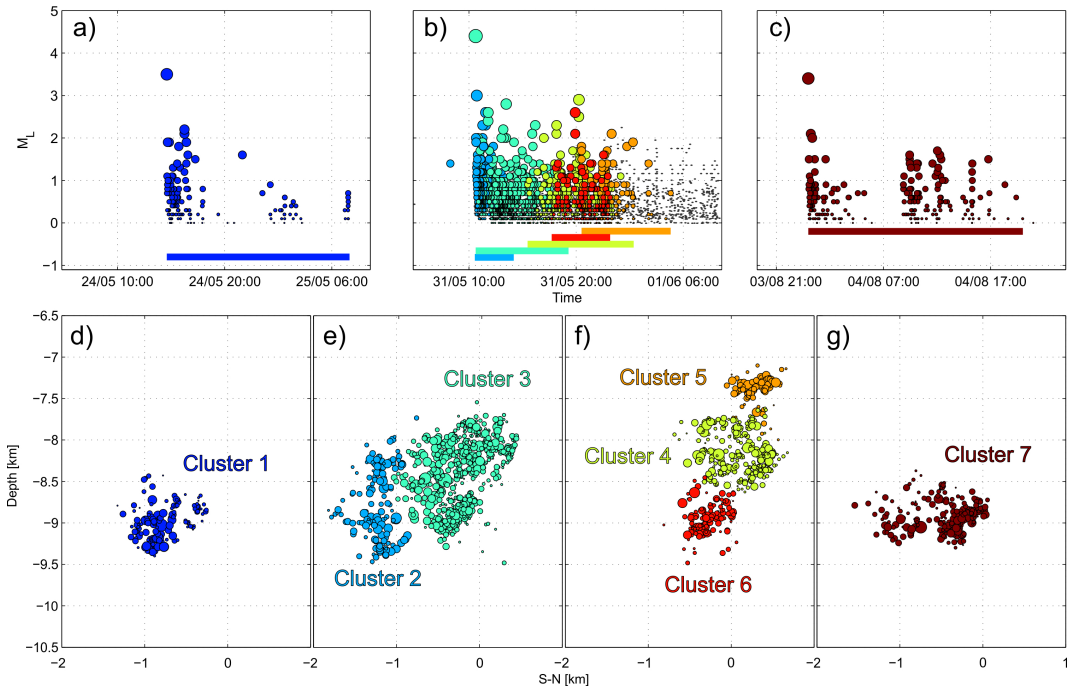

FIGURE 6.8: 7 spatio-temporal clusters delineated from the 2014 activity: a)-c) temporal evolution of the three mainshock-aftershock series with clusters indicated with different colors; d)-g) side view of the fault plane showing the spatial distribution of the clusters; for better visibility plotted separately into four figures. Gray dots in b) represent continuation of the aftershock activity with insufficient clustering potential.

The first and third mainshock-aftershock sequences were treated as two single clusters, despite the fact they could be clustered in more distinct sub-clusters. This step was necessary due to a small number of events within these two sequences (157 and 123).

Despite the high number of omitted events, the final clustering was found to be optimal for the given dataset and allowed an unbiased estimation of V_P / V_S (selection/omission of the events does not affect the velocity ratio values). From the spatial point of view the clusters mapped the whole area activated in the fault zone (Figure 6.8).

Events within the clusters were paired and differential times between P and S wave arrivals of each pair were measured by using cross-correlation. Waveforms were filtered by a 3-pole

Nr.	Diam. [km]	Ev.	Ev. pairs	Diff. t.	V_P/V_S	[+/-]
1	0.96	157	259	1130	1.59	0.02
2	2.2	150	169	697	1.6	0.03
3	1.81	649	727	3039	1.71	0.01
4	1.52	282	409	1753	1.73	0.01
5	0.65	131	474	2023	1.72	0.01
6	1.08	132	82	352	1.64	0.04
7	1.68	123	67	273	1.6	0.03

TABLE 6.1: Cluster characteristics and V_P/V_S results: cluster diameter, number of events, number of event pairs, number of differential times used for the regression, V_P/V_S, and error.

1-15 Hz band-pass Butterworth filter. Only events with similar magnitudes were paired and correlated to avoid errors in differential time estimation. For each time difference we obtained a cross-correlation coefficient which describes the similarity of the waveforms, hence quantifying the quality of the estimated difference time.

Hypocentres of the 2014 sequence lie on an almost vertical plane forming a 2-D structure (Figure 6.5). To analyze the area covered by the events (the pairs of events) only stations with ray paths more or less parallel with this 2-D plane (general fault orientation) were used. Use of the other stations lying perpendicular to the plane deteriorated the V_P/V_S estimation since they produce time differences which were too small. This was caused by the short travel distance across the fault. The 5 stations that passed this criterion were distributed uniformly above the analyzed hypocentres (Figure 6.9). The positions of stations along the hypocentre trend resulted in a uniform distribution of inter-event ray path directions within the clusters, which is essential for successful V_P/V_S estimation. Only event pairs with at least 4 differential times and a cross-correlation coefficient higher than 0.7 were accepted for data processing and analysis.

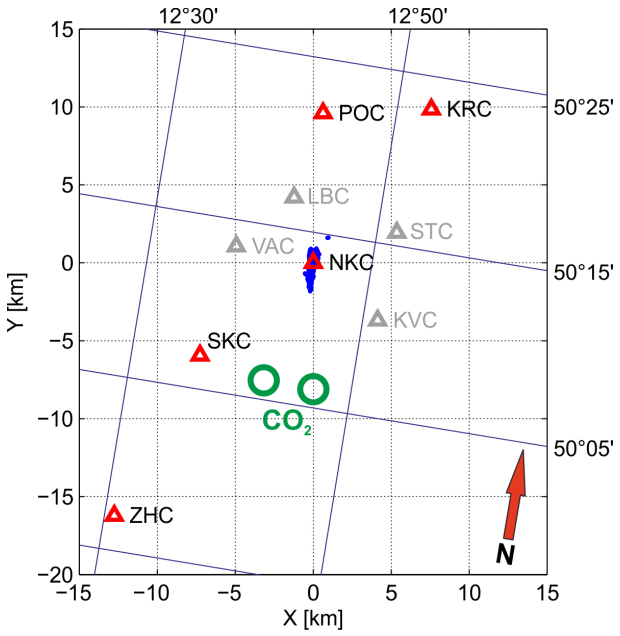

FIGURE 6.9: Map of the West Bohemia area with epicentres of the 2014 activity (blue dots) and selected stations of the WEBNET seismic network (red triangles) used in this study. Gray stations were not used for the analysis, green circles represent the Soos and Hartoušov moffets area, where CO_2 springs are located.

6.6 Results

We tested a variety of clustering approaches, cross-correlation thresholds, and stations for analysis to avoid possible trade-offs between estimated V_P/V_S ratios and cluster properties (size, number of events, number of event pairs, and number of used differential times). We optimized the method so that no clear correlation between the above-mentioned parameters was apparent and the resulting velocity ratios reflected only the mean V_P/V_S ratios of the volume covered by a single cluster. The resulting V_P/V_S estimates of each cluster with their errors are shown in Figure 6.10 and Table 6.2.

Nr.	Diam. [km]	Ev.	Ev. pairs	Diff. t.	V_P/V_S	[+/-]
1	0.96	157	259	1130	1.59	0.02
2	2.2	150	169	697	1.6	0.03
3	1.81	649	727	3039	1.71	0.01
4	1.52	282	409	1753	1.73	0.01
5	0.65	131	474	2023	1.72	0.01
6	1.08	132	82	352	1.64	0.04
7	1.68	123	67	273	1.6	0.03

TABLE 6.2: Cluster characteristics and V_P/V_S results: cluster diameter, number of events, number of event pairs, number of differential times used for the regression, V_P/V_S, and error.

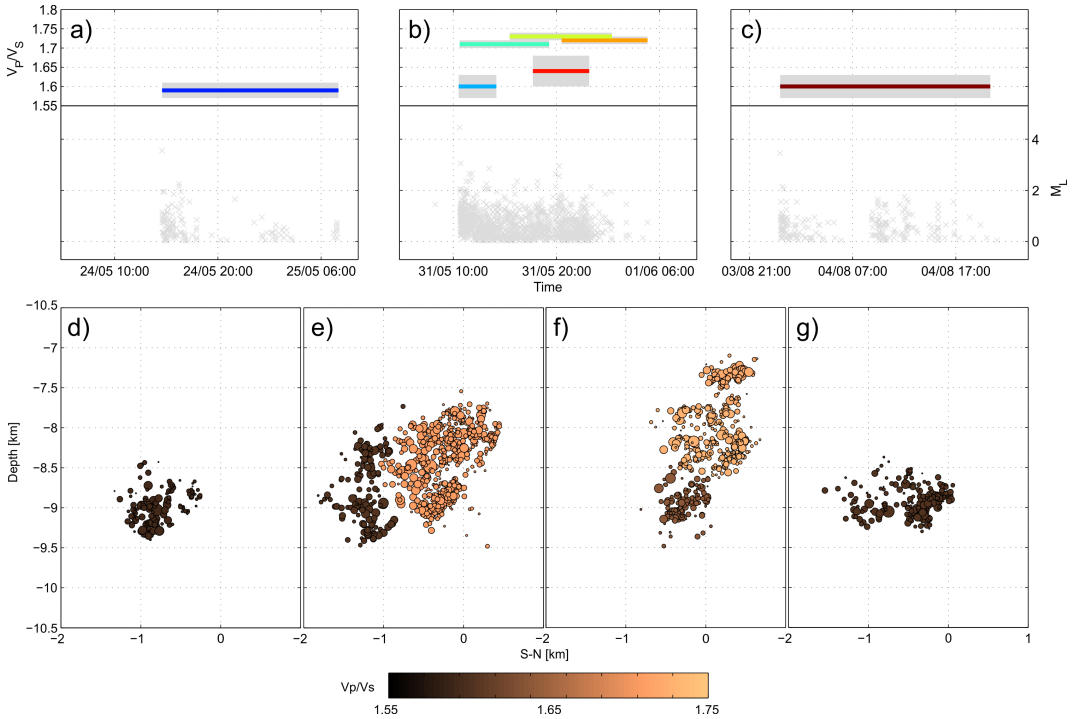

FIGURE 6.10: Resulting temporal and spatial distribution of V_P/V_S: a)-c) V_P/V_S with errors (grey) for different clusters - shown in a temporal view (clusters colored as in Figure 6.8); d)-g) Resulting V_P/V_S for different clusters with colors reflecting the value of estimated V_P/V_S (darker for lower values) - side view of the fault plane.

6.7 Discussion

Our analysis revealed significant V_P/V_S variations in space and time. The obtained precision of one hundredth is lower than the precision achieved in the similar study by Lin and Shearer (2009) of thousandths, which is caused by the relatively low number of stations involved in our analysis. The V_P/V_S variations are strong enough to be recognizable even if the most pessimistic accuracy scenario is applied with modeled error of 0.05. Measured values vary between 1.59 ± 0.02 and 1.73 ± 0.01, what is slightly lower than values expected in Earth's mantle (Christensen, 1996). However, lower V_P/V_S levels are in accordance to velocity models and tomographies. The influence of a bias due to the inequality of P- and S-wave take-off angles above mentioned seems to be of a small importance.

Generally, the application of the double-difference method to estimate the V_P/V_S on very local scales with sparse coverage of stations requires careful data processing. To eliminate the influence of technical aspects (cross-correlation threshold, number of differential times, and fitting method), clusters should only contain nearby events with common characteristics occurring during a short time window. This is especially important in areas where strong V_P/V_S variations are expected, such as the West Bohemian area (Dahm and Fischer, 2014).

From this technical point of view, clusters 1-5 fulfill the above stated conditions and produce a sufficient number of differential times (Table 6.2) even after applying the cross-correlation threshold to at least 4 stations. Therefore, their estimated V_P/V_S is considered reliable. Despite this stability, there are higher error estimates of ± 0.02 and ± 0.03 for clusters 1 and 2, which both show anomalous velocity ratios of 1.59 ± 0.02 and 1.6 ± 0.03. Higher errors combined with a high number of differential times (implies better stability of the fit) can be explained as a result of velocity ratio instabilities within the analyzed cluster. In fact the bootstrapping method of error estimation is sensitive to the V_P/V_S stability of all event pairs involved. Stable V_P/V_S inside the area of the cluster and through the whole duration of the cluster lowers the estimated error. As a result, the larger errors in cluster 1 and 2 might stem from changes of velocity ratio during the analyzed time interval or from the presence of V_P/V_S heterogeneities smaller than the cluster-based method can detect.

On the contrary, clusters 6 and 7, despite having a similar number of events as cluster 1 (157 events with 1130 differential times), produced a significantly smaller number of usable differential times (352 and 273, Table 6.2). The reason might be the dissimilarity of earthquake waveforms, as the selected cluster might be composed of several small groups of events with different source mechanisms. These dissimilarities would result in lower cross-correlation coefficients than the required 0.7. A lower number of differential times causes higher errors (0.04 and 0.03). However, both of these clusters (even with the errors taken into account) show low V_P/V_S ratios of 1.64 ± 0.04 and 1.6 ± 0.03.

We must keep in mind, that transforming the problem of V_P/V_S estimation on a vertical plane into a 2-D (by proper stations selection) we measured V_P/V_S only in the directions along the fault plane. Effect like anisotropy often observed could not have been studied.

Observed behavior of V_P/V_S can be viewed from two points of view: spatial, as a dependence on crustal material composition and temporal, as an indicator of dynamic processes inside the fault zone (rupturing, fault saturation etc.)

6.7.1 Spatial V_P/V_S dependence

The distribution of V_P/V_S along the activated fault plane reveals significant spatial dependence. Areas of V_P/V_S below 1.65 are located at depths deeper than 8.5 km, whereas the shallower depths clearly show values higher than 1.7 (Figure 6.11). However, this apparent spatial dependence is broken by an unstable area (see Figure 6.11 - blue dashed rectangle) at depths from 8.5 to 9.5 km and S-N coordinate from -1 km to 0 km. The instability is a result of the varying velocity ratio estimations for this area from clusters 6 and 7 with low V_P/V_S and cluster 3 with high V_P/V_S. These variations may be an artifact of the method or may have a real physical interpretation as a changing V_P/V_S with time in this area. This was pointed out by Dahm and Fischer (2014) for the previous West Bohemian seismic swarms. Meanwhile the anomaly is related to the seismicity structure within cluster 3, whose V_P/V_S ratio does not represent a precise velocity ratio throughout the studied area, but instead the mean V_P/V_S of the cluster 3 coverage.

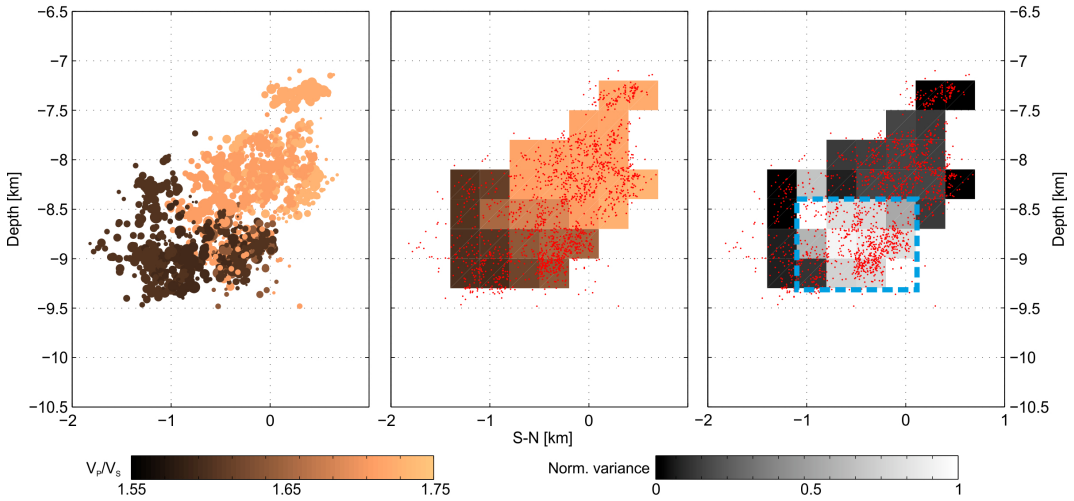

FIGURE 6.11: Pseudo-tomographical representation of the results: a) events colored according to the V_P/V_S of the cluster they belong to; b) mean V_P/V_S for the grid with bin size 300 m (bin V_P/V_S value computed as a mean of the event velocity ratios located in the bin); c) Uncertainty of velocity ratio estimates expressed as normalized variance of the V_P/V_S ratio estimated within the single bin; high normalized variance represents bins where dramatic changes over time appear.

Our V_P/V_S values correspond to Poisson ratios ranging from 0.173 to 0.249. That is less than the typical range of 0.24 to 0.29 for crustal rocks (Christensen, 1996). Generally, low values may indicate the presence of quartz-rich rocks at focal depths from 7 to 11 km. Quartz has a V_P/V_S of 1.5 and its increasing content results in lowering the mean velocity ratio of the rock material (e.g. Christensen, 1996; Lin and Shearer, 2009).

6.7.2 V_P/V_S as a function of time

Analyzing the V_P/V_S ratio as a function of time shows that low values of the velocity ratios are associated with outbursts of activity and with the mainshocks (clusters 1, 2 and 7), while the higher ratios are common for the aftershock series (clusters 3-5). Cluster 6 is an exception as it covers part of the aftershock sequence, but has lower V_P/V_S of 1.64 ± 0.04. Observed temporal changes in this study require a different interpretation based on dynamic changes of the porous media. We applied the Biot-Gassmann theory for poroelastic media (e.g. Mavko, Tapan, and

Dvorkin, 2003). The Biot-Gassmann equations predict the theoretical V_P/V_S ratio for a porous medium saturated with liquid or compressible gas. Currently, it is only one of the theoretical models developed (e.g. Walsch, 1969; O'Connell and Budiansky, 1974), but its agreement with our results (below) makes it suitable for interpretation. According to the model, the velocity ratio V_P/V_S of a porous media can be expressed as

$$\frac{V_P{}^2}{V_S} = \frac{K_{dry}}{\mu} + \frac{4}{3} + \frac{K_p}{\mu}, \tag{6.7.1}$$

with

$$K_p = \frac{\alpha^2}{\frac{\Phi}{K_f} - \frac{1-\Phi}{K_s} - \frac{K_{dry}}{K_s^2}}, \tag{6.7.2}$$

$$K_{dry} = K_s()1 - \alpha, \tag{6.7.3}$$

where K_s and K_f are bulk moduli of matrix and interstitial fluid, μ represents the shear modulus of the solid phase, Φ is porosity and α is the Biot–Willis coefficient with values from 0 to 1. Assuming the above-mentioned mechanical parameters of the solid medium to be constant in the focal depths, V_P/V_S becomes a function of porosity and the interstitial fluid bulk modulus. Moreover, when expecting only a single-phase fluid to be present, the resulting velocity ratio is only a function of porosity due to the fragmentation of the focal zone. According to the geodynamic setting, pressure and temperature characteristics of the focal depths of 7-9 km, we investigated two different fluids - liquid water and supercritical CO_2, with K_f of 2 GPa and 0.5 GPa, respectively. We used average values for the crystalline basement with respect to the expected geological structure (e.g. Fischer et al., 2014; Ružek and Horálek, 2013; Alexandrakis et al., 2014): $K_s = 50$ GPa, $\mu = 30$ GPa, $\alpha = 0.5$. Theoretical velocity ratios for both fluids decrease with porosity (Figure 6.12).

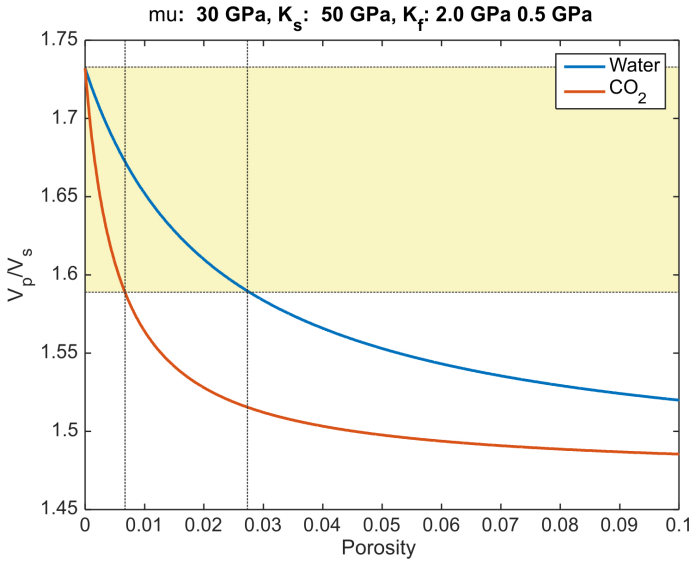

FIGURE 6.12: Theoretical velocity ratios of water and supercritical CO_2 as a function of porosity in a typical crystalline rock $K_s = 50$ GPa, $\mu = 30$ GPa, $\alpha = 0.5$. The observed values of V_P/V_S from 1.59 to 1.73 (yellow band) correspond to porosity variations between 0 and 0.01 for supercritical CO_2 and between 0 and 0.03 for water.

The physical effect beyond the V_P/V_S decrease is that S-waves are carried by the solid matrix of the fractured rock and their velocity is less affected by the fluid intrusion into the pore space. On the contrary, P-waves are carried by the whole material (matrix and pore filling) and their velocity is controlled more significantly by the interstitial fluid. The P-wave velocity decrease is stronger than that of S-waves, and therefore the V P /V S ratio decreases with porosity increase, or when pores are filled with gas (Dahm and Fischer, 2014).

The lowest observed V_P/V_S value of 1.59 ± 0.02 requires porosities less than 0.01 (CO_2) and 0.03 (water). The question remains, what kind of fluid is more probable to be present in the focal zone during the rupturing process. Wagner et al. (1997) found free water and open fractures down to a depth of about 9.4 km at the KTB borehole (50 km SW). However, massive CO_2 releases (up to 500 m^3/h (Fischer et al., 2014)) are observed in the seismoactive area with dynamic behavior. In some cases CO_2 flow variations correlate with seismic activity. Therefore we favor a system with over-pressured mantle-derived CO_2 in its supercritical phase filling the fractures of the hypocentral area during the seismic activity, or at least during the initial outbursts of the seismic sequences. Variations of the V_P/V_S ratios appear to reflect changes in the porosity due to the fracturing process.

Further evidence of fluid intrusion and its influence on the characteristics of seismic activity was given by Hainzl et al. (2016), who analyzed the same 2014 dataset as our study. By analyzing the aftershock sequence of the strongest event (in May 31^{st} with $M_L = 4.5$) they concluded the mainshock opened the fluid pathways from a finite fluid source into the fault plane, which explained the unusual rate (high and constant activity during the first 0.3 day after the mainshock followed by aftershock decay according to the Omori law) and migration characteristics of aftershocks.

The onsets of the three mainshock-aftershock sequences were always located in the deeper part of the fault zone beneath a depth of 8.5 km. Dense aftershock activity and high intensity of the rupturing process are accompanied by low velocity ratios (down to 1.59 ± 0.02). Later, as the aftershock series evolved above 8.5 km and its rate slowed, the expected decrease of porosity correlates well with higher V_P/V_S values (up to 1.73 ± 0.01). This behavior might indicate a distinct structural boundary at depths of 8.5 km between two geological volumes with different responses to the fluid intrusion. On the other hand, this boundary might only be apparent and just a result of the changing fluid dynamics as the role of fluids is dominant at the beginning of the activity, which was always located below 8.5 km. The onset of the 2014 seismic activity is associated with an anomalously increased aftershock rate (Hainzl et al., 2016) and low V_P/V_S down to 1.6 ± 0.03. With the continuation of activity the aftershock rate becomes more standard in terms of the Omori law (Hainzl et al., 2016) and V_P/V_S rises up to 1.73 ± 0.01. A change of triggering mechanism is a possible explanation of the observed behavior — from fluid induced triggering to a standard elastic stress transfer. For the strongest event on May 31^{st} we observed this change in V_P/V_S about 8-10 h after the mainshock. Interestingly, this agrees with the time when the aftershock characteristics started to decrease according to the Omori law, 0.3 days after the mainshock (Hainzl et al., 2016).

6.7.3 Comparison with similar studies

The high resolution achieved by the double-difference version of the Wadati method depends on the data quality (earthquake density and distribution) and is beyond the capabilities of tomographic methods. Moreover, the ability to analyze the temporal dynamics of the V_P/V_S is unattainable by tomography. Therefore a direct comparison of our 'dynamic' results with existing 'static' tomographic studies is not meaningful. Despite this, for comparison reasons

we computed the mean V_P/V_S of the focal zone using the double-difference Wadati method for the whole activity. This yields an average velocity ratio of 1.71 ± 0.01 (Figure 6.13). In contrast to the tomographic results of Ružek and Horálek (2013) (1.55) and Alexandrakis et al. (2014) (1.73 ± 0.04), we do not find the mean velocity ratio on the fault zone to be anomalous. V_P/V_S anomalies are of short duration and of small size in comparison with the whole fault zone.

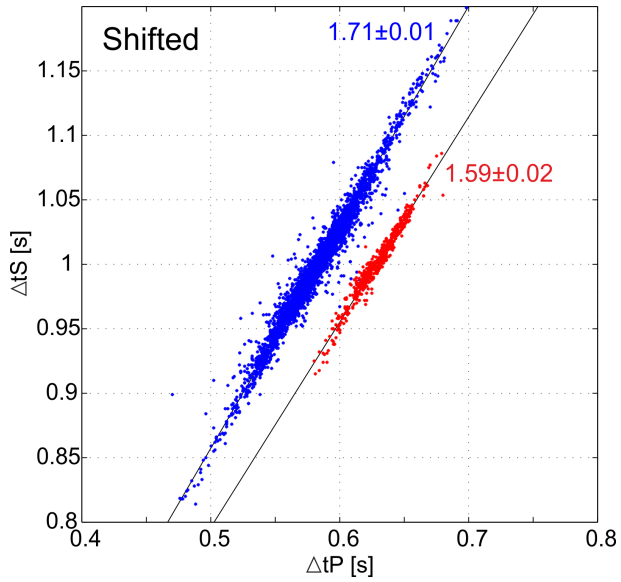

FIGURE 6.13: Mean V_P/V_S of the Nový Kostel focal zone (blue dots). Computed for the whole time interval of the 2014 activity using the double-difference modification of the standard Wadati method. Red dots represent a sub-cluster of $V_P/V_S 1.59 \pm 0.02$ for comparison. Both datasets are shifted from the demeaned zero position to highlight the difference of slopes.

6.8 Conclusions

For the West Bohemian activity, the double-difference Wadati method is applicable and returns reasonable results. The method itself has many 'hidden traps', but with careful data processing and knowledge of method behavior (based on error modeling) it can be a valuable tool.

Our conclusions are:

- V_P/V_S estimates for the single clusters are stable and vary between 1.59 and 1.73.
- V_P/V_S are in accordance with other structural or velocity resolving studies in the area.
- Behavior of V_P/V_S appears to indicate a geological boundary at 8.5 km depth expressed in V_P/V_S change from 1.6 to 1.7.
- The behavior can be with equal acceptability explained as a result of fracturing process inside the fault zone with saturating the cracks with over-pressured mantle fluids - supercritical V_P/V_S.

6.9 Modified master-event technique

Master event technique (Stoddard and Woods, 1990) searches location and origin time of slave event with respect to a known master event. For proper method application a reliable location of the master-event must be provided and slave-event must be in its vicinity, so the assumption of identical take-off angles can be made. These conditions are valid if the inter-event separation distance is much shorter that event-station trajectory.

If the assumptions are valid, the master- and slave-event share the normal vector $N(N_x, N_y, N_z)$ with direction from the master to a station (Figure 6.14). For simplicity the master-event's location is set to $(0, 0, 0)$ and slave is $L(X_s, Y_s, Z_s)$ km apart. Origin time of the master-event is $t_{0m} = 0$ and slave's $t_{0s} = t_{0m} + \delta t_0$.

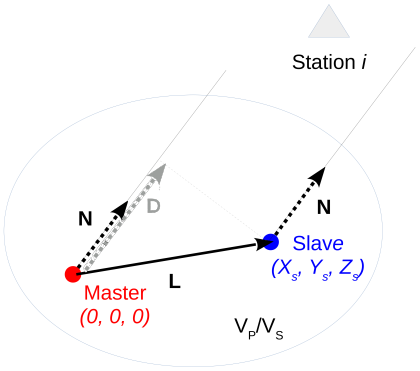

FIGURE 6.14: Slave-event (blue) vs. master-event (red). Events are so far from station that their take-off angles are assumed to be identical. Between master and slave the V_P/V_S is stable. N is the normal vector of master(slave)-station orientation, L is the total vector of master-slave distance and D is projection of L to the station i.

The travel time difference δT_i between master and slave ($D_i(D_{ix}, D_{iy}, D_{iz})$) in direction to station i is

$$\delta T_i = \frac{D_i(D_{ix}, D_{iy}, D_{iz})}{V} = \frac{N_i(N_{ix}, N_{iy}, N_{iz}) \cdot L(X_s, Y_s, Z_s)}{V} \tag{6.9.1}$$

When incorporating arrival times instead of travel times $t_i = T_i + t_0$ for master and slave, we obtain

$$\delta t_i = t_{is} - t_{im} = -\frac{N_i(N_{ix}, N_{iy}, N_{iz}) \cdot L(X_s, Y_s, Z_s)}{V} + (t_{0s} - t_{0m}), \tag{6.9.2}$$

what can be rewritten into a matrix form

$$\begin{pmatrix} \delta t_i \\ \vdots \end{pmatrix} = \begin{pmatrix} t_{is} - t_{im} \\ \vdots \end{pmatrix} = \begin{pmatrix} -\frac{N_{xi}}{V} & -\frac{N_{yi}}{V} & -\frac{N_{zi}}{V} & 1 \\ \vdots & \vdots & \vdots & \vdots \end{pmatrix} \begin{pmatrix} X_s \\ Y_s \\ Z_s \\ t_{0s} - t_{0m} \end{pmatrix}, \tag{6.9.3}$$

or

$$d_i = G_{ij} m_j \tag{6.9.4}$$

Data vector d_i is the vector of arrival time differences of master and slave δt_i for given phase on station i, sensitivity matrix G_{ij} is defined by the a priori known master-event location and seismic velocity V. m_j is the vector of $j = 4$ unknown components - three space components and one time difference between master and slave. Problem can be solved analytically as

$$m_j = (G_{ij}^T G_{ij})^{-1} G_{ij}^T d_i \tag{6.9.5}$$

The method can resolve relative locations of master- and slave-event even when the master location is not perfectly known. However, the master-slave distance is in trade-off relation with seismic velocity V. Different positions of relocated slaves may be equally good for different seismic velocities (Figure 6.15). The trade-off must be taken into account when interpreting the results.

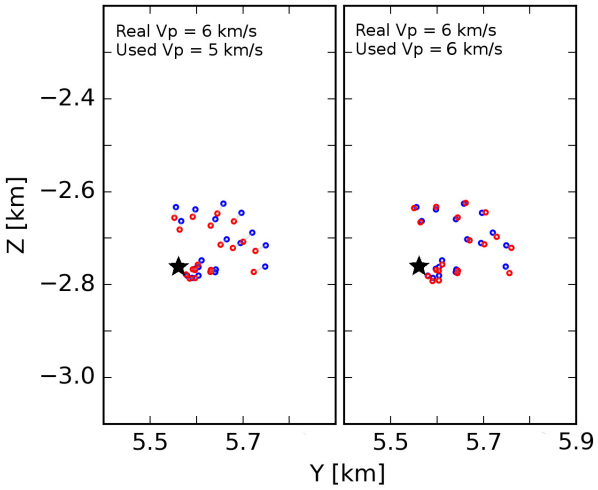

FIGURE 6.15: Relocation of synthetic dataset of shallow cluster only from P waves. Left: red relocations vs. blue real locations. The difference is due to a different V_P used during inversion. Right: the same situation but with correctly set V_P velocity. Both cases are equally good from mathematical point of view. All events were taken as slaves respecting the master - black star.

Master-event problem might be extended by the use of both, P- and S-wave arrivals. S-waves arrival time differences are inserted into the system of linear equations:

$$\begin{pmatrix} \delta t_i^P \\ \delta t_i^S \\ \vdots \end{pmatrix} = \begin{pmatrix} t_{is}^P - t_{im}^P \\ t_{is}^S - t_{im}^S \\ \vdots \end{pmatrix} = \begin{pmatrix} -\frac{N_{xi}^P}{V_P} & -\frac{N_{yi}^P}{V_P} & -\frac{N_{zi}^P}{V_P} & 1 \\ -\frac{N_{xi}^S}{V_S} & -\frac{N_{yi}^S}{V_S} & -\frac{N_{zi}^S}{V_S} & 1 \\ \vdots & \vdots & \vdots & \vdots \end{pmatrix} \begin{pmatrix} X_s \\ Y_s \\ Z_s \\ t_{0s} - t_{0m} \end{pmatrix}, \tag{6.9.6}$$

Different normal vectors $N_i^P(N_x i^P, N_y i^P, N_z i^P)$, $N_i^S(N_x^P, N_y^P, N_z^P)$ are simply respecting the fact, that for a given non-homogeneous velocity model the take-off angles of P and S-waves might differ.

If we have a pair of observations for each station - P- an S-wave arrival time differences, the method allows us to search for seismic velocities V_P and V_S. The trade-off relations disables estimating their values, but putting them into a problem together enables resolving their ratio - V_P/V_S.

- For a given (V_P, V_S) we relocate the slave (Eq. 6.9.5)

- For computed slave location we compute the synthetic differential times δt_i^{synt} on all stations.
- Station differences between $\delta t_i^{P,Ssynt}$ and $\delta t_i^{P,S}$ are computed in terms of L2 norm:

$$msft(V_P, V_S) = \sum_{i=1}^{N} (\delta t_i^{P,Ssynt} - \delta t_i^{P,S})^2, \tag{6.9.7}$$

  where i is the reading index and N is the number of readings (twice the number of stations).
- The process is repeated for various (V_P, V_S) combinations.
- Minimum of $msft(V_P, V_S)$ is searched and marks the best combination of V_P and V_S

For stabilizing the procedure a joint processing of a large amount of master-slave pairs is needed. Each (V_P, V_S) combination is tested for all possible event pairs and a joint misfit function is computed as:

$$msft(V_P, V_S) = \sum_{k=1}^{K} \frac{\sum_{i=1}^{N} (\delta t_i^{P,Ssynt} - \delta t_i P, S)^2}{N} \tag{6.9.8}$$

for K event pairs (master-slaves) indexed k. Misfit function for a dataset plotted in Figure 6.15 is plotted in Figure 6.16. Minimum is not sharp, and forms a valley with slope of V_P/V_S. V_P/V_S stays stable.

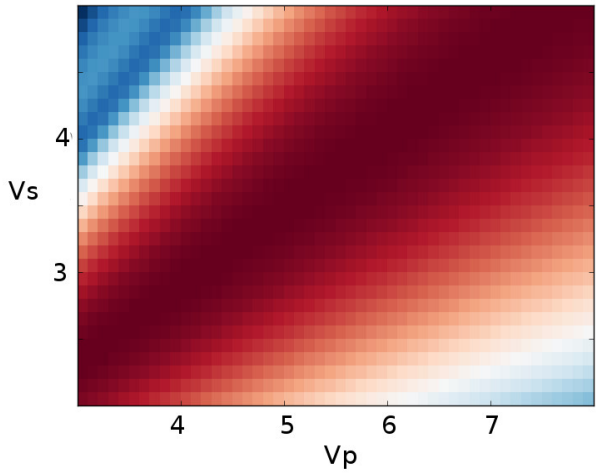

FIGURE 6.16: Misfit function $msft(V_P, V_S)$. Velocity ratio stays 1.78 as modeled, but estimation of a single velocities is impossible due to a trade-off with master-slave distances.

Apart from the double-difference Wadati method described earlier in this chapter, search for V_P/V_S using master-event does not require the assumption of identical take-off angles for P- and S-waves: $\phi_P =' phi_S$ and as a consequence $\delta l_P = \delta l_P$. However, the incorporation of another inversion (relocating) into an inversion itself brings complications reflected in worse robustness and misfit function is barely as clear as the one plotted. As a result, only clusters with a large number of event pairs with both P- and S-waves arrival time differences of high quality are analyzable. Waveform cross-correlation is the best and only option how to get data of appropriate quality.

We tested the method on the cluster one (Figures 6.8, 6.17) from 2014 activity and used available records from 16 stations of WEBNET and SXNET (Figure 2.5). We estimated the $V_P/V_S =$

1.54 ± 0.05. It is lower that estimated by the double-difference method Wadati method (1.59 ± 0.02) and lower then velocity model prediction (1.68, Málek, Horálek, and Jánský, 2005). Taking the errors into the account the result is in accordance with the observation by the double-difference Wadati method. It only confirms the fact that velocity ratio in this place or at this time was anomalously low.

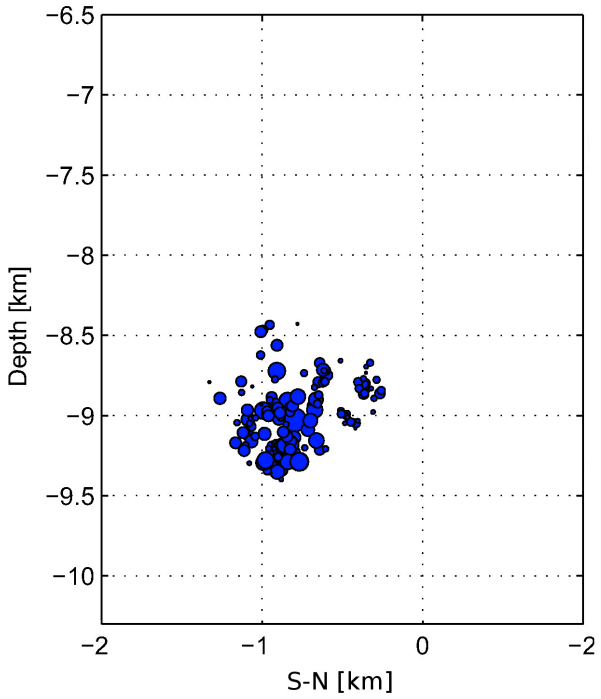

FIGURE 6.17: Cross-section of relocated West Bohemian earthquakes - cluster 1. Events lie on a 2-D plane. View from East to West. Estimated $V_P / V_S = 1.54$. Predicted by model - 1.68 (Málek, Horálek, and Jánský, 2005).

Estimating V_P / V_S using modified master-event technique was developed at Karlsruhe Institute for Technology in Karlsruhe, Germany, under the guidance of Emmanuel Gaucher. The work was funded by DAAD exchange agency.

Chapter 7

Included papers

Bachura, M. and T. Fischer (2016). "Coda attenuation analysis of the West Bohemia/Vogtland earthquake swarm area". In: *Pure and Applied Geophysiscs* 173, pp. 426-437.

URL: http://dx.doi.org/10.1007/s00024-015-1137-3 .

Bachura, M. and T. Fischer (2016). "Detailed velocity ratio mapping during the aftershock sequence as a tool to monitor the fluid activity within the fault plane." In: *Earth and Planetary Science Letters* 453, pp. 215-222.

URL: https://doi.org/10.1016/j.epsl.2016.08.017.

Hainzl, S. and Fischer, T. and Čermáková, H. and Bachura, M. and J. Vlček (2016). "Aftershocks triggered by fluid-intrusion: Evidence for the afterhosck sequence occured 2014 in West Bohemia/Vogtland". In: *Journal of Geophysical Research: Solid Earth* 121.

URL : http://dx.doi.org/10.1002/2015JB012582.

Bibliography

Abubakirov, I. and A. Gusev (1990). "Estimation of Scattering Properties of Lithosphere of Kamchatka Based on Monte-Carlo Simulation of Record Envelope of a Near Earthquake". In: *Physics of the Earth's and Planetary Interiors* 64, pp. 52–67. URL: https://doi.org/10.1016/0031-9201(90)90005-I.

Aki, K. (1980). "Attenuation of shear-waves in the litosphere for frequencies from 0.05 to 25 Hz". In: *Physics of the Earth's and Planetary Interiors* 21, pp. 50–60. URL: https://doi.org/10.1016/0031-9201(80)90019-9.

Aki, K. and B. Chouet (1975). "Origin of coda waves: Source, attenuation and scattering effects". In: *Journal of Geophysical Research* 80, pp. 3322–3342. URL: https://doi.org/10.1029/JB80i023p03322.

Aki, K. and M. Tsujiura (1959). "Correlation study of near earthquake waves". In: *Bulletin of Earthquake Research Institute at University of Tokyo* 37, pp. 207–232.

Alexandrakis, C. et al. (2014). "Velocity structure and role of fluids in the West Bohemia seismic zone". In: *Solid Earth* 5, pp. 863–872. URL: http://dx.doi.org/10.5194/se-5-863-2014.

Babuška, V., J. Plomerová, and T. Fischer (2007). "Intraplate seismicity in the western Bohemian Massif (central Europe): a possible correlation with a paleoplate junction". In: *Journal of Geodynamics* 44, pp. 149–159.

Bachura, M. and T. Fischer (2016a). "Coda attenuation analysis of the West Bohemia/Vogtland earthquake swarm area". In: *Pure and Applied Geophysiscs* 173, pp. 426–437. URL: http://dx.doi.org/10.1007/s00024-015-1137-3.

– (2016b). "Detailed velocity ratio mapping during the aftershock sequence as a tool to monitor the fluid activity within the fault plane." In: *Earth and Planetary Science Letters* 453, pp. 215–222. URL: https://doi.org/10.1016/j.epsl.2016.08.017.

Barton, N. (2007). *Rock Quality, Seismic Velocity, Attenuation and Anisotropy*. Taylor and Francis Group.

Bora, N. and R. Biswas (2017). "Quantifying Regional Body Wave Attenuation in a Seismic Prone Zone of Northeast India". In: *Pure and Applied Geophysics* 174, pp. 1953–1963. URL: https://doi.org/10.1007/s00024-017-1515-0.

Bouchaala, F., V. Vavryčuk, and T. Fischer (2013). "Accuracy of the master-event and double-difference locations: synthetic tests and application to seismicity in West Bohemia, Czech Republic". In: *Journal of Seismology* 17, pp. 841–859. URL: http://dx.doi.org/10.1007/s10950-013-9357-4.

Brauer, K. et al. (2003). "Isotropic evidence ($^3He/^4He$,$^{13}CCO_2$) of fluid-triggered intraplate seismicity". In: *Journal of Geophysical Research* 108, p. 2000. URL: http://dx.doi.org/10.1029/2002JB002077.

Calvet, M. and L. Margerin (2013). "Lapse-Time Dependence of Coda Q: Anisotropic Multiple-Scattering Models and Application to the Pyrenees". In: *Bulletin of Seismological Society of America* 103, pp. 1–16. URL: https://doi.org/10.1785/0120120239.

Carcolé, E. and H. Sato (2010). "Spatial distribution of scattering loss and intrinsic absorption of short-period S waves in the lithosphere of Japan on the basis of the Multiple Lapse Time Window Analysis of Hi-net data". In: *Geophysical Journal International* 180, pp. 268–290. URL: https://doi.org/10.1111/j.1365-246X.2009.04394.x.

Chandrasekhar (1960). *Radiative Transfer*. London, UK: Dover Publications.

Christensen, N.I. (1996). "Poisson's ratio and crustal seismology". In: *Journal of Geophysical Ressearch* 101, pp. 3139–3156. URL: http://dx.doi.org/10.1029/95JB03446.

Dahm, T. and T. Fischer (2014). "Velocity ratio variations in the source region of earthquake swarms in NW Bohemia obtained from travel time double-differences". In: *Geophysical Journal International* 196, pp. 957–970. URL: http://dx.doi.org/10.1093/gji/ggt410.

Dainty, A. et al. (1974). "Seismic scattering and shallow structure of the moon in Oceanus Procellarum". In: *The Moon* 9, pp. 11–29.

Davis, P.M. and R.W. Clayton (2013). "Application of the telegraph modelto codaQ variations in southern California," in: *Journal of Geophysical Research: Solid Earth* 112, B09302. URL: https://doi.org/10.1029/2006JB004542.

Del Pezzo, E., R. Allota, and D. Patané (1990). "Dependence of Q c (coda Q) on coda duration time interval: Model or depth effect?" In: *Bulletin of Seismological Society of America* 80, pp. 1028–1033.

Dominguez, L.A. and P.M. Davis (2013). "Seismic attenuation in the Middle America Region and the frequencydependence of intrinsic Q". In: *Journal of Geophysical Research: Solid Earth* 118, pp. 2164–2175. URL: https://doi.org/10.1002/jgrb.50163.

Farrokhi, M. and H. Hamzehloo (2017). "Body wave attenuation characteristics in the crust of Alborz region and North Central Iran". In: *Journal of Seismology* 21, pp. 631–646. URL: http://dx.doi.org/10.1007/s10950-016-9624-2.

Faul, U.H., J.D. Fitzgerald, and I. Jackson (2004). "Shear wave attenuationand dispersion in melt-bearing olivine polycrystals: 2. Microstructuralinterpretation and seismological implications". In: *Journal of Geophysical Research* 109, B06202. URL: https://doi.org/10.1029/2003JB002407.

Fehler, M. et al. (1992). "Separation of Scattering and Intrinsic Attenuation for the Kanto-Tokai Region, Japan, Using Measurements of S-wave Energy versus Hypocentral Distance". In: *Geophysical Journal International* 108, pp. 787–800. URL: https://doi.org/10.1111/j.1365-246X.1992.tb03470.x.

Fischer, T. (2003). "Automatic Location of Swarm Earthquakes from Local Network Data". In: *Studia Geophysica et Geodetica* 47, pp. 83–98. URL: http://dx.doi.org/10.1023/A:1022251605990.

Fischer, T. and M. Bachura (2014). "Detection capability of seismic network based on noise analysis and magnitude of completeness". In: *Journal of Seismology* 18, pp. 137–150. URL: http://dx.doi.org/10.1007/s10950-013-9407-y.

Fischer, T. and J. Horálek (2003). "Space-time distribution of earthquake swarms in the principal focal zone of the NW Bohemia/Vogtland seismoactive region: period 1985-2001". In: *Journal of Geodynamics* 35, pp. 125–144.

Fischer, T., C. Matyska, and J. Heinecke (2017). "Earthquake-enhanced permeability – evidence from carbon dioxide release following the ML 3.5 earthquake in West Bohemia". In: *Earth and Planetary Science Letters* 460, pp. 60–67. URL: http://dx.doi.org/10.1016/j.epsl.2016.12.001.

Fischer, T. et al. (2010). "The 2008 West Bohemia earthquake swarm in the light of the WEBNET network". In: *Journal of Seismology* 14, pp. 665–682. URL: http://dx.doi.org/10.1007/s10950-010-9189-4.

Fischer, T. et al. (2014). "Intra-continental earthquake swarms in West-Bohemia and Vogtland: A review". In: *Tectonophysics* 611, pp. 1–27. URL: http://dx.doi.org/10.1093/gji/ggt410.

Fitch, T. (1975). "Compressional velocity in source regions of deep earthquakes: an application of the master event technique". In: *Earth and Planetary Science Letters* 26, pp. 156–166. URL: http://dx.doi.org/10.1016/0012-821X(75)90083-7.

Frankel, A. and L. Wennerberg (1987). "Energy-flux Model of Seismic Coda: Separation of Scattering and Intrinsic Attenuation". In: *Bulletin of Seismological Society of America* 77, pp. 1223–1251.

Gaebler, P.J., T. Eulenfeld, and U. Wegler (2015). "Seismic scattering and absorption parameters in the W-Bohemia/Vogtland region from elastic and acoustic radiative transfer theory". In: *Geophysical Journal International* 203, pp. 1471–1481. URL: https://doi.org/10.1093/gji/ggv393.

Geiger, L. (1910). "Herbsetimmung bei Erdbeben aus den Ankunfzeiten". In: *Gesell. Wiss. Goettingen* 14, pp. 331–349.

– (1912). "Probability method for the determination of earthquake epicenters from the arrival time only". In: *Bulletin of St. Loius University* 8, pp. 60–71.

Gritto, R. and S.P. Jarpe (2014). "Temporal variation of Vp/Vs-ratio at The Geysers geothermal field,USA". In: *Geothermics* 52, pp. 112–119. URL: http://dx.doi.org/10.1016/j.geothermics.2014.01.012.

Gusev, A. and I. Abubakirov (1987). "Monte-Carlo simulation of record envelope of a near earthquake". In: *Physics of the Earth's and Planetary Interiors* 49, pp. 30–36. URL: https://doi.org/10.1016/0031-9201(87)90130-0.

Gusev, A.A. (1995). "Vertical Profile of Turbidity and Coda Q". In: *Geophysical Journal International* 123, pp. 665–672. URL: https://doi.org/10.1111/j.1365-246X.1995.tb06882.x.

Hainzl, S., T. Fischer, and T. Dahm (2012). "Seismicity-based estimation of the driving fluid pressure in the case of swarm activity in Western Bohemia". In: *Geophysiscal Journal International* 191, pp. 271–281. URL: http://dx.doi.org/10.1111/j.1365-246X.2012.05610.x.

Hainzl, S. et al. (2016). "Aftershocks triggered by fluid-intrusion: Evidence for the afterhosck sequence occured 2014 in West Bohemia/Vogtland". In: *Journal of Geophysical Research: Solid Earth* 121. URL: http://dx.doi.org/10.1002/2015JB012582.

Hasegawa, H.S. (1985). "Attenuation of Lg waves in the Canadian Shield". In: *Bulletin of Seismological Society of America* 75, pp. 1569–1582. URL: https://doi.org/10.1785/0120140259.

Havskov, J. et al. (2016). "Coda Q in Different Tectonics Areas, influence of Processing Parameters". In: *Bulletin of the Seismological Society of America* 106, pp. 956–970. URL: http://dx.doi.org/10.1785/0120150359.

Horálek, J. and T. Fischer (2008). "Role of crustal fluids in triggering the West Bohemia/Vogtland earthquake swarms: Just what we know (a review)". In: *Studia Geophysica et Geodetica* 52, pp. 455–471. URL: https://doi.org/10.1007/s11200-008-0032-0.

Horálek, J. and J. Šílený (2013). "Source mechanisms of the 2000 earthquake swarm in the West Bohemia/Vogtland region (Central Europe)". In: *Geophysical Journal International* 194, pp. 979–999. URL: https://doi.org/10.1093/gji/ggt138.

Hoshiba, M. (1995). "Estimation of nonisotropic scattering in western Japan using coda wave envelopes: Application of a multiple nonisotropic scattering model". In: *Journal of Geophysical Research* 100, pp. 645–657. URL: https://doi.org/10.1029/94JB02064.

Hrubcová, P. et al. (2013). "Moho depth determination from waveforms of microearthquakes in the West Bohemia/Vogtland swarm area". In: *Journal of Geophysical Research* 118, pp. 1–17. URL: https://doi.org/10.1029/2012JB009360.

Ito, A. (1985). "High resolution relative hypocenters of similar earthquakes by cross-spectral analysis method". In: *Journal of Physocs of the Earth* 33, pp. 279–294.

Jackson, I. and U.H. Faul (2010). "Grainsize-sensitive viscoelastic relax-ation in olivine: Towards a robust laboratory-based model for seis-mological application". In: *Physics of the Earth's and Planetary Interiors* 183, pp. 151–164. URL: https://doi.org/10.1016/j.pepi.2010.09.005.

Jakoubková, H., J. Horálek, and T. Fischer (2017). "2014 Mainshock-Aftershock Activity Versus Earthquake Swarms in West Bohemia, Czech Republic". In: *Journal of Seismology*. URL: http://dx.doi.org/10.1007/s00024-017-1679-7.

Kisslinger, C. and E. Engdahl (1973). "The interpretation of the Wadati diagram with relaxed assumptions". In: *Bulletin of Seismological Society of America* 63, pp. 1723–1736.

Knopoff, L. (1964). "Q". In: *Reviews of Geophysics* 2, pp. 625–660.

Konstantinou, K.I. et al. (2013). "Seismicity, Vp/Vs and shear wave anisotropy variations during the 2011 unrest at Santorini caldera, southern Aegean". In: *Journal of Volcanology and Geothermal Reaseach* 267, pp. 57–67. URL: http://dx.doi.org/10.1016/j.jvolgeores.2013.10.001.

Korn, M., S. Funke, and S. Wendt (2008). "Seismicity and seismotectonics of West Saxony, Germany — new insights from recent seismicity observed with the Saxonian seismic network". In: *Studia Geophysica et Geodaetica* 52, pp. 479–486. URL: https://doi.org/10.1007/s11200-008-0033-z.

Lay, T. and T.C. Wallace (1995). *Modetrn Global Seismology*. Cambridge Massetchussets, USA: Academic Press.

Leary, P. and R. Abercombie (1994). "Frequency dependent crustal scattering and absorption at 5-160 Hz from coda decay observed 2.5 km depth". In: *Geophysical Research Letters* 21, pp. 971–974. URL: https://doi.org/10.1029/94GL00977.

Lin, G. and P. Shearer (2007). "Estimation local Vp/Vs ratios within similar earthquake clusters". In: *Bulletin of the Seismological Society of America* 97, pp. 379–388. URL: http://dx.doi.org/10.1029/2009GL039098.

– (2009). "Evidcence of water-filled cracks in earthquake source regions". In: *Geophysical Research Letters* 36, p. L17315. URL: http://dx.doi.org/10.1785/0120060115.

Lomax, A. et al. (2000). *Probabilistic earthquake location in 3–D and leyered models in Advances in Seismic Event Location by Thurber, C.H. and Rabinowitz, N.* Springer Science and Business Media.

Majstorovic, J. et al. (2017). "Intrinsic and scattering attenuation of high-frequency S-waves in the central part of the External Dinarides". In: *Physics of the Earth's and Planetary Interiors* 270, pp. 73–83. URL: https://doi.org/10.1016/j.pepi.2017.06.005.

Margerin, L., M. Campillo, and N. Shapiro (1999). "Residence time ofdiff use waves in the crust as a physical interpretation of coda Q:Application to seismograms recorded in Mexico". In: *Geophysical Journal International* 138, pp. 343–352. URL: https://doi.org/10.1046/j.1365-246X.1999.00897.x.

Margerin, L., M. Campillo, and B. Van Tiggelen (2000). "Monte Carlo simulations of multiple scattering of elastic waves". In: *Journal of Geophysical Research* 105, pp. 7873–7892. URL: http://dx.doi.org/10.1029/1999JB900359.

Maurer, H. and N. Deichmann (1995). "Microearthquake cluster detection based on waveform similarities, with and application to the western Swiss Alps". In: *Geophysical Journal International* 123, pp. 588–600. URL: http://dx.doi.org/10.1111/j.1365-246X.1995.tb06873.x.

Mavko, G., M. Tapan, and J. Dvorkin (2003). *The Rock Physics Handbook: Tools for Seismic Analysis of Porous Media*. Cambridge University Press.

Mayor, J., L. Margerin, and M. Calvet (2014). "Sensitivity of coda waves to spatial variations of absorption and scattering: radiative transfer theory and 2-D examples". In: *Geophysical Journal International* 197, pp. 1117–1137. URL: https://doi.org/10.1093/gji/ggu046.

Mayor, J. et al. (2016). "Crustal structure of the Alps as seen by attenuation tomography". In: *Earth and Planetary Science Letters* 439, pp. 71–80. URL: https://doi.org/10.1016/j.epsl.2016.01.025.

Meirova, T. and V. Pinsky (2014). "Seismic wave attenuation in Israel region estimated from the multiple lapse time window analysis and S-wave coda decay rate". In: *Geophysical Journal International* 197, pp. 581–590. URL: https://doi.org/10.1093/gji/ggu005.

Michalek, J. and T. Fischer (2013). "Source parameters of the swarm earthquakes in West Bohemia/Vogtland". In: *Geophysical Journal International* 195, pp. 1196–1210. URL: https://doi.org/10.1093/gji/ggt286.

Michálek, J. and T. Fischer (2013). "Source parameters of the 2000-swarm earthquakes in West Bohemia/Vogtland determined in spectral domain". In: *Geophysical Journal International* 195, pp. 1196–1210. URL: https://doi.org/10.1093/gji/ggt286.

Mousavi, S. et al. (2015). "Seismic tomography reveals a mid-crustal intrusive body, fluid pathways and their relation to the earthquake swarms in West Bohemia/Vogtland". In: *Geophysical Journal International* 203, pp. 1113–1127. URL: http://dx.doi.org/10.1093/gji/ggv338.

Mousavi, S. et al. (2017). "Attenuation tomography in West Bohemia/Vogtland". In: *Tectonophysics* 695, pp. 64–75. URL: http://doi.org/10.1016/j.tecto.2016.12.010.

Mukhopadhyay, S. et al. (2008). "Lapse-time dependence of coda Q in the source region of the 1999 Chamoli earthquake". In: *Bulletin of Seismological Society of America* 98, pp. 2080–2086. URL: https://doi.org/10.1785/0120070258.

Muller, G. (1983). "Rheological properties and velocity dispersion of a medium with power-law dependence of Q on frequency". In: *Journal of Geophysics* 54, pp. 20–29.

Málek, J., J. Horálek, and J. Jánský (2005). "One-dimensional qP-wave velocity model of the upper crust for the West Bohemia/Vogtland earthquake swarm region". In: *Studia Geophysica et Geodetica* 49, pp. 501–524. URL: http://dx.doi.org/10.1007/s11200-005-0024-2.

Novotný, J., J. Málek, and J. Boušková (2016). "Wadati method as a simple tool to study seismically active fault zones: a case study from the West-Bohemia/Vogtlad region, central Europe". In: *Studia Geophysica et Geodynamica* 60, pp. 248–267. URL: http://dx.doi.org/10.1007/s11200-015-1206-1.

Novotný, O. (1995). "A preliminary seismic model for the region of the west-Bohemian earthquake swarms". In: *Studia Geophysica et Geodetica* 40, pp. 353–366.

O'Connell, R.J. and B. Budiansky (1974). "Seismic velocities in dry and saturated cracked solids". In: *Journal of Geophysical Research* 79, pp. 5412–5426. URL: http://dx.doi.org/10.1029/JB079i035p05412.

Paasschens, J. (1997). "Solution of the time-dependent Boltzmann equation". In: *Physical Reviews E* 56, pp. 1135–1141. URL: http://dx.doi.org/10.1103/PhysRevE.56.1135.

Padhy, S. and N. Subhadra (2004). "The Source-Scanning Algorithm: mapping the distribution of seismic sources in time and space". In: *Geophysical Journal International* 157, pp. 589–594. URL: https://doi.org/10.1111/j.1365-246X.2004.02276.x.

– (2013). "Separation of intrinsic and scattering seismic wave attenuation in Northeast India". In: *Geophysical Journal International* 195, pp. 1892–1903. URL: https://doi.org/10.1093/gji/ggt350.

Palo, M., F. Tilmann, and B. Schurr (2016). "Applicability and Bias of V-P/V-S Estimates by P and S Differential Arrival Times of Spatially Clustered Earthquakes". In: *Bulletin of the Seismological Society of America* 106, pp. 1055–1063. URL: http://dx.doi.org/10.1785/0120150300.

Poupinet, G. and W. Ellsworth (1984). "Monitoring velocity variations in the crust using earthquake doublets: and application to the Calaveras fault, California". In: *Journal of Geophysical Ressearch* 89, pp. 5719–5731. URL: http://dx.doi.org/10.1029/JB089iB07p05719.

Prudencio, J. et al. (2017). "Separation of scattering and intrinsic attenuation at Asama volcano (Japan): Evidence of high volcanic structural contrasts". In: *Journal of Volcanology and Geothermal Research* 333, pp. 96–103. URL: https://doi.org/10.1016/j.jvolgeores.2017.01.014.

Przybilla, J., M. Korn, and U. Wegler (2006). "Radiative transfer of elastic waves versus finite difference simulations in two-dimensional random media". In: *Journal of Geophysical Research* 111, pp. 1–13. URL: https://doi.org/10.1029/2005JB003952.

Rachman, A.N. et al. (2015). "Separation of Intrinsic and Scattering Attenuation Using Single Event Source in South Korea". In: *Bulletin of Seismological Society of America* 105, pp. 858–872. URL: https://doi.org/10.1785/0120140259.

Rautian, T.G. and V.I. Khalturin (1978). "The Use of the Coda for Determination of the Earthquake Source Spectrum". In: *Bulletin of Seismological Society of America* 68, pp. 923–948.

Rhyznik, L., G. Papanicolau, and J. Keller (1996). "Transport equations for elastic and other waves in random media". In: *Wave Motion* 24, pp. 327–370. URL: https://doi.org/10.1016/S0165-2125(96)00021-2.

Roecker, S.W. et al. (1982). "Estimates of Q in central Asia as a function of frequency and depth using the coda of locally recorded earthquakes". In: *Bulletin of Seismological Society of America* 72, pp. 129–149.

Rurner, J.A. and R.L. Weaver (1994). "Radiative transfer of ultrasound". In: *Journal of the Acoustical Society of America* 96, pp. 3654–3674. URL: http://dx.doi.org/10.1121/1.410586.

Ružek, B. and J. Horálek (2013). "Three dimensional seismic velocity model of the West Bohemia/Vogtland seismoactive region". In: *Geophysical Journal International* 195, pp. 1251–1266. URL: http://dx.doi.org/10.1093/gji/ggt295.

Saito, T., H. Sato, and M. Ohtake (2002). "Envelope broadening of spherically outgoing waves in three-dimensional random media having power law spectra". In: *Journal of Geophysical Research* 107, pp. 2089–2103. URL: http://dx.doi.org/10.1029/2001JB000264.

Sato, H. (1978). "Mean free path of S-waves under Kanto district of Japan". In: *Journal of Physics of Earth* 26, pp. 185–198.

– (1989). "Broadening of seismogram envelopes in the randomly inhomogeneous lithosphere based on the parabolic approximation: Southeastern Honshu, Japan". In: *Journal of Geophysical Research* 94, pp. 17735–17747. URL: http://dx.doi.org/10.1029/JB094iB12p17735.

Sato, H., M. Fehler, and T. Mayeda (2012). *Seismic Wave Propagation and Scattering in the Heterogeneous Earth*. Verlag Berlin Heidelberg, Germany: Springer.

Scherbaum, F. and J. Wendler (1986). "Cross spectral analysis of Swabian Jura (SW Germany) three-component microearthquake recordings". In: *Journal of Geophysiscs* 60, pp. 157–166.

Shapiro, N.M. et al. (2000). "The energy partitioning and the diffusive character of the seismic coda". In: *Bulletin of Seismological Society of America* 90, pp. 655–665. URL: https://doi.org/10.1785/0119990021.

Shearer, P. (1999). *Introduction to seismology*. Cambridge University Press.

Singh, C. et al. (2017). "Relative role of intrinsic and scattering attenuation beneath the Andaman Islands, India and tectonic implications". In: *Physics of the Earth's and Planetary Interiors* 271, pp. 19–28. URL: https://doi.org/10.1016/j.pepi.2017.08.002.

Stein, S. and M. Wysession (2003). *An Introduction to Seismology, Earthquakes and Earth Structure*. Haboken New Jersey, USA: Blackwell Publishing.

Stoddard, P. and M. Woods (1990). "Master event relocation of Gorda Block earthquakes: Implications for deformation". In: *Geophysical Resaerch Letters* 17, pp. 961–964. URL: http://dx.doi.org/10.1029/GL017i007p00961.

Tselentis, G.A. (1993). "Depth-dependent seismic attenuation in western Greece". In: *Tectonophysics* 225, pp. 523–528. URL: https://doi.org/10.1016/0040-1951(93)90313-9.

Tsujiura, M. (1978). "Spectral analysis of the coda waves from local earthquakes". In: *Bulletin of Earthquake Research Institute at University of Tokyo* 53, pp. 1–48.

Ugalde, A. and E Carcolé (2009). "Comments on "Separation of Qi and Qs from passive data at Mt. Vesuvius: A reappraisal of the seismic attenuation estimates"by E. Del Pezzo et al. (2006)". In: *Physics of the Earth's and Planetary Interiors* 173, pp. 191–194. URL: https://doi.org/10.1016/j.pepi.2008.10.001.

Vavryčuk, V. (2011). "Principal earthquakes: theory and observations from the 2008 West Bohemia swarm". In: *Earth and Planetary Science Letters* 305, pp. 290–296. URL: http://dx.doi.org/10.1016/j.epsl.2011.03.002.

Vavryčuk, V. et al. (2017). "Moment tensor inversion based on the principal component analysis of waveforms: Method and application to microearthquakes in West Bohemia, Czech Republic". In: *Seismological research letters* 88, pp. 1303–1315. URL: https://doi.org/10.1785/0220170027.

Wadati, K. (1928). "Shallow and deep earthquakes". In: *Geophysiscs and Magnetism* 1, pp. 162–202.

Wagner, G.A. et al. (1997). "Post-Variscan thermal and tectonic evolution of the KTB site and its surroundings". In: *Journal of Geophysical Research* 102, pp. 18221–18232. URL: http://dx.doi.org/10.1029/96JB02565.

Waldhauser, F. and W.L. Ellsworth (2000). "A double-difference earthquake location algorithm: method and application to the Northern Hayward Fault, California". In: *Bulletin of the Seismological Society of America* 90, pp. 1353–1368. URL: http://dx.doi.org/10.1785/0120000006.

Walsch, J.B. (1969). "New analysis of attenuation in partially melted rock". In: *Journal of Geophysical Research* 74, pp. 4333–4337. URL: http://dx.doi.org/10.1029/JB074i017p04333.

Weaver, R.L. (1990). "Diffusivity of Ultrasound in Polycrystals". In: *Journal of the Mechanics and Physics of Solids* 38, pp. 55–86. URL: https://doi.org/10.1016/0022-5096(90)90021-U.

Wegler, U., M. Korn, and J. Przybilla (2006). "Modeling full seismogram envelopes using radiative transfer theory with Born scattering coefficients". In: *Pure and Applied Geophysics* 163, pp. 503–531. URL: https://doi.org/10.1007/s00024-005-0027-5.

Wegler, U. and B.G. Luhr (2001). "Scattering behaviour at Merapi volcano (Java) revealed from active seismic experiment". In: *Geophysical Journal International* 145, pp. 579–592. URL: https://doi.org/10.1046/j.1365-246x.2001.01390.x.

Wu, R. (1985). "Multiple scattering and energy transfer of seismic waves — separation of scattering effect from intrinsic attenuation — I. Theoretical modelling". In: *Geophysical Journal International* 82, pp. 57–80. URL: https://doi.org/10.1111/j.1365-246X.1985.tb05128.x.

Yoshimoto, K., H. Sato, and M. Ohtake (1993). "Frequency dependent attenuation of P and S waves in the Kanto area, japan, based on the coda normalization method". In: *Geophysical Journal International* 114, pp. 165–174. URL: https://doi.org/10.1111/j1365-246X.1993.tb01476.x.

Zeng, Y. (1993). "Theory of scattered P- and S-wave energy in a random isotropic scattering medium". In: *Bulletin of Seismological Society of America* 83, pp. 1264–1276.

Zeng, Y., F. Su, and K. Aki (1991). "Scattering Wave Energy Propagation in a Random Isotropic scattering Medium 1. Theory". In: *Journal of Geophysical Research* 96, pp. 607–619. URL: http://dx.doi.org/10.1029/90JB02012.

Zhang, F. and S. Papageorgiou (2010). "Attenuation Characteristics of Taiwan: Estimation of Coda Q, S-wave Q, Scattering Q, Intrinsic Q, and Scattering Coefficient". In: *Seismological Research Letters* 81, pp. 769–777. URL: https://doi.org/10.1785/gssrl.81.5.769.

Zhang, H. and C.H. Thurber (2003). "Double-difference tomography: the method and its application to the Hayward fault, California". In: *Bulletin of Seismological Society of America* 93, pp. 1175–1189. URL: http://dx.doi.org/10.1785/0120020190.

Čermáková, H. and J. Horálek (2015). "The 2011 West Bohemia (Central Europe) earthquake swarm compared with the previous swarms of 2000 and 2008". In: *Journal of Seismology* 19, pp. 899–913. URL: http://dx.doi.org/10.1007/s10950-015-9502-3.

Pure Appl. Geophys. 173 (2016), 425–437

DOI 10.1007/s00024-015-1137-3

Pure and Applied Geophysics

Coda Attenuation Analysis in the West Bohemia/Vogtland Earthquake Swarm Area

Martin Bachura[1] and Tomáš Fischer[1,2]

Abstract—Seismic coda represents a valuable source of information about the attenuation of the high-frequency waves in the studied region. The quality factor Q derived from coda is an integral parameter of the volume surrounding the hypocenter and seismic station and, according to the applied method, represents the total attenuation or the intrinsic and scattering parts. We analyzed records of 13 selected earthquakes in the magnitude range 1.7–2.9 of the 2011 swarm from West Bohemian/Vogtland area (central Europe), which were recorded at epicentral distances from 7 to 50 km. Two methods were applied: coda method for estimation of the Q_c and the Multiple Lapse Time Windows Analysis for separation of the scattering and intrinsic loss by estimation of Q_i and Q_{sc}. Careful selection of the analyzed events was necessary due to the frequent contamination of coda decays by the running seismic swarm activity. The resulting coda Q_c is relatively high with respect to the geodynamic activity and varies between 100 and 2500 within the analyzed frequency range of 1–18 Hz. The intrinsic loss dominates over scattering attenuation with Q_i increasing from 100 and 1850 and Q_{sc} from 300 to 3400 in the same frequency range, which is consistent with the geodynamic activity of the region. We find that the intrinsic attenuation in West-Bohemia/Vogtland is higher that in neighboring Germany, which could be attributed to the heterogeneity of the crust in central Europe.

Key words: Coda, attenuation, Q, scattering, intrinsic loss, West Bohemia.

1. Introduction

Information on seismic wave attenuation is useful for investigations of the Earth's structure, seismic source characteristics, and seismic wave propagation studies. Attenuation can be expressed by a dimensionless quality factor Q (e.g. Knopoff and MacDonald 1958), respectively, by its inverse Q^{-1} representing seismic attenuation.

Currently, many methods have been developed to estimate attenuation properties of the medium from seismograms by studying the direct waves or coda waves. Each approach has its advantages and disadvantages. Direct wave analysis brings very local information about total attenuation within an exactly specified area, while the coda analysis somehow extracts global information. Advantage of the coda approach is that precise locations, stations distribution, source parameters, and velocity model has minimal impacts on the results (depends on the method), while for the direct wave analysis of these parameters—especially locations and station positions strongly affect the possibilities of the analysis. The purpose of this work was to adopt the coda approach and apply different coda methods to derive the attenuation parameters of the crust in the area of West Bohemia/Vogtland, where no similar research has been provided yet.

First studies by Aki and Chouet (1975) analyzed the decay rate and shape of coda to estimate coda quality factor Q_c using simple algebra-exponential equation:

$$A(f,t) = S(f)t^{-m}\mathrm{e}^{(\pi ft/Q_c(f))}, \qquad (1)$$

where $A(f,t)$ is the coda amplitude in the seismogram for a narrow bandwidth signal with central frequency f as a function of lapse time t. $S(f)$ represents coda source factor at frequency f, the term t^{-m} represents geometrical spreading; m is exponent describing the waves propagation regime—1 for single backscattering model and 0.75 for diffusion model (see below).

Aki and Chouet (1975) proposed two physical models describing the propagation of the coda waves: single backscattering model and diffusion model.

[1] Faculty of Science, Charles University in Prague, Prague, Czech Republic. E-mail: martin.bachura@natur.cuni.cz; fischer@natur.cuni.cz

[2] Institute of Geophysics, Academy of Sciences, Prague, Czech Republic.

Single backscattering model assumes that waves are backscattered only once (Born approximation) and heterogeneities are distributed randomly and uniformly within the ellipsoidal area with foci in the hypocenter and receiver inhomogeneous half-space. Size and volume of the ellipsoid are given by the selected length of the studied lapse time window (with increasing lapse time window length the volume increases). Resulting Q_c then reflects both—intrinsic loss Q_i and scattering Q_{sc} quality factors:

$$Q_c^{-1} = Q_i^{-1} + Q_{sc}^{-1} \quad (2)$$

Use of the model itself does not allow us to separate these two attenuation mechanisms.

The diffusion model represents the end-member case of multiple scattering. It assumes that seismic waves propagate in the diffusive regime and are attenuated only by intrinsic loss. Resulting Q_c then reflects only intrinsic Q_i (Aki and Chouet 1975; Shapiro *et al.* 2000):

$$Q_c = Q_i \quad (3)$$

The value of exponent m in Eq. (1) is then 1 for single-scattering and 1.5 for diffusion model and is fixed a priori during the analysis—the equation itself does not allow to distinguish the more suitable model. Different model selection using different m of 1 or 0.75 results in Q_c values differing only by ± 10 % (Calvet and Margerin 2013) and, therefore, does not play the key role in the Q_c estimation.

Both single-scattering and diffusion are valid physical models that predict the observed decay, but imply different physical interpretations of Q_c. Early coda studies primarily used the single-backscattering model for homogeneous half-space with Q_c having been estimated in geological regions worldwide. This method was favored by the authors. It was found that Q_c is high in seismically stable areas and that Q_c is not independent on the lapse time in coda—attenuation generally decreases with lapse time (e.g. Rautian and Khalturin 1978; Roecker and Hatzfeld 1982; Tselentis 1993; Mukhopadhyay and Kayal 2008). This dependence was discussed and interpreted by Rautian and Khalturin (1978) in the terms of a single backscattering model—as a spatial decrease of the attenuation properties of the Earth with depth. Further research development of this idea was carried out by Gusev (1995) who developed a stratified model of scattering properties in the lithosphere. On the other hand, Del Pezzo *et al.* (1990) pointed out that the increase of Q_c with lapse time may be simply caused by the inability of Eq. (1) to describe the full complexity of the attenuation process in the Earth.

Isotropic single backscattering works properly when fitting the coda envelopes to the later parts of coda, but generally does not work when fitting the early coda at short lapse times (e.g. Gusev and Abubakirov 1987; Hoshiba 1995; Calvet and Margerin 2013). Due to these shortcomings new models implying multiple scattering and anisotropy have been developed (Sato 1989; Saito *et al.* 2002; Calvet and Margerin 2013).

In recent decades the role of the single scattering has been replaced by the idea of multiple scattering (e.g. Wu 1985; Gusev and Abubakirov 1987; Frankel and Wennerberg 1987; Abubakirov and Gusev 1990). Radiation transfer theory was introduced to seismology (Hoshiba 1991) and developed by other authors (e.g. Zeng *et al.* 1991; Paasschens 1997). Radiative transfer equation for energy density describes the generation and propagation of the scattered seismic energy in time and space. Due to computational complexities of the radiative transfer equation for the elastic waves (Ugalde and Carcole 2009), two approximate solutions have been proposed: Zengs *et al.* (1991) and Paasschens' (1997)—both solutions are described in the Sect. 4. These two solutions along with Hoshibas' (1991) numerical models form the theoretical background of the methods studying the contribution of intrinsic loss and scattering. The most frequently used among these methods is *M*ultiple *L*apse *T*ime *W*indows *A*nalysis (MLTWA—described in 4) proposed by Fehler *et al.* (1992).

All these models assume homogeneous distribution of isotropic scatterers with a constant background velocity and contrary to Eq. (1) allow authors to estimate the total Q_t as the sum of the intrinsic loss and scattering:

$$Q_t^{-1} = Q_i^{-1} + Q_{sc}^{-1} \quad (4)$$

Previous models have used acoustic approximation. Derivation of elastic radiative transfer theory equation taking into account the wave polarization and mode conversion between P and S waves was

done by, e.g. Weaver (1990), Papanicolaou *et al.* (1996).

Implementation of the multiple scattering brought also a new insight to the interpretation of the Q_c. Shapiro *et al.* (2000) showed that the wave field at later lapse times enters a diffusive regime which can be described by asymptotic approximation of diffusive wave field in simple uniform half space. Therefore, Q_c is estimated from later coda which is equal to Q_i. The same result, $Q_i = Q_c$ but at longer lapse times, was acknowledged by Calvet and Margerin (2013) using anisotropic multiple scattering model for the Pyrenees.

Margerin *et al.* (1998) also studied the effect of Mohorovicic discontinuity on the form of coda envelopes. By solving the radiative transfer equations in a model containing a heterogeneous layer overlaying a transparent half-space, they found that at higher frequencies (>10 Hz) Q_c is dominated by intrinsic absorption in the crust. At lower frequencies around 1 Hz leakage of the diffuse energy in the mantle can dominate the data. Thus, at frequencies around 1 Hz, Q_c depends strongly on the mean free path of the seismic waves in the crust and crustal thickness. Q_c at low frequencies is, therefore, expected to have strong regional variations due to the heterogeneity of the crust and its thickness.

The purpose of this paper was to apply different coda analyzing methods to derive attenuation parameters (Q_c of coda waves attenuation and Q_i and Q_{sc} for intrinsic loss and scattering) of the crust in the West Bohemian seismo-active area. We have interpreted these results in terms of the discussed recent theoretical background to provide physically acceptable quality factors for other seismology disciplines studying the region, like seismic source dynamics, wave propagation studies, etc.

2. Geodynamic and Tectonic Settings

West Bohemia/Vogtland area is located at the intersection of two tectonic structures: ENE-WSW striking Eger Rift and N-S striking Regensburg–Leipzig–Rostock Zone. The Regensburg–Leipzig–Rostock Zone is seismically active in its middle (Bankwitz *et al.* 2003) and delimited from the east by the ~100 km long Mariánské Lázně Fault striking NNW-SSE. The intersection area is covered by 300 m of tertiary sediments from Cheb Basin. The Mariánské Lázně fault intersects the main area of seismic activity beneath Nový Kostel, where more than 80 % of seismic energy was released within the past 25 years (Fischer and Michálek 2008). The hypocenters in the Nový Kostel focal zone align in a N-S prolonged, steeply dipping zone 12 km in length, with depths ranging from 6 to 11 km, and striking 170°. Apart from seismic swarms, other geodynamic activity includes the Quaternary volcanoes Komorní Hůrka and Železná Hůrka, CO_2 rich mineral springs, and hydrothermal vents.

Seismic activity is strongly related to the occurrence of earthquake swarms. Most activity in the past 30 years has been associated with the Nový Kostel focal zone. During the past 30 years, 6 earthquake swarms with maximum magnitudes exceeding M_L 3 have occurred: in 1985/1986 (maximum M_L of 4.6), 1997, 2000, 2008, 2011 and the most recent 2014 with maximum M_L of 4.5. Swarms usually last from weeks to few months with thousands of events occurring. The earthquakes are assumed to be triggered by high-pressure crustal fluids (Horálek and Fischer 2008).

3. Data

Monitoring of earthquake activity in West Bohemia/Vogtland area is carried out by the WEBNET seismic network operated by the Institute of Geophysics of Academy of Sciences of the Czech Republic in Prague. It consists of 13 permanent and 10 temporary stations (Fischer *et al.* 2010). Stations provided three-component continuous data with sampling frequency of 250 sps. Stations were equipped with seismometers SM-3 or Guralp 40-T and produced velocigrams in a frequency band of at least 0.5–60 Hz with the dynamic range exceeding 120 dB. The broader seismic region is monitored by Saxonian network (SXNET) (Korn *et al.* 2008) operated by the Institute for Geophysics and Geology in University of Leipzig (sampling frequency 100 sps). For data analysis we used records from 7 WEBNET stations and 4 SXNET stations (Fig. 1).

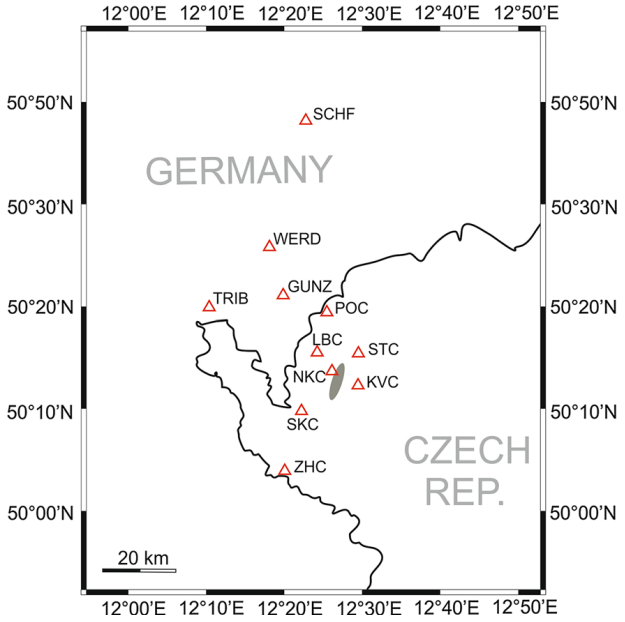

Figure 1
Map of the studied area—*red triangles* represent stations used in this study, and *grey ellipse* near NKC station shows the Nový Kostel focal zone

Seismograms were selected from the 2011 earthquake swarm. We used 13 events recorded on 10 stations (11 stations for MLTWA) with M_L from 1.7 to 2.9 and hypocentral distances ranging from 7 to 26 km (50 km for MLTWA). Focal depths ranged from 8 to 9 km.

4. Data Processing

4.1. Coda Method

Taking the natural logarithm of Eq. (1) and choosing $m = 0.75$ to account for diffusion modeling leads to

$$\ln(A(f,t)t^{0.75}) = \ln(S(f) - (\pi ft/Q_c(f))), \quad (5)$$

where $Q_c(f)$ can be determined by a linear regression of Eq. (5) and solved for the slope b:

$$Q_c(f) = -\pi f/b \quad (6)$$

By applying Eqs. (5) and (6) on the selected parts of coda signal (trimmed coda windows) we can directly estimate Q_c. To remove the codas disturbed by aftershocks, only cross-correlation coefficient higher than 0.95 was accepted.

Frequency dependence of Q_c can be expressed by the power law as

$$Q_c = Q_0 f^n \quad (7)$$

Individual steps of the data processing are shown in Fig. 2. Waveforms with *S*/*N* ratio greater than 3 were analyzed. Since the shapes of S-wave coda of vertical and horizontal components of small earthquakes are approximately similar (Sato and Fehler 1998), only the vertical component was used for this analysis. Seismograms were filtered on central frequencies of 1.5, 3, 6, 9, 12, 18 and 24 Hz with bandwidths of 1, 2, 4, 6, 8, 12 and 16 Hz using the 3-pole Butterworth filter. Coda envelopes of the seismograms were computed as an instantaneous amplitude (modulus of the analytical signal).

The crucial part of using the coda method is the selection of the lapse time window length and starting time of the measurement. A traditional approach is to start at the double S-wave travel time and analyze lapse time windows of different lengths. This approach has its limitations, especially in the cases of short hypocentral distances up to 50 km. Calvet and Margerin (2013) showed that using double S—wave travel time as the starting time of the studied time windows, causes strong hypocentral distance dependence of the resulting Q_c. This dependence reflects the fact that at the shorter distances (for station NKC it is 7 km) the coda window starts right after the ballistic S—wave front where the decay of the coda is fastest, while at larger distance (at the station ZHC it is 26 km) the analysis starts well after the passage of the ballistic front and presumably samples multiple-scattered waves. Analyzing the later lapse times fulfils the assumption that all scattered coda waves recorded by all stations are equally multiple scattered and propagate in the diffusive regime. Therefore, the energy is homogeneously distributed within the studied area.

The selection of the lapse time window length does influence the stability of results and noise effects. Using shorter windows (up to 20 s) brought problems with unstable line fitting, while using longer windows (up to 50 s) produced strong noise influence to the later part of the coda.

We tested the different Q_c window lengths (from 10 to 50 s) and different starting times for Q_c

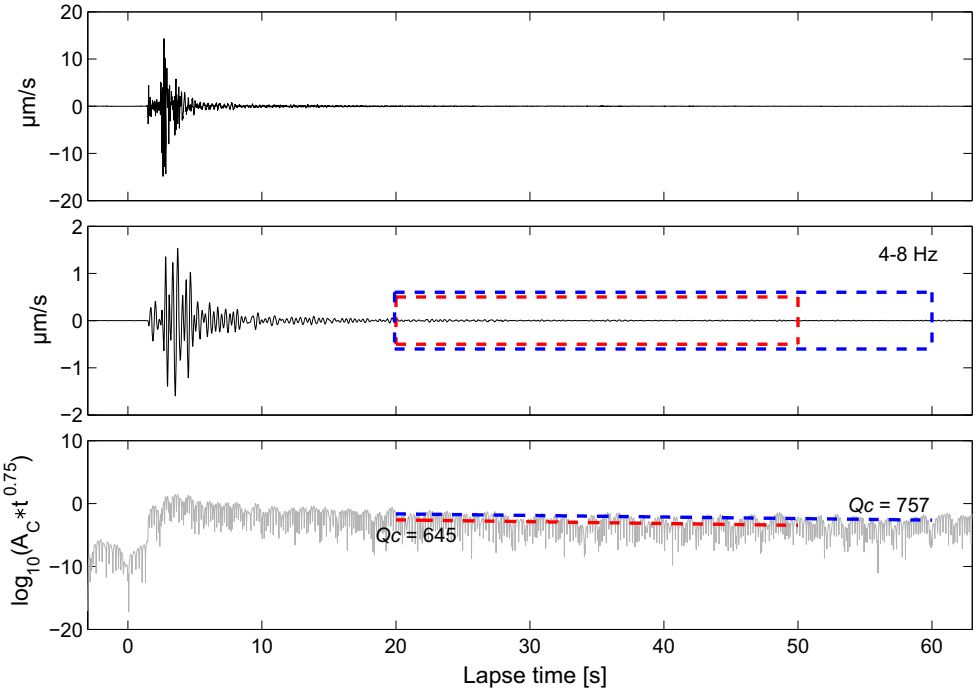

Figure 2
Data processing of the coda method—from *top*: raw data (Z-component), filtered data with selected lapse windows of length 30 and 40 s starting at $t = 20$ s after the origin time, linear regression of the processed data in selected lapse time windows

determination with respect to the stability of linear fit, *S/N* ratio, overall shape of the coda, and ballistic wavefront. Accordingly, two window lengths of both 30 and 40 s and a starting time at 20 s after the origin time were found optimum. The selected starting time is still far behind the S arrivals, even at the farthest stations (S wave travel time at ZHC is 6–7 s).

We analyzed every event and station combination separately. Finally, we computed the resulting Q_c as a mean of every computed Q_c with standard deviation as an error. Our Q_c represents the average over the regional area mapped by selected WEBNET and SXNET stations.

4.2. *Multiple Lapse Time Window Analysis (MLTWA)*

Multiple lapse time windows analysis was first introduced by Fehler *et al.* (1992). It uses approximate solutions to the radiative transfer equation to model the synthetic seismograms for comparison with observed data. There are two approximate solutions: Zengs' hybrid single scattering diffusion solution (Eqs. (8)–(9)) and Paasschens' solution (Eqs. (10)–(11)):

$$E(r,t) \approx E_0 e^{\eta v t}\left[\delta\left(\frac{(t-r/v)}{4\pi r v^2}\right) + \eta_s H \frac{(t-r/v)}{4\pi v r t}\ln\frac{1+r/vt}{1-r/vt}\right] + cH(t-r/v)\left(\frac{3\eta_{sc}}{4\pi v t}\right)^{1.5} e^{3\eta_{sc} r^2/4vt - \eta_i v t} \tag{8}$$

$$c = E_0 \frac{[1-(1+\eta_{sc} v t)e^{-\eta_{sc} v t}]}{\frac{r}{\pi}\int_0^{\sqrt{3\eta_{sc} v t}/2} e^{-\alpha^2}\alpha^2 d\alpha}, \quad \alpha = \frac{vt}{r} \tag{9}$$

$$E(r,t) \approx E_0 \frac{e^{-\eta v t}}{4\pi r^2 v}\delta\left(t-\frac{r}{v}\right) + E_0 H\left(t-\frac{r}{v}\right)\frac{(1-r^2/v^2t^2)^{1/8}}{(4\pi v t/3\eta B_0)^{3/2}} e^{-\eta v t} \times G\left(v t \eta B_0 (1-\frac{r^2}{v^2 t^2})^{0.75}\right) \tag{10}$$

$$G(x) \approx e^x \sqrt{1+2.026/x} \tag{11}$$

where E_0 is the energy at $t = 0$, t is the lapse time from the origin, r is the hypocentral distance, v is the shear wave velocity, H is Heaviside function, δ is

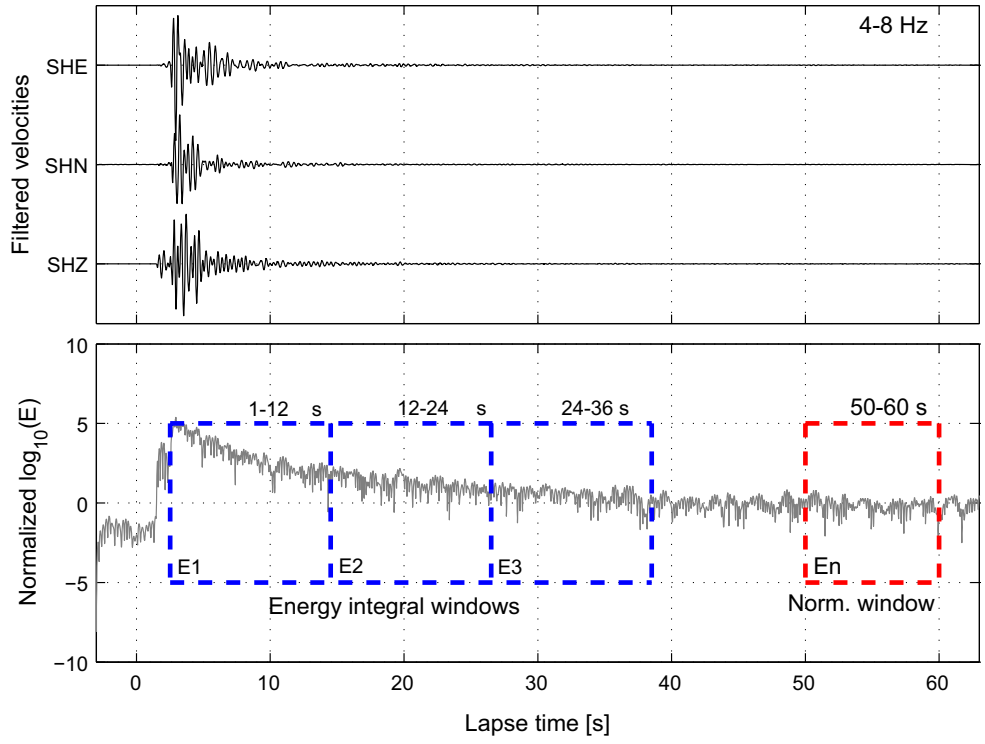

Figure 3
Data processing in the MLTWA. *Top* filtered 3-component record. *Bottom* sum of the energies with three consecutive windows starting at the S-arrival (*blue*) and reference coda window (*red*) for normalization starting at 50 s after origin time and 10 s long

delta function, $\eta_i = \frac{2\pi f}{vQ_i}$ is intrinsic attenuation coefficient, $\eta_{sc} = \frac{2\pi f}{vQ_{sc}}$ is scattering attenuation coefficient (often marked as g_0), $\eta = \eta_i + \eta_{sc}$ is total attenuation coefficient (or so-called extinction length inverse Le^{-1}), and B_0 is seismic albedo $B_0 = \eta_{sc}/\eta$. An alternative parameter describing the scattering properties is the mean free path $l = \eta_{sc}^{-1}$ – inverse of scattering coefficient. Based on trials and tests we adopted Zengs' solution (discussed in Sect. 6).

For successful application of MLTWA on our data, 3-component seismograms of earthquakes in wide range of hypocentral distances are essential (with uniform distribution). Our dataset contains one tight cluster of events with stations scattered around at different distances allowed us to work with non-uniformly distributed hypocentral distances in the extent of 15–50 km. We reduced the number of the frequent near records <15 km in order to not suppress the weight of the farther records on the results.

Processing MLTWA is shown in Fig. 3. We estimated Q_i and Q_{sc} in the same frequency bands as in the coda method. Energy envelopes were computed as the squares of the smoothed band-pass filtered data of each component.

To compare different events each coda is normalized by the amplitudes of their later coda portions. This is based on the fact that at later lapse times the coda energy is homogeneously distributed, so the coda amplitude is then only controlled by the source and station constants only (Aki 1980). A normalizing factor was then computed as the mean of coda energy in a reference interval between 50 and 60 s after the origin time. The whole seismogram is then normalized as

$$En_i^{obs} = Ec_i^{obs}/E_i^{ref}, \quad i = 1\ldots3, \tag{12}$$

where En_i^{obs} is the normalized observed energy for ith component, Ec_i^{obs} is the observed coda energy for ith component, and E_i^{ref} is the normalizing factor for each component.

After normalizing, the sum of the energies of single components (13) is trimmed into three consecutive lapse time windows of chosen length starting at the S wave arrival time (14) and then integrated.

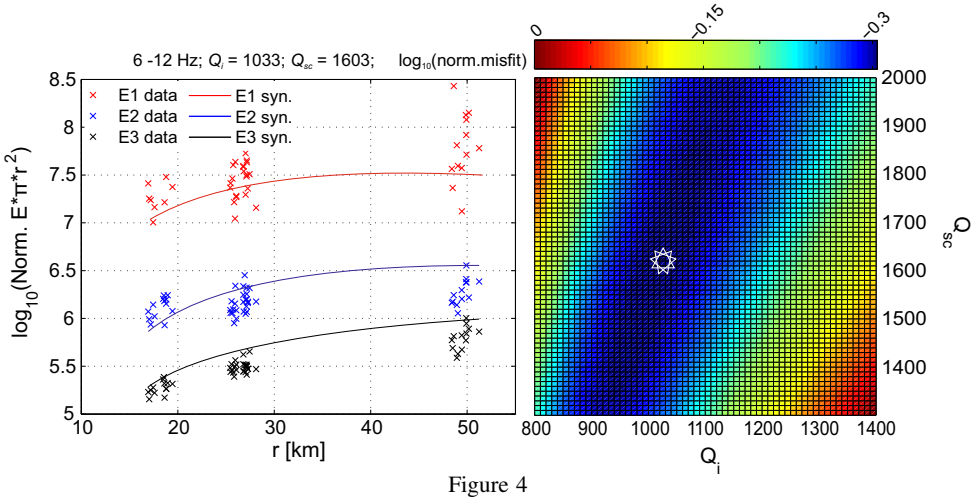

Figure 4

Comparison of synthetic (*lines*) and observed (*crosses*) data: *Left plot* is in the terms of misfit function (Eq. (15)), *right plot* is the normalized $\log_{10}$ of the normalized misfit function. *Red ellipse* represents the Q_i, Q_{sc} combination within the 95 % confidence region. *White star* shows the minimal residual

$$E^{\text{obs}} = \sum_{i=1}^{3} En_i^{\text{obs}} \tag{13}$$

$$E_1^d = \int_{t_1}^{t_2} E^{\text{obs}}, \quad E_2^d = \int_{t_2}^{t_3} E^{\text{obs}}, \quad E_3^d = \int_{t_3}^{t_4} E^{\text{obs}} \tag{14}$$

Windows with lengths of 12 s were chosen and used for analysis. Three consecutive 12 s windows were optimal for the length of our codas.

Finally, the three energy integrals E_i^d are corrected for the hypocentral distance (multiplying by $4\pi r^2$) and plotted against hypocentral distance. A similar approach is then applied to synthetic coda energy envelopes modeled using Eqs. (8) and (9) with input parameters Q_i, Q_{sc}, f, and r. By choosing regular spacing of hypocentral distances we obtain a line plot of synthetic envelope integrals (Fig. 4).

Finally, the best fit between synthetic curves and scattered data points for a selected central frequency f is searched using a misfit function:

$$M(Q_i, Q_{sc}) = \sum_{k=1}^{N} \sum_{i=1}^{3} w_i (\log_{10} E_i^d(r_k) - \log_{10} E_i^{\text{syn}}(r_k))^2, \; i = 1\ldots3, k = 1\ldots N, \tag{15}$$

where N is the number of recordings of single event station combinations on unique hypocentral distance. Weighting term w_i is used to increase the weight of the integrated windows E_2 and E_3, since they do not contain the ballistic wave front and, therefore, are not influenced by the source radiation characteristics. This results in lower scatter of the plot points. In our case, $w_i = (0.5, 1, 1)$ was selected for the analysis. The best solution for Q_i and Q_{sc} (minimum of Eq. (15)) was searched using the simplex optimization algorithm.

For every resulting pair of Q_i and Q_{sc} we estimated 95 % confidence region within the misfit function to evaluate the errors.

After the estimation of Q_i, Q_{sc} and their errors we computed the total quality factor Q_t (or total attenuation Q_t^{-1}) as pointed in Eq. (4).

5. Results

5.1. Coda Method

Resulting frequency dependences of Q_c for time windows of lengths 30 and 40 s starting 20 s after origin time are shown in Fig. 5. Three main differences are visible between the time window lengths: the overall values of Q_c are higher for 40 s window (despite the values being within the estimated error), error is higher as well, and the frequency dependence is more linear in the shorter time window.

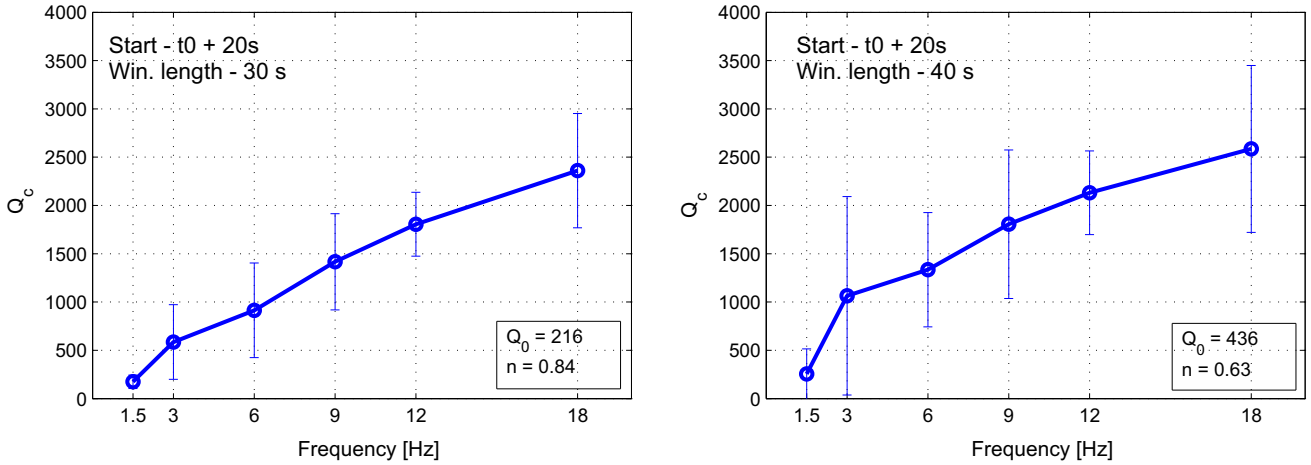

Figure 5
Frequency dependence of the Q_c for lapse time windows 30 and 40 s starting at the 20 s after the origin time. Q_0 and exponent n (Eq. (7)) shown in the right lower corner of each plot

5.2. MLTWA

In general, there is a loose agreement between our observed data and synthetic energies, which is worse than the fits shown by other authors (e.g. Meirova and Pinsky 2014; Padhy and Subhydra 2013; Zhang and Papageorgiou 2011). Figure 6 shows the comparison of the synthetic curves and observed data with corresponding misfit function.

Frequency dependences of the Q_i, Q_{sc}, and Q_t with estimated errors are plotted in Fig. 7. Q_i is generally lower except the 3 Hz frequency as intrinsic loss is stronger than the scattering. Frequency dependence of the Q_{sc} is almost linear (1.08), Q_i has an exponent of 0.74, and Q_t is 0.86.

Contributions of the scattering and intrinsic attenuation are expressed in the terms of the seismic albedo B_0 and total attenuation coefficient (extinction length inverse Le^{-1}) is also shown in Fig. 7. B_0 generally decreases with increasing frequency and is (with the exception of 3 Hz) lower than 0.5. This means that intrinsic loss is the dominant attenuation mechanism. Le^{-1} increases with frequency with the exception of 1.5 Hz. Scattering coefficient g_0 and mean free path l do not have any significant frequency dependence and their values are around 0.01 (g_0) and 100 km (l).

6. Discussion

Application of the coda and MLTWA methods on the West Bohemia/Vogtland earthquake records pointed out some significant questions about the data and methods itself. The first problem observed was the general coda quality. To successfully apply the coda methods, it is essential to have the intact undisturbed coda in an interval of interest from 20 to 60 s after the origin time. Unfortunately, the seismic swarm activity in the West Bohemia involves bursts of seismic activity with large number of events, each one occurring shortly after the previous one reduced the amount of seismograms to a small number of applicable ones. This deficit in seismograms was strongly affecting the application and results of the coda method. It prevented us from analyzing all seismograms fully automatically with satisfying results. Another question for both methods is the analysis of the lowest central frequency of 1.5 Hz. Resulting quality factors, seismic albedo, and extinction length are anomalous in comparison with higher frequencies (Fig. 7). The reason for this behavior could be the anomalous attenuation parameters of the medium on low frequencies. It is more probable that analyzing the S-waves with

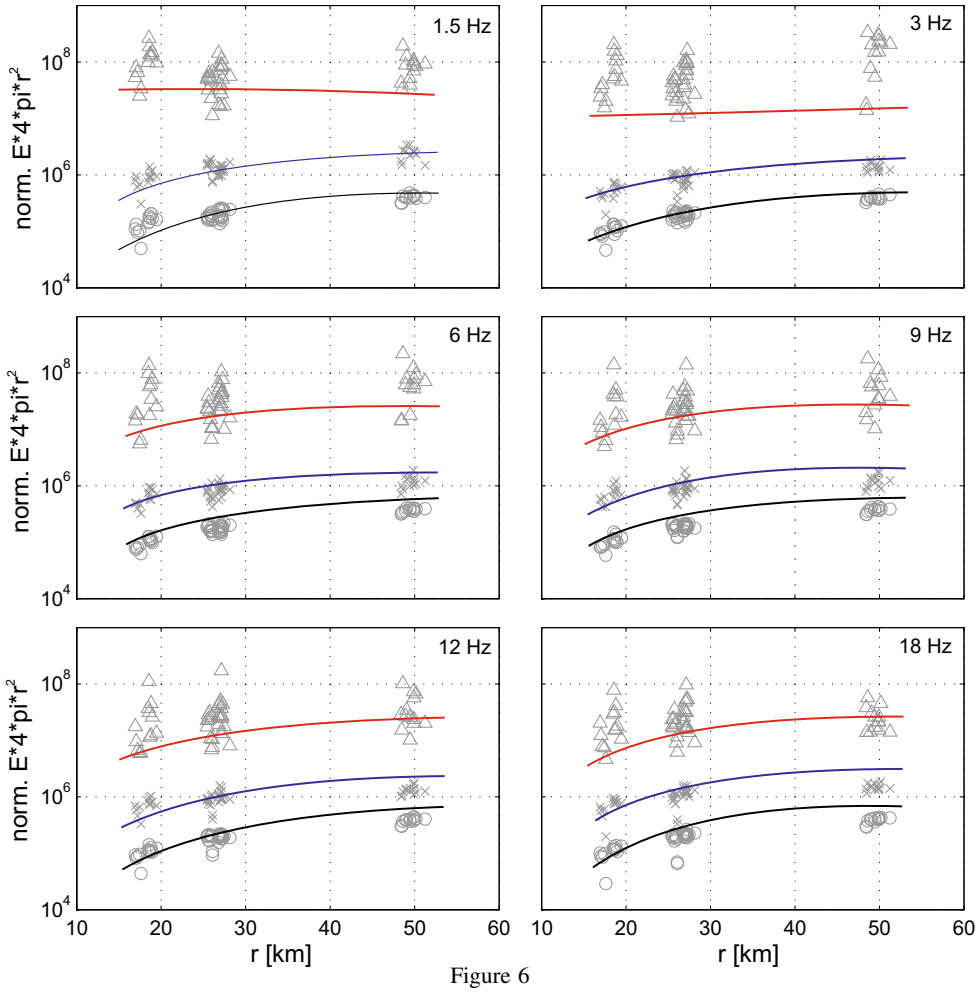

Figure 6
Normalized energies in three time windows: 1–12 s (*triangles*), 12–24 s (*crosses*), and 24–36 s (*circles*) versus hypocentral distance. The *lines* represent the best first obtained for the Q_i and Q_{sc} pair giving minimum of the misfit function Eq. (15)

wavelengths corresponding to 1.5 Hz on rather small hypocentral distances is problematic and produces incorrect results.

6.1. Coda method

By application of the coda method on West Bohemian records we had to deal with serious difficulties related mostly to the coda quality as mentioned above. Most of our codas within the interval of interest were disturbed by other earthquakes or Moho reflections which significantly affected the regression and resulting Q_c.

Differences in Q_c levels for 30 and 40 s long time windows are rather small, but systematic. This could by caused by a number of things, such as the stronger influence of noise in the later coda parts. There is also the fact that our assumption that all scattered coda waves propagate in the diffusive regime may not be complete (Calvet and Margerin 2013). Due to low *S*/*N* and disturbances in the signal after the S-wave arrival, longer windows are required but increases error.

6.2. MLTWA

An average agreement between observed and synthetic energies has been mentioned in previous chapter. This may occur due to an insufficiency in dataset settings such as a small studied area, non-uniform distribution of the hypocentral distances, or lower suitability of the used model (Zengs' approximation of the radiative transfer equation, as opposed to using Passchens).

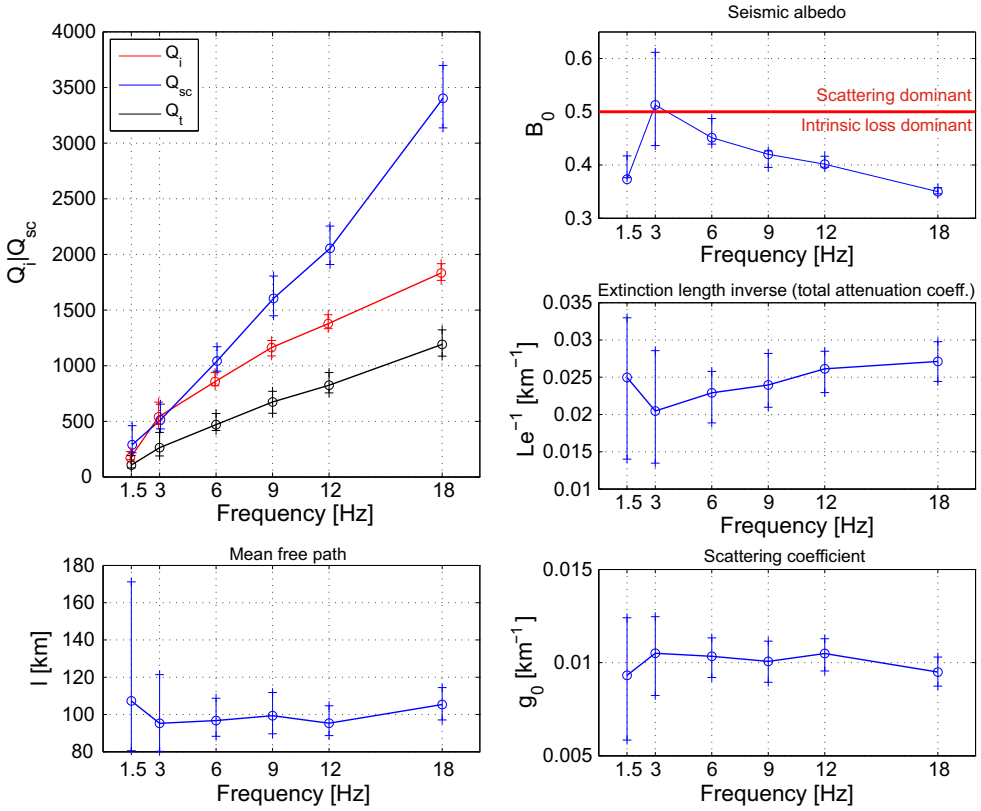

Figure 7
Resulting frequency dependence of the Q_i, Q_{sc}, Q_t, seismic albedo B_0, total attenuation coefficient (extinction length inverse) Le^{-1}, scattering coefficient g_0 and mean free path l

The latter one is of the question. In recent years the Paasschens' approximate solution of the radiative transfer equation is favored by the authors (e.g. Abubakirov (2005); Padhy and Subhadra 2013), since it is more accurate (Ugalde and Carcole 2009). However, Zengs' solution is still popular (e.g. Meirova and Pinsky 2014; Zhang and Papageorgiou 2011). In our case we tried to apply both of them, but only with Zengs' approach did we obtain reliable results and an acceptable fit of the synthetic and observed data.

Also in question are the absolute values of the Q_i and Q_c. According to theory, these two parameters should be similar if Q_c is measured correctly with a long lapse time window containing only diffusive coda energy (Eq. (3)). In our study, we obtained significantly lower Q_i than Q_c values. This can occur as a result due to an inappropriate model or dataset character. Taking the general coda quality, data character, and methods into account, we suggest that the results of MLTWA are more reliable than those of coda method, despite using Zengs' approximation.

MLTWA shows one significant result—intrinsic loss is a dominant attenuation parameter. Intrinsic loss is often caused by the presence of fluids in the medium and is associated with higher temperature (Barton 2007). Post volcanic activity in the studied area is characterized by the presence of hot mineral springs and moffetes with CO_2 of mantle origin. Changes in CO_2 flow correlate with outbursts of seismic activity and earthquakes are believed to be triggered by stress changes controlled by fluid content in the focal area (Horálek and Fischer 2008; Fischer *et al.* 2014). Therefore, our results—dominance of intrinsic loss, are in very good agreement with tectonic settings.

Our Q_i, Q_{sc}, and Q_c estimates for the small area of West Bohemia/Vogtland are very local in comparison with other studies (e.g. Israel—Meirova and Pinsky 2014; India—Padhy and Sybhadra 2013; South Korea—Rachman *et al.* 2015). Comparisons of

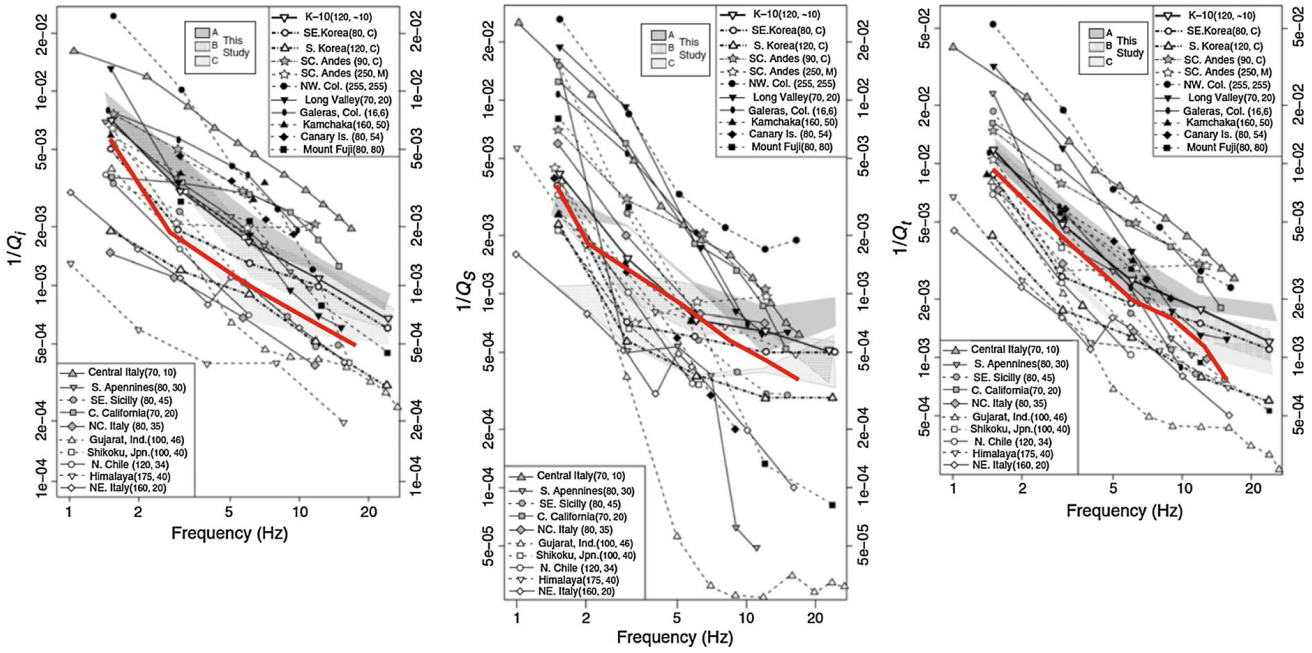

Figure 8
Comparison of Q_i^{-1} (*left*), Q_{sc}^{-1} (*center*) and Q_t^{-1} (*right*) from our study (*red*) with those from the other studies worldwide. The *numbers* in the parentheses behind the names of the areas show maximum measured hypocentral distance and the maximum depth of the events. Figure published by RACHMAN *et al.* (2015), all references herein

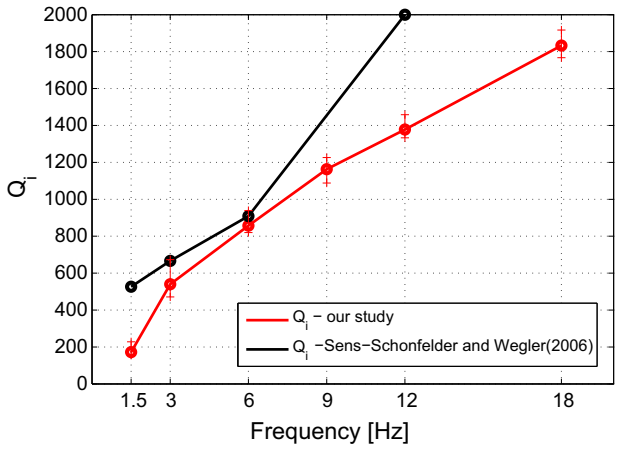

Figure 9
Comparison of our results of Q_i for West Bohemia/Vogtland with SENS-SCHONFELDER and WEGLERS' (2006) results for Germany

quality factors are problematic, since not all the authors use the same methodology for Q estimations. The use of different lapse time window positions and different tectonic settings such as deep vs. shallow earthquakes strongly affect resulting Q_cs.

Comparison of MLTWA results is plotted in the Fig. 8. Values and frequency dependence are similar to the result of other studies worldwide.

An interesting comparison is with the results of SENS-SCHOONFELDER and WEGLER (2006), who estimated the seismic moments, regional Q_i, and mean free path using the radiative transfer theory for neighboring areas of Germany. They evaluated $Q_i = 500$ below 3 Hz and a mean free path independent on frequency averaged around 690 km. Our Q_i is slightly lower (Fig. 9) and mean free path significantly lower—around 100 km (Fig. 7).

7. Conclusions

We applied standard coda method to estimate the coda quality factor Q_c and MLTWA method to separate the intrinsic quality factor Q_i and scattering quality factor Q_{sc} in the geologically active small area of West Bohemia/Vogtland. The relatively short epicentral distances and using the earthquake swarm data contaminated by later seismic events required careful selection of the analyzed events in both methods. The resulting Q_c varies between circa 100 (1.5 Hz) and 2500 (18 Hz) and is relatively high for such an active area as West Bohemia (low Q_c

correlates with seismically active areas (SATO and FEHLER 1998)). Q_i varies between 100 (1.5 Hz) and 1850 (18 Hz) and Q_{sc} varies between 300 (1.5 Hz) and 3400 (18 Hz) and shows the intrinsic loss dominance over scattering attenuation at high frequencies, which is consistent with the geodynamic activity of the region.

Resulting Q_i, Q_{sc}, and Q_t are comparable with other studies worldwide. The most important is the comparison with SENS-SCHONFELDER and WEGLERS' (2006) study from neighboring Germany. Apart from the fact that they worked with significantly different data (strong events $4 < M_L < 6$ and hypocentral distances in hundreds to thousands of km) the higher attenuation in the West-Bohemia/Vogtland area could be attributed to the strong lateral variations of the crustal attenuation properties in the central European area.

Acknowledgments

We would like to thank Josef Horálek and the WEBNET Group at the Institute of Geophysiscs (Czech Academy of Sciences, Prague) and Sigward Funke (Institut fuer Geophysik und Geologie, Universitaet Leipzig) for providing the data from WEBNET and SXNET seismic networks. This work was supported by the Charles University in Prague under the project number 4500-243-259577, by the Grant Agency of the Czech Republic under the grant No. P2010/12/2336, and by the infrastructure project CzechGeo/EPOS, no. LM2010008.

REFERENCES

ABUBAKIROV, I.R. (2005), *Attenuation Characteristics of Transverse Waves in the Litosphere of Kamchatka Estimated from Observations at the Petropavlovsk Digital Broadband Station*, Physics of the Solid Earth *41*, 813–824.

ABUBAKIROV, I.R., and GUSEV, A.A. (1990), *Estimation of Scattering Properties of Lithosphere of Kamchatka Based on Monte-Carlo Simulation of Record Envelope of a Near Earthquake*, Phys. Earth Planet. In. *64*, 52–67.

AKI, K. (1980), *Attenuation of Shear Waves in the Lithosphere for Frequencies from 0.05 to 25 Hz*, Physics of the Earth and Planetary Interiors *21*, 50–60.

AKI, K., and CHOUET, B. (1975), *Origin of Coda Waves: Source, Attenuation and Scattering Effects*, J. Geophys. Res. *80*, 3322–3342.

BANKWITZ, P., SCHNEIDER, G., KAMPF, H., and BANKWITZ, E. (2003), *Structural Characteristics of Epicentral Areas in Central Europe: Study Case Cheb Basin (Czech Republic)*, J. Geodyn. *44*, 149–159.

BARTON, N., Rock Quality, Seismic Velocity, Attenuation and Anisotropy (Taylor&Francis Group, London 2007).

CALVET, M., and MARGERIN L. (2013), *Lapse-Time Dependence of Coda Q: Anisotropic Multiple-Scattering models and Application to the Pyrenees*, Bull. Seism. Soc. Am. *103*, 1–18.

DEL PEZZO, E., ALLOTA, R., and PATANÉ, D. (1990), *Dependence of Q_c (coda Q) on coda duration time interval: Model or depth effect?* Bull. Seism. Soc. Am. *80*, 1028–1033.

FEHLER, M., HOSHIBA, M., SATO, H., and OBARA, K. (1992), *Separation of Scattering and Intrinsic Attenuation for the Kanto-Tokai Region, Japan, Using Measurements of S-wave Energy versus Hypocentral Distance*, Geophys. J. Int. *108*, 787–800.

FISCHER, T., and MICHÁLEK, J. (2008), *Post 2008-swarm Microearthquake Activity in the Principal Focal Zone of the West Bohemia/Vogtland: Space–Time Distribution and Waveform Similarity Analysis*, Stud. Geophys. Geod. *52*, 493–511.

FISCHER, T., HORÁLEK, J., MICHÁLEK, J., and BOUŠKOVÁ, A. (2010), *The 2008-West Bohemia Earthquake Swarm in the Light of the WEBNET network*, J. Seismol. *14*, 665-682.

FISCHER, T., HORÁLEK, J., HRUBCOVA, P., VAVRYČUK, V., BRAUER, K., and KAMPF, H. (2014), *Intra-continental earthquake swarms in West-Bohemia and Vogtland: A review*, Tectonophysiscs *611*, 1–27.

FRANKEL, A., and WENNERBERG, L. (1987). *Energy-flux Model of Seismic Coda: Separation of Scattering and Intrinsic Attenuation*, Bull. Seismol. Soc. Am. *77*, 1223–1251.

GUSEV, A.A. (1995), *Vertical Profile of Turbidity and Coda Q*, Geophys. J. Int. *123*, 665–672.

GUSEV, A., and ABUBAKIROV, I. (1987), *Monte-Carlo simulation of record envelope of a near earthquake*, Phys. Earth Planet. In. *49*, 30–36.

HORÁLEK, J., and FISCHER, T. (2008), *Role of Crustal Crustal Fluids in Triggering the West Bohemia/Vogtland Earthquake Swarms: Just What We Know (a Review)*. Stud. Geophys. Geod. *52*, 455–478.

HOSHIBA, M. (1991), *Simulation of Multiple-Scattered Coda Wave Excitation Based on the Energy-Conservation Law*, Phys. Earth Planet. In. *67*, 123–136.

HOSHIBA, M. (1995), *Estimation of nonisotropic scattering in western Japan using coda wave envelopes: Application of a multiple nonisotropic scattering model*, J. Geophys. Res. *100*, 645–657.

KNOPOFF, L., and MACDONALD, G.J.F. (1958), *Attenuation of Small Amplitude Stress Waves in Solids*, Reviews of the Modern Physiscs *30*, 1178–1192.

KORN, M., FUNKE, S., and WENDT, S. (2008), *Seismicity and Seismotectonics of West Saxony, Germany – New Insights from Recent Seismicity Observed with the Saxonian Seismic Network*, Stud. Geophys. et Geodaet. *52*, 479–492.

MARGERIN, L., M. CAMPILLO, and VAN TIGGELEN. B. (1998), *Radiative transfer and diffusion of waves in a layered medium: New insight into coda Q*, Geophys. J. Int. *134*, 596–612.

MEIROVA, T., and PINSKY V. (2014), *Seismic wave attenuation on Israel region estimated from the multoplne palse time window analysis and S-wave coda decay rate*, Geophys. J. Int. *197*, 581–590.

MUKHOPADHYAY, S., J. SHARMA, R. MASSEY, and KAYAL, J. (2008), *Lapse-time dependence of coda Q in the source region of the 1999 Chamoli earthquake*, Bull. Seism. Soc. Am. *98*, 2080–2086.

PAASSCHENS, J.C.J. (1997), *Solution of the time-dependent Boltzmann equation*, Phys. Rev., E *56*, 1135–1141.

PADHY, S., and SUBHADRA, N. (2013), *Separation of intrinsic and scattering seismic wave attenuation in Northeast India*, Geophys. J. Int. *195*, 1892–1903.

PAPANICOLAOU, G.C., RHYZNIK, L.V., and KELLER, J.B. (1996), *Stability of the P to S Ratio in the Diffusive Regime*, Bull. Seismol. Soc. Am. *86*, 1107–1115.

RACHMAN, A.N., CHUNG, T.W., YOSHIMOTO, K., and BUSOON, S. (2015). *Separation of Intrinsic Attenuation Using Single Event Source in South Korea*, Bull. Seismil. Soc. Am. *105*, 858–872.

RAUTIAN, T. G., and KHALTURIN, V.I. (1978), *The Use of the Coda for Determination of the Earthquake Source Spectrum*, Bull. Seism. Soc. Am. *68*, 923–948.

ROECKER, S. W., B. TUCKER, J. KING, and HATZFELD, D. (1982), *Estimates of Q in central Asia as a function of frequency and depth using the coda of locally recorded earthquakes*, Bull. Seism. Soc. Am. *72*, 129–149.

SAITO, T., H. SATO, and OHTAKE, M. (2002). *Envelope broadening of spherically outgoing waves in three-dimensional random media having power law spectra*, J. Geophys. Res. *107*, 2089–2103.

SATO, H. (1989), *Broadening of seismogram envelopes in the randomly inhomogeneous lithosphere based on the parabolic approximation: Southeastern Honshu, Japan*, J. Geophys. Res. *94*, 17735.

SATO, H., and FEHLER, M., Seismic Wave Propagation and Scattering in the Heterogeneous Earth (AIP Press/Springer Verlag, New York 1998).

SENS-SCHONFELDER, C., and WEGLER, U. (2006), *Radiative transfer theory for estimation of the seismic moment*, Geophys. J. Int. *167*, 1363–1372.

SHAPIRO, N.M., CAMPILLO, M., MARGERIN, L., SINGH, S.K., KOSTOGLODOV, V., and PACHECO, J. (2000), *The energy partitioning and the diffusive character of the seismic coda*, Bull. Seism. Soc. Am. *90*, 655–665.

TSELENTIS, G. A. (1993), *Depth-dependent seismic attenuation in western Greece*, Tectonophysics *225*, 523–528.

UGALDE, A., and CARCOLÉ, E. (2009), *Comments on "Separation of Qi and Qs from passive data at Mt. Vesuvius: A reappraisal of the seismic attenuation estimates" by E. Del Pezzo* et al. *(2006)*, Phys. Earth Planet. In. *173*, 191–194.

WEAVER, R.L. (1990), *Diffusivity of Ultrasound in Polycrystals*, J. Mech. Phys. Solids. *38*, 55–86.

WU, R.S. (1985), *Multiple Scattering and Energy Transfer of Seismic Waves—Separation of Scattering Effect from Intrinsic Attenuation—I. Theoretical Modeling*, Geophys. J. R. Astron. Soc. *82*, 57–80.

ZENG, Y., SU, F., and AKI, K. (1991), *Scattering Wave Energy Propagation in a Random Isotropic scattering Medium 1. Theory*, J. Geophys. Res. *96*, 607–619.

ZHANG, F., and PAPAGEORGIOU, A. (2011), *Attenuation Characteristics of Taiwan: Estimation of Coda Q, S-wave Q, Scattering Q, Intrinsic Q, and Scattering Coefficient*, Seismil. Res. Letters *81*, 769–777.

(Received September 26, 2014, revised June 5, 2015, accepted July 6, 2015, Published online July 27, 2015)

Earth and Planetary Science Letters 453 (2016) 215–222

Contents lists available at ScienceDirect

Earth and Planetary Science Letters

www.elsevier.com/locate/epsl

Detailed velocity ratio mapping during the aftershock sequence as a tool to monitor the fluid activity within the fault plane

Martin Bachura [a,*], Tomáš Fischer [a,b]

[a] Faculty of Science, Charles University in Prague, Albertov 6, 12843 Prague 2, Czech Republic
[b] Institute of Geophysics, Czech Academy of Sciences, Boční II/1401, 14131, Prague 4, Czech Republic

ARTICLE INFO

Article history:
Received 17 March 2016
Received in revised form 5 August 2016
Accepted 10 August 2016
Available online 26 August 2016
Editor: P. Shearer

Keywords:
velocity ratio
V_P/V_S
earthquake swarms
West Bohemia/Vogtland
fluids
CO_2

ABSTRACT

The rheological properties of Earth materials are expressed by their seismic velocities and V_P/V_S ratio, which is easily obtained by the Wadati method. Its double-difference version based on cross-correlated waveforms enables focusing on very local structures and allows tracking, monitoring and analysing the fluid activity along faults. We applied the method to three 2014 mainshock–aftershock sequences in the West Bohemia/Vogtland (Czech Republic) earthquake swarm area and found pronounced V_P/V_S variations in time and space for different clusters of events located on a steeply dipping fault zone at depths ranging from 7 to 11 km. Each cluster reflects the spatial distribution of earthquakes along the fault plane but also the temporal evolution of the activity. Low values of V_P/V_S ratio down to 1.59 ± 0.02 were identified in the deeper part of the fault zone whereas higher values up to 1.73 ± 0.01 were estimated for clusters located on a shallower segment of the fault. Temporally the low V_P/V_S values are associated with the early aftershocks, while the higher V_P/V_S ratios are related only to later aftershocks. We interpret this behaviour as a result of saturation of the focal zone by compressible fluids: in the beginning the mainshock and early aftershocks driven by over-pressured fluids increased the porosity due to opening the fluid pathways. This process was associated with a decrease of the velocity ratio. In later stages the pressure and porosity decreased and the velocity ratio recovered to levels of 1.73, typical for a Poissonian medium and Earth's crust.

1. Introduction

The West Bohemia/Vogtland region in the Czech Republic (Fig. 1) has been the focus of several highly active seismic episodes, expressed in the form of seismic swarms. Previously recorded episodes have occurred in 1997, 2000, 2008, 2011 and 2014 (Fischer et al., 2014). During the weeks-long or months-long swarm activity, thousands of events were observed with the strongest magnitudes above $M_L = 4$. All events were located in a small planar area beneath the village Nový Kostel at depths ranging from 7 to 11 km below sea level.

Characteristics of the spatio-temporal evolution of the local seismicity indicate the presence of over-pressured fluids within the focal area, which plays a significant role as a triggering mechanism of swarms (Fischer et al., 2014; Hainzl et al., 2012; Hainzl et al., 2016). Further evidence of the fluid activity is visible on the surface in the form of massive releases of CO_2 originating from the Earth's mantle (Brauer et al., 2003).

Aside from studying the physical properties of processes causing the seismic activity, analysis of the rheological characteristics of the medium is of utmost importance. The seismic velocity ratio V_P/V_S is one of the most common parameters estimated worldwide (e.g. Gritto and Jarpe, 2014; Konstantinou, 2013; Novotný et al., 2016, to mention only a few).

The classical Wadati diagram approach (Wadati, 1928) is the most widely used method to resolve the mean velocity ratio of the medium beneath a seismic network (e.g. Kisslinger and Engdahl, 1973; Dahm and Fischer, 2014). This method produces the most reliable V_P/V_S estimates for datasets where event-station ray paths uniformly cover the Earth's volume beneath the seismic network and the earthquakes are widely spread. However, the non-uniform distribution of events concentrated in source regions has led to the development of new methods enabling us to derive more local information about the seismic velocities and their ratio.

Fitch (1975) resolved local seismic velocities for the source region of an earthquake cluster while implementing the master event location method. His approach was further developed by Poupinet and Ellsworth (1984) who monitored velocity vari-

* Corresponding author.
E-mail addresses: martin.bachura@natur.cuni.cz (M. Bachura), fischer@natur.cuni.cz (T. Fischer).

http://dx.doi.org/10.1016/j.epsl.2016.08.017
0012-821X/

ations by analysing earthquake doublets using cross-correlations to measure precise differential times. Further development in the topic was conducted by e.g. Ito (1985), Scherbaum and Wendler (1986) and Maurer and Deichmann (1995). The last two studies (Maurer and Deichmann, 1995) pointed out the potential of cross-correlation methods. The most important step in direct V_P/V_S estimation was achieved by Lin and Shearer (2007) and Dahm and Fischer (2014). They both independently developed a double-difference version of the standard Wadati method to estimate the local velocity ratio within the source volume of earthquake clusters. This method allows focusing on very small clusters (up to hundreds of meters in diameter). With suitable datasets and proper data processing the temporal behaviour of V_P/V_S can be monitored as well (Dahm and Fischer, 2014).

In addition to the standard Wadati method and its double-difference modification, tomographic approaches are widely used to map the spatial distribution of seismic velocities and their ratio (e.g. TomoDD algorithm by Zhang and Thurber, 2003). The main difference between tomography and the double-difference Wadati method lies in the mapping of an analysed area. Tomography images the area covered by the seismic rays of various origin (earthquakes, controlled source shots, explosions). Analysed volumes do not necessarily contain any earthquake hypocentres. As a result, tomography produces a complete picture of the underground sampled by the seismic rays. On the other hand, the double-difference Wadati method focuses on one single area covered by hypocentres and computes V_P/V_S directly for this volume, with no influence of the medium around. Tomography can be applied to any catalog data (locations and arrival times), while double-difference Wadati method requires tightly clustered earthquakes and provides remarkably better resolution of results in these localized regions. Moreover, tomography is not well suited to deal with temporal changes of seismic velocities.

In West Bohemia/Vogtland several efforts have analysed the rheological properties of the active area. Růžek and Horálek (2013) and Alexandrakis et al. (2014) applied tomographic approaches to derive 3-D models for P and S waves and computed maps of the V_P/V_S ratio. Dahm and Fischer (2014) used the double-difference Wadati method to analyse temporal variations of local V_P/V_S within the focal area of the 1997, 2000 and 2008 activity. The two tomographic studies showed opposite V_P/V_S anomalies in the focal zone: a negative anomaly of 1.55 by Růžek and Horálek interpreted as a volume with increased ability to have brittle failure vs. a positive anomaly of 1.73 ± 0.004 by Alexandrakis et al. interpreted as the presence of liquid water within the over-pressured fractured fault zone (based on studies of Ito et al. (1979) and Popp and Kern (1994)). Both papers analysed the 2008 activity. Alexandrakis et al. used only the swarm earthquakes, while the dataset of Růžek and Horálek consisted of the swarm earthquakes and controlled source shots.

Dahm and Fischer (2014) studied the temporal characteristics of the velocity ratio, showing strong decreases of local V_P/V_S at the beginning phase of the activity (values down to 1.4), which was interpreted as the presence of over-pressured gas filling the pores and fractured space within the material of the focal zone. Recently Novotný et al. (2016) applied the Wadati method and estimated an average value of V_P/V_S for the West Bohemia/Vogtland region of 1.68 ± 0.01.

The aim of this study is to analyse the local V_P/V_S ratio estimated by the double-difference version of the Wadati method (proposed by Lin and Shearer (2007) and Dahm and Fischer (2014)) applied to three mainshock–aftershock sequences of the 2014 activity. As double-difference Wadati methods focus on the area covered by tightly clustered events, the choice of the studied area and time interval is affected implicitly by the migration of seismicity in space and time. To improve the resolution in V_P/V_S mapping along the fault, we divided the events into space–time clusters, which are then subjected to the double-difference V_P/V_S analysis.

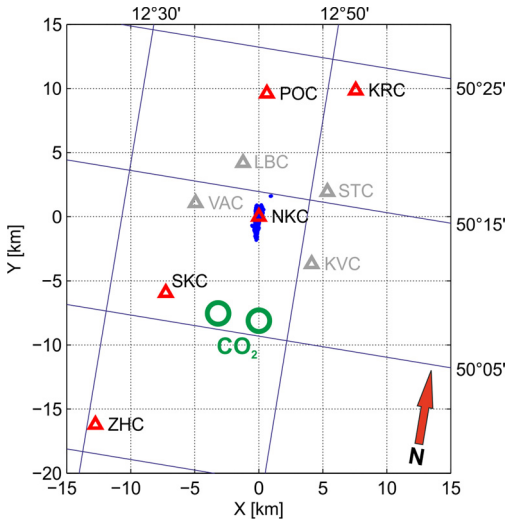

Fig. 1. Map of the West Bohemia/Vogtland area with epicentres of the 2014 activity (blue dots) and selected stations of the WEBNET seismic network (red triangles) used in this study. Gray stations were not used for the analysis, green circles represent the Soos and Hartoušov moffets area, where CO_2 springs are located. (For interpretation of the references to colour in this figure legend, the reader is referred to the web version of this article.)

2. Data – 2014 seismicity

Recent seismic episodes in the West Bohemia/Vogtland area were expressed in the form of seismic swarms. Different segments of the Nový Kostel fault zone were activated and as a result thousands of events occurred. The uniqueness of the 2014 activity lies in its non-swarm character. The activity consists of three separate mainshock–aftershock sequences with events located on the same focal zone where only swarm-type seismicity was present during the last two decades. Despite its non-swarm character, statistical analysis of the aftershock sequences (Hainzl et al., 2016) shows an unusually high rate of aftershocks in the first 8–10 h after the strongest earthquake and their migration pattern can be explained by the presence of over-pressured fluids within the focal zone. Activated fault segments form almost a vertical plane of 3×3 km at depths from 7 to 10 km (Fig. 2). The fault plane is oriented from the south to the north with a strike of 169° (Fischer et al., 2014).

The first sequence started with a $M_L = 3.5$ earthquake (on May 24th) followed by circularly distributed aftershocks evolving from the south to the north and continuing for two days. The second sequence started with a $M_L = 4.5$ earthquake (on May 31st), lasted for one week, and aftershocks evolved through the whole fault zone. The third sequence was very similar to the first, with one mainshock of $M_L = 3.5$ (on August 3rd) and circular south–north evolution of the aftershocks lasting for two days (Hainzl et al., 2016).

From the total number of more than 8000 events recorded, 3800 with magnitudes ranging $M_L = 0$–4.5 were relocated by the HypoDD algorithm (Waldhauser and Ellsworth, 2000). Processing through HypoDD reflected our effort to obtain as precise relative locations as possible. P and S wave arrival time differences at 9 stations (Fig. 1) were computed by waveform cross-correlation and checked with care in order to avoid mis-locations due to the wide magnitude range of the events. Different magnitudes with different frequency content of correlated pulses yield the best cross-correlation coefficients when shifted to the maximum, not to the first onset of the wave arrival (see suppl. material). Therefore it

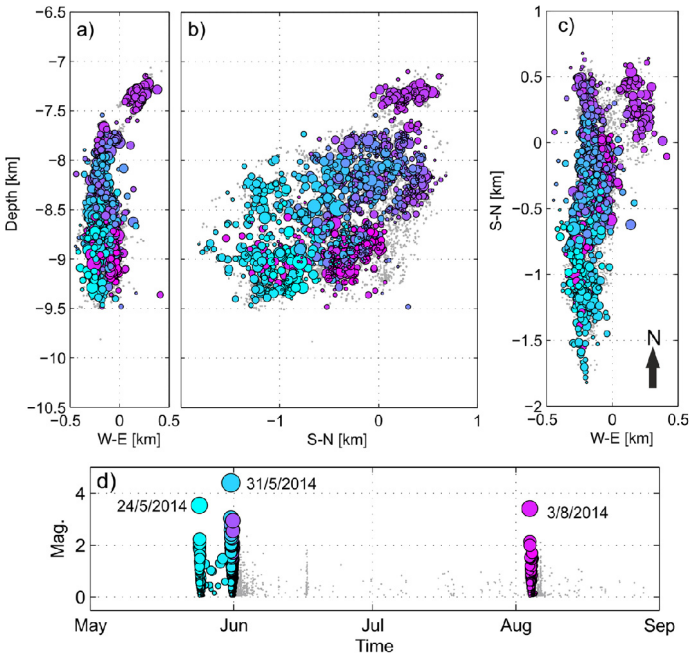

Fig. 2. Locations of the study-selected 1624 events (out of a total number of 3800) that occurred during the 2014 mainshock–aftershock sequences: a) front view; b) side view; c) map view; d) temporal evolution. The size of the circles scales with M_L. Gray dots represent events which were omitted from analysis throughout the data processing.

is crucial to correlate only waveforms of earthquakes with similar magnitudes. As a result of our relocation procedure our location errors estimated by the HypoDD SVD inversion method were ±18 m in the horizontal plane and ±25 m in the vertical coordinate.

3. Method

The double-difference Wadati method was proposed by Lin and Shearer (2007) and in a slightly modified version by Dahm and Fischer (2014). Similar to double-difference location methods it makes use of arrival time differences between pairs of events, thus cancelling the effects of unknown medium variations beyond the studied area with common raypaths. Assuming two closely spaced events within the focal zone, the differences in their P and S travel times (and therefore V_P/V_S) are caused only by the different velocity conditions inside the fault area. Accordingly, by plotting the P wave arrival time differences of a single event pair at different stations vs. their S wave arrival time differences at the corresponding stations, one can derive the local V_P/V_S ratio inside the focal zone from the slope of the resulting scatter plot.

When numerous event pairs are located within the fault zone, each produces P vs. S arrival time differences, which lie on parallel lines with the same slope, but shifted from zero due to differences in their origin times. In order to allow for fitting a common line it is desirable to gather the data of all event pairs in a single cluster. This is achieved by demeaning, i.e., subtracting the absolute differential times of each event pair in x and y coordinates to shift them into the zero position. After demeaning we fit a line through the data points by means of orthogonal regression with a combined L1–L2 norm (Lin and Shearer, 2007) (Fig. 3).

The method can be described by the equation

$$\Delta t_{ij}^{P} - \langle \Delta t_{ij}^{P} \rangle_j = \left(\frac{V_P}{V_S} \right) \left(\Delta t_{ij}^{S} - \langle \Delta t_{ij}^{S} \rangle_j \right),$$

where i is the event pair index and j is the station index. Terms inside the angle brackets represent the mean of the arrival time differences for each event pair i at all stations j.

For accurate V_P/V_S recording, clusters with a random distribution of the interevent raypath directions are necessary together with a uniform distribution of stations on the surface. These conditions will suppress possible errors due to different take-off angles for P and S waves (Lin and Shearer, 2007). To achieve this, a 3-D distribution of events within a cluster is ideal. However, even the planar 2-D clusters with appropriate coverage of the stations should produce a collection of event pairs with a random distribution of directions suitable for V_P/V_S estimation.

Uncertainties were estimated using a bootstrap method (Lin and Shearer, 2007), where randomly selected events pairs were removed, others were randomly doubled, tripled etc. and the V_P/V_S ratios were computed repeatedly for every "biased" dataset. The error was then estimated as a standard deviation of the resulting velocity ratios of these datasets.

4. Data processing

The data processing consisted of two steps: first, subdividing the activity into clusters, and then estimating the V_P/V_S ratios using the double-difference method described above.

Appropriate selection of the earthquake clusters was the key factor for success in identifying reliable variations of velocity ratios. We used a nearest-neighbour clustering algorithm for the rough clustering and then manually checked, adjusted, combined and sorted the clusters in order to provide them with desired characteristics: short time window, homogeneous spatial distribution of events, and sufficient number of events within a single cluster.

The first automatic clustering step (the nearest-neighbour clustering algorithm applied to the 2014 data) sorted events into more

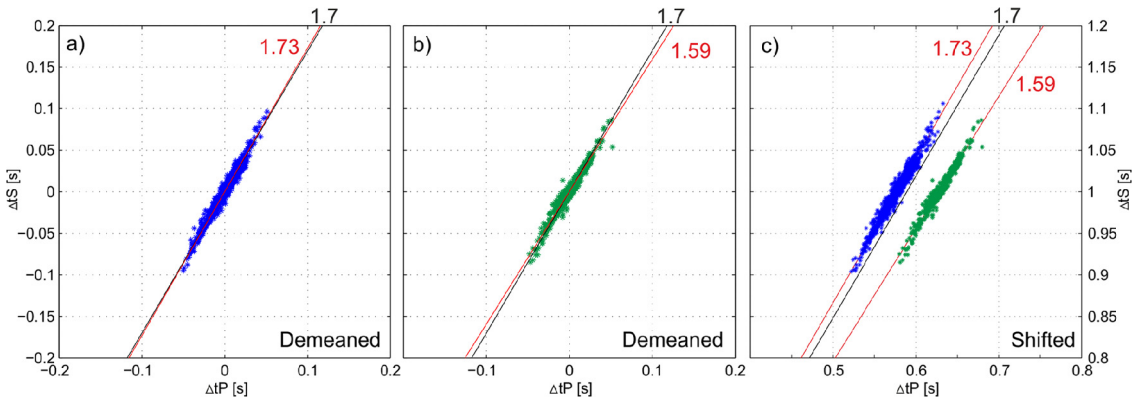

Fig. 3. Two different datasets with different V_P/V_S: a) 1.59; b) 1.73. Black lines represent the velocity ratio of 1.7 for comparison. In plot c the same clusters are shifted from the demeaned zero position to highlight their difference in slopes.

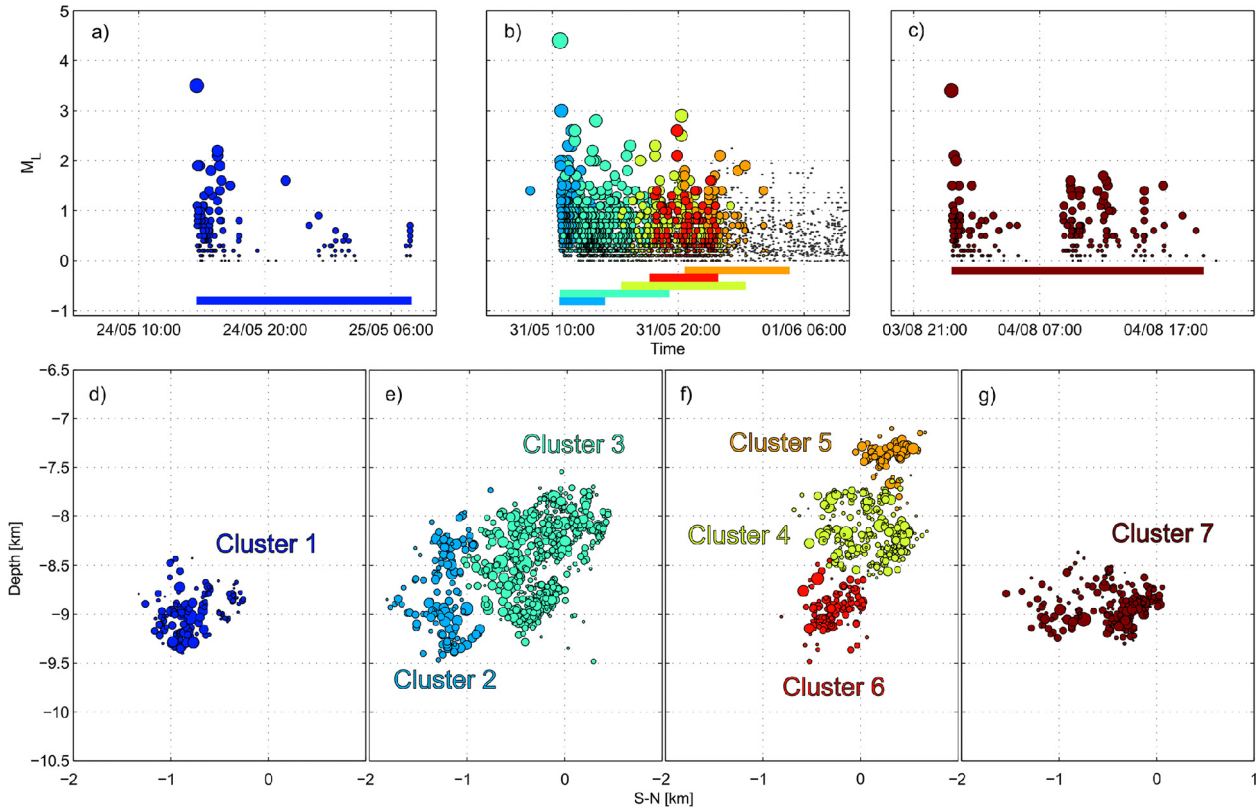

Fig. 4. 7 spatio-temporal clusters delineated from the 2014 activity: a)–c) temporal evolution of the three mainshock–aftershock series with clusters indicated with different colours; d)–g) side view of the fault plane showing the spatial distribution of the clusters; for better visibility plotted separately into four figures. Gray dots in b) represent continuation of the aftershock activity with insufficient clustering potential.

than 30 initial groups. About 20% of the events were omitted since they did not show an adherence to any cluster or only created small groups of outliers. In the next step, all of the automatically produced clusters were manually checked and processed with respect to their spatial and temporal significance, size and general relation to the whole activity evolution.

The crucial deciding parameter of cluster acceptance/rejection was the rate of events (events per hour) within a single cluster, as we required clusters with a high event rate. These were attainable during the early aftershock sequences (with events rate up to 70 events per hour, Table 1). With the continuation of the aftershock activity, the rate of potential clusters lowers. Therefore, in order to obtain a cluster with a sufficient number of events, a longer time window was necessary.

By testing the method on different test clusters we concluded that only clusters containing at least 100 earthquakes produced reliable V_P/V_S estimates. Generally, we removed the less numerous clusters from the analysis. In some cases, smaller groups of events were combined into a single acceptable cluster to prevent the loss of the V_P/V_S information for a given time and space window, despite the low value of temporal density (e.g., the first and third mainshock aftershock sequences were treated as single clusters).

As a result of our combined automatic–manual clustering procedure, 7 clusters with a total of 1624 events out of 3800 were selected (Fig. 4 and Table 1). Cluster 1 contains the activity of the first mainshock–aftershock sequence that started on May 24th. Clusters 2–6 monitor the activity of the $M_L = 4.5$ mainshock from May 31st and 1.5 days of its aftershocks. Clusters 2 and 3 cover the first 8 h after the mainshock. They are overlapped in time, but not space. Cluster 2 maps the earthquakes to the south of the main event, while cluster 3 maps the northwardly propagating activity. Clusters 4, 5 and 6 slightly overlap in time, but are also strictly distinguished in space. Cluster 4 is the continuation of

Table 1
Cluster characteristics: cluster ID, cluster diameter, number of events, cluster duration, rate – number of events per hour within a single cluster.

ID	Diam. (km)	Ev.	Dur. (h)	Rate (ev./dur.)
1	0.96	157	17	9.2
2	2.2	150	3	50
3	1.81	649	9	72.1
4	1.52	282	10	28.2
5	0.65	131	6	21.8
6	1.08	132	8	16.5
7	1.68	123	20	6.15

cluster 3, cluster 5 covers the separate activity above the fault zone and cluster 6 contains the activity propagated in depth. Further continuation of the aftershock activity was too sparse in time and too scattered in space to generate clusters short enough and small enough to undergo the analysis. The third mainshock–aftershock sequence from August the 3rd was grouped in cluster 7.

The first and third mainshock–aftershock sequences were treated as two single clusters, despite the fact they could be clustered in more distinct subclusters. This step was necessary due to a small number of events within these two sequences (157 and 123).

Despite the high number of omitted events, the final clustering was found to be optimal for the given dataset and allowed an unbiased estimation of V_P/V_S (selection/omission of the events does not affect the velocity ratio values). From the spatial point of view the clusters mapped the whole area activated in the fault zone (Fig. 2).

Events within the clusters were paired and differential times between P and S wave arrivals of each pair were measured by using cross-correlation. Waveforms were filtered by a 3-pole 1–15 Hz band-pass Butterworth filter. Only events with similar magnitudes

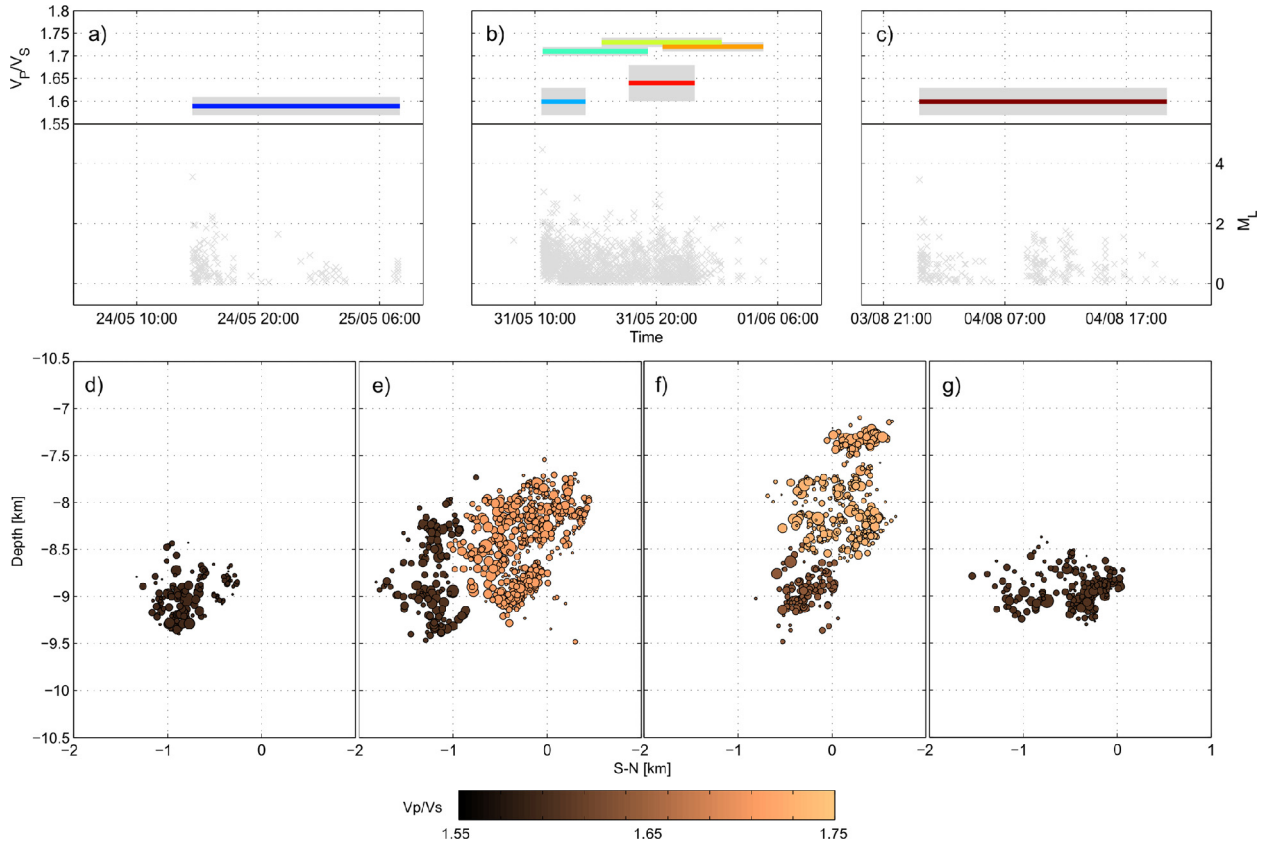

Fig. 5. Resulting temporal and spatial distribution of V_P/V_S: a)–c) V_P/V_S with errors (grey) for different clusters – shown in a temporal view (clusters coloured as in Fig. 4); d)–g) Resulting V_P/V_S for different clusters with colours reflecting the value of estimated V_P/V_S (darker for lower values) – side view of the fault plane.

were paired and correlated to avoid errors in differential time estimation. For each time difference we obtained a cross-correlation coefficient which describes the similarity of the waveforms, hence quantifying the quality of the estimated difference time.

Hypocentres of the 2014 sequence lie on an almost vertical plane forming a 2-D structure. To analyse the area covered by the events (the pairs of events) only stations with ray paths more or less parallel with this 2-D plane (general fault orientation) were used (Fig. 1). Use of the other stations lying perpendicular to the plane deteriorated the V_P/V_S estimation since they produce time differences which were too small. This was caused by the short travel distance across the fault. The 5 stations that passed this criterion were distributed uniformly above the analysed hypocentres. The positions of stations along the hypocentre trend resulted in a uniform distribution of interevent ray path directions within the clusters, which is essential for successful V_P/V_S estimation (as discussed in chapter 3 – Method). Only event pairs with at least 4 differential times and a cross-correlation coefficient higher than 0.7 were accepted for data processing and analysis.

5. Results

We tested a variety of clustering approaches, cross-correlation thresholds, and stations for analysis to avoid possible trade-offs between estimated V_P/V_S ratios and cluster properties (size, number of events, number of event pairs, and number of used differential times). We optimized the method so that no clear correlation between the above-mentioned parameters was apparent and the resulting velocity ratios reflected only the mean V_P/V_S ratios of the volume covered by a single cluster. The resulting V_P/V_S estimates of each cluster with their errors are shown in Fig. 5 and Table 2.

Table 2
Cluster characteristics and V_P/V_S results: cluster ID, number of events, number of event pairs, number of differential times used for the regression, V_P/V_S, and error.

ID.	Ev.	Ev. pairs	Diff. t.	V_P/V_S	[±]
1	157	259	1130	1.59	0.02
2	150	169	697	1.6	0.03
3	649	727	3039	1.71	0.01
4	282	409	1753	1.73	0.01
5	131	474	2023	1.72	0.01
6	132	82	352	1.64	0.04
7	123	67	273	1.6	0.03

We found low values of the velocity ratio down to 1.59 ± 0.02 in clusters 1, 2, 6, and 7, and higher values up to 1.73 ± 0.01 in clusters 3, 4, and 5. For the lower velocity ratios the variance is larger than for the higher ones, ± 0.02 to ± 0.04 compared to ± 0.01. To obtain higher precision more stations would be necessary. The V_P/V_S estimates are most reliable for those clusters where a sufficient number of differential times are available: clusters 1, 2, 3, 4 and 5. Clusters 6 and 7 have only a limited number of differential times which exceed the 0.7 cross-correlation threshold. Higher values were observed at shallower depths where only the aftershocks of the strongest event (May 31st with $M_L = 4.5$) occurred (Fig. 5e, f), whereas the lower values were associated with deeper parts of the activated fault plane, such as in the area of the 1st and 3rd mainshock–aftershock series and early aftershocks of the 2nd sequence (Fig. 5d, e, g).

6. Discussion and conclusions

Our analysis revealed significant V_P/V_S variations in space and time. The obtained precision of a hundredth is lower than the precision achieved in the similar study by Lin and Shearer (2009) of

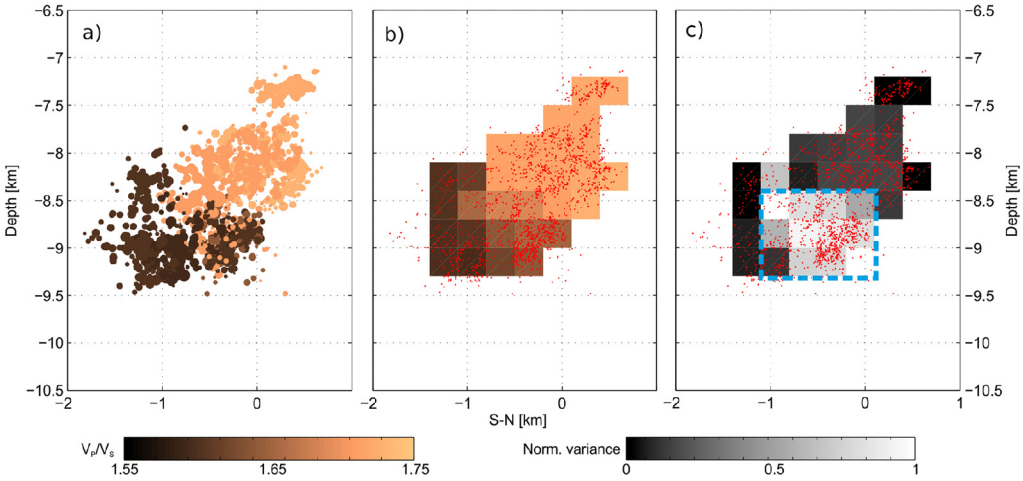

Fig. 6. Pseudotomographical representation of the results: a) events coloured according to the V_P/V_S of the cluster they belong to; b) mean V_P/V_S for the grid with bin size 300 m (bin V_P/V_S value computed as a mean of the event velocity ratios located in the bin); c) Uncertainty of velocity ratio estimates expressed as normalized variance of the V_P/V_S ratio estimated within the single bin; high normalized variance represents bins where dramatic changes over time appear. (For interpretation of the references to colour in this figure, the reader is referred to the web version of this article.)

thousandths, which is caused by the relatively low number of stations involved in our analysis.

Generally, the application of the double-difference method to estimate the V_P/V_S on very local scales with sparse coverage of stations requires careful data processing. To eliminate the influence of technical aspects (cross-correlation threshold, number of differential times, and fitting method), clusters should only contain nearby events with common characteristics occurring during a short time window. This is especially important in areas where strong V_P/V_S variations are expected, such as the West Bohemian/Vogtland area (Dahm and Fischer, 2014).

From this technical point of view, clusters 1–5 fulfil the above-stated conditions and produce a sufficient number of differential times (Table 2) even after applying the cross-correlation threshold to at least 4 stations. Therefore, their estimated V_P/V_S is considered reliable. Despite this stability, there are higher error estimates of ± 0.02 and ± 0.03 for clusters 1 and 2, which both show anomalous velocity ratios of 1.59 ± 0.02 and 1.6 ± 0.03. Higher errors combined with a high number of differential times (implies better stability of the fit) can be explained as a result of velocity ratio instabilities within the analysed cluster. In fact the bootstrapping method of error estimation is sensitive to the V_P/V_S stability of all event pairs involved. Stable V_P/V_S inside the area of the cluster and through the whole duration of the cluster lowers the estimated error. As a result, the larger errors in cluster 1 and 2 might stem from changes of velocity ratio during the analysed time interval or from the presence of V_P/V_S heterogeneities smaller than the cluster-based method can detect.

On the contrary, clusters 6 and 7, despite having a similar number of events as cluster 1 (157 events with 1130 differential times), produced a significantly smaller number of usable differential times (352 and 273, Table 2). The reason might be the dissimilarity of earthquake waveforms, as the selected cluster might be composed of several small groups of events with different source mechanisms. These dissimilarities would result in lower cross-correlation coefficients than the required 0.7. A lower number of differential times causes higher errors (0.04 and 0.03). However, both of these clusters (even with the errors taken into account) show low V_P/V_S ratios of 1.64 ± 0.04 and 1.6 ± 0.03.

The distribution of V_P/V_S along the activated fault plane reveals significant spatial dependence. Areas of V_P/V_S below 1.65 are located at depths deeper than 8.5 km, whereas the shallower depths clearly show values higher than 1.7 (Fig. 6). However, this apparent spatial dependence is broken by an unstable area (see Fig. 6 – blue dashed rectangle) at depths from 8.5 to 9.5 km and S–N coordinate from -1 km to 0 km. The instability is a result of the varying velocity ratio estimations for this area from clusters 6 and 7 with low V_P/V_S and cluster 3 with high V_P/V_S. These variations may be an artifact of the method or may have a real physical interpretation as a changing V_P/V_S with time in this area. This was pointed out by Dahm and Fischer (2014) for the previous West Bohemian seismic swarms. Meanwhile the anomaly is related to the seismicity structure within cluster 3, whose V_P/V_S ratio does not represent a precise velocity ratio throughout the studied area, but instead the mean V_P/V_S of the cluster 3 coverage.

Analysing the V_P/V_S ratio as a function of time shows that low values of the velocity ratios are associated with outbursts of activity and with the mainshocks (clusters 1, 2 and 7), while the higher ratios are common for the aftershock series (clusters 3–5). Cluster 6 is an exception as it covers part of the aftershock sequence, but has lower V_P/V_S of 1.64 ± 0.04. As mentioned above, reasons for this behaviour may be evidence of temporal changes during the aftershock series.

Our V_P/V_S values correspond to Poisson ratios ranging from 0.173 to 0.249. That is less than the typical range of 0.24 to 0.29 for crustal rocks (Christensen, 1996). Generally, low values may indicate the presence of quartz-rich rocks at focal depths from 7 to 11 km. Quartz has a V_P/V_S of 1.5 and its increasing content results in lowering the mean velocity ratio of the rock material (e.g. Christensen, 1996; Lin and Shearer, 2009). However, observed temporal changes in this study require a different interpretation based on dynamic changes of the porous media. We applied the Biot–Gassmann theory for poroelastic media (e.g. Mavko et al., 2003). The Biot–Gassmann equations predict the theoretical V_P/V_S ratio fora porous medium saturated with liquid or compressible gas. Currently, it is only one of the theoretical models developed (e.g. Walsch, 1969; O'Connell and Budiansky, 1974), but its agreement with our results (below) makes it suitable for interpretation. According to the model, the velocity ratio V_P/V_S of a porous media can be expressed as

$$\left(\frac{V_P}{V_S}\right)^2 = \frac{K_{dry}}{\mu} + \frac{4}{3} + \frac{K_p}{\mu},$$

with

$$K_p = \frac{\alpha^2}{\frac{\phi}{K_f} - \frac{1-\phi}{K_s} - \frac{K_{dry}}{K_s^2}}$$

$$K_{dry} = K_s(1-\alpha),$$

where K_s and K_f are bulk moduli of matrix and interstitial fluid, μ represents the shear modulus of the solid phase, ϕ is porosity and α is the Biot–Willis coefficient with values from 0 to 1. Assuming the above-mentioned mechanical parameters of the solid medium to be constant in the focal depths, V_P/V_S becomes a function of porosity and the interstitial fluid bulk modulus. Moreover, when expecting only a single-phase fluid to be present, the resulting velocity ratio is only a function of porosity due to the fragmentation of the focal zone. According to the geodynamic setting, pressure and temperature characteristics of the focal depths of 7–9 km, we investigated two different fluids — liquid water and supercritical CO_2, with K_f of 2 GPa and 0.5 GPa, respectively. We used average values for the crystalline basement with respect to the expected geological structure (e.g. Fischer et al., 2014; Růžek and Horálek, 2013; Alexandrakis et al., 2014): $K_s = 50$ GPa, $\mu = 30$ GPa, $\alpha = 0.5$. Theoretical velocity ratios for both fluids decrease with porosity (Fig. 7).

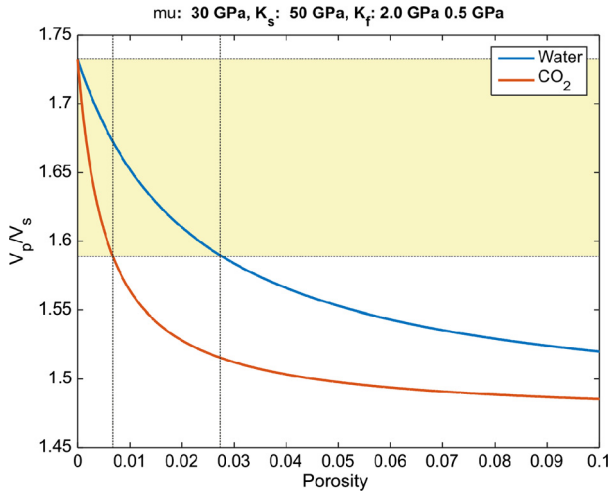

Fig. 7. Theoretical velocity ratios of water and supercritical CO_2 as a function of porosity in a typical crystalline rock $K_s = 50$ GPa, $\mu = 30$ GPa, $\alpha = 0.5$. The observed values of V_P/V_S from 1.59 to 1.73 (yellow band) correspond to porosity variations between 0 and 0.01 for supercritical CO_2 and between 0 and 0.03 for water. (For interpretation of the references to colour in this figure legend, the reader is referred to the web version of this article.)

The physical effect beyond the V_P/V_S decrease is that S-waves are carried by the solid matrix of the fractured rock and their velocity is less affected by the fluid intrusion into the pore space. On the contrary, P-waves are carried by the whole material (matrix and pore filling) and their velocity is controlled more significantly by the interstitial fluid. The P-wave velocity decrease is stronger than that of S-waves, and therefore the V_P/V_S ratio decreases with porosity increase, or when pores are filled with gas (Dahm and Fischer, 2014).

The lowest observed V_P/V_S value of 1.59 ± 0.02 requires porosities less than 0.01 (CO_2) and 0.03 (water). The question remains, what kind of fluid is more probable to be present in the focal zone during the rupturing process. Wagner et al. (1997) found free water and open fractures down to a depth of about 9.4 km at the KTB borehole (50 km SW). However, massive CO_2 releases (up to 500 m^3/h (Fischer et al., 2014)) are observed in the seismoactive area with dynamic behaviour. In some cases CO_2 flow variations correlate with seismic activity. Therefore we favour a system with overpressured mantle-derived CO_2 in its supercritical phase filling the fractures of the hypocentral area during the seismic activity, or at least during the initial outbursts of the seismic sequences. Variations of the V_P/V_S ratios appear to reflect changes in the porosity due to the fracturing process.

Further evidence of fluid intrusion and its influence on the characteristics of seismic activity was given by Hainzl et al. (2016), who analysed the same 2014 dataset as our study. By analysing the aftershock sequence of the strongest event (in May 31st with $M_L = 4.5$) they concluded the mainshock opened the fluid pathways from a finite fluid source into the fault plane, which explained the unusual rate (high and constant activity during the first 0.3 day after the mainshock followed by aftershock decay according to the Omori law) and migration characteristics of aftershocks.

The onsets of the three mainshock–aftershock sequences were always located in the deeper part of the fault zone beneath a depth of 8.5 km. Dense aftershock activity and high intensity of the rupturing process are accompanied by low velocity ratios (down to 1.59 ± 0.02). Later, as the aftershock series evolved above 8.5 km and its rate slowed, the expected decrease of porosity correlates well with higher V_P/V_S values (up to 1.73 ± 0.01). This behaviour might indicate a distinct structural boundary at depths of 8.5 km between two geological volumes with different responses to the fluid intrusion. On the other hand, this boundary might only be apparent and just a result of the changing fluid dynamics as the role of fluids is dominant at the beginning of the activity, which was always located below 8.5 km. The onset of the 2014 seismic activity is associated with an anomalously increased aftershock rate (Hainzl et al., 2016) and low V_P/V_S down to 1.6 ± 0.03. With the continuation of activity the aftershock rate becomes more standard in terms of the Omori law (Hainzl et al., 2016) and V_P/V_S rises up to 1.73 ± 0.01. A change of triggering mechanism is a possible explanation of the observed behaviour — from fluid induced triggering to a standard elastic stress transfer. For the strongest event on May 31st we observed this change in V_P/V_S about 8–10 h after the mainshock. Interestingly, this agrees with the time when the aftershock characteristics started to decrease according to the Omori law, 0.3 days after the mainshock (Hainzl et al., 2016).

The high resolution achieved by the double-difference version of the Wadati method depends on the data quality (earthquake density and distribution) and is beyond the capabilities of tomographic methods. Moreover, the ability to analyse the temporal dynamics of the V_P/V_S is unattainable by tomography. Therefore a direct comparison of our 'dynamic' results with existing 'static' tomographic studies is not meaningful. Despite this, for comparison reasons we computed the mean V_P/V_S of the focal zone using the double-difference Wadati method for the whole activity. This yields an average velocity ratio of 1.71 ± 0.01 (Fig. 8). In contrast

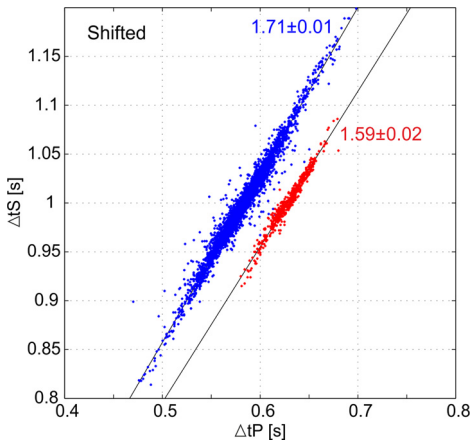

Fig. 8. Mean V_P/V_S of the Nový Kostel focal zone (blue dots). Computed for the whole time interval of the 2014 activity using the double-difference modification of the standard Wadati method. Red dots represent a subcluster of V_P/V_S 1.59 ± 0.02 for comparison. Both datasets are shifted from the demeaned zero position to highlight the difference of slopes. (For interpretation of the references to colour in this figure legend, the reader is referred to the web version of this article.)

to the tomographic results of Růžek and Horálek (2013) (1.55) and Alexandrakis et al. (2014) (1.73 ± 0.04), we do not find the mean velocity ratio on the fault zone to be anomalous. V_P/V_S anomalies are of short duration and of small size in comparison with the whole fault zone.

For the West Bohemian/Vogtland activity, the double-difference Wadati method is able to detect and monitor the occurrence and behaviour of V_P/V_S ratios within small clusters of events. Moreover, when interpreting changing V_P/V_S ratios as a result of fluid intrusion, the method allows to track and monitor this fluid activity.

Acknowledgements

We would like to thank Josef Horálek and the WEBNET group at the Institute of Geophysics (Czech Academy of Sciences, Prague) for providing the data from WEBNET seismic network. This work was supported by the Charles University in Prague under the project number 4500-243-259577 and by the Grant Agency of the Czech Republic under the grant No. P210/12/2336.

Appendix A. Supplementary material

Supplementary material related to this article can be found online at http://dx.doi.org/10.1016/j.epsl.2016.08.017.

References

Alexandrakis, C., Calo, M., Bouchala, F., Vavryčuk, V., 2014. Velocity structure and role of fluids in the West Bohemia seismic zone. Solid Earth 5, 863–872. http://dx.doi.org/10.5194/se-5-863-2014.

Brauer, K., Kampf, H., Strauch, G., Weise, S., 2003. Isotropic evidence (^{3}He/^{4}He,$^{13}CCO_2$) of fluid-triggered intraplate seismicity. J. Geophys. Res. 108, 2000. http://dx.doi.org/10.1029/2002JB002077.

Christensen, N., 1996. Poisson's ratio and crustal seismology. J. Geophys. Res. 101, 3139–3156. http://dx.doi.org/10.1029/95JB03446.

Dahm, T., Fischer, T., 2014. Velocity ratio variations in the source region of earthquake swarms in NW Bohemia obtained from travel time double-differences. Geophys. J. Int. 196, 957–970. http://dx.doi.org/10.1093/gji/ggt410.

Fischer, T., Horálek, J., Hrubcová, P., Vavryčuk, V., Brauer, K., 2014. Intra-continental earthquake swarms in West-Bohemia and Vogtland: a review. Tectonophysics 611, 1–27. http://dx.doi.org/10.1093/gji/ggt410.

Fitch, T., 1975. Compressional velocity in source regions of deep earthquakes: an application of the master event technique. Earth Planet. Sci. Lett. 26, 156–166. http://dx.doi.org/10.1016/0012-821X(75)90083-7.

Gritto, R., Jarpe, S., 2014. Temporal variation of V_p/V_s-ratio at The Geysers geothermal field, USA. Geothermics 52, 112–119. http://dx.doi.org/10.1016/j.geothermics.2014.01.012.

Hainzl, S., Fischer, T., Čermáková, H., Bachura, M., Vlček, J., 2016. Aftershocks triggered by fluid-intrusion: evidence for the aftershock sequence occurred 2014 in West Bohemia/Vogtland. J. Geophys. Res., Solid Earth 121. http://dx.doi.org/10.1002/2015JB012582.

Hainzl, S., Fischer, T., Dahm, T., 2012. Seismicity-based estimation of the driving fluid pressure in the case of swarm activity in Western Bohemia. Geophys. J. Int. 191, 271–281. http://dx.doi.org/10.1111/j.1365-246X.2012.05610.x.

Ito, A., 1985. High resolution relative hypocentres of similar earthquakes by cross-spectral analysis method. J. Phys. Earth 33, 279–294.

Ito, H., De Vilbiss, J., Nur, A., 1979. Compressional and shear waves in saturated rock during water–steam transition. J. Geophys. Res. 89, 4731–4735. http://dx.doi.org/10.1029/JB084iB09p04731.

Kisslinger, C., Engdahl, E., 1973. The interpretation of the Wadati diagram with relaxed assumptions. Bull. Seismol. Soc. Am. 63, 1723–1736.

Konstantinou, K., 2013. Seismicity, V_p/V_s and shear wave anisotropy variations during the 2011 unrest at Santorini caldera, southern Aegean. J. Volcanol. Geotherm. Res. 267, 57–67. http://dx.doi.org/10.1016/j.jvolgeores.2013.10.001.

Lin, G., Shearer, P., 2007. Estimation local V_p/V_s ratios within similar earthquake clusters. Bull. Seismol. Soc. Am. 97, 379–388. http://dx.doi.org/10.1029/2009GL039098.

Lin, G., Shearer, P., 2009. Evidence of water-filled cracks in earthquake source regions. Geophys. Res. Lett. 36, L17315. http://dx.doi.org/10.1785/0120060115.

Maurer, H., Deichmann, N., 1995. Microearthquake cluster detection based on waveform similarities, with and application to the western Swiss Alps. Geophys. J. Int. 123, 588–600. http://dx.doi.org/10.1111/j.1365-246X.1995.tb06873.x.

Mavko, G., Tapan, M., Dvorkin, J., 2003. The Rock Physics Handbook: Tools for Seismic Analysis of Porous Media. Cambridge University Press.

Novotný, J., Málek, J., Boušková, J., 2016. Wadati method as a simple tool to study seismically active fault zones: a case study from the West-Bohemia/Vogtlad region, central Europe. Stud. Geophys. Geod. 60, 248–267. http://dx.doi.org/10.1007/s11200-015-1206-1.

O'Connell, R., Budiansky, B., 1974. Seismic velocities in dry and saturated cracked solids. J. Geophys. Res. 79, 5412–5426. http://dx.doi.org/10.1029/JB079i035p05412.

Popp, T., Kern, H., 1994. The influence of dry and water saturated cracks on seismic velocities of crustal rocks – a comparison of experimental data with theoretical model. Surv. Geophys. 15, 443–465. http://dx.doi.org/10.1007/BF00690169.

Poupinet, G., Ellsworth, W., 1984. Monitoring velocity variations in the crust using earthquake doublets: and application to the Calaveras fault, California. J. Geophys. Res. 89, 5719–5731. http://dx.doi.org/10.1029/JB089iB07p05719.

Růžek, B., Horálek, J., 2013. Three dimensional seismic velocity model of the West Bohemia/Vogtland seismoactive region. Geophys. J. Int. 195, 1251–1266. http://dx.doi.org/10.1093/gji/ggt295.

Scherbaum, F., Wendler, J., 1986. Cross spectral analysis of Swabian Jura (SW Germany) three-component microearthquake recordings. J. Geophys. 60, 157–166.

Wadati, K., 1928. Shallow and deep earthquakes. Geophys. Mag. 1, 162–202.

Wagner, G., Coyle, D., Duyster, J., Henjes-Kunst, F., Peterek, A., Schröder, B., Stöckhert, B., Kemmer, K., Zulauf, G., Ahrendt, H., Bischoff, R., Hejl, E., Jacobs, J., Menzel, D., Nand, L., Van den Haute, P., Vercoutere, C., Welzel, B., 1997. Post-Variscan thermal and tectonic evolution of the KTB site and its surroundings. J. Geophys. Res. 102, 18221–18232. http://dx.doi.org/10.1029/96JB02565.

Waldhauser, F., Ellsworth, W., 2000. A double-difference earthquake location algorithm: method and application to the Northern Hayward Fault, California. Bull. Seismol. Soc. Am. 90, 1353–1368. http://dx.doi.org/10.1785/0120000006.

Walsch, J., 1969. New analysis of attenuation in partially melted rock. J. Geophys. Res. 74, 4333–4337. http://dx.doi.org/10.1029/JB074i017p04333.

Zhang, H., Thurber, C., 2003. Double-difference tomography: the method and its application to the Hayward fault, California. Bull. Seismol. Soc. Am. 93, 1175–1189. http://dx.doi.org/10.1785/0120020190.

AGU PUBLICATIONS

JGR

Journal of Geophysical Research: Solid Earth

RESEARCH ARTICLE
10.1002/2015JB012582

Key Points:
- Three aftershock sequences occurred after 30 years of swarms on the same fault plane
- Mainshocks activated a fault jog and had oblique mechanisms compared to aftershocks
- Mainshock-triggered fluid intrusion explains observed earthquake migration and high activity rates

Correspondence to:
S. Hainzl,
hainzl@gfz-potsdam.de

Citation:
Hainzl, S., T. Fischer, H. Čermáková, M. Bachura, and J. Vlček (2016), Aftershocks triggered by fluid intrusion: Evidence for the aftershock sequence occurred 2014 in West Bohemia/Vogtland, *J. Geophys. Res. Solid Earth*, *121*, doi:10.1002/2015JB012582.

Received 5 OCT 2015
Accepted 18 MAR 2016
Accepted article online 22 MAR 2016

Aftershocks triggered by fluid intrusion: Evidence for the aftershock sequence occurred 2014 in West Bohemia/Vogtland

S. Hainzl[1], T. Fischer[2,3], H. Čermáková[3], M. Bachura[2], and J. Vlček[2]

[1]GFZ German Research Centre for Geosciences, Potsdam, Germany, [2]Faculty of Science, Charles University, Prague, Czech Republic, [3]Institute of Geophysics, Czech Academy of Sciences, Prague, Czech Republic

Abstract The West Bohemia/Vogtland region, central Europe, is well known for its repeating swarm activity. However, the latest activity in 2014, although spatially overlapping with previous swarm activity, consisted of three classical aftershock sequences triggered by M_L3.5, 4.4, and 3.5 events. To decode the apparent system change from swarm-type to mainshock-aftershock characteristics, we have analyzed the details of the major M_L4.4 sequence based on focal mechanisms and relocated earthquake data. Our analysis shows that the mainshock occurred with rotated mechanism in a step over region of the fault plane, unfavorably oriented to the regional stress field. Most of its intense aftershock activity occurred in-plane with classical characteristics such as (i) the maximum magnitude of the aftershocks is significantly less than the mainshock magnitude and (ii) the decay can be well fitted by the Omori-Utsu law. However, the absolute number of aftershocks and the fitted Omori-Utsu c and p parameters are much larger than for typical sequences. By means of the epidemic-type aftershock sequence model, we show that an additional aseismic source with an exponentially decaying strength triggered a large fraction of the aftershocks. Corresponding pore pressure simulations with an exponentially decreasing flow rate of the fluid source show a good agreement with the observed spatial migration front of the aftershocks extending approximately with $\log(t)$. Thus, we conclude that the mainshock opened fluid pathways from a finite fluid source into the fault plane explaining the unusual high rate of aftershocks, the migration patterns, and the exponential decrease of the aseismic signal.

1. Introduction

Earthquake swarms, as specific type of seismic sequences, are characterized by close clustering in time and space and missing dominant events. Instead, several earthquakes of similarly large magnitudes occur so that smaller events are not associated with any identifiable mainshock. Earthquake swarms consist mostly of earthquakes occurring within several hours to several months at varying tectonic environments, both at boundaries of the lithospheric plates and within the plates. The absence of a dominating large event in seismic swarms is usually attributed to the heterogeneity of the stress field and/or weakened crust, which lacks a single well-developed fault and is incapable of sustaining higher strain [*Mogi*, 1963]. A large group of earthquake swarms is related to volcanic activity, but others appear as of purely tectonic origin [*Horálek et al.*, 2015]. As a result, two types of driving force of seismic swarms have been suggested: fluid pressure increase due to migration of magma and other crustal fluids [e.g., *Duverger et al.*, 2015; *Shelly et al.*, 2015] and stress changes associated to aseismic slip [e.g., *Vidale and Shearer*, 2006; *Lohman and McGuire*, 2007].

In contrast to earthquake swarms, typical earthquake clusters occurring at plate boundaries are mainshock-aftershock sequences initiated by a single mainshock, with a magnitude typically one or more magnitude units higher than those of the aftershocks (Båth law) [*Båth*, 1965]. The tectonic environment of aftershock sequences predestinates their driving force, which is the elastic stress readjustment in the area of mainshock [*Lay and Wallace*, 1995]. The aftershock rate R generally decays according to the Omori-Utsu law,

$$R(t) = K_0(c + t)^{-p}, \quad (1)$$

where t is the elapsed time since the mainshock and K_0, c, and p are constants; see *Utsu et al.* [1995] for a review. The exponent p is mostly in the range of 0.8–1.2, and K_0 is known to depend exponentially on M [*Utsu et al.*, 1995; *Hainzl and Marsan*, 2008]. Detailed aftershock studies showed that the delay parameter c

is very small, in the order of one to several minutes or even less [e.g., *Peng et al.*, 2006; *Enescu et al.*, 2007; *Lengliné and Ampuero*, 2015], while larger estimations often result from incomplete recordings directly after the occurrence of larger earthquakes [*Kagan*, 2004]. The Omori-Utsu law has been explained, among others, by the mainshock-induced (i) poroelastic response [*Nur and Booker*, 1972], (ii) afterslip [*Perfettini and Avouac*, 2004], or (iii) delayed earthquake nucleation due to rate- and state-dependent friction [*Dieterich*, 1994; *Stein*, 1999]. The release of pressurized fluids by the mainshock may also contribute to driving aftershock activity as documented by *Miller et al.* [2004] for the 1997 Umbria-Marche seismic sequence in North Appenines, Italy.

Earthquake swarms and mainshock-aftershock sequences usually show exclusive occurrence; in some cases they occur in parallel at broader areas, similarly to the Central Apennines where the year 2009 M_w6.3 L'Aquila earthquake was followed by a swarm in the NW direction from the mainshock [*Chiaraluce*, 2012]. Swarms sometimes also precede large earthquakes like the *M*7.3 Tottori earthquake in 2000 that was preceded by swarms in 1989, 1990, and 1997 whose hypocenters lied at the fault plane of future mainshock [*Ohmi et al.*, 2002]. Partially similar to our studied area, a M_w4.1 mainshock occurred in 2012 in French Alps, 10 km from the area activated by the preceding 2003–2004 Ubaye swarm [*Courboulex et al.*, 2013].

Our study deals with the mainshock-aftershock sequences that occurred 2014 in the West Bohemia/Vogtland region of Central Europe. Hypocenters of the 2014 mainshock-aftershock activity significantly overlap with the hypocenters of swarms that occurred within the previous 30 years on the same fault patch. West Bohemia/Vogtland is an intraplate region which was previously only characterized by repeated occurrence of earthquake swarms and degassing of CO_2 of upper mantle origin [*Fischer et al.*, 2014]. This region is located at an intersection of two regional tectonic structures: NE-SW trending Eger Rift and NNW-SSE trending Mariánské Lázně Fault (Figure 1). Instrumental observations started in early 1960, which were replaced by permanent digital recording at early 1990 since when precise hypocenter locations are available [*Fischer et al.*, 2014]. The seismicity from this period is distributed within a N-S elongated area of 60 × 110 km extent and concentrates in the zone of Nový Kostel (indicated by a rectangle in Figure 1). In this time period, six M_L3+ earthquake sequences have occurred in this zone: swarms in 1985/1986 (maximum M_L of 4.6), 1997, 2000, 2008, 2011, and the most recent sequence in 2014 with maximum M_L of 4.4. Although the activity before 2014 included some embedded mainshock-aftershock sequences [*Hainzl and Fischer*, 2002], previous sequences showed overall typical swarm characteristics. In contrast, the activity in 2014 consisted of three classical mainshock-aftershock sequences related to mainshocks with local magnitude of 3.5 (24 May), 4.4 (31 May), and 3.5 (3 August) which triggered Omori-Utsu-type aftershock activity. On top of the nonswarm character of these sequences, their hypocenter locations overlapped significantly with the hypocenters of previous swarms (Figure 1), which opens the question of the generating mechanisms of the earthquakes, which creates either swarms or mainshocks at the same fault segment. To reveal the underlying processes, we analyze in this study the focal zone geometry, source mechanisms, and the spatiotemporal evolution of the most intense mainshock-aftershock sequence related to the largest M_L4.4 event.

2. Earthquake Data and Processing

We used data recorded by the WEBNET seismic network that consists of 13 telemetered and 9 autonomous seismic stations sampled at 250 Hz with seismograms proportional to the ground velocity in the frequency band of at least 1 - 80 Hz [*Fischer et al.*, 2010]. The analyzed seismic catalog of the 2014 activity was obtained by supplementing the manually processed data with automatic picks provided by the Pepin picker and locator. It is based on the method of *Fischer* [2003a, 2003b], which is implemented at WEBNET real-time preprocessing (http://ig.cas.cz/en/structure/observatories/west-bohemia-seismic-network-webnet/map-epicenters). The automatic and manual catalogs were combined using the criterion of unique origin times. The precision of arrival time measurements and related location quality were homogenized by delay times for pairs of events measured using cross-correlation technique and double-difference relocation. To this purpose, waveforms were filtered to a frequency band 1–10 Hz (three-pole Butterworth band-pass filter) or 1–7 Hz when an event with magnitude higher than M_L3 occurred in the correlated event pair. Time intervals of 1 s and 1.5 s duration centered at the measured *P* and *S* arrival times, respectively, were trimmed and cross correlated to obtain absolute arrival time difference for *P* and *S* waves. Resulting arrival time differences along with the cross-correlation coefficients as weighting factors were used as inputs for hypoDD relocation [*Waldhauser and Ellsworth*, 2000; *Waldhauser*, 2001]. As a result, the combined 2014 catalog comprised 3757 relocated events of which 1902 were processed manually and 1855 automatically; the automatically obtained events contributed only to the magnitude level below M_L 1.8.

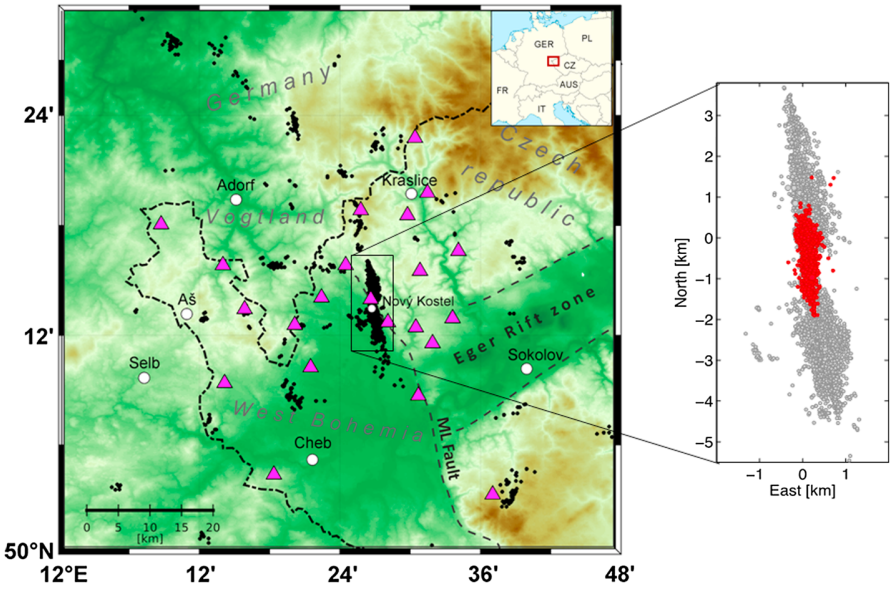

Figure 1. The area of West Bohemia Vogtland; rectangle indicates the Nový Kostel zone with dominating seismic activity. The 2014 hypocenters are indicated by red; the hypocenters of previous swarms are gray, and triangles refer to the seismic stations of the WEBNET.

Focal mechanisms of the 2014 activity were determined by the AMT code [*Vavryčuk*, 2009] that inverts the *P* wave amplitudes for full moment tensor; here we use the double-couple part only. At least 14 stations were used for determining the focal mechanisms, and the stability of the solution was tested by omitting individual stations from the data set. We chose the optimum fault plane from the two nodal planes using the fault instability criterion [*Vavryčuk*, 2014], which is based on comparing the proximity of the stress state to the failure envelope in the Mohr-Coulomb diagram.

3. Results

Figure 2a shows the temporal evolution of the 2014 earthquake activity which started on 24 May 2014 at 14:35 UTC by a M_L3.5 earthquake occurring after a long period of quiescence; only two small events occurred in the Nový Kostel area within 1 week prior to this event, and no activity was observed few months before. This earthquake was followed by 170 aftershocks located in the near vicinity of the mainshock. The aftershock activity ceased after few hours followed by a period of relative quiescence until the second mainshock on 31 May 2014. This M_L4.4 earthquake was the largest in the sequence; it occurred at 10:37 UTC and was preceded by a single M_L1.3 foreshock 2 h ahead. Its aftershock sequence lasted for a week and involved almost 3000 located events. Sporadic seismic activity in the next 2 months culminated by the third mainshock on 3 August 2014, 23:58 UTC with M_L =3.5, which was preceded by about 10 M_L <1 events occurred a few hours before and triggered itself about 440 aftershocks. The moment magnitudes were M_w3.4, 3.8, and 3.4 for the 24 May, 31 May, and 3 August mainshocks (V. Vavryčuk, personal communication and U.S. Geological Survey, 2015).

3.1. Frequency-Magnitude Distribution

The frequency-magnitude distribution of the sequence is shown in Figure 3, indicating a Gutenberg-Richter distribution with a *b* value of approximately 1.2 for magnitudes $M_L \geq 1$, while the deviation for M_L <1 events might be related to partial incompleteness. In the same figure, the distribution is also shown for the aftershocks occurred in the first 10 days after the M_L4.4 mainshock. Here we ignored the first aftershocks, because of the typical incompleteness of earthquake catalogs directly after mainshocks [*Kagan*, 2004]. For $M_L \geq 1$ events, the incompleteness period *t* is approximately 50 min for a mainshock of $M = 4.4$ according to the empirical dependence of the completeness magnitude M_c on time (in days) and mainshock magnitude, $M_c(M, t) = M - 4.5 - 0.75 \log(t)$, derived for aftershock sequences in California [*Helmstetter et al.*, 2006]. The frequency-magnitude distribution of the aftershocks is found to have a very similar trend as the overall distribution, indicating a completeness magnitude of at least M_c =1.0. We use this conservative threshold

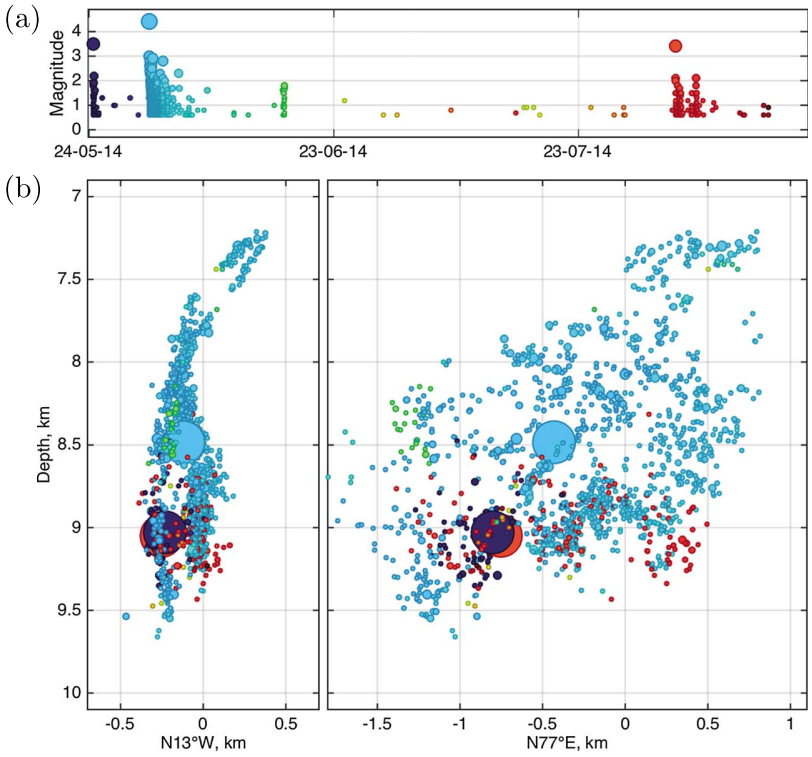

Figure 2. (a) Magnitude-time plot of the 2014 sequence and (b) two vertical sections oriented across and along the hypocenter trend, where symbol size is proportional to magnitude; the size of main shocks is exaggerated. Events are color coded according to their occurrence times.

for later model fits requiring complete data, while all events are used to study the spatial distribution and migration pattern. The resolved *b* value of 1.2 lies in the upper part of the *b* value interval reported for West-Bohemia/Vogtland swarms. The existing studies [e.g., *Neunhöfer and Hemmann*, 2005] found *b* values ranging from 0.5 to 1.5 with temporal variations; the most striking was probably the decrease of *b* from about 1.3 in the beginning of the 2000 swarm down to 0.8 in the second swarm period that was accompanied by the increase of the mean seismic moment [*Hainzl and Fischer*, 2002]. Hence, the 2014 mainshock-aftershock sequence is not anomalous in terms of the *b* value level, compared to the previous swarm-like seismicity.

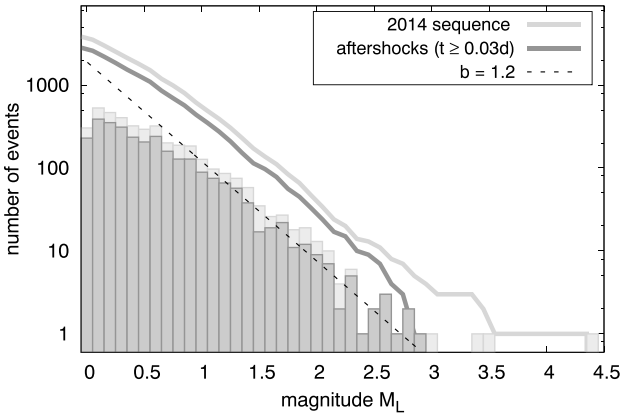

Figure 3. Frequency-magnitude distribution of the whole activity (light color) and the first 10 days of aftershock activity following the M_L 4.4 event (dark color). The dashed line refers to a Gutenberg-Richter relation with $b = 1.2$. The bar diagram shows the corresponding histogram of the magnitudes.

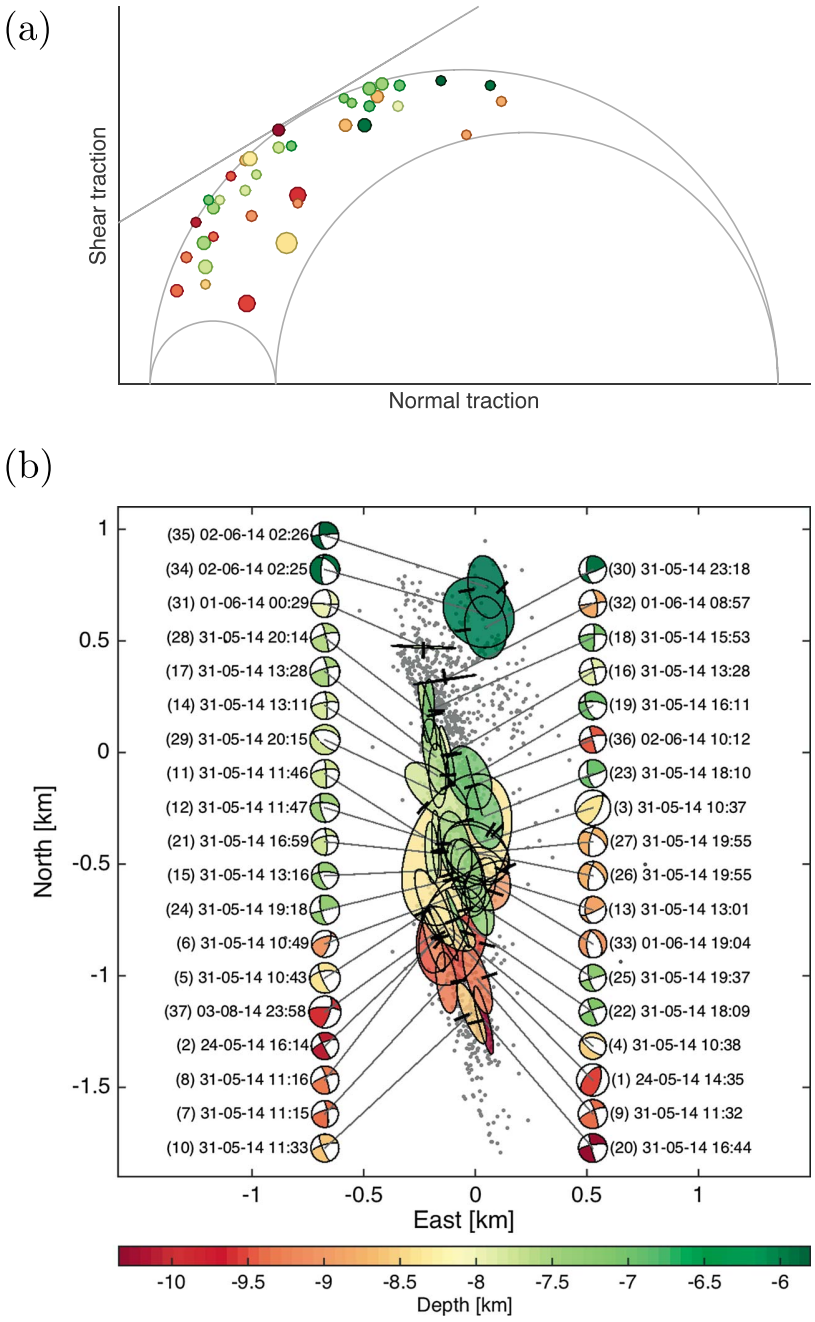

Figure 4. Source mechanisms of the $M_L \geq 2$ events occurred during the sequence in the year 2014: (a) Mohr-Coulomb plot showing the shear and normal tractions resolved on the optimal fault planes indicated in Figure 5b; where a friction coefficient of 0.6 and the regional stress of *Vavryčuk* [2014] are assumed. Note that the fault planes of the three mainshocks (large red and yellow circles) are the most stable showing one of the largest perpendicular distances to the failure envelope. (b) Epicenters (gray points) and focal mechanisms, where the ellipses show the optimal fault planes selected by the instability criterion; their size is scaled with magnitude. Horizontal projection of circular rupture is shown with short line indicating the dip direction. Mainshocks are indicated by numbers 1, 3, and 37.

3.2. Spatial Distribution

The activity in 2014 occurred on an inclined planar structure within an oval area of 2.5 × 2.5 km size centered at 8.5 km depth (Figure 2b). While the subsequences related to the two $M_L = 3.5$ mainshocks occurred only in the deeper part of the plane, the aftershocks of the M_L4.4 event extended over the whole area. However, all

sequences activated two parallel clusters, which are separated by a gap of few hundred meters length, where the southern cluster was activated first followed by the northern cluster. The lower parts of the two clusters can be approximated by two subvertical planes with an offset of about 250 m. The mainshocks themselves occurred all near to this gap between the two clusters, less than 500 m apart from each other. The mainshocks thus appear to be related to the offset/jog of a preexisting fault plane. It is of interest that the first and last mainshock locations overlap which is verified by bootstrap estimates of the location error. It is hard to distinguish these two mainshock locations, while the largest M_L4.4 mainshock of 31 May has a clearly distinct position.

The focal mechanisms of $M_L \geq 2$ events occurred during the largest sequence are quite self-similar with prevalence of oblique strike-slip events whose fault planes match the NNW-SSE trend of hypocenters (Figure 5b). The fit is, however, interrupted by the fault jog pronounced also in the offset of ellipses indicating the fault planes. Note that the whole Nový Kostel fault zone trends 169° [*Fischer et al.*, 2014] with the typical strike of 355° and 164° for oblique normal events and oblique reverse events, respectively [*Čermáková and Horálek*, 2015], which is consistent with most of the 2014 focal mechanisms. It should be noted that the estimated source mechanisms of this sequence show negligible isotropic component of about 15%; however, their CLVD component ranges from 10 to 70%, which points to the possible unequality of the fault surfaces or inconsistency in the data or velocity model. Anyway, this would have no significant impact on our study, which is based on the more stable double-couple part represented by the angles of the fault planes. Despite the general homogeneity of the estimated focal mechanisms, a few events (1, 5, 8, 28, 29, 32, and 33) show anomalous solutions with different strike and a large normal or reverse component. These anomalous events include all the three mainshocks with preferred rupture planes striking 25–41° (dip = 56–65°, rake = 64–73°), which intersect the two parallel fault planes of the southern and northern clusters striking 347°.

Displacement spectra of three mainshocks were inverted for corner frequencies and station-specific attenuation using the approach of *Michálek and Fischer* [2013] (Figure 4). It appears that despite the different low-frequency level, the spectra are quite self-similar with f_c ranging from 7.5 to 10 Hz; the largest M_L4.4 mainshock showing the medium corner frequency. This points to quite small source areas with rupture radii in the interval from 110 to 150 m and high stress drops ranging from 20 to 120 MPa. Large stress drops exceeding 100 MPa with prevailing values 10–20 MPa have been already reported for previous swarms in this area [*Michálek and Fischer*, 2013]. It should be noted that the small rupture size of the mainshocks is consistent with the focal geometry where the rupture fits well in the fault step over of about 250 m (Figures 2 and 6).

We fitted a plane to the hypocenters of the 2014 earthquakes occurred deeper than 8 km. The least squares fit results in a strike of 356.0° and a dip of 85.4° for this plane. Figure 6 shows the projection of the hypocenters on this plane, color coded by their perpendicular distance. The geometrical step over of the fault at the location of the largest mainshock hypocenter is clearly visible. Furthermore, we compared the mainshock rupture plane given by the focal mechanism solution (strike = 25°, dip = 56°) with this plane fitted to the hypocenter distribution of the earthquake sequence. In particular, we similarly color coded the perpendicular offset of the mainshock rupture plane in the inset of Figure 6. It shows that the mainshock rupture plane nicely connects the location of the hypocenters of one side of the gap with those on the other side, supporting our conclusion that mainshock rupture interconnected both fault planes.

The Mohr-Coulomb diagram in Figure 5a shows the tractions for the estimated focal mechanisms of the $M_L \geq 2$ events. Here we assumed a regional stress field characterized by azimuth/plunge of 139°/35° and 233°/6° for σ_1 and σ_3, respectively, and a shape ratio of 0.8 [*Wirth et al.*, 2000; *Vavryčuk*, 2014]. It appears that the fault planes of all three mainshock are strongly unfavorably oriented to the regional stress with the smallest instability value of all analyzed events.

Because of its unfavorable orientation, the fault jog likely acted as a barrier which did not rupture during previous swarm occurrences on the fault plane. However, previous activity might have facilitated the shear failure of this unfavorably oriented mainshock mechanism. To verify this, we tested a simplified model of this geometry by considering a step of a vertical fault with an offset of 300 m in fault perpendicular and 400 m in strike direction. By means of the analytic formulas for an elastic half-space [*Okada*, 1992; *Toda et al.*, 2011], we found that precursory activity on both sides of the fault leads in this case to an increased Coulomb stress for the mainshock mechanism in the step over. Assuming a friction coefficient of 0.6 and two M_w3.4 events on both parts of the fault with stress drop of 20 MPa, a mean Coulomb stress increase of 0.3 MPa is found at the oblique link of the two faults. Vice versa, slip in the step over region with the mainshock mechanism is found

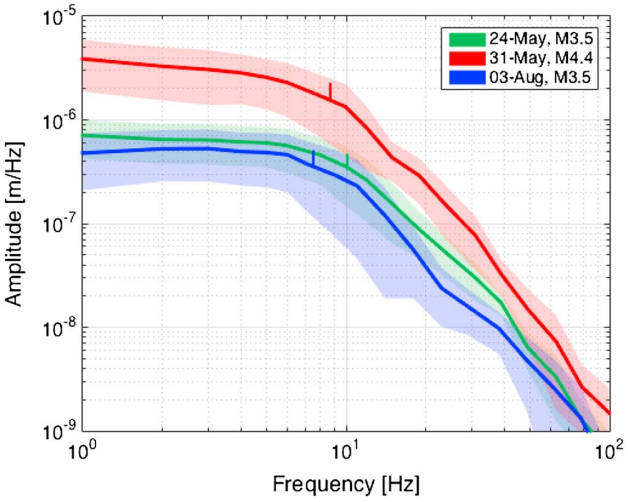

Figure 5. Displacement spectrum of the three mainshocks obtained as the mean value of spectra of 11 stations corrected for station-specific attenuation; shaded areas indicate the standard deviations. Corner frequencies obtained similar to *Michálek and Fischer* [2013] are indicated by vertical bars.

in the same model to increase the Coulomb failure stress for slip on the fault segments, as expected for static stress triggering of aftershocks [*Stein*, 1999].

3.3. Temporal Distribution

Figure 7 shows the sequences observed in the years 2008, 2011, and 2014, where each is stacked relative to the occurrence time of the largest earthquake. The comparison demonstrates that the sequence in 2014 was extraordinary in its characteristics consisting of (i) a rapid onset of the activity at the mainshock time, (ii) a strong decay of the activity after the mainshock, and (iii) a significant gap between mainshock magnitude and the magnitudes of the other events. None of these characteristics, which point to a typical mainshock-aftershock sequence, is observed for the two preceding sequences occurred in the same location. In the following, we quantify the characteristics of the 2014 seismicity in detail. Here we concentrate on the most active mainshock-aftershock sequence related to the M_L4.4 mainshock which allows a meaningful statistical evaluation.

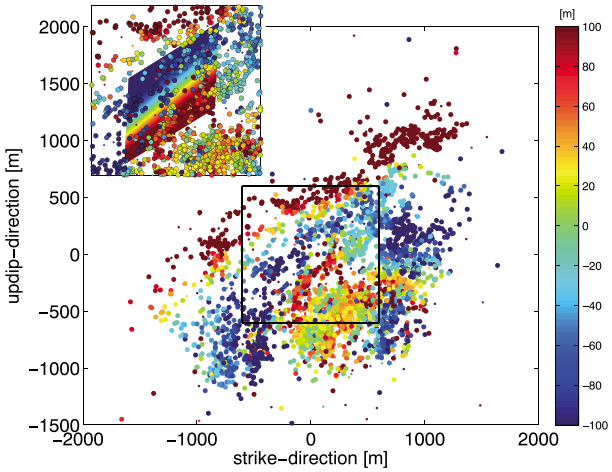

Figure 6. Projection of the hypocenters on the fitted plane, where the mainshock is positioned at the origin of the local coordinate system. The plane-normal distances are color coded highlighting the geometrical discontinuity in the mainshock area. Large points refer to hypocenters with location errors less than 5 m. The inset shows the region marked by the box with the surface representing the mainshock rupture plane according to the inverted focal mechanism, where colors refer to the perpendicular distance of the mainshock rupture plane to the plane fitted to the earthquake hypocenters. The mainshock rupture size corresponds to stress drop of approximately 20 MPa.

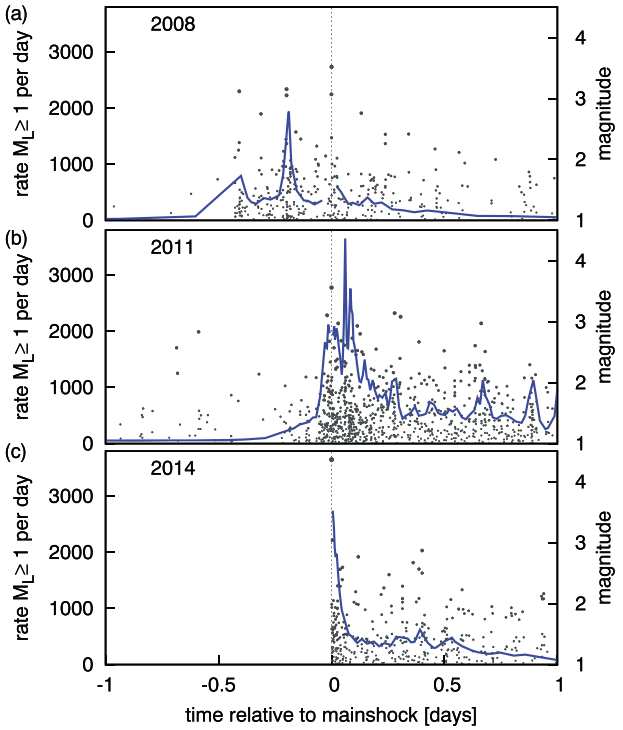

Figure 7. Rate of $M_L \geq 1.0$ events (lines) as function of time relative to the largest earthquakes observed in the years (a) 2008, (b) 2011, and (c) 2014. In all plots, rates are calculated for 30 subsequent events with a step size of 10, while points indicate the magnitudes of the events with scale on right.

3.3.1. Omori-Type Aftershock Decay

We fitted the Omori-Utsu law (equation (1)) to the first 10 days of the $M_L \geq 1$ aftershocks following the M_L4.4 mainshock. The maximum likelihood estimation [see, e.g., *Utsu et al.*, 1995] yields the parameters $K_0 = 4.1 \cdot 10^4, c = 2.0$ days, and $p = 5.1$. Figure 8 shows that the aftershock activity can be very well fitted after 0.3 days indicating a classical aftershock sequence. However, the aftershock productivity is found to be unusually high. To demonstrate this, we compare in Figure 8 the observed number with the Reasenberg-Jones aftershock model derived for aftershock sequences in California [*Reasenberg and Jones*, 1994], showing that the productivity exceeds the expectation of this standard model by more than a factor of 3. In addition to

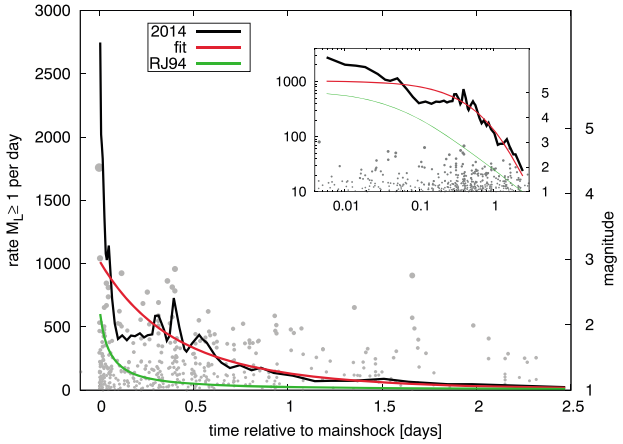

Figure 8. Aftershock decay following the year 2014 mainshock (see Figure 7c) in comparison to the fit of the Omori-Utsu law ($c = 2.0$ days, $p = 5.1$) and the average empirical aftershock decay in California according to the RJ94 model [*Reasenberg and Jones*, 1994]. The inset presents the result in double logarithmic scale.

Table 1. Estimated ETAS Parameters for $M \geq 1.0$ Events Where Lowest AIC Values Indicate the Best Fit, and the Background Fraction Gives the Fraction of Aftershocks Which Are Associated to the Background Forcing[a]

	Background	Fraction	K	c [s]	α	p	AIC
Nonparametric	$n_{opt} = 15$	0.49	0.0038	24.2	0.35	1.46	−4076.1
… with fixed α	$n_{opt} = 10$	0.59	0.0007	26.8	1.0	1.52	−4041.9
… with fixed p, α	$n_{opt} = 3$	0.75	0.0025	0.3	1.0	1.0	−3999.2
Exponential fit	$0.7 + 418\exp(-1.49t)$	0.62	0.00002	61.3	0.31	2.37	−4086.6
… with fixed α	$0.6 + 445\exp(-1.51t)$	0.65	0.0002	35.4	1.0	1.74	−4043.1
… with fixed p, α	$0.0 + 498\exp(-1.81t)$	0.59	0.0045	0.7	1.0	1.0	−3977.2
Constant	0.08	0.001	0.025	38.0	0.33	1.27	−4037.9
… with fixed α	≈0.0	≈0.0	0.0066	28.5	1.0	1.25	−3973.4
… with fixed p, α	≈0.0	≈0.0	0.012	2.6	1.0	1.0	−3900.6

[a] In the case of nonparametric fits, n_{opt} refers to the value of smoothing parameter n leading to the minimum AIC value provided in the last column.

the productivity, the shape of the decay is also unusual: The exponent $p = 5.1$ is much higher than typical p values of aftershock sequences which are found to range in the interval 0.8–1.2 [*Utsu et al.*, 1995; *Hainzl and Marsan*, 2008], and the c value is much larger than the incompletely recorded time interval after the mainshock. Note that the high values are likely related to the almost constant rate of observed events within the first half-day and the trade-off between the c and p value estimation [*Holschneider et al.*, 2012]. Furthermore, secondary aftershock activity triggered by aftershocks themselves might have also affected the decay.

3.3.2. Aseismic Forcing

Now we test whether the observed seismicity can be solely explained by aftershock triggering, or an additional aseismic source is required to fit the activity. Here we consider the empirical observation that not only the mainshock but also aftershocks themselves can trigger Omori-Utsu-type aftershock sequences, where the productivity scales exponentially with the event magnitude. This is the basic assumption of the epidemic-type aftershock sequence (ETAS) model [*Ogata*, 1988], describing the seismicity rate $R(t)$ as superposition of a constant (tectonic) background rate μ and aftershock rates according to

$$R(t) = \mu(t) + \sum_{i:t_i<t} K\, 10^{\alpha(M_i - M_c)}\, (c + t - t_i)^{-p}\,, \tag{2}$$

where t_i and $M_i \geq M_c$ are the occurrence times and local magnitudes of the observed earthquakes. In the case of the occurrence of an aseismic source such as transient creep or pore pressure changes, the seismicity is additionally forced and the background rate $\mu(t)$ becomes time dependent [*Hainzl and Ogata*, 2005]. We apply the approach of *Marsan et al.* [2013], which has been further tested and applied by *Hainzl et al.* [2013] to detect aseismic forcing, if occurred, by statistically separating $\mu(t)$ from the activity related to earthquake-earthquake interactions. The methodology uses an iterative optimization procedure to estimate the triggering parameters K, α, c, and p and the background rate $\mu(t)$ simultaneously via maximum likelihood estimation. In each iteration, the probability of every event to be triggered by the background rate is determined by $\mu(t)/R(t)$ [*Zhuang and Ogata*, 2004]. Then $\mu(t)$ is recalculated at the occurrence time of events based on these probabilities and the time interval of the $\pm n$ neighbors. Thus, n defines the smoothing window of the $\mu(t)$ estimate. The algorithm is iterated until convergence, and the optimal smoothing parameter n is determined by the Akaike Information Criterion (AIC).

We apply this method to the earthquake sequence of $M_L \geq M_c = 1$ events of the mainshock sequence in the time interval [−1 10] days relative to the M_L4.4 event, ignoring the time period directly after the occurrence of the mainshock which is potentially incomplete according to the empirical relation of *Helmstetter et al.* [2006]. The result shows (Table 1) that the best fit with minimum AIC is obtained for transient aseismic forcing with optimal smoothing parameter of $n = 15$ neighbors. The corresponding ETAS parameters yield now a small c value (approximately 30 s) and $p = 1.46$ as shape parameters of the Omori-Utsu law. The latter is still higher than 1 but close to typical values, while the inverted α value of 0.35 is significantly smaller than those values observed for typical aftershock sequences. However, smaller α values have been previously found to be indicative for swarm activity.

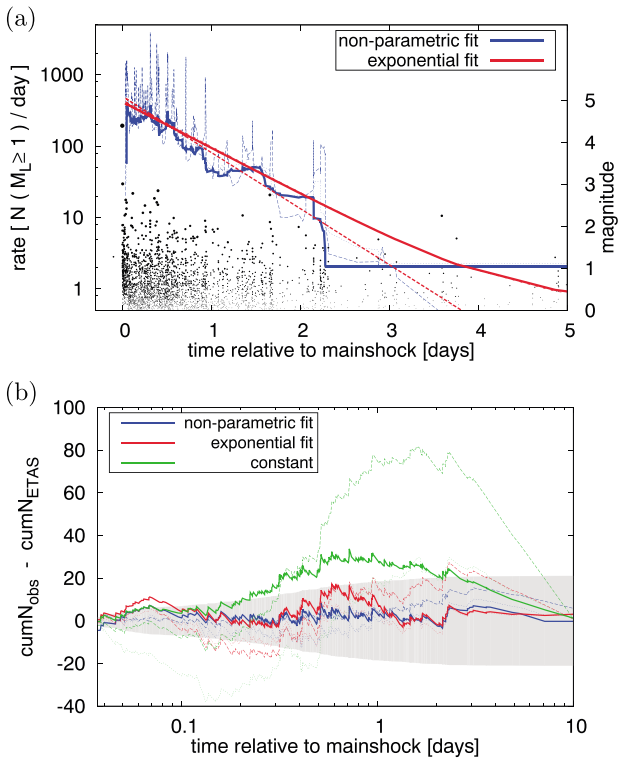

Figure 9. ETAS fit as function of time: (a) Inverted background rate and occurred earthquakes (points) with magnitude scale on the right. (b) The difference between the observed and modeled cumulative number of $M_L \geq 1$ aftershocks, where the potentially incomplete time period directly after the mainshock ([0, 0.034] days) is ignored in both cases. Results are shown for the ETAS model (equation (2)) with nonparametric (blue), exponential function (red), and constant (green) background rate, where solid lines refer to the fit with all parameters while dotted and dashed curves refer to the results with fixed $\alpha = 1$ and $p = \alpha = 1$, respectively. Note that the values of the estimated constant background rate are not shown in Figure 9a but can be found in Table 1. The shaded gray area in Figure 9b refers to ± 1 standard deviation assuming a Poisson distribution with the observed number of events.

To check the influence of these parameters, we additionally performed the maximum likelihood fit with fixed α or/and p values set to typical values at tectonic plate boundaries ($\alpha = p = 1.0$). The results show that in all cases, a time-dependent background rate is also clearly preferential indicated by AIC values which are at least 38 units smaller than the corresponding values for the ETAS model with constant μ (which is also shown in Table 1). However, the model with free p and α values gives a significantly better fit based on the AIC values. In all cases, the aseismic forcing is identified to have triggered a substantial part of the observed seismicity. In particular, the estimated fraction of earthquakes associated to the aseismic transient source is found to range between 50% and 75% of the total activity. Besides more reasonable Omori-Utsu parameters, the transient aseismic forcing can thus also explain the unusually high aftershock productivity.

The inverted background rates are shown by blue lines in Figure 9a. To evaluate the quality of the corresponding fit of the ETAS model, Figure 9b shows, as function of time, the difference between the observed cumulative number of $M_L \geq 1$ events and that expected by the ETAS model (i.e., integration of equation (2)). The visual comparison shows that the ETAS model with time-dependent background fits the observation well, while the standard ETAS model with constant background results in strong deviations. Interestingly, the estimated time-dependent aseismic rates seem to follow approximately an exponential decay corresponding to a linear decay in the semilogarithmic plot of Figure 9a. Thus, we directly test a model with parameterized exponential background rate in the form $\mu(t) = \mu_0 + c_1 e^{-c_2 t}$. It turns out that this model is preferred based on the AIC value which is smaller than that of the best nonparametric version of $\mu(t)$ (Table 1 and red lines in Figure 9). While the absolute fit (likelihood value) is slightly worse in the case of the exponential model, the number of free parameters is significantly reduced, and thus, it is preferred by the information criteria, compliant with the Occam's razor principle. Accordingly, this result leads to the conclusion that an aseismic

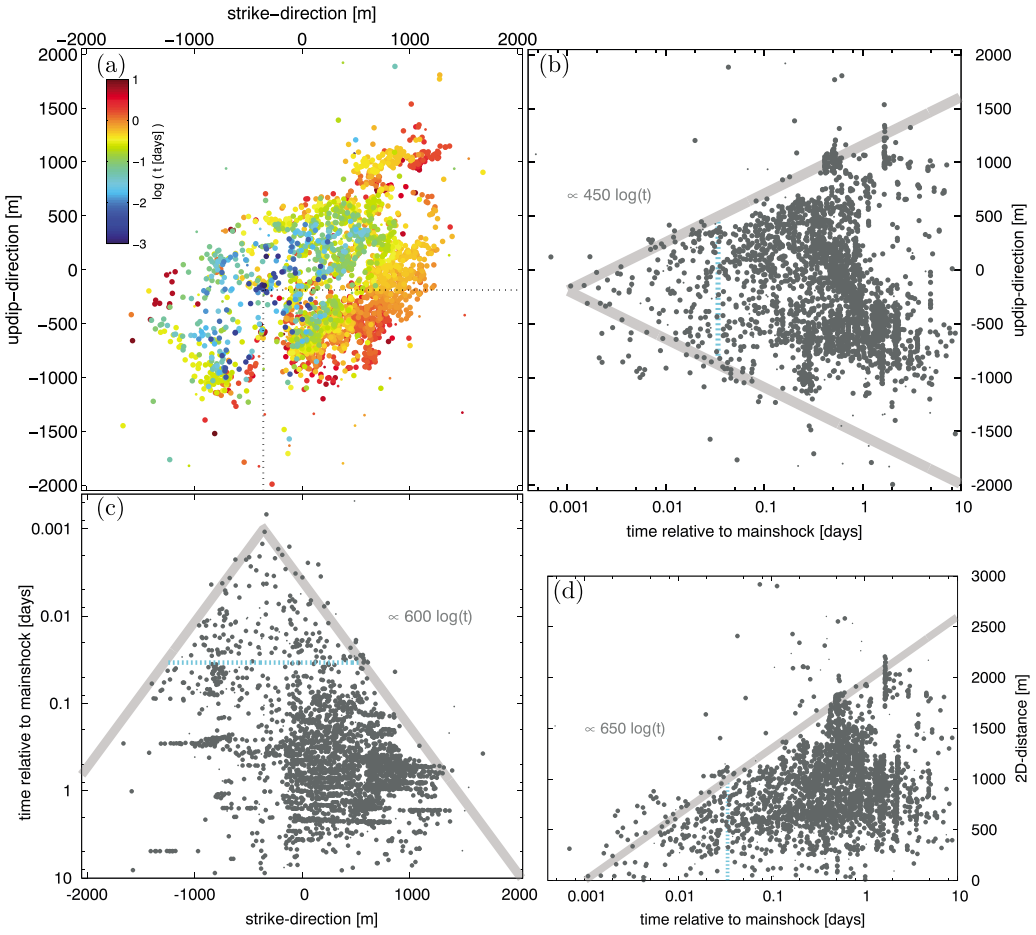

Figure 10. Migration of the first 10 days aftershock activity following the *M*4.4 mainshock: (a) Hypocenters projected on the plane with colors referring to the time relative to the mainshock. (b and c) The locations are shown as a function of time relative to the mainshock in strike and dip direction. Note that the mainshock occurred at the origin of the local coordinate system. (d) The 2-D distances measured to the reference point marked in Figure 10a by dotted lines. Large points indicate hypocenters with location errors $\leq$ 5 m. Gray lines refer to the functional growth denoted in the corresponding plots. The dashed lines in Figures 10b and 10c indicate the end of the first 0.034 days period which is likely incomplete. The catalog incompleteness might explain the sparser density of locations in the first period.

process has been initiated at the same time as the mainshock with a triggering potential that decayed approximately exponentially in time.

3.4. Spatiotemporal Migration

In addition to the inverted temporal signal of the aseismic source, the spatiotemporal migration of the hypocenters can help to reveal the underlying process. In Figure 10a, the projections of all hypocenters on the fitted plane are color coded according their occurrence times. A clear spreading of the hypocenters is visible, which becomes even clearer by analyzing the in-plane distances. In Figures 10b and 10c, the spatial distances relative to the M_L4.4 hypocenter are shown as a function of log(t) for the dip and strike direction. A clear symmetrical and approximately linear growth is observed in both directions. Such a log(t) expansion of the aftershock zone has been previously observed for the early aftershocks of the 2014 *M*6 Parkfield event [*Peng and Zhao*, 2009]. It has also been forecasted for faults governed by rate-state-dependent friction, where the rupture of the mainshock asperity triggers postseismic creep in the surrounding velocity-strengthening region (creep zone). Simulations show that this creep leads to a log(t) migration front of aftershocks which are triggered in smaller embedded asperities [*Kato*, 2007]. However, in contrast to these simulations and the Parkfield case, the migration seems to start in our case from a point (or areal source with small dimension) and the final extension of the hypocenters is several times larger than in the beginning. The central point of this migration is located 360 m south and 190 m downdip of the mainshock hypocenter, which is on the left end

of the mainshock rupture plane plotted in the inset of Figure 6. While the simulations with expanding creep show only an approximately twofold increase of the initial source radius within the first 10 days [*Kato*, 2007], based on the source radius estimate of 130 m, the increase is significantly larger (at least tenfold) in our case. In the following, we thus provide an alternative explanation of the observed migration pattern by means of poroelastic stress changes related to fluid intrusion, which might also be applicable for sequences observed in other places in the world.

3.5. Pore Pressure Modeling

The area of interest is typified by strong CO_2 degassing; the total flow rate in mofettes and mineral springs is estimated more than 500 m^3/h [*Geissler et al.*, 2005]. The isotopic signatures of He and C show mantle origin of the gas [e.g., *Braeuer et al.*, 2007], which indicates its possible involvement in the faulting process. Further indications of the role of fluids came from the analysis of the spatiotemporal patterns of previous swarms showing clear hypocenter migration and reloading [*Parotidis et al.*, 2003; *Hainzl et al.*, 2012]. An intrusion of fluids or magma has thus been suggested to be a driving force of previous activity in this region. New evidence for the involvement of fluids in local seismicity triggering comes from the observation of a sudden increase of CO_2 flow in a nearby mofette during the studied sequence of 2014 (J. Heinicke, personal communication, 2015). Accordingly, we try to model the migration of the aftershock hypocenters by pore pressure changes related to an intrusion of fluids, starting with the occurrence of the M_L4.4 mainshock. For that, we use the knowledge that the rate of events triggered in the whole activated area is generally proportional to the flow rate in the case of fluid injections based on theoretical reasoning and empirical observations [*Shapiro et al.*, 2013; *McGarr*, 2014]. Combining this assumption with our ETAS-based observation that the earthquake rate related to the aseismic source decayed exponentially with time after the mainshock, the injection flow rate should be an exponential function. Note that such an exponentially decaying flow rate is expected for the successive emptying of an overpressured fluid reservoir. We assume that the corresponding fluid migration is then limited to a rather thin damage zone of the fault, leading to a quasi two-dimensional pore pressure diffusion. In particular, based on the results of ETAS modeling, we assume, according to above consideration, that fluid intrusion starts at time $t = 0$ (mainshock time) with a flow rate $q(t) = C\exp(-1.5t)$ (see Table 1) at the central point of the migration patterns (see Figure 10). For simplicity, we set the initial flow to $C = 1$ L/s. Integration of the flow rate over time leads to a total injected volume of 58 m^3, which is rather small compared to volumes injected by humans, e.g., in scientific experiments at KTB (200 m^3), hydraulic fracturing ($\sim 10^4$ m^3), or waste water disposals ($10^4 - 10^6$ m^3) [*McGarr*, 2014]. However, all resulting pressures would be simply scaled by C if this proportionality factor is set to another value.

In the case of instantaneous triggering and uniformly distributed criticality values (i.e., the differences between the stress state and the instability threshold), the rate of triggered earthquakes in a particular location is expected to be proportional to the rate of Coulomb stress increase, $dCFS/dt \sim dp/dt$, considering a simple clock advance [*Hainzl et al.*, 2010]. Note that this is in agreement with the assumption that the total seismicity rate is proportional to the flow rate, because the spatial integration of the solution of dp/dt can be shown to yield a constant which is proportional to the flow rate in the case of the analytic solution of $p(r, t)$ in response to a step change of the flow rate [*Rudnicki*, 1986; *Segall and Lu*, 2015]. As function of the distance r to the injection point, the affected area increases with the distance r; in particular, in case of a 2-D fault zone, the area A of an annulus with mean radius of r and a width of Δ is $A = 2\pi r\Delta$ and thus proportional to r. Assuming a spatially uniform distribution, the number of nucleation sites N is consequently assumed to linearly increase with the value of r, $N \propto r$. Thus, the total rate of triggered earthquakes at distance r is expected to be proportional to $r \cdot dp/dt$.

We utilize the analytic solution for the pore pressure evolution in a poroelastic medium in response to a step change of the flow rate [*Rudnicki*, 1986; *Segall and Lu*, 2015] by discretizing $q(t)$ in time steps of 0.001 days and summing the analytic solution for the corresponding step changes of the flow rate. Here we assumed the same parameters as *Segall and Lu* [2015] for the drained and undrained Poisson's ratios ($\nu = 0.25, \nu_u = 0.3$), the shear modulus (20 GPa), and the Biot coefficient (0.31). The hydraulic diffusivity D is left as the only free fitting parameter.

For $D = 10$ m^2/s, the pressure expansion is found to be in good agreement with the observed hypocenter distances relative to the central point of the aftershock sequence. The corresponding pore pressure field $p(r, t)$ is shown in Figure 11a, and $r \cdot dp/dt$ is compared in Figure 11b to the occurrences of the observed events. The result shows that the apparent $\log(t)$ migration is reproduced in its main parts: The onset as well as the stop

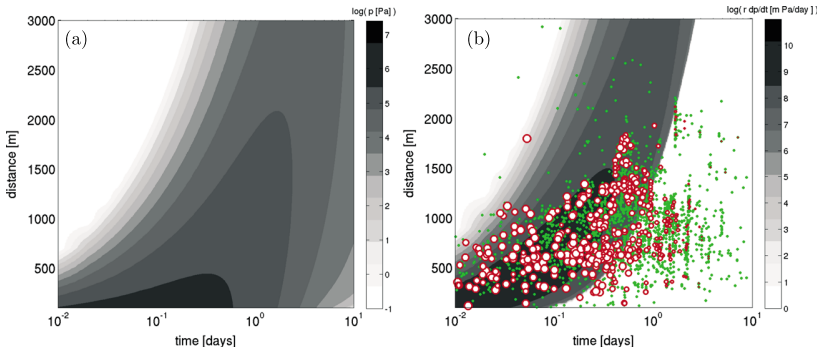

Figure 11. (a) Pore pressures as a function of time resulting from an injection with exponentially decaying flow rate in a fault zone with hydraulic diffusivity of $D = 10$ m^2/s. (b) Time derivative of the pressure scaled by distance, $r \cdot \mathrm{d}p/\mathrm{d}t$, where small green crosses refer to $M_L < 1$ events and red circles refer to $M_L \geq 1$ events with size proportional to the ETAS-determined probability to be triggered by the aseismic source and not by precursory earthquakes.

of activity at different distances corresponds well with the field of positive pore pressure change (Figure 11b), despite from our simplified approximations. For example, a finite source of radius 300 m would simply shift the calculated pressure field by 300 m which would even better fit. Nevertheless, the simple model already explains most of the activity. In Figure 11b, the scaled pressure increase rates are particularly compared to the ETAS-based probability of the events to be triggered by the background rate which is here related to the pressure changes. For $M_L \geq 1$ events, the symbol size represents this probability which is given as the ratio of the background rate to the total seismicity rate by $\mu(t)/R(t)$ [*Zhuang and Ogata*, 2004] and calculated for the parameters of our best fitting ETAS model (equation (2)), namely, the model with exponential aseismic forcing (see Table 1). A good agreement between the $r \cdot \mathrm{d}p/\mathrm{d}t$ field and the probability to be triggered by the aseismic source is found. In particular, the majority of earthquakes associated to the aseismic source occur where the pore pressure model predicts high rates. In contrast, events occurred where $r \cdot \mathrm{d}p/\mathrm{d}t$ predicts low external forcing are very likely triggered by the mainshock or its aftershocks according to the result of the ETAS model. Anyway, some late events could be also directly explained by pore pressure changes, if some delayed triggering mechanism applies such as rate-and-state-dependent nucleation [*Dieterich*, 1994].

4. Discussion and Conclusions

We analyzed the mainshock-aftershock sequences occurred in May–August 2014 in West Bohemia/Vogtland in order to reveal the origin of this type of seismicity in a typical location of repeated swarm activity. Our detailed investigation of the M_L4.4 sequence uncover some important characteristics:

a. The mainshock occurred at a fault jog and its rupture showed the most unfavorable orientation to the regional stress field of all the analyzed events. It has interconnected two preexisting parallel fault segments activated by aftershocks whose ruptures were optimally oriented.
b. The aftershock decay is anomalous in its high activity level and its shape, which is both explained by the identified strong aseismic driving force which decayed almost exponentially since the mainshock and triggered the majority of aftershocks.
c. The striking migration patterns of the aftershocks can be well modeled by pore pressure diffusion along a 2-D fault due to fluid intrusion.

Accordingly, we interpret the mainshock-aftershock sequence as a result of combined action of tectonic stress, Coulomb stress change due to mainshock rupture, and migration of overpressurized fluids along the preexisting fault planes. This is supported by the following independent reasoning: To bring the unfavorably oriented mainshock rupture to failure requires the decrease of the effective normal stress, most likely by high fluid pressure. Furthermore, the detected aseismic forcing according to an exponential function is characteristic for emptying a pressured fluid reservoir, which has been opened by the mainshock rupture. Finally, pore pressure diffusion in response to an exponentially decaying injection rate gives excellent prediction of the observed spatiotemporal evolution of aftershock hypocenters, particularly of those events associated to background forcing.

The presence of pressurized fluids (most probably CO_2) in the faults in West Bohemia/Vogtland has been suggested before by various studies. By analyzing the moment tensors of the 1997 swarm and the corresponding fault tractions, *Vavryčuk* [2002] has estimated the fluid pressure acting on the fault was almost lithostatic. *Hainzl et al.* [2012] has attributed the vertical asymmetry of the hypocenter migration during the 2008 swarm to driving stress gradients, which allowed to estimate that the injection pressure responsible for driving the activity exceeded the minimum stress component by about 20 MPa. Also, in other regions, the release of crustal fluids has been previously identified to trigger seismicity, e.g., during the 1997 Umbria-Marche sequence [*Miller et al.*, 2004] and after the 2009 L'Aquila earthquake [*Chiarabba et al.*, 2015]. Evidence comes also from strong earthquakes as in the case of 2008 Wenchuan M_s8.0 [*Liu et al.*, 2014] and 2011 Tohoku-oki M_w9.0 [*Terakawa et al.*, 2013] mainshocks, whose aftershocks were, based on pore pressure diffusion and Coulomb failure analysis, partly driven by an increase of fluid pressure in the fault.

The occurrence of classical mainshock-aftershock sequences in a location of repeated swarm activity as reported in our study raises the general question about the generation mechanism of swarm and mainshock-aftershock sequences. Can a fault zone undergo a system change with time from swarm-type to main shock-aftershock-type seismic energy release? If yes, this could have important implications for the regional seismic hazard assessment. However, our study shows that this is probably not the case in the source region of Nový Kostel. The occurrence of the mainshocks seems to be related to the geometrical step over of the fault plane, which is less favorably oriented to the regional stress field than in-plane activity, explaining why it has not been ruptured during previous swarms. However, the mainshock was likely facilitated by positive static stress transfers from precursory swarm activity and finally failed. Its rupture seemed to open a fluid pathway connecting hydraulically a high-pressure source with the fault zone leading to a fluid intrusion with exponentially decreasing rate due to a limited source volume. In addition to the static stress changes of the mainshock, the pressure changes associated to the fluid intrusion likely triggered the observed seismicity in the fault plane. This explains the migration patterns as well as the unusual productivity and shape parameters of the observed Omori-Utsu aftershock decay.

Acknowledgments

We are grateful to the Editor Yehuda Ben-Zion, the anonymous Associate Editor, and two reviewers for their helpful suggestions. This work was supported by the grant project P210/12/2336 of the Grant Agency of the Czech Republic, and the monitoring system WEBNET providing earthquake data was supported by the Ministry of Education, Youth, and Sport of the Czech Republic (project LM2010080). The authors thank Josef Horálek for providing the waveform data of the WEBNET [*Institute of Geophysics*, 1991] seismic network. For the relocated earthquake catalog and obtained focal mechanisms, please contact Tomas Fischer (fischer@natur.cuni.cz).

References

Braeuer, K., H. Kaempf, U. Koch, S. Niedermann, and G. Strauch (2007), Seismically induced changes of the fluid signature detected by a multi-isotope approach (He, CO_2, CH_4, N_2) at the Wettinquelle, Bad Brambach (central Europe), *J. Geophys. Res.*, *112*, B04307, doi:10.1029/2006JB004404.

Båth, M. (1965), Lateral inhomogeneities in the upper mantle, *Tectonophysics*, *2*, 483–514, doi:10.1016/0040-1951(65)90003-X.

Čermáková, H., and J. Horálek (2015), The 2011 West Bohemia (Central Europe) earthquake swarm compared with the previous swarms of 2000 and 2008, *J. Seismol.*, *19*, 899–913, doi:10.1007/s10950-015-9502-3.

Chiarabba, C., P. De Gori, and P. M. Mele (2015), Recent seismicity of Italy: Active tectonics of the central Mediterranean region and seismicity rate changes after the M_w6.3 L'Aquila earthquake, *Tectonophysics*, *638*, 82–93, doi:10.1016/j.tecto.2014.10.016.

Chiaraluce, L. (2012), Unravelling the complexity of Apenninic extensional fault systems: A review of the 2009 L'Aquila earthquake (Central Apennines, Italy), *J. Struct. Geol.*, *42*, 2–18, doi:10.1016/j.jsg.2012.06.007.

Courboulex, F., A. Dujardin, M. Vallee, B. Delouis, C. Sira, A. Deschamps, L. Honore, and F. Thouvenot (2013), High-frequency directivity effect for an M_w 4.1 earthquake, widely felt by the population in southeastern France, *Bull. Seismol. Soc. Am.*, *103*, 3347–3353.

Dieterich, J. H. (1994), A constitutive law for rate of earthquake production and its application to earthquake clustering, *J. Geophys. Res.*, *99*, 2601–2618.

Duverger, C., M. Godano, P. Bernard, and H. Lyon-Caen (2015), The 2003–2004 seismic swarm in the western Corinth rift: Evidence for a multiscale pore pressure diffusion process along a permeable fault system, *Geophys. Res. Lett.*, *42*, 7374–7382, doi:10.1002/2015GL065298.

Enescu, B., J. Mori, and M. Miyazawa (2007), Quantifying early aftershock activity of the 2004 mid-Niigata Prefecture earthquake (M_w6.6), *J. Geophys. Res.*, *112*, B04310, doi:10.1029/2006JB004629.

Fischer, T. (2003a), Automatic location of swarm earthquakes from local network data, *Stud. Geophys. Geod.*, *47*, 83–98.

Fischer, T. (2003b), The August-December 2000 earthquake swarm in NW Bohemia: The first results based on automatic processing of seismograms, *J. Geodyn.*, *35*(1–2), 59–81.

Fischer, T., J. Horálek, J. Michálek, and A. Boušková (2010), The 2008-West Bohemia earthquake swarm in the light of the WEBNET network, *J. Seismol.*, *14*, 665–682.

Fischer, T., J. Horálek, P. Hrubcová, V. Vavryčuk, K. Braeuer, and H. Kaempf (2014), Intra-continental earthquake swarms in West-Bohemia and Vogtland: A review, *Tectonophysics*, *611*, 1–27, doi:10.1016/j.tecto.2013.11.001.

Geissler, W., H. Kämpf, R. Kind, K. Braeuer, K. Klinge, T. Plenefisch, J. Horalek, J. Zednik, and V. Nehybka (2005), Seismic structure and location of a CO_2 source in the upper mantle of the western Eger (Ohre) Rift, central Europe, *Tectonics*, *24*, TC5001, doi:10.1029/2004TC001672.

Hainzl, S., and T. Fischer (2002), Indications for a successively triggered rupture growth underlying the 2000 earthquake swarm in Vogtland/NW Bohemia, *J. Geophys. Res.*, *107*(B12), 2338, doi:10.1029/2002JB001865.

Hainzl, S., and D. Marsan (2008), Dependence of the Omori-Utsu law parameters on mainshock magnitude: Observations and modeling, *J. Geophys. Res.*, *113*, B10309, doi:10.1029/2007JB005492.

Hainzl, S., and Y. Ogata (2005), Detecting fluid signals in seismicity data through statistical earthquake modeling, *J. Geophys. Res.*, *110*, B05S07, doi:10.1029/2004JB003247.

Hainzl, S., G. B. Brietzke, and G. Zöller (2010), Quantitative earthquake forecasts resulting from static stress triggering, *J. Geophys. Res.*, *115*, B11311, doi:10.1029/2010JB007473.

Hainzl, S., T. Fischer, and T. Dahm (2012), Seismicity-based estimation of the driving fluid pressure in the case of swarm activity in Western Bohemia, *Geophys. J. Int.*, *191*, 271–281.
Hainzl, S., O. Zakharova, and D. Marsan (2013), Impact of aseismic transients on the estimation of aftershock productivity parameters, *Bull. Seismol. Soc. Am.*, *103*, 1723–1732, doi:10.1785/0120120247.
Helmstetter, A., Y. Y. Kagan, and D. D. Jackson (2006), Comparison of short-term and time-independent earthquake forecast models for southern California, *Bull. Seismol. Soc. Am.*, *96*(1), 90–106.
Holschneider, M., C. Narteau, P. Shebalin, Z. Peng, and D. Schorlemmer (2012), Bayesian analysis of the modified Omori law, *J. Geophys. Res.*, *117*, B06317, doi:10.1029/2011JB009054.
Horálek, J., T. Fischer, P. Einarsson, and S. Jakobsdotirr (2015), Earthquake swarms, in *Encyclopedia of Earthquake Engineering*, edited by M. Beer et al., pp. 1–16, Springer, Berlin., doi:10.1007/978-3-642-36197-5_294-1
Institute of Geophysics, A. o. S. o. t. C. R. (1991), West Bohemia local seismic network,International Federation of Digital Seismograph Networks, Other/Seismic Network, doi:10.7914/SN/WB.
Kagan, Y. Y. (2004), Short-term properties of earthquake catalogs and models of earthquake source, *Bull. Seismol. Soc. Am.*, *94*(4), 1207–1228.
Kato, N. (2007), Expansion of aftershock areas caused by propagating post-seismic sliding, *Geophys. J. Int.*, *168*, 797–808.
Lay, T., and T. C. Wallace (1995), *Modern Global Seismology*, Academic Press, San Diego, Calif.
Lengliné, O., and J.-P. Ampuero (2015), Insights on earthquake triggering processes from early aftershocks of repeating micro-earthquakes, *J. Geophys. Res. Solid Earth*, *120*, 6977–6992, doi:10.1002/2015JB012287.
Liu, Y., T. Chen, F. Xie, F. Du, D. Yang, L. Zhang, and L. Xu (2014), Analysis of fluid induced aftershocks following the 2008 Wenchuan M_S8.0 earthquake, *Tectonophysics*, *619–620*, 149–158, doi:10.1016/j.tecto.2013.09.010.
Lohman, R. B., and J. J. McGuire (2007), Earthquake swarms driven by aseismic creep in the Salton Trough, California, *J. Geophys. Res.*, *112*, B04405, doi:10.1029/2006JB004596.
Marsan, D., E. Prono, and A. Helmstetter (2013), Monitoring aseismic forcing in fault zones using earthquake time series, *Bull. Seismol. Soc. Am.*, *103*(1), 169–179.
McGarr, A. (2014), Maximum magnitude earthquakes induced by fluid injection, *J. Geophys. Res. Solid Earth*, *119*, 1008–1019, doi:10.1002/2013JB010597.
Michálek, J., and T. Fischer (2013), Source parameters of the swarm earthquakes in West Bohemia/Vogtland, *Geophys. J. Int.*, *195*, 1196–1210.
Miller, S. A., C. Collettini, L. Chiaraluce, M. Cocco, M. Barchi, and B. J. P. Kaus (2004), Aftershocks driven by a high-pressure CO_2 source at depth, *Nature*, *427*, 724–727.
Mogi, K. (1963), Some discussions on aftershocks, foreshocks and earthquake swarms—The fracture of a semi-infinite body caused by an inner stress origin and its relation to the earthquake phenomena (third paper), *Bull. Earthquake Res. Inst. Univ. Tokyo*, *41*, 615–658.
Neunhöfer, H., and A. Hemmann (2005), Earthquake swarms in the Vogtland/Western Bohemia region: Spatial distribution and magnitude-frequency distribution as an indication of the genesis of swarms?, *J. Geodyn.*, *39*, 361–385.
Nur, A., and J. R. Booker (1972), Aftershocks caused by pore fluid flow?, *Science*, *175*, 885–887.
Ogata, Y. (1988), Statistical models for earthquake occurrence and residual analysis for point processes, *J. Am. Stat. Assoc.*, *83*, 9–27.
Ohmi, S., K. Watanabe, T. Shibutani, N. Hirano, and S. Nakao (2002), The 2000 Western Tottori earthquake—Seismic activity revealed by the regional seismic networks, *Earth Planets Space*, *54*, 831–845.
Okada, Y. (1992), Internal deformation due to shear and tensile faults in a half-space, *Bull. Seismol. Soc. Am.*, *82*, 1018–1040.
Parotidis, M., E. Rothert, and S. A. Shapiro (2003), Pore-pressure diffusion: A possible triggering mechanism for the earthquake swarms 2000 in Vogtland/NW-Bohemia, central Europe, *Geophys. Res. Lett.*, *30*(20), 2075, doi:10.1029/2003GL018110.
Peng, Z. G., J. E. Vidale, and H. Houston (2006), Anomalous early aftershock decay rate of the 2004 M_w6.0 Parkfield, California, earthquake, *Geophys. Res. Lett.*, *33*, L17307, doi:10.1029/2006GL026744.
Peng, Z., and P. Zhao (2009), Migration of early aftershocks following the 2004 Parkfield earthquake, *Nat. Geosci.*, *2*, 877–881.
Perfettini, H., and J.-P. Avouac (2004), Postseismic relaxation driven by brittle creep: A possible mechanism to reconcile geodetic measurements and the decay rate of aftershocks, application to the Chi-Chi earthquake, Taiwan, *J. Geophys. Res.*, *109*, B02304, doi:10.1029/2003JB002488.
Reasenberg, P. A., and L. M. Jones (1994), Earthquake aftershocks: Update, *Science*, *265*, 1251–1252.
Rudnicki, J. W. (1986), Fluid mass sources and point forces in linear elastic diffusive solids, *Mech. Mater.*, *5*(4), 383–393.
Segall, P., and S. Lu (2015), Injection-induced seismicity: Poroelastic and earthquake nucleation effects, *J. Geophys. Res. Solid Earth*, *120*, 5082–5103, doi:10.1002/2015JB012060.
Shapiro, S. A., C. Krüger, and C. Dinske (2013), Probability of inducing given-magnitude earthquakes by perturbing finite volumes of rocks, *J. Geophys. Res. Solid Earth*, *118*, 3557–3575, doi:10.1002/jgrb.50264.
Shelly, D. R., T. A. Taira, S. G. Prejean, D. P. Hill, and D. S. Dreger (2015), Fluid-faulting interactions: Fracture-mesh and fault-valve behavior in the February 2014 Mammoth Mountain, California, earthquake swarm, *Geophys. Res. Lett.*, *42*, 5803–5812, doi:10.1002/2015GL064325.
Stein, R. S. (1999), The role of stress transfer in earthquake occurrence, *Nature*, *402*, 605–609.
Terakawa, T., C. Hashimoto, and M. Matsu'ura (2013), Changes in seismic activity following the 2011 Tohoku-oki earthquake: Effects of pore fluid pressure, *Earth Planet. Sci. Lett.*, *365*, 17–24, doi:10.1016/j.epsl.2013.01.017.
Toda, S., R. S. Stein, V. Sevilgen, and J. Lin (2011), Coulomb 3.3 graphic-rich deformation and stress-change software for earthquake, tectonic, and volcano research and teaching user guide, *U.S. Geol. Surv. Open-File Rep. 2011-1060*, p. 63, U.S. Geol. Surv., Reston, Va.
Utsu, T., Y. Ogata, and R. S. Matsu'ura (1995), The centenary of the Omori formula for a decay law of aftershock activity, *J. Phys. Earth*, *43*, 1–33.
Vavryčuk, V. (2002), Non-double-couple earthquakes of January 1997 in West Bohemia, Czech Republic: Evidence of tensile faulting, *Geophys. J. Int.*, *149*, 364–373.
Vavryčuk, V. (2009), *The Amplitude Moment Tensor Inversion—Program AMT, Comput. Codes Lib.*, Inst. of Geophys., Prague.
Vavryčuk, V. (2014), Iterative joint inversion for stress and fault orientations from focal mechanisms, *Geophys. J. Int.*, *199*, 69–77, doi:10.1093/gji/ggu224.
Vidale, J. E., and P. M. Shearer (2006), A survey of 71 earthquake bursts across southern California: Exploring the role of pore fluid pressure fluctuations and aseismic slip as drivers, *J. Geophys. Res.*, *111*, B05312, doi:10.1029/2005JB004034.
Waldhauser, F. (2001), hypoDD: A computer program to compute double-difference hypocenter locations, *U.S. Geol. Surv. Open File Rep. 01113*, pp. 1–25, U.S. Geol. Surv., Menlo Park, Calif.
Waldhauser, F., and W. Ellsworth (2000), A double-difference earthquake location algorithm: Method and application to the northern Hayward fault, California, *Bull. Seismol. Soc. Am.*, *90*(6), 1353–1368, doi:10.1785/0120000006.

Wirth, W., T. Plenefisch, K. Klinge, K. Stammler, and D. Seid (2000), Focal mechanisms and stress field in the region Vogtland/Western Bohemia, *Stud. Geophys. Geod.*, *44*, 126–141.

Zhuang, J., and Y. Ogata (2004), Analyzing earthquake clustering features by using stochastic reconstruction, *J. Geophys. Res.*, *109*, B05301, doi:10.1029/2003JB002879.